REDUCED-ORDER MODEL FRAMEWORK FOR THERMOCHEMICAL NON-EQUILIBRIUM HYPERSONIC FLOWS

BY

ROBYN LINDSAY MACDONALD

DISSERTATION

Submitted in partial fulfillment of the requirements
for the degree of Doctor of Philosophy in Aerospace Engineering
in the Graduate College of the
University of Illinois at Urbana-Champaign, 2019

Urbana, Illinois

Doctoral Committee:

Associate Professor Marco Panesi, Chair and Director of Research
Professor J. Craig Dutton
Professor So Hirata
Dr. Richard L. Jaffe, Senior Research Scientist, NASA Ames Research Center

Abstract

The study of vehicles traveling at hypersonic speeds is extremely complex and involves many different non-equilibrium physical phenomena occurring on many different time-scales. As a result, work focused on modeling this type of flowfield has been hindered by inaccurate physical and chemical models. For example, the conventional approach to model chemical non-equilibrium, still widely used today, was developed nearly 40 years ago and relies heavily on calibration with heritage experimental data. However, advances in both computational chemistry and computational power have enabled the construction of extremely detailed models for the chemical non-equilibrium effects based on *ab initio* quantum chemistry data, called the state-to-state (StS) approach. Although the StS approach affords unprecedented accuracy for predictions of thermochemical non-equilibrium, it cannot be applied to study molecule-molecule interactions due to the massive computational cost. Unfortunately, due to the enormous cost of both computing data for and applying the StS approach, this method can only be used in highly simplified test cases. This motivates the development of reduced order models for chemical non-equilibrium which can capture the essential physics at a massively reduced cost. The objective of this work is twofold: first to present a model reduction framework for application to chemical non-equilibrium based on fundamental physics principles; and second, to use this framework to study thermochemical non-equilibrium in a variety of conditions for a gas composed of nitrogen atoms and molecules. In order to construct the reduced order model directly from *ab initio* quantum chemistry data, kinetic data is calculated directly for the model using the quasi-classical trajectory (QCT) method. This bypasses the need to compute StS kinetic data for 10^{15} reactions resulting from the interaction between two nitrogen molecules, an impossible task. The model reduction framework, called the multi-group maximum-entropy quasi-classical trajectory (MGME-QCT) method, provides a crucial link between the *ab initio* quantum chemistry data and multi-dimensional computational fluid dynamics (CFD).

The MGME-QCT method is used to construct a reduced order model for a mixture of nitrogen atoms and molecules using an *ab initio* potential energy surface (PES) to describe the interaction between particles. In the MGME model, energy states are lumped together into groups containing states with similar properties, and the distribution of states within each of these groups is reconstructed by leveraging the maximum entropy principle. Two types of reduced order models are constructed: one based on conventional wisdom which relies on the assumption of strict separation of rotational and vibrational energy, and one which relies on the assumption of strong rovibrational coupling. In a study of the isothermal relaxation of nitrogen molecules, it is found using these two approaches that the underlying assumptions made in conventional chemical non-equilibrium models (*i.e.*, that vibrational and rotational modes are decoupled) result in incorrect predictions about the dissociation process. In contrast, the groups constructed assuming rovibrational equilibrium better capture the dynamics of the dissociation process. This finding is confirmed through comparison with a detailed molecular dynamics approach. Finally, the applicability of the MGME-QCT method to CFD is demonstrated through application to a handful of simple test cases including a standing shock wave, and the flow through a nozzle. These test cases demonstrate the flexibility of this approach in modeling a variety of flow regimes (*e.g.*, both compressing and expanding flows).

For my family.

Acknowledgments

First, I would like to thank my advisor, Professor Marco Panesi, for his support and mentorship. Marco has been an excellent mentor and source of inspiration. His passion for research is infectious and provides a constant source of motivation.

I would like to thank my committee, Professor Panesi, Professor Dutton, Professor Hirata, and Dr. Jaffe for their constructive comments and evaluation of my work.

I am grateful to Dr. Richard Jaffe and Dr. David Schwenke from NASA Ames Research Center for the fruitful discussions and their patience in answering my questions. I would also thank Rich and David for providing me the VVTC code, PESs, and kinetic database as a starting point for my project.

I would like to thank my collaborators at the University of Minnesota: Professor Tom Schwartzentruber and Dr. Maninder Grover. I am grateful to Professor Elena Kustova from Saint Petersburg State University for her helpful comments on the kinetic theory portion of this work.

I am extremely grateful to the wonderful mentors and educators at the University of Illinois, especially to Professor Craig Dutton for his excellent mentoring and unwavering support throughout both my undergraduate and graduate careers.

I would like to thank my colleagues at the University of Illinois, Andrea Alberti, Vegnesh Jayaraman, Dr. Bruno Lopez, Dr. Alessandro Munafò, Przemyslaw Rostkowski, Amal Sahai, Maitreyee Sharma, Simone Venturi, and all others who have passed through the lab for their constant support and constructive feedback. I am particularly grateful to Dr. Alessandro Munafò for providing me access to your many computational tools you have developed (KONIG - 0/1D solver, Max-Entropy, Plato, and HEGEL).

I would like to thank my parents, Loch and Sheilah, my siblings, Erin and Iain, and of course Sunshine for their constant love and support. Finally, to Greg, thank you for your support and

understanding throughout these past five and a half years. I would not be where I am today without their encouragement.

I was supported by the Department of Defense (DoD) through the National Defense Science & Engineering Graduate Fellowship (NDSEG) Program. This work was supported by the Air Force Office of Scientific Research Young Investigators Program No. FA9550-15-1-0132 with Program Officer Dr. Ivett Leyva. The large computations for this work were carried out on the NASA Pleiades Supercomputer at NASA Ames Research Center.

Table of Contents

List of Tables

List of Figures

List of Abbreviations

B	Bound
BGK	Bhatnagar-Gross-Krook
CCSD(T)	Coupled-cluster single double
CFD	Computational fluid dynamics
CVD	Coupled vibration dissociation
d	Diffusion
dis	Dissociation
DMS	Direct molecular simulation
DSMC	Direct simulation Monte Carlo
e	Electron
EAST	Electric arc shock tube
el	Elastic
exc	Exchange
FHO	Forced harmonic oscillator
in	Non-reactive inelastic
int	Internal
LEPS	London-Eyring-Polanyi-Sato
MGME	Multi-group maximum-entropy
MGMEL	Multi-group maximum-entropy linear
MGMET	Multi-group maximum-entropy thermal
MT	Multi-temperature
n	Nuclear

PES	Potential energy surface
QB	Quasi-bound
QCT	Quasi-classical trajectory
QSS	Quasi-steady-state
re	Reactive
SSH	Schwartz-Slawsky-Herzfeld
StS	State-to-state
tra	Translational
VT	Vibration-translation
VV	Vibration-vibration
VVTC	Vectorized Variable timestep Trajectory Code
WKB	Wentzel-Kramers-Brillouin

List of Symbols

A	Species
a	Degeneracy
B	Species
b	Impact parameter
C	Species
C	Group reaction rate coefficient or energy transfer coefficient
$\mathcal{C}$	Collision set
$\mathbf{C}$	Peculiar velocity vector
$\mathbf{c}$	Molecular velocity vector
D	Species
E	Species
E	Level energy or total system energy
$\mathcal{E}$	Set of electrons
e	Energy density
$\mathcal{F}$	Distribution of internal energy states
f	Velocity distribution function
$\mathbf{G}$	Center of mass velocity vector
$\mathbf{g}$	Relative velocity vector
g	Relative velocity magnitude
$\mathcal{H}$	Set of nuclei
$\hat{H}$	Hamiltonian operator
$\mathrm{h_P}$	Planck's constant

$\hbar$	Reduced Planck's constant
h	Enthalpy density
$\mathcal{I}$	Set of internal energy levels
i	Energy level index
J	Rotational quantum number
$\mathbf{J}$	Angular momentum vector
j	Energy level index
K	Group reaction rate coefficient or energy transfer coefficient
k	Energy level index
$\mathrm{k_B}$	Boltzmann's constant
l	Energy level index
m	Mass, moment, or energy level index
$\mathcal{N}_s$	Set containing all species and their internal levels
n	Number density
$\mathbf{P}$	Center of mass momentum vector
P	Differential probability of transition or center of mass momentum component
$\mathbf{p}$	Momentum vector
p	Group index or momentum component
$\mathbf{Q}$	Center of mass position vector
Q	Collision operator, partition function, or center of mass position component
q	Group index
r	Group index or internuclear distance
$\mathbf{R}$	Nuclear coordinates
$\mathbf{r}$	Electron coordinates
R	Distance between centers of mass
$\mathcal{S}$	Set of species
S	Entropy
s	Group index
T	Temperature or kinetic energy

$\hat{T}$	Kinetic energy operator
t	Time or group index
$\mathbf{V}$	Relative velocity vector
$\hat{V}$	Potential energy operator
$\mathbf{v}$	Hydrodynamic velocity vector
$\mathfrak{v}$	Entropy source term
v	Vibrational quantum number
W	Transition probability density
$\mathbf{w}$	Group average velocity vector
$\mathbf{x}$	Position vector
x	Position component
Z	Atomic number
α	Group coefficient
β	Statistical weight or group coefficient
$\boldsymbol{\gamma}$	Group coefficient vector
δ	Group coefficient or Kronecker-Delta function
ε	Polar angle
ε_0	Permittivity of free space
η	Orientation of rotational momentum
θ	Azimuthal angle
κ	State-to-state reaction rate coefficient
μ	Reduced mass
ρ	Density
σ	Cross-section
τ	Time scale
ϕ	Electronic wavefunction or polar angle
χ	Nuclear wavefunction or symmetry factor
$\boldsymbol{\psi}$	Collisional invariant vector
ψ	Wavefunction

$\dot{\Omega}$ Energy source term

$\boldsymbol{\omega}$ Scattering direction unit vector

$\dot{\omega}$ Mass source term

Chapter 1

Introduction

1.1 Motivation

Motivated by both national defense and space exploration, hypersonic aerothermodynamics has been the subject of study for decades. Examples of the types of vehicles traveling in this flow regime are shown in Fig. 1.1. One obvious application of hypersonic flight is during atmospheric entry (Fig. 1.1b), but improvements in propulsion systems have motivated studies and the development of advanced aircraft designed to travel at hypersonic speeds within the atmosphere (Fig. 1.1a). During hypersonic flight a multitude of physical phenomena, including chemistry, radiation, turbulence, and ablation, occur simultaneously. As a result, the study of hypersonic flows requires integration among many fields including chemistry, kinetic theory, high-performance computing, electromagnetism, and material science, to name a few. Due to the exorbitant cost of hypersonic flight testing, we must rely heavily on computational fluid dynamics (CFD) for vehicle design. However, the complex multi-physics nature of these flowfields necessitates accurate models for all these fundamental physics. Differences in both the spatial and temporal scales for different processes make accurately simulating hypersonic flows a formidable task.

One key feature of hypersonic flows is the presence of strong shock waves. Because the velocity of the flow is so large, the temperature across the shock wave can jump by tens of thousand of Kelvin. The kinetic energy of the flow is instantaneously converted to thermal energy of the constituent molecules of the gas. However, the internal modes (*i.e.*, electronic, vibrational, and rotational) cannot instantaneously adjust to this transfer of energy and are thus referred to as frozen across the shock wave [1, 2]. Therefore, immediately behind the shock wave the gas is in a state of internal energy non-equilibrium. Moreover, if there is sufficient energy available, chemical reactions including exchange, dissociation, and eventually ionization can occur. Because the shock wave is

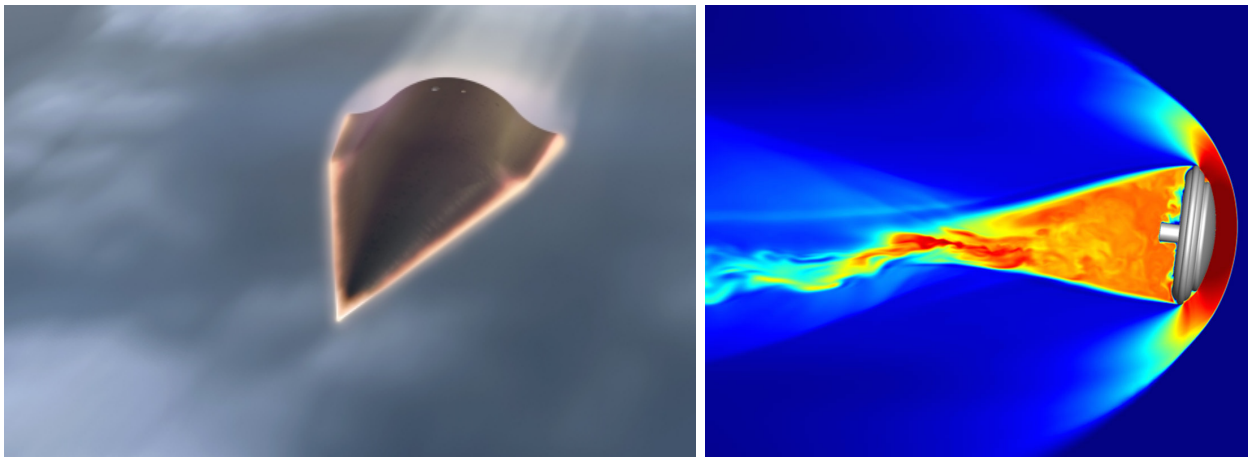

(a) DARPA Hypersonic Test Vehicle (Credit: DARPA).

(b) CFD simulation of a free flying model in a ballistic range (Credit: Joseph Brock, NASA Ames Research Center)

Figure 1.1: Examples of applications of hypersonic flows.

a discontinuity in the flow characterized by an instantaneous change in the flow properties, the finite nature of these chemical processes is important. Chemical processes can have an impact on both the heat flux (convective and radiative) experienced by the vehicle as well as the aerodynamic performance. The rapid compression of gas is not the only source of non-equilibrium in hypersonic flows. In regions where the gas expands, such as around the shoulder of an atmospheric entry vehicle, these non-equilibrium effects play a major role. Due to rapid expansion, it is possible that the time required for the flow to reach equilibrium exceeds the time scale of the flowfield. This causes the flow to freeze, and the composition of the gas remains unchanged throughout the flowfield despite changes in the thermodynamic state. In this situation, the composition of the gas must be determined using finite rate chemistry, and the relevant reactions include exothermic processes such as recombination. All these chemical processes couple with a multitude of other physical phenomena occurring, such as those specified in Fig. 1.2, creating an extremely complex multi-physics flowfield. Moreover, models for the other physical effects (*e.g.*, ablation and radiation) rely on accurate predictions of the state of gas as this can have significant impacts on phenomena such as material response and radiation.

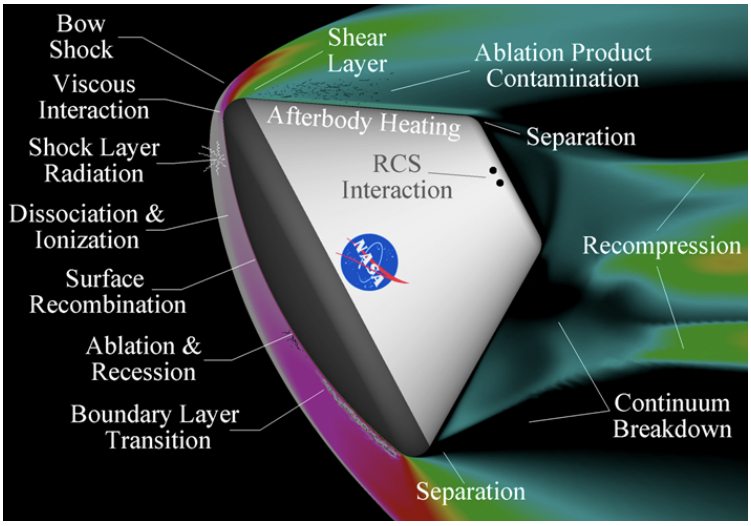

Figure 1.2: Annotated schematic of a vehicle entering the atmosphere with the various physical phenomena noted (Credit: NASA).

1.2 Literature review

Efforts to accurately simulate non-equilibrium chemistry for application to CFD range from computationally inexpensive, purely empirical models developed by calibrating experimental data to model form parameters to highly accurate quantum chemistry studies which are computationally intractable for application to multi-dimensional CFD simulations.

1.2.1 Multi-temperature models

The multi-temperature (MT) model was first proposed by Appleton and Bray [3] to model ionized gases using a heavy particle temperature and electron temperature and a form for the energy exchange terms derived from kinetic theory. Lee [4] extended this approach further in 1984, applying it to account also for vibrational non-equilibrium. Park simplified this approach in the 1980's, applying it generally to the internal energy modes of heavy particles (*i.e.*, rotational, vibrational, and electronic modes) [2, 5–8]. In the MT model, the conservation equations comprise the conservation of species mass, total momentum, total energy, and additional equations for conservation of energy modes (*e.g.*, conservation of vibrational, electron, and electronic energy as in the Park two-temperature model). A detailed description of the conservation equations for the two- and three-temperature models can be found in Ref. [9]. The additional conservation equations required

for the MT approach require energy coupling terms which describe the rate at which energy is transferred among various modes and depend on the collisional processes.

Several models exist for describing energy transfer among various modes. In particular there has been significant work in describing the exchange between translational and vibrational (VT) energy [10, 11], exchanges of energy among vibrational modes (VV) [12, 13], and the coupling between vibrational energy and the dissociation process [2, 14]. The reason for this is twofold: first, the relatively large energy spacing between vibrational states means it is significantly slower to relax or equilibrate with faster modes such as rotational and translational; second, the rate of dissociation is believed to have a strong dependence on the vibrational energy. Moreover, VV terms are of particular interest because different molecules can have significantly different vibrational energy spacing. This can lead to non-equilibrium among vibrational modes of different molecules (*i.e.*, multiple vibrational temperatures are required to describe the non-equilibrium distribution of a mixture). Because low lying vibrational states in particular have relatively constant energy spacing, resonant transitions are possible both among molecules of the same species as well as different species. These resonant transitions can enhance vibrational relaxation within as well as among species [15]. Therefore, in the MT framework it is not uncommon to use a different vibrational temperature for each individual species to account for this difference in relaxation times.

The Landau-Teller model, first published in 1936, is widely used to describe the VT energy transfer terms, making use of relaxation times derived from theory or calibrated from experiments [2, 16, 17]. One of the primary limitations with this approach is the assumption of mono-quantum transitions in the derivation; however, Park [18] demonstrated that particularly in the shock-layer, there is sufficient energy available in the flow that multi-quantum transitions are significant [19]. In addition to the source terms related to the exchange of energy among vibrational modes, the energy equations in the MT model require terms to describe energy lost or gained due to chemical reactions. In particular there are several models for the energy lost from the vibrational mode due to dissociation reactions. The first attempt to quantify the energy loss from the vibrational mode due to dissociation, called the coupled vibration-dissociation (CVD) model, was accomplished by Hammerling *et al* [20]. This model is a preferential dissociation model, which

assumes that the energy lost from the vibrational mode due to dissociation is significantly higher than the average vibrational energy. There has been significant work to improve upon this type of preferential dissociation model, using both empirical methods as well as theoretical approaches. Losev provides a fairly extensive list of the existing chemistry coupling models for dissociation [21]. Broadly, these models can be lumped into one of three groups: empirical, semi-empirical, and theoretical. In the first category, empirical models, is the widely used Park model which uses a geometric average of the vibrational and translational temperatures to calculate rate coefficients which are calibrated against experimental data [2, 22]. Semi-empirical models generally couple a non-equilibrium factor with a dissociation rate. This factor accounts for the non-equilibrium distribution which exists during the dissociation process and is a function of the translational and vibrational temperatures [14, 20, 23–29]. Finally, the theoretical models avoid the use of empirical factors by building a model purely on a theoretical basis [11, 27, 30–32].

In contrast, there has been comparatively little work focused on rotational non-equilibrium. This is because it is generally assumed that the rotational mode instantly reaches equilibrium with the translational mode due to the relatively small energy spacing among rotational states. There were a handful of experimental studies of the non-equilibrium rotational distribution completed in the 1960's [33, 34]. In order to model the rotational relaxation process, both the exponential band gap [35, 36] and power law [37] models were developed. Recently however, Panesi *et al.* [38] found that particularly at high temperatures, the rotational mode does not reach equilibrium with the translational mode throughout the dissociation process. Moreover, the rotational relaxation time approaches the same time scale as the vibrational relaxation time for high temperature cases. Therefore, an accurate model which accounts simultaneously for rotational and vibrational non-equilibrium is necessary for strong non-equilibrium conditions.

1.2.2 State-to-state models

The State-to-State (StS) approach to modeling chemical non-equilibrium aims to overcome the limitations of the MT model by directly tracking the individual state populations. The composition of each energy state is solved for directly by considering the depleting and replenishing processes for that state [19]. This can be done to varying levels of accuracy ranging from electronic StS (least

accurate) to ro-vibronic StS (most accurate). Electronic StS models consider only the electronic states of atoms or molecules and have been used to study both atomic and molecular species in several applications [39–44]. The vibrational StS model considers separately the vibrational states of molecules in a mixture. This method can be considered in two forms: one in which the rotational mode is assumed to be in equilibrium with the translational mode, and one in which the molecules are assumed to be rotationless [45–57]. Finally, the rovibrational StS model considers each individual rovibrational state independently. Because even a simple diatomic molecule can have on the order of hundreds of thousands of rovibrational states, this approach rapidly becomes computationally intractable. However, it can and has been used for simple relaxation and dissociation studies to help understand the physics of the non-equilibrium dissociation process [38, 58, 59].

The accuracy of the simulations depends on the accuracy of the underlying kinetic data. In the realm of vibrational StS models, up until quite recently most of the data was based on empirical models, such as the ladder climbing model [60, 61], or semi-classical models such as the Forced Harmonic Oscillator (FHO) [62–69] or the Schwartz-Slawsky-Herzfeld (SSH) model [15, 26, 70]. In addition, Procaccia and Levine developed a theory for calculating vibrational StS rates based on surprisal analysis [71–73]. However, due to advances in computational chemistry, recent work has focused on making use of *ab initio* quantum chemistry data to both construct kinetic data necessary for StS models as well as inform new models.

1.2.3 *Ab initio* chemistry models

Advances in computational power have enabled a multitude of work recently aimed at calculating directly from the Schrödinger equation the potential energy surfaces (PESs) for systems relevant to air chemistry. The PES describes the potential energy felt among a system of nuclei. This can be calculated directly from the Schrödinger equation or can be inferred from experimental data. There has been significant work recently to characterize the PESs for several systems of interest to high-temperature air chemistry. These include the N_2-N system [74–76], N_2-N_2 system [77–79], O_2-O system [80], O_2-O_2 system [81, 82], N_2-O system [83], and N_2-O_2 system [84].

The PES can be used to calculate the kinetic data for a system by using a scattering method to determine transition probabilities. Using the *ab initio* PES allows for the construction of a high-

fidelity StS kinetic mechanism for certain simple systems (*e.g.*, three-body interactions such as N_2-N). Several scattering methods exist for this approach, ranging from classical approaches, such as the quasi- and semi-classical trajectory approaches to fully quantum mechanical approaches [85]. The quasi-classical trajectory (QCT) method, which will be used in this work, assumes that the motion of the nuclei can be assumed to occur classically; however, the initial and final states for trajectory calculations are mapped from discrete quantum states [86–88]. In this approach, many collisions between particles are simulated by integrating Hamilton's equations of motion for the nuclei, using the PES calculated from the Schrödinger equation. After many collisions have been calculated, the probability that a given transition occurred can be calculated. This probability is related to the transition cross-section or reaction rate coefficient, which can be used in a Direct Simulation Monte Carlo (DSMC) or CFD calculation.

This approach of coupling the *ab initio* PES with QCT calculations to determine kinetic data has been used to study several systems including rovibrational studies of the N_2-N system [38, 59], O_2-O system [51, 52], and the O_2-N system [54] as well as vibrational StS studies of the N_2-Ar [45], N_2-N_2 [46–49, 89], N_2-N [46, 48, 49, 89–93], O_2-O_2 [50, 55], O_2-O [50–52, 56, 57, 94, 95], and O_2-N [57] systems. However, while the use of *ab initio* PESs is increasing, several of these works rely on the use of semi-empirical models to infer reaction rate coefficients. Moreover, it remains prohibitively expensive to construct a full rovibrational StS model for anything more complicated than atom-diatom systems. Therefore despite the level of detail afforded by quantum chemistry calculations, we still require a reduced order model to make use of the quantum chemistry data. Despite a multitude of recent work to make use of the quantum chemistry data to construct CFD models, there is no clear and rigorous path towards a physics based reduced-order model for non-equilibrium chemistry.

1.2.4 Reduced order chemistry models

There has been significant work in recent years to use quantum chemistry data to inform flow chemistry models for application to CFD. Making use of the PESs calculated by Paukku *et al.* [77, 78], Bender *et al.* [79] conducted a detailed study on the two-temperature dynamics of dissociation of nitrogen molecules. This work was extended by Chaudhry *et al.* [96] to consider both nitrogen

and oxygen dissociation with the aim of computing model parameters for a MT approach using *ab initio* data. Using a similar approach, Voelkel *et al.* [97] computed three-temperature dissociation rate coefficients for the N_2-N_2 system using the PES of Paukku *et al.* [77,78]. While this approach of re-computing multi-temperature rates from *ab initio* PES data is appealing because the underlying framework which has been used for decades can be preserved, this approach maintains the same underlying assumption as the MT models. Therefore, it is only valid in near equilibrium conditions. Singh and Schwartzentruber [98] presented a model for describing rotational and vibrational non-equilibrium using surprisal analysis based on results from the Direct Molecular Simulation (DMS) method [99–101]. In this approach, the non-equilibrium distribution of energy states is accounted for using a simple functional form based on surprisal analysis, and couples the non-equilibrium distribution with the dissociation process. Kulakhmetov *et al.* [102] attempted to construct and reduce a full vibrational StS model using the maximum entropy principle detailed in Levine and Bernstein [103]. However, this approach used the maximum entropy principle to infer reaction rate coefficients, rather than inform a model form.

One such approach to reduced order modeling is the multi-group maximum entropy (MGME) model. In this approach, energy states are lumped together according to some metric (*e.g.*, internal energy, vibrational state, etc.), and the states within a group are assumed to equilibrate instantaneously with each other. This approach was initially developed to account for the non-equilibrium electronic distribution of atomic species [41, 104, 105]. It was generalized by Liu *et al.* [106] and used to study the rovibrational states of molecular nitrogen. There has been a multitude of work in studying the N_2-N system using the MGME model because it has known StS kinetic data and can be used for validation [106–115]. This approach is similar to that proposed by Haug *et al.* [72, 73] which lumps energy states together, assuming groups of states reach equilibrium with each other; however, Haug *et al.* only considers the population of each group, assuming the internal distribution of the states is in equilibrium with the translational mode. The MGME model is derived by assuming that the entropy within each group is maximized. Then, depending on the order of reconstruction used, macroscopic governing equations are derived. These can include conservation of group mass and group energy equations. The advantage of this approach is that because the form of the distribution of states is derived by maximizing the entropy, the solution will tend towards an

equilibrium Maxwell-Boltzmann distribution given sufficient time. Moreover, the MGME model framework is general and other simplified models, such as the MT approach, can be derived using the MGME framework. However, one of the main drawbacks with the MGME model is that it relies on the knowledge of microscopic StS kinetic data. Unfortunately, *ab initio* kinetic data is available for very few systems due to the computational cost associated with constructing a complete StS kinetic database. For example, to compute StS data for the N_2-N_2 system would generate on the order of one quadrillion reaction rate coefficients ($\mathcal{O}(10^{15})$). This is an impossible amount of data to both compute and use. Therefore, we need a way to link the MGME model with the scattering calculations performed using the *ab initio* PESs.

1.3 Scope of this thesis

In this thesis, a framework for coupling the MGME model with scattering calculations using the QCT method along with an *ab initio* PES is presented. This approach uses the MGME model to express the distribution of states within a group, and using this distribution, samples initial states for QCT calculations [116–119]. Therefore, the grouped kinetic data for the MGME model can directly be computed. This bypasses the computationally expensive step of constructing a rovibrational StS kinetic model. One of the key advantages to this approach is that the principle of micro-reversibility is used to construct the model. As a result, the model is not only self-consistent, but it can capture both dissociating and recombining flows without the need to simulate trajectories in both directions (*i.e.*, no need to simulate recombining trajectories). Next the kinetic data can be used in CFD calculations to account for the non-equilibrium chemistry.

First, in Chapter 2, a detailed derivation of the full MGME model is presented starting from kinetic theory. This is illuminating because it very clearly shows what assumptions are made in not only the MGME model, but also in the whole range of MT models. The maximum entropy distribution is found to be a linear combination of the collisional invariants. Using this distribution along with the Maxwell transfer equations (moments of the Boltzmann equation), the macroscopic flow governing equations are derived. The grouping model differs from the conventional MT model by introducing additional mass and energy equations for the individual groups.

Next, in Chapter 3 the link is drawn between the kinetic theory derivation and the QCT

method, yielding the MGME-QCT model. This is done by examining the collision integrals present in both the conservation of group mass and group energy equations and re-casting them in terms of variables sampled in the QCT method. In addition, at this point we introduce the concept of micro-reversibility and use it to derive expressions for reverse rates (*i.e.*, de-excitation and recombination).

In Chapter 4, a detailed study of the non-equilibrium excitation and dissociation process in a zero-dimensional isothermal reactor is presented. Two models are compared: a conventional vibrational StS approach (cast in the MGME-QCT framework), and a simple energy based grouping technique. The computational cost in both constructing and running the two models is similar, but the results show significant differences due to the underlying assumptions in each approach.

Chapter 5 presents a demonstration of the full MGME-QCT model, using the micro-reversibility relation to calculate recombination rates from dissociating trajectories. This approach is validated using the N_2-N system.

Chapter 6 presents a comparison of the MGME-QCT model shown in Chapter 4 with the highly accurate DMS method. This comparison highlights the shortcomings of the conventional vibrational StS model, demonstrating that this approach cannot capture accurately the physics of non-equilibrium dissociation.

Chapter 7 demonstrates the applicability of the MGME-QCT model to CFD using a variety of test cases. These include the quasi-one-dimensional flow through a nozzle, and the flow behind a standing shock wave. This demonstrates that the MGME-QCT model is flexible enough for application to a variety of flow conditions.

Finally, in Chapter 8 a summary of the significant findings is presented as well as future work.

1.4 Outcomes of this work

The following publications resulted from this research:

1. **R. L. Macdonald**, R. L. Jaffe, D. W. Schwenke, M. Panesi. "Construction of a coarse-grain quasi-classical trajectory method. I: Theory and application to N_2-N_2 system." *The Journal of Chemical Physics*, Vol. 148, No. 5, 2018, pp. 054309. *Editor's Pick.*

2. **R. L. Macdonald**, M. Grover, T. E. Schwartzentruber, M. Panesi. "Construction of a coarse-grain quasi-classical trajectory method. II: Comparison against the direct molecular simulation method." *The Journal of Chemical Physics*, Vol. 148, No. 5, 2018, pp. 054310.

3. F. Esposito, **R. L. Macdonald**, I. D. Boyd, K. Neitzel, D. A. Andrienko, "Heavy-particle elementary processes in hypersonic flows," in *Hypersonic Meteoroid Entry Physics*, edited by G. Colonna, M. Capitelli, and A. Laricchuita, IOP Series in Plasma Physics, chap. 16, IOP Publishing, 2019.

The following peer reviewed conference publications resulted from this research:

1. **R. L. Macdonald**, R. L. Jaffe, M. Panesi. "Hybrid Reduced Order Model For N_2-N Interactions For Application To Dissociation And Energy Transfer Processes." *Proceedings of the 31st International Symposium on Rarefied Gas Dynamics*, 2018. Accepted.

The following conference publications resulted from this research:

1. A. Munafò, S. Venturi, **R. Macdonald**, M. Panesi. "State-to-state and reduced-order models for recombination and energy transfer in aerothermal environments." *54th AIAA Aerospace Sciences Meeting*, AIAA Paper 2016-0505, San Diego, CA, 2016.

2. **R. L. Macdonald**, A. Munafò, M. Panesi. "Rovibrational grouping for $N_2(X^1\Sigma_g^+)-N_2(X^1\Sigma_g^+)$ energy transfer using state-to-state model." *46th AIAA Thermophysics Conference*, AIAA Paper 2016-4315, Washington, D.C, 2016.

3. **R. L. Macdonald**, R. L. Jaffe, D. W. Schwenke, A. Munafò, M. Panesi. "Ab initio based rovibrational grouping model for $N_2(X^1\Sigma_g^+) - N_2(X^1\Sigma_g^+)$ energy transfer and dissociation." *47th AIAA Thermophysics Conference*, AIAA Paper 2017-3164, Denver, CO, 2017.

4. **R. L. Macdonald**, M. Grover, T. E. Schwartzentruber, M. Panesi. "Coarse grain modeling and direct molecular simulation of nitrogen dissociation." *47th AIAA Thermophysics Conference*, AIAA Paper 2017-3165, Denver, CO, 2017.

5. **R. L. Macdonald**, M. S. Grover, T. E. Schwartzentruber, M. Panesi. "State-to-State and Direct Molecular Simulation Study of energy transfer and dissociation in nitrogen mixtures." *2018 AIAA Aerospace Sciences Meeting*, AIAA Paper 2018-0239, Kissimmee, FL, 2018.

6. **R. L. Macdonald**, M. Panesi. "Coarse Grain Model for Energy Transfer and Dissociation," *2018 AIAA Aerospace Sciences Meeting*, AIAA Paper 2018-1230, Kissimmee, FL, 2018.

Chapter 2

From Particle to Continuum Fluid Modeling

In this chapter, the MGME method will be presented and used to derive macroscopic flow governing equations from kinetic theory. The derivation starts with the Boltzmann equation, which describes the statistical behavior of a gas in non-equilibrium conditions [120]. Through this approach we can directly obtain the flow governing equations for the MGME model in terms of macroscopic quantities of interest. Previous work on the MGME method started from the master equation to derive the governing equations. However, this approach is not general and it is more rigorous and insightful to start from the Boltzmann equation. While starting from the master equation enables the derivation of conservation equations for the MGME model in the absence of flow, starting from the Boltzmann equation allows us to derive a set of conservation equations considering both flow and chemistry. With this approach we will introduce additional collisional invariants to facilitate model closure. In addition, we will use the form of the collision integrals in the Boltzmann equation to link the governing equations with the scattering calculations used to obtain kinetic data for the grouping model. The kinetic theory approach to deriving the MGME governing equations follows the framework presented by Giovangigli [121]. This chapter is organized as follows. Section 2.1 will present the Boltzmann equation and velocity distribution function. Section 2.2 will present the collisional processes considered in this work and the respective forms of the collision integrals. Section 2.3 will present the Maxwell transfer equation used to construct the governing equations. Section 2.4 will derive the MGME method for grouping energy states from the definition of kinetic entropy. Section 2.5 will present the final set of governing equations for the MGME method. Finally, Section 2.6 will present the mass and energy source terms for the MGME method, followed by a summary in Section 2.7.

2.1 Boltzmann equation

Consider a particle of species A in internal state i, at some time t: the position of this particle can be described by vector $\mathbf{x}$, while the velocity can be described by vector $\mathbf{c}_\mathrm{A}$ in the absolute reference frame. If instead we consider all the particles of species A in state i, at time t, the expected number of particles located between $(\mathbf{x}, \mathbf{x} + \mathrm{d}\mathbf{x})$ in physical space and $(\mathbf{c}_\mathrm{A}, \mathbf{c}_\mathrm{A} + \mathrm{d}\mathbf{c}_\mathrm{A})$ in velocity space is given by $f_{\mathrm{A}_i}(\mathbf{x}, \mathbf{c}_\mathrm{A}, t)$. Therefore, the velocity distribution function, f_{A_i}, can be defined:

$$f_{\mathrm{A}_i}(\mathbf{x}, \mathbf{c}_\mathrm{A}, t)\,\mathrm{d}\mathbf{c}_\mathrm{A}\,\mathrm{d}\mathbf{x} = \text{the expected number of particles of species A in state } i \text{ located in volume element } \mathrm{d}\mathbf{x} \text{ about } \mathbf{x} \text{ whose velocities lie within } \mathrm{d}\mathbf{c}_\mathrm{A} \text{ about } \mathbf{c}_\mathrm{A} \text{ at time } t$$

In the absence of external forces (*e.g.* gravity, or magnetic field), the change in the distribution as a function of time can be described by the Boltzmann equation:

$$\frac{\partial f_{\mathrm{A}_i}}{\partial t} + \mathbf{c}_\mathrm{A} \cdot \nabla_\mathbf{x} f_{\mathrm{A}_i} = Q_{\mathrm{A}_i} = Q^{\mathrm{el}}_{\mathrm{A}_i} + Q^{\mathrm{in}}_{\mathrm{A}_i} + Q^{\mathrm{re}}_{\mathrm{A}_i} \tag{2.1}$$

where $\nabla_\mathbf{x}$ denotes the spatial gradient, and Q_{A_i} denotes the collision operator which can be split to account for the contribution of various types of collisions: elastic ($Q^{\mathrm{el}}_{\mathrm{A}_i}$), non-reactive inelastic ($Q^{\mathrm{in}}_{\mathrm{A}_i}$), and reactive ($Q^{\mathrm{re}}_{\mathrm{A}_i}$). The left hand side of the equation accounts for the streaming influence on the velocity distribution function, and the right hand side accounts for the influence of the collisions on the velocity distribution function.

2.2 Collisional processes

Before detailing the collisional processes in this work, some sets need to be defined. First, the set $\mathcal{S}$ denotes the ensemble of chemical components considered. The species will be denoted by $(\mathrm{A}, \mathrm{B}, \mathrm{C}, \mathrm{D}, \mathrm{E})$ and energy levels will be specified by the indices (i, j, k, l, m). The set $\mathcal{I}_A$ denotes all the states of species A. The elastic processes comprise collisions in which no reaction occurs and only translational energy varies. The form of the elastic reaction is given by:

$$\mathrm{A}_i(\mathbf{c}_\mathrm{A}) + \mathrm{B}_j(\mathbf{c}_\mathrm{B}) \leftrightarrows \mathrm{A}_i(\mathbf{c'}_\mathrm{A}) + \mathrm{B}_j(\mathbf{c'}_\mathrm{B}), \quad \mathrm{A}, \mathrm{B} \in \mathcal{S}, \quad i \in \mathcal{I}_\mathrm{A}, \quad j \in \mathcal{I}_\mathrm{B}$$

where the primed variables indicate the post-collision velocities. Non-reactive inelastic processes comprise collisions in which internal energy changes, but the post collision species are the same as the pre-collision species. This type of reaction can be written as:

$$\mathrm{A}_i(\mathbf{c}_\mathrm{A}) + \mathrm{B}_j(\mathbf{c}_\mathrm{B}) \leftrightarrows \mathrm{A}_k(\mathbf{c'}_\mathrm{A}) + \mathrm{B}_l(\mathbf{c'}_\mathrm{B}), \quad \mathrm{A} \in \mathcal{S}, \quad i \in \mathcal{I}_\mathrm{A}, \quad (\mathrm{B}_j, \mathrm{A}_k, \mathrm{B}_l) \in \mathcal{C}^{\mathrm{in}}_{\mathrm{A}_i}$$

where the set $\mathcal{C}_{\mathrm{A}_i}$ is defined as $\mathcal{C}^{\mathrm{in}}_{\mathrm{A}_i} = \{(\mathrm{B}_j, \mathrm{A}_k, \mathrm{B}_l) \,|\, \mathrm{B} \in \mathcal{S}, \quad (i \neq k \vee j \neq l) \wedge (i \neq k \wedge j \neq l), \quad k \in \mathcal{I}_\mathrm{A}, \quad j, l \in \mathcal{I}_\mathrm{B}\}$. Finally, we consider two types of reactive collisions: two body exchange collisions, and dissociation-recombination collisions. Two body exchange collisions can be written as:

$$\mathrm{A}_i(\mathbf{c}_\mathrm{A}) + \mathrm{B}_j(\mathbf{c}_\mathrm{B}) \leftrightarrows \mathrm{C}_k(\mathbf{c'}_\mathrm{C}) + \mathrm{D}_l(\mathbf{c'}_\mathrm{D}), \quad \mathrm{A} \in \mathcal{S}, \quad i \in \mathcal{I}_\mathrm{A}, \quad (\mathrm{B}_j, \mathrm{C}_k, \mathrm{D}_l) \in \mathcal{C}^{\mathrm{exc}}_{\mathrm{A}_i}$$

where the set $\mathcal{C}^{\mathrm{exc}}_{\mathrm{A}_i}$ is defined as $\mathcal{C}^{\mathrm{exc}}_{\mathrm{A}_i} = \{(\mathrm{B}_j, \mathrm{C}_k, \mathrm{D}_l) | (\mathrm{A} \neq \mathrm{C} \wedge \mathrm{B} \neq \mathrm{D}) \wedge (\mathrm{A} \neq \mathrm{C} \vee \mathrm{B} \neq \mathrm{D}), \quad \mathrm{B}, \mathrm{C}, \mathrm{D} \in \mathcal{S}, \quad j \in \mathcal{I}_\mathrm{B}, \quad k \in \mathcal{I}_\mathrm{C}, \quad l \in \mathcal{I}_\mathrm{D}\}$. Dissociation-recombination reactions are restricted to three body reactions in this work, and are written as:

$$\mathrm{A}_i(\mathbf{c}_\mathrm{A}) + \mathrm{B}_j(\mathbf{c}_\mathrm{B}) \leftrightarrows \mathrm{C}_k(\mathbf{c'}_\mathrm{C}) + \mathrm{D}_l(\mathbf{c'}_\mathrm{D}) + \mathrm{B}_m(\mathbf{c'}_\mathrm{B}), \ \mathrm{A} \in \mathcal{S}, \ i \in \mathcal{I}_\mathrm{A}, \ (\mathrm{B}_j, \mathrm{C}_k, \mathrm{D}_l, \mathrm{B}_k) \in \mathcal{C}^{\mathrm{dis}}_{\mathrm{A}_i}$$

where the set $\mathcal{C}^{\mathrm{dis}}_{\mathrm{A}_i}$ denotes the set of species and energy levels participating in the dissociation-recombination reaction. It is very difficult to define this set in the same way as the previous sets, but the key feature is that the species C and D together make species A.

2.2.1 Collision integrals

Elastic collision integral

The elastic collision integral accounts for effects of elastic collisions and can be written as:

$$Q^{\mathrm{el}}_{\mathrm{A}_i} = \sum_{\substack{\mathrm{B} \in \mathcal{S} \\ j \in \mathcal{I}_\mathrm{B}}} Q_{\mathrm{A}_i \mathrm{B}_j}, \quad \mathrm{A} \in \mathcal{S}, \quad i \in \mathcal{I}_\mathrm{A} \tag{2.2}$$

where $Q_{\mathrm{A}_i\mathrm{B}_j} = Q_{\mathrm{A}_i\mathrm{B}_j}(\mathbf{x}, \mathbf{c}_\mathrm{A}, t)$ is the partial elastic collision operator. The partial collision operator can be written as a function of the pre- and post-collision velocity distribution functions:

$$Q_{\mathrm{A}_i\mathrm{B}_j} = \iiint\limits_{\mathbb{R}^3\times\mathbb{R}^3\times\mathbb{R}^3} \left(f'_{\mathrm{A}_i} f'_{\mathrm{B}_j} - f_{\mathrm{A}_i} f_{\mathrm{B}_j} \right) W_{\mathrm{A}_i\mathrm{B}_j}^{\mathrm{A}'_i\mathrm{B}'_j} \, \mathrm{d}\mathbf{c}_\mathrm{B} \, \mathrm{d}\mathbf{c}'_\mathrm{A} \, \mathrm{d}\mathbf{c}'_\mathrm{B} \tag{2.3}$$

where $W_{\mathrm{A}_i\mathrm{B}_j}^{\mathrm{A}'_i\mathrm{B}'_j}$ (units of $((\mathrm{m}^3/\mathrm{s})\ (\mathrm{m/s})^{-3}\ (\mathrm{m/s})^{-3}$) denotes the probability density that this transition will occur (*i.e.*, the probability that a specific transition will occur in an infinitesimal velocity element $(\mathbf{c}_\mathrm{A}, \mathbf{c}_\mathrm{A} + \mathrm{d}\mathbf{c}_\mathrm{A})$ and $(\mathbf{c}_\mathrm{B}, \mathbf{c}_\mathrm{B} + \mathrm{d}\mathbf{c}_\mathrm{B})$ per unit time per unit volume). At this point it is useful to transform variables from the absolute reference frame to a center-of-mass reference frame. The relative and center-of-mass velocities are denoted respectively by $\mathbf{g}$ and $\mathbf{G}$. Full details of this transformation can be found in Appendix A. The relative and center-of-mass velocities are written:

$$\mathbf{g} = \mathbf{c}_\mathrm{A} - \mathbf{c}_\mathrm{B}, \quad \mathbf{G} = \frac{m_\mathrm{A}\mathbf{c}_\mathrm{A} + m_\mathrm{B}\mathbf{c}_\mathrm{B}}{m_\mathrm{A} + m_\mathrm{B}} \tag{2.4}$$

where m_A and m_B denote the masses of species A and B respectively. Using this transformation provides a relationship between the differential absolute velocities and the differential center-of-mass velocities:

$$\mathrm{d}\mathbf{c}_\mathrm{A} \, \mathrm{d}\mathbf{c}_\mathrm{B} = \mathrm{d}\mathbf{g} \, \mathrm{d}\mathbf{G} = g^2 \, \mathrm{d}g \, \mathrm{d}\boldsymbol{\omega} \, \mathrm{d}\mathbf{G}, \quad \mathrm{d}\mathbf{c}'_\mathrm{A} \, \mathrm{d}\mathbf{c}'_\mathrm{B} = \mathrm{d}\mathbf{g}' \, \mathrm{d}\mathbf{G}' = g'^2 \, \mathrm{d}g' \, \mathrm{d}\boldsymbol{\omega}' \, \mathrm{d}\mathbf{G}' \tag{2.5}$$

where $g = |\mathbf{g}|$, and $\boldsymbol{\omega}$ denotes the initial solid angle through which the particles pass or the pre-scattered direction of the particles. The transition probability density is related to the transition differential cross-section, $\sigma = \sigma(g, \boldsymbol{\omega}')$, through the following relationship:

$$\sigma_{\mathrm{A}_i\mathrm{B}_j}(g, \boldsymbol{\omega}') g \, \mathrm{d}\boldsymbol{\omega}' = W_{\mathrm{A}_i\mathrm{B}_j}^{\mathrm{A}'_i\mathrm{B}'_j} \, \mathrm{d}\mathbf{c}'_\mathrm{A} \, \mathrm{d}\mathbf{c}'_\mathrm{B} = W_{\mathrm{A}_i\mathrm{B}_j}^{\mathrm{A}'_i\mathrm{B}'_j} g'^2 \, \mathrm{d}g' \, \mathrm{d}\boldsymbol{\omega}' \, \mathrm{d}\mathbf{G}' \tag{2.6}$$

The differential cross-section has units of area per solid angle. To relate the differential cross-sections for forward and inverse processes, we invoke Fermi's golden rule which states that: $W_{\mathrm{A}_i\mathrm{B}_j}^{\mathrm{A}'_i\mathrm{B}'_j} = W_{\mathrm{A}'_i\mathrm{B}'_j}^{\mathrm{A}_i\mathrm{B}_j}$ [121, 122]. Using this along with the conservation of momentum, and energy relationships

for a collision reveals that the forward and inverse collision differential cross-sections are the same:

$$\sigma_{\mathrm{A}_i\mathrm{B}_j}(g, \boldsymbol{\omega'}) = \sigma_{\mathrm{A}_i\mathrm{B}_j}(g', \boldsymbol{\omega}) \tag{2.7}$$

The partial elastic collision operator can be partially transformed to center-of-mass variables as well to yield a differential cross-section formulation:

$$Q_{\mathrm{A}_i\mathrm{B}_j} = \iint\limits_{\mathscr{L}^2\times\mathbb{R}^3} \left(f'_{\mathrm{A}_i} f'_{\mathrm{B}_j} - f_{\mathrm{A}_i} f_{\mathrm{B}_j}\right) g\sigma_{\mathrm{A}_i\mathrm{B}_j}(g, \boldsymbol{\omega'})\, \mathrm{d}\mathbf{c}_\mathrm{B}\, \mathrm{d}\boldsymbol{\omega'} \tag{2.8}$$

where $\mathscr{L}^2$ denotes the integration over the solid angle.

Inelastic Collision Integral

The inelastic collision integral accounts for the effects of inelastic collisions. The inelastic collision operator can be written as a function of the partial inelastic collision operators:

$$Q^{\mathrm{in}}_{\mathrm{A}_i} = \sum_{\substack{(\mathrm{B}_j,\mathrm{A}_k,\mathrm{B}_l)\\ \in\mathcal{C}^{\mathrm{in}}_{\mathrm{A}_i}}} Q^{\mathrm{A}_k\mathrm{B}_l}_{\mathrm{A}_i\mathrm{B}_j}, \quad \mathrm{A}\in\mathcal{S}, \quad i\in\mathcal{I}_\mathrm{A} \tag{2.9}$$

where the partial collision operator reads:

$$Q^{\mathrm{A}_k\mathrm{B}_l}_{\mathrm{A}_i\mathrm{B}_j} = \iiint\limits_{\mathbb{R}^3\times\mathbb{R}^3\times\mathbb{R}^3} \left(\frac{\beta_{\mathrm{A}_k}\beta_{\mathrm{B}_l}}{\beta_{\mathrm{A}_i}\beta_{\mathrm{B}_j}} f'_{\mathrm{A}_k} f'_{\mathrm{B}_l} - f_{\mathrm{A}_i} f_{\mathrm{B}_j}\right) W^{\mathrm{A}_k\mathrm{B}_l}_{\mathrm{A}_i\mathrm{B}_j}\, \mathrm{d}\mathbf{c}_\mathrm{B}\, \mathrm{d}\mathbf{c'}_\mathrm{A}\, \mathrm{d}\mathbf{c'}_\mathrm{B} \tag{2.10}$$

where $\beta_{\mathrm{A}_i} = \mathrm{h}_\mathrm{P}^3/(a_{\mathrm{A}_i} m_\mathrm{A}^3)$, h_P denotes Planck's constant, and a_{A_i} denotes the degeneracy (statistical weight) of state i of species A. Again, we will transform to center-of-mass coordinates and make use of the conservation of momentum, and energy relations for the collision. Details of this procedure can be found in Appendix A. Following this procedure, the relationship between forward and inverse collision differential cross-sections finally reads:

$$\sigma^{\mathrm{A}_i\mathrm{B}_l}_{\mathrm{A}_k\mathrm{B}_l}(g', \boldsymbol{\omega}) = \sigma^{\mathrm{A}_k\mathrm{B}_l}_{\mathrm{A}_i\mathrm{B}_j}(g, \boldsymbol{\omega'}) \left(\frac{a_{\mathrm{A}_i} a_{\mathrm{B}_j}}{a_{\mathrm{A}_k} a_{\mathrm{B}_l}}\right) \left(1 - \frac{2\Delta E^{\mathrm{A}_k\mathrm{B}_l}_{\mathrm{A}_i\mathrm{B}_j}}{g^2 \mu_{\mathrm{AB}}}\right)^{-1} \tag{2.11}$$

where $\Delta E^{\mathrm{A}_k\mathrm{B}_l}_{\mathrm{A}_i\mathrm{B}_j} = (E_{\mathrm{A}_k} + E_{\mathrm{B}_l}) - (E_{\mathrm{A}_i} + E_{\mathrm{B}_j})$, E_{A_i} denotes the internal energy of state i of species A, and $\mu_{\mathrm{AB}} = m_{\mathrm{A}} m_{\mathrm{B}} / (m_{\mathrm{A}} + m_{\mathrm{B}})$ denotes the reduced mass of the system of particles A and B. Likewise, the partial collision operator can be partially transformed to center-of-mass coordinates to read:

$$Q^{\mathrm{A}_k\mathrm{B}_l}_{\mathrm{A}_i\mathrm{B}_j} = \iint\limits_{\mathscr{L}^2\times\mathbb{R}^3} \left(\frac{a_{\mathrm{A}_i} a_{\mathrm{B}_j}}{a_{\mathrm{A}_k} a_{\mathrm{B}_l}} f'_{\mathrm{A}_k} f'_{\mathrm{B}_l} - f_{\mathrm{A}_i} f_{\mathrm{B}_j} \right) g \sigma^{\mathrm{A}_k\mathrm{B}_l}_{\mathrm{A}_i\mathrm{B}_j} \, \mathrm{d}\mathbf{c}_{\mathrm{B}} \, \mathrm{d}\boldsymbol{\omega}' \tag{2.12}$$

Reactive collision integral

In this work, the reactive collision integral is broken down into two parts: one for exchange processes and one for dissociation/recombination processes.

Exchange Collision Integral The collision operator for exchange reactions can be written as the sum of the partial collision operators:

$$Q^{\mathrm{exc}}_{\mathrm{A}_i} = \sum_{\substack{(\mathrm{B}_j,\mathrm{C}_k,\mathrm{D}_l) \\ \in \mathcal{C}^{\mathrm{exc}}_{\mathrm{A}_i}}} Q^{\mathrm{C}_k\mathrm{D}_l}_{\mathrm{A}_i\mathrm{B}_j}, \quad \mathrm{A} \in \mathcal{S}, \quad i \in \mathcal{I}_{\mathrm{A}} \tag{2.13}$$

The partial collision operator can be written:

$$Q^{\mathrm{C}_k\mathrm{D}_l}_{\mathrm{A}_i\mathrm{B}_j} = \iiint\limits_{\mathbb{R}^3\times\mathbb{R}^3\times\mathbb{R}^3} \left(\frac{\beta_{\mathrm{C}_k}\beta_{\mathrm{D}_l}}{\beta_{\mathrm{A}_i}\beta_{\mathrm{B}_j}} f'_{\mathrm{C}_k} f'_{\mathrm{D}_l} - f_{\mathrm{A}_i} f_{\mathrm{B}_j} \right) W^{\mathrm{C}_k\mathrm{D}_l}_{\mathrm{A}_i\mathrm{B}_j} \, \mathrm{d}\mathbf{c}_{\mathrm{B}} \, \mathrm{d}\mathbf{c}'_{\mathrm{C}} \, \mathrm{d}\mathbf{c}'_{\mathrm{D}} \tag{2.14}$$

Using the same transformation as for the elastic and non-reactive inelastic collisions (details can be found in Appendix A), the relationship between the forward and inverse collision differential cross-sections can be written:

$$\sigma^{\mathrm{A}_i\mathrm{B}_j}_{\mathrm{C}_k\mathrm{D}_l}(g', \boldsymbol{\omega}) = \sigma^{\mathrm{C}_k\mathrm{D}_l}_{\mathrm{A}_i\mathrm{B}_j}(g, \boldsymbol{\omega}') \left(\frac{\beta_{\mathrm{C}_k}\beta_{\mathrm{D}_l}}{\beta_{\mathrm{A}_i}\beta_{\mathrm{B}_j}} \right) \left(\frac{\mu_{\mathrm{CD}}}{\mu_{\mathrm{AB}}} \right) \left(\frac{\mu_{\mathrm{AB}}}{\mu_{\mathrm{CD}}} - \frac{2\Delta E^{\mathrm{C}_k\mathrm{D}_l}_{\mathrm{A}_i\mathrm{B}_j}}{\mu_{\mathrm{CD}} g^2} \right)^{-1} \tag{2.15}$$

Likewise, the partial collision operator is transformed partially to center-of-mass coordinates to yield:

$$Q^{\mathrm{C}_k\mathrm{D}_l}_{\mathrm{A}_i\mathrm{B}_j} = \iint\limits_{\mathscr{L}^2\times\mathbb{R}^3} \left(\frac{\beta_{\mathrm{C}_k}\beta_{\mathrm{D}_l}}{\beta_{\mathrm{A}_i}\beta_{\mathrm{B}_j}} f'_{\mathrm{C}_k} f'_{\mathrm{D}_l} - f_{\mathrm{A}_i} f_{\mathrm{B}_j} \right) g \sigma^{\mathrm{C}_k\mathrm{D}_l}_{\mathrm{A}_i\mathrm{B}_j} \, \mathrm{d}\mathbf{c}_{\mathrm{B}} \, \mathrm{d}\boldsymbol{\omega}' \tag{2.16}$$

Dissociation Collision Integral The collision operator for the two to three body dissociation reactions can be written as the sum of the partial collision operators:

$$Q_{\mathrm{A}_i}^{\mathrm{dis}} = \sum_{\substack{(\mathrm{B}_j,\mathrm{C}_k,\mathrm{D}_l,\mathrm{B}_m)\\ \in \mathcal{C}_{\mathrm{A}_i}^{\mathrm{dis}}}} Q_{\mathrm{A}_i\mathrm{B}_j}^{\mathrm{C}_k\mathrm{D}_l\mathrm{B}_m}, \quad \mathrm{A} \in \mathcal{S}, \quad i \in \mathcal{I}_{\mathrm{A}} \tag{2.17}$$

The partial collision operator can be written:

$$Q_{\mathrm{A}_i\mathrm{B}_j}^{\mathrm{C}_k\mathrm{D}_l\mathrm{B}_m} = \iiiint\limits_{\substack{\mathbb{R}^3\times\mathbb{R}^3\\ \times\mathbb{R}^3\times\mathbb{R}^3}} \left(\frac{\beta_{\mathrm{C}_k}\beta_{\mathrm{D}_l}\beta_{\mathrm{B}_m}}{\beta_{\mathrm{A}_i}\beta_{\mathrm{B}_j}} f'_{\mathrm{C}_k} f'_{\mathrm{D}_l} f'_{\mathrm{B}_m} - f_{\mathrm{A}_i} f_{\mathrm{B}_j} \right) W_{\mathrm{A}_i\mathrm{B}_j}^{\mathrm{C}_k\mathrm{D}_l\mathrm{B}_m} \, \mathrm{d}\mathbf{c}_{\mathrm{B}} \, \mathrm{d}\mathbf{c}'_{\mathrm{C}} \, \mathrm{d}\mathbf{c}'_{\mathrm{D}} \, \mathrm{d}\mathbf{c}'_{\mathrm{B}} \tag{2.18}$$

Again, the cross section is related to the transition probability through the following definition:

$$W_{\mathrm{A}_i\mathrm{B}_j}^{\mathrm{C}_k\mathrm{D}_l\mathrm{B}_m} \, \mathrm{d}\mathbf{c}'_{\mathrm{C}} \, \mathrm{d}\mathbf{c}'_{\mathrm{D}} \, \mathrm{d}\mathbf{c}'_{\mathrm{B}} = g\sigma_{\mathrm{A}_i\mathrm{B}_j}^{\mathrm{C}_k\mathrm{D}_l\mathrm{B}_m}(g, \boldsymbol{\omega'}) \, \mathrm{d}\boldsymbol{\omega'} \tag{2.19}$$

The micro-reversibility relation reads:

$$\beta_{\mathrm{C}_k}\beta_{\mathrm{D}_l}\beta_{\mathrm{B}_m} W_{\mathrm{A}_i\mathrm{B}_j}^{\mathrm{C}_k\mathrm{D}_l\mathrm{B}_m} = \beta_{\mathrm{A}_i}\beta_{\mathrm{B}_j} W_{\mathrm{C}_k\mathrm{D}_l\mathrm{B}_m}^{\mathrm{A}_i\mathrm{B}_j} \tag{2.20}$$

Thus, the partial collision operator can be written as a function of the differential collision cross-section:

$$Q_{\mathrm{A}_i\mathrm{B}_j}^{\mathrm{C}_k\mathrm{D}_l\mathrm{B}_m} = \iint\limits_{\mathbb{R}^3\times\mathscr{L}^2} \left(\frac{\beta_{\mathrm{C}_k}\beta_{\mathrm{D}_l}\beta_{\mathrm{B}_m}}{\beta_{\mathrm{A}_i}\beta_{\mathrm{B}_j}} f'_{\mathrm{C}_k} f'_{\mathrm{D}_l} f'_{\mathrm{B}_m} - f_{\mathrm{A}_i} f_{\mathrm{B}_j} \right) g\sigma_{\mathrm{A}_i\mathrm{B}_j}^{\mathrm{C}_k\mathrm{D}_l\mathrm{B}_m} \, \mathrm{d}\mathbf{c}_{\mathrm{B}} \, \mathrm{d}\boldsymbol{\omega'} \tag{2.21}$$

2.3 Maxwell transfer equation

Because the Boltzmann equation provides a particle description of the gas, in order to derive macroscopic conservation equations we must take moments of the Boltzmann equation. The moments of the Boltzmann equation yield the Maxwell transfer equations which describe the change in some averaged molecular property (*e.g.* density) due to bulk motion and collisions [120]. For a given molecular property, $\varphi_{\mathrm{A}_i} = \varphi_{\mathrm{A}_i}(\mathbf{c}_{\mathrm{A}})$, the molecular average property, $\bar{\varphi}_{\mathrm{A}_i} = \bar{\varphi}_{\mathrm{A}_i}(\mathbf{x}, t)$, and the gas

molecular average property, $\bar{\varphi} = \bar{\varphi}(\mathbf{x}, t)$, can be defined as:

$$\bar{\varphi} = \sum_{\substack{\mathrm{A}\in\mathcal{S} \\ i\in\mathcal{I}_\mathrm{A}}} \bar{\varphi}_{\mathrm{A}_i}, \quad \bar{\varphi}_{\mathrm{A}_i} = \int_{\mathbb{R}^3} f_{\mathrm{A}_i} \varphi_{\mathrm{A}_i} \, \mathrm{d}\mathbf{c}_\mathrm{A}, \quad \mathrm{A} \in \mathcal{S}, \quad i \in \mathcal{I}_\mathrm{A} \tag{2.22}$$

Using these definitions, the Maxwell transfer equations can be derived from the Boltzmann equation, Eq. (2.1), by multiplying each side by φ_{A_i} and integrating over velocity space:

$$\int_{\mathbb{R}^3} \varphi_{\mathrm{A}_i} \frac{\partial f_{\mathrm{A}_i}}{\partial t} \, \mathrm{d}\mathbf{c}_\mathrm{A} + \int_{\mathbb{R}^3} \varphi_{\mathrm{A}_i} \mathbf{c}_\mathrm{A} \cdot \nabla_\mathbf{x} f_{\mathrm{A}_i} \, \mathrm{d}\mathbf{c}_\mathrm{A} = \int_{\mathbb{R}^3} \varphi_{\mathrm{A}_i} \left(Q^{\mathrm{el}}_{\mathrm{A}_i} + Q^{\mathrm{in}}_{\mathrm{A}_i} + Q^{\mathrm{re}}_{\mathrm{A}_i} \right) \mathrm{d}\mathbf{c}_\mathrm{A} \tag{2.23}$$

It is useful at this point to define several macroscopic properties, or moments of the velocity distribution function. These will be used to facilitate simplifying the Maxwell transfer equations. First, the number density of particles in state i of species A is defined as:

$$n_{\mathrm{A}_i} = \int_{\mathbb{R}^3} f_{\mathrm{A}_i} \, \mathrm{d}\mathbf{c}_\mathrm{A}, \quad \mathrm{A} \in \mathcal{S}, \quad i \in \mathcal{I}_\mathrm{A} \tag{2.24}$$

Next, we define the state density, ρ_{A_i}, and gas density, ρ, as:

$$\rho = \sum_{\substack{\mathrm{A}\in\mathcal{S} \\ i\in\mathcal{I}_\mathrm{A}}} \rho_{\mathrm{A}_i}, \quad \rho_{\mathrm{A}_i} = \int_{\mathbb{R}^3} m_\mathrm{A} f_{\mathrm{A}_i} \, \mathrm{d}\mathbf{c}_\mathrm{A}, \quad \mathrm{A} \in \mathcal{S}, \quad i \in \mathcal{I}_\mathrm{A} \tag{2.25}$$

Now, we define the hydrodynamic velocity, $\mathbf{v}$ as:

$$\rho\mathbf{v} = \sum_{\substack{A\in\mathcal{S} \\ i\in\mathcal{I}_\mathrm{A}}} m_\mathrm{A} \int_{\mathbb{R}^3} \mathbf{c}_\mathrm{A} f_{\mathrm{A}_i} \, \mathrm{d}\mathbf{c}_\mathrm{A} = \sum_{\substack{A\in\mathcal{S} \\ i\in\mathcal{I}_\mathrm{A}}} m_\mathrm{A} \bar{\mathbf{c}}_\mathrm{A} \tag{2.26}$$

The peculiar velocity, denoted by $\mathbf{C}_\mathrm{A}$ and describing the thermal motion of the particles in the absence of mean flow, can be defined for each species from the hydrodynamic velocity and the molecular velocity such that $\mathbf{C}_\mathrm{A} = \mathbf{c}_\mathrm{A} - \mathbf{v}$. Finally, we define the diffusion velocity, $\mathbf{v}^d_{\mathrm{A}_i}$ as:

$$\mathbf{v}^d_{\mathrm{A}_i} = \frac{m_\mathrm{A}}{\rho_{\mathrm{A}_i}} \int_{\mathbb{R}^3} \mathbf{C}_\mathrm{A} f_{\mathrm{A}_i} \, \mathrm{d}\mathbf{c}_\mathrm{A}, \quad \mathrm{A} \in \mathcal{S}, \quad i \in \mathcal{I}_\mathrm{A} \tag{2.27}$$

Therefore, we obtain the following relationship, which will be used later in this chapter:

$$\sum_{\substack{\mathrm{A}\in\mathcal{S}\\ i\in\mathcal{I}_{\mathrm{A}}}} \rho_{\mathrm{A}_i}\mathbf{v}^d_{\mathrm{A}_i} = \sum_{\substack{\mathrm{A}\in\mathcal{S}\\ i\in\mathcal{I}_{\mathrm{A}}}} m_{\mathrm{A}}\bar{\mathbf{C}}_{\mathrm{A}} = 0 \tag{2.28}$$

Using these definitions, the Maxwell transfer equations [120] can be written in terms of the hydrodynamic and peculiar velocities:

$$\frac{\partial\bar{\varphi}_{\mathrm{A}_i}}{\partial t} + \nabla_{\mathbf{x}}\cdot(\bar{\varphi}_{\mathrm{A}_i}\mathbf{v}) + \nabla_{\mathbf{x}}\cdot\int_{\mathbb{R}^3}\mathbf{C}_{\mathrm{A}}f_{\mathrm{A}_i}\varphi_{\mathrm{A}_i}\,\mathrm{d}\mathbf{C}_{\mathrm{A}} = \int_{\mathbb{R}^3}\varphi_{\mathrm{A}_i}\left(Q^{\mathrm{el}}_{\mathrm{A}_i} + Q^{\mathrm{in}}_{\mathrm{A}_i} + Q^{\mathrm{re}}_{\mathrm{A}_i}\right)\mathrm{d}\mathbf{C}_{\mathrm{A}} \tag{2.29}$$

For the gas mixture, the Maxwell transfer equation can be written:

$$\frac{\partial\bar{\varphi}}{\partial t} + \nabla_{\mathbf{x}}\cdot(\bar{\varphi}\mathbf{v}) + \nabla_{\mathbf{x}}\cdot\sum_{\substack{\mathrm{A}\in\mathcal{S}\\ i\in\mathcal{I}_{\mathrm{A}}}}\int_{\mathbb{R}^3}\mathbf{C}_{\mathrm{A}}f_{\mathrm{A}_i}\varphi_{\mathrm{A}_i}\,\mathrm{d}\mathbf{C}_{\mathrm{A}} = \sum_{\substack{\mathrm{A}\in\mathcal{S}\\ i\in\mathcal{I}_{\mathrm{A}}}}\int_{\mathbb{R}^3}\varphi_{\mathrm{A}_i}\left(Q^{\mathrm{el}}_{\mathrm{A}_i} + Q^{\mathrm{in}}_{\mathrm{A}_i} + Q^{\mathrm{re}}_{\mathrm{A}_i}\right)\mathrm{d}\mathbf{C}_{\mathrm{A}} \tag{2.30}$$

In the Maxwell transfer equations, the left hand side comprises three terms. The first term simply denotes the change in some macroscopic quantity due to the effects of all the other terms in the equation. The second describes the convective flux at the hydrodynamic velocity. The third term is attributed to the diffusive or transport flux. The right hand side accounts for the impact of collisions detailed in Sec. 2.2 on the quantity of interest.

2.4 Multi-group maximum entropy model

Before proceeding to derive the flow governing equations, the MGME model will be described. The MGME can be broken down into two steps:

1. **Local representation and reconstruction**: the states are lumped together into groups, and within each group the distribution is retrieved through maximization of the entropy.

2. **Macroscopic governing equations**: the macroscopic governing equations for the groups are derived using collisional invariants in the Maxwell transfer equations.

The first step, local representation and reconstruction can be subdivided into two parts. First, the energy states are broken into groups. This can be done with respect to internal energy (quan-

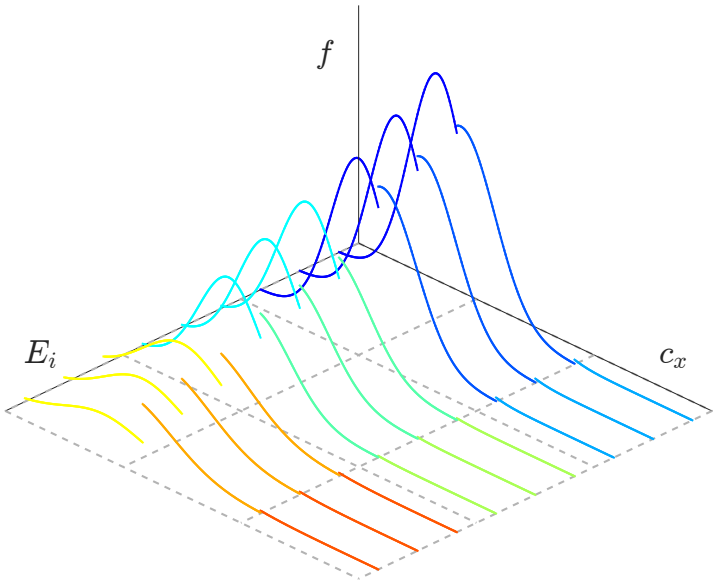

Figure 2.1: Schematic of the grouping of internal energy and velocity states; different colors indicate different groups.

tized) or translational energy (assumed to be continuous). This is illustrated in Fig. 2.1, which shows that the internal and translational energy space has been divided into groups. For illustration purposes, the figure only shows one dimension of the translational velocity. However, if we consider translational energy as well as internal energy grouping, the bin space is four dimensional: three directions of velocity, and one internal energy coordinate. Within each group, the velocity distribution function and internal energy distribution function are reconstructed by maximizing the entropy.

The maximum entropy form used in this work relies on the separation of time scales for various processes. That is to say that the characteristic time of the energy transfer processes among groups is significantly slower than that of the energy transfer processes within a group. This separation of time scales allows for the definition of additional collisional invariants required to close the system and retrieve the correct multi-temperature reconstruction of internal energy states. In the following sections, this distribution will be rigorously derived. However, we can anticipate that it

will resemble a multi-temperature distribution split by internal and translational energy:

$$f_{\mathrm{A}_i} = f^{\mathrm{tra}}_{\mathrm{A}_i} f^{\mathrm{int}}_{\mathrm{A}_i} \tag{2.31}$$

$$f^{\mathrm{tra}}_{\mathrm{A}_i} = \left(\frac{m_{\mathrm{A}}}{2\pi \mathrm{k_B} T}\right)^{3/2} \exp\left(-\frac{m_{\mathrm{A}}}{2\mathrm{k_B}T}\mathbf{C}_{\mathrm{A}} \cdot \mathbf{C}_{\mathrm{A}}\right) \tag{2.32}$$

$$f^{\mathrm{int}}_{\mathrm{A}_i} = n_{\mathrm{A}_p} \frac{a_{\mathrm{A}_i} \exp\left(-\frac{E_{\mathrm{A}_i}}{\mathrm{k_B} T^{\mathrm{int}}_{\mathrm{A}_p}}\right)}{\sum\limits_{i \in \mathcal{I}_p} a_{\mathrm{A}_i} \exp\left(-\frac{E_{\mathrm{A}_i}}{\mathrm{k_B} T^{\mathrm{int}}_{\mathrm{A}_p}}\right)} \tag{2.33}$$

where $f^{\mathrm{tra}}_{\mathrm{A}_i}$ denotes the translational contribution to the velocity distribution function, $f^{\mathrm{int}}_{\mathrm{A}_i}$ denotes the internal energy contribution, $\mathrm{k_B}$ denotes the Boltzmann constant, T is the kinetic temperature, $T^{\mathrm{int}}_{\mathrm{A}_p}$ denotes the internal temperature of particles in group p of species A, n_{A_p} denotes the number density of particles in group p of species A, and the set $\mathcal{I}_p$ denotes the set of states within group p.

The second step, constructing macroscopic governing equations, is realized by using collisional invariants in the Maxwell transfer equations to derive conservation equations for the groups. What we seek is a set of Euler-like equations for the grouping model. However, to account for the separate equilibrium states of the different groups, we will find separate conservation of mass and energy equations for each group, in addition to the conservation of momentum and total energy for the mixture. Finally, the collisional terms can be re-cast to resemble what is evaluated in the QCT method, providing the final link between the flow governing equations and the microscopic chemical processes.

2.4.1 Local representation and reconstruction

The group reconstruction relies on maximizing the entropy of each group to retrieve the distribution of states within the group. In this work, we will restrict this framework to two models: the multi-group maximum entropy thermal (MGMET) model and the multi-group maximum entropy linear (MGMEL) model. The MGMET model is a particular simplification of the MGMEL model. To derive the MGMEL model, we first present a brief discussion about the separation of time scales, which will be used together with the definition of kinetic entropy to derive the Boltzmann H-Theorem and find the form of the distribution function which ensures that the entropy production

in each group is zero. Next, we represent the distribution as a linear combination of collisional invariants. Finally, using constraints based on these collisional invariants we find a relationship between these constraints and macroscopic variables which will be determined from the conservation equations derived in the next section.

Separation of time scales

To derive the Boltzmann H-Theorem for the groups, we need to consider the different time scales of the various processes occurring [123]. We also introduce the notion of groups at this point; in this work we will restrict ourselves to internal energy groups, integrating over the entire velocity space and assuming that all groups have the same velocity distribution. This is a good approximation because elastic collisions, which force the translational energy into equilibrium, occur significantly faster than the chemical reactions which we are interested in studying. Therefore, we can divide the inelastic processes into two categories: ones in which the groups do not change (intra-group), and ones in which the groups change (inter-group). With this, we can introduce the assumption that certain processes prevail, forcing the groups into local equilibrium. Let us define the following time scales:

τ_{react}	time scale of chemical reactions (*e.g.*, dissociation, recombination, etc.)
τ_{pq}	time scale of processes among groups (inter-group)
$\tau_{pp,\,\text{large}\Delta E}$	time scale of processes within a group with "large" energy jumps (intra-group)
$\tau_{pp,\,\text{small}\Delta E}$	time scale of processes within a group with "small" energy jumps (intra-group)

If we rank these time scales, we find that:

$$\tau_{\text{react}} \simeq \tau_{pq} \gg \tau_{pp,\,\text{large}\Delta E} \gg \tau_{pp,\,\text{small}\Delta E} \tag{2.34}$$

That is to say that the time scale of the reactive collisions are on the same order as those among groups. The processes among groups are much slower than those within a group. However, we can split the processes within a group into two categories: one characterized by large jumps in energy, and one characterized by small jumps in energy. Therefore, we assume that the mechanism which forces the states within a group into equilibrium (*i.e.*, maximization of entropy) is these intra-group

processes characterized by small energy jumps. Accordingly, we will use the collision operator for these processes to derive the distribution of states within the groups. It should be noted that this implies that the groups should be constructed such that there are minimal "fast" processes among groups. We will see the implications associated with the grouping scheme in Chapters 4 and 6.

Proof of positivity of entropy production

To find the form of the velocity distribution function which maximizes the entropy, we consider the conservation of kinetic entropy equation. The kinetic entropy of a group per unit volume, $S^{\text{kin}}_{\text{A}_p}$, can be defined [121]:

$$S^{\text{kin}}_{\text{A}_p} = -\text{k}_\text{B} \sum_{i \in \mathcal{I}_p} \int_{\mathbb{R}^3} f_{\text{A}_i} \left(\ln \left(\beta_{\text{A}_i} f_{\text{A}_i} \right) - 1 \right) \, \text{d}\mathbf{c}_\text{A} \tag{2.35}$$

To obtain the kinetic entropy conservation equation, we multiply the Boltzmann equation by $\ln \left(\beta_{\text{A}_i} f_{\text{A}_i} \right)$, integrate over velocity space, and sum over states within group p. Details of this procedure can be found in Appendix B. After some algebra, we can write the conservation of entropy expression as:

$$\frac{\partial S^{\text{kin}}_{\text{A}_p}}{\partial t} + \text{k}_\text{B} \sum_{i \in \mathcal{I}_p} \int_{\mathbb{R}^3} \left[\mathbf{c}_\text{A} \cdot \nabla_\mathbf{x} \left(f_{\text{A}_i} \left(\ln \left(\beta_{\text{A}_i} f_{\text{A}_i} \right) \right) - 1 \right) \right] \, \text{d}\mathbf{c}_\text{A} = \mathfrak{v}^{\text{kin}}_{\text{A}_p} \tag{2.36}$$

where the entropy source term, $\mathfrak{v}^{\text{kin}}_{\text{A}_p}$, is defined as the sum of the elastic, inelastic scattering, and reactive entropy source terms, $(\mathfrak{v}^{E}_{\text{A}_p}, \mathfrak{v}^{S}_{\text{A}_p}, \mathfrak{v}^{C}_{\text{A}_p})$ respectively:

$$\mathfrak{v}^{\text{kin}}_{\text{A}_p} = \mathfrak{v}^{E}_{\text{A}_p} + \mathfrak{v}^{S}_{\text{A}_p} + \mathfrak{v}^{C}_{\text{A}_p}, \tag{2.37}$$

$$\mathfrak{v}^{E}_{\text{A}_p} = -\text{k}_\text{B} \sum_{i \in \mathcal{I}_p} \int_{\mathbb{R}^3} Q^{\text{el}}_{\text{A}_i} \ln \left(\beta_{\text{A}_i} f_{\text{A}_i} \right) \text{d}\mathbf{c}_\text{A}, \tag{2.38}$$

$$\mathfrak{v}^{S}_{\text{A}_p} = -\text{k}_\text{B} \sum_{i \in \mathcal{I}_p} \int_{\mathbb{R}^3} Q^{\text{in}}_{\text{A}_i} \ln \left(\beta_{\text{A}_i} f_{\text{A}_i} \right) \text{d}\mathbf{c}_\text{A}, \tag{2.39}$$

$$\mathfrak{v}^{C}_{\text{A}_p} = -\text{k}_\text{B} \sum_{i \in \mathcal{I}_p} \int_{\mathbb{R}^3} Q^{\text{re}}_{\text{A}_i} \ln \left(\beta_{\text{A}_i} f_{\text{A}_i} \right) \text{d}\mathbf{c}_\text{A} \tag{2.40}$$

The right hand side depends on the collision integrals defined in Sec. 2.2.1. Using these expressions for the collision integrals we can write the entropy source term. However, recalling the separation

of time scales, we can see that the intra-group inelastic scattering terms are significantly faster than both inter-group inelastic scattering terms as well as reactive scattering terms. Therefore, we can separate the entropy source terms according to these time scales, and consider the "fast" process entropy source terms and the "slow" entropy source terms separately. We can therefore write the "fast" (intra-group inelastic scattering) entropy source term:

$$\mathfrak{v}^S_{\mathrm{A}_p} = -\mathrm{k_B} \sum_{\mathrm{B}\in\mathcal{S}} \sum_{q\in\mathrm{B}} \sum_{(i,k)\in\mathcal{I}_p} \sum_{(j,l)\in\mathcal{I}_q} \iiiint\limits_{\substack{\mathbb{R}^3\times\mathbb{R}^3 \\ \times\mathbb{R}^3\times\mathbb{R}^3}} \left(\frac{\beta_{\mathrm{A}_k}\beta_{\mathrm{B}_l}}{\beta_{\mathrm{A}_i}\beta_{\mathrm{B}_j}} f'_{\mathrm{A}_k} f'_{\mathrm{B}_l} - f_{\mathrm{A}_i} f_{\mathrm{B}_j} \right) \times W^{\mathrm{A}'_k\mathrm{B}'_l}_{\mathrm{A}_i\mathrm{B}_j} \ln\left(\beta_{\mathrm{A}_i} f_{\mathrm{A}_i}\right) \mathrm{d}\mathbf{c}_\mathrm{A}\, \mathrm{d}\mathbf{c}_\mathrm{B}\, \mathrm{d}\mathbf{c}'_\mathrm{A}\, \mathrm{d}\mathbf{c}'_\mathrm{B} \tag{2.41}$$

After some algebra making use of properties of the inverse collision (details can be found in Appendix B), we can finally write the following expression for the inelastic scattering entropy source term:

$$\mathfrak{v}^S_{\mathrm{A}_p} = -\frac{1}{4}\mathrm{k_B} \sum_{\mathrm{B}\in\mathcal{S}} \sum_{q\in\mathrm{B}} \sum_{(i,k)\in\mathcal{I}_p} \sum_{(j,l)\in\mathcal{I}_q} \iiiint\limits_{\substack{\mathbb{R}^3\times\mathbb{R}^3 \\ \times\mathbb{R}^3\times\mathbb{R}^3}} \ln\left(\frac{\beta_{\mathrm{A}_i}\beta_{\mathrm{B}_j}}{\beta_{\mathrm{A}_k}\beta_{\mathrm{B}_l}} \frac{f_{\mathrm{A}_i} f_{\mathrm{B}_j}}{f'_{\mathrm{A}_k} f'_{\mathrm{B}_l}} \right) \left(\frac{\beta_{\mathrm{A}_k}\beta_{\mathrm{B}_l}}{\beta_{\mathrm{A}_i}\beta_{\mathrm{B}_j}} f'_{\mathrm{A}_k} f'_{\mathrm{B}_l} - f_{\mathrm{A}_i} f_{\mathrm{B}_j} \right) \times W^{\mathrm{A}'_k\mathrm{B}'_l}_{\mathrm{A}_i\mathrm{B}_j} \mathrm{d}\mathbf{c}_\mathrm{A}\, \mathrm{d}\mathbf{c}_\mathrm{B}\, \mathrm{d}\mathbf{c}'_\mathrm{A}\, \mathrm{d}\mathbf{c}'_\mathrm{B} \tag{2.42}$$

Now let's analyze the sign of the integral. Define x and y as:

$$x = \frac{\beta_{\mathrm{A}_k}\beta_{\mathrm{B}_l}}{\beta_{\mathrm{A}_i}\beta_{\mathrm{B}_j}} f'_{\mathrm{A}_k} f'_{\mathrm{B}_l}, \quad y = f_{\mathrm{A}_i} f_{\mathrm{B}_j} \tag{2.43}$$

We know that x and y are always positive. Looking at the value of the integrand in terms of x and y we have $I = (\ln x - \ln y)(x - y)$. Therefore:

$$\text{If} \quad x > y: \quad I > 0$$

$$\text{If} \quad x < y: \quad I > 0$$

$$\text{If} \quad x = y: \quad I = 0$$

Therefore, the fast entropy source term satisfies: $\mathfrak{v}^S_{\mathrm{A}_p} \geq 0$. This condition is the outcome of the Boltzmann H-Theorem, and tells us that the system of particles will tend towards some condition given by the relation $\mathfrak{v}^S_{\mathrm{A}_p} = 0$. This is the maximum entropy condition. Therefore, we find that the entropy is maximized when the following relationship holds:

$$\ln\left(\beta_{\mathrm{A}_k} f'_{\mathrm{A}_k}\right) + \ln\left(\beta_{\mathrm{B}_l} f'_{\mathrm{B}_l}\right) = \ln\left(\beta_{\mathrm{A}_i} f_{\mathrm{A}_i}\right) + \ln\left(\beta_{\mathrm{B}_j} f_{\mathrm{B}_j}\right) \tag{2.44}$$

This relation in conjunction with mechanics allows us to write the distribution as a linear combination of the collisional invariants for the intra-group inelastic processes characterized by small energy jumps. Furthermore, Kennard [124] showed that this linear combination is the only form of $\log\left(\beta_{\mathrm{A}_i} f_{\mathrm{A}_i}\right)$ which satisfies this relation. The same process can be used to demonstrate that not only is the entropy strictly increasing or zero due to the fast processes, but also due to the slow processes (inter-group inelastic scattering and reactive). However, the procedure is the same as for the fast processes and for brevity will not be presented here.

Collisional invariants

We find based on the analysis of time scales that we can define four collisional invariants. The first three collisional invariants are fairly obvious and comprise the quantities conserved in any collision: mass, momentum, and total energy. The final collisional invariant arises because of the separation of time scales discussed earlier. Because we derive our group distribution from the fast process collision term, we take our collisional invariants to correspond to those processes. Therefore, because we assumed the processes characterized by small internal energy changes to be the fastest, the final collisional invariant corresponds to the internal energy. This assumption is directly related to the assumption that resonant vibrational transitions occur the fastest in a two-temperature model: this allows for the definition of the vibrational energy as a collisional invariant, eventually introducing a separate vibrational energy conservation equation. However, in this case it is more general, and not restricted solely to resonant vibrational transitions. Therefore, for the MGMEL model, we can express the $\log\left(\beta_{\mathrm{A}_i} f_{\mathrm{A}_i}\right)$ as the linear combination of these collisional

invariants:

$$\ln\left(\beta_{\mathrm{A}_i} f_{\mathrm{A}_i}\right) = \alpha_{\mathrm{A}_p} m_{\mathrm{A}} + \boldsymbol{\gamma}_{\mathrm{A}_p} \cdot \left(m_{\mathrm{A}} \mathbf{c}_{\mathrm{A}}\right) + \delta_{\mathrm{A}_p}\left(\frac{1}{2} m_{\mathrm{A}} \mathbf{c}_{\mathrm{A}} \cdot \mathbf{c}_{\mathrm{A}} + E_{\mathrm{A}_i}\right) + \beta_{\mathrm{A}_p} E_{\mathrm{A}_i} \tag{2.45}$$

To solve for the coefficients $(\alpha_{\mathrm{A}_p}, \boldsymbol{\gamma}_{\mathrm{A}_p}, \delta_{\mathrm{A}_p}, \beta_{\mathrm{A}_p})$, we apply constraints. These constraints correspond to the collisional invariants and comprise the group mass, group momentum, group total energy, and group internal energy:

$$n_{\mathrm{A}_p} = \sum_{i \in \mathcal{I}_p} \int_{\mathbb{R}^3} f_{\mathrm{A}_i} \, \mathrm{d}\mathbf{c}_{\mathrm{A}} \tag{2.46}$$

$$\rho_{\mathrm{A}_p} \mathbf{w}_{\mathrm{A}_p} = \sum_{i \in \mathcal{I}_p} \int_{\mathbb{R}^3} m_{\mathrm{A}} f_{\mathrm{A}_i} \mathbf{c}_{\mathrm{A}} \, \mathrm{d}\mathbf{c}_{\mathrm{A}} \tag{2.47}$$

$$n_{\mathrm{A}_p} E^{\mathrm{tra}}_{\mathrm{A}_p} = \sum_{i \in \mathcal{I}_p} \int_{\mathbb{R}^3} \frac{1}{2} m_{\mathrm{A}} \left(\mathbf{c}_{\mathrm{A}} + \frac{1}{\delta_{\mathrm{A}_p}} \boldsymbol{\gamma}_{\mathrm{A}_p}\right) \cdot \left(\mathbf{c}_{\mathrm{A}} + \frac{1}{\delta_{\mathrm{A}_p}} \boldsymbol{\gamma}_{\mathrm{A}_p}\right) f_{\mathrm{A}_i} \, \mathrm{d}\mathbf{c}_{\mathrm{A}} \tag{2.48}$$

$$n_{\mathrm{A}_p} E^{\mathrm{int}}_{\mathrm{A}_p} = \sum_{i \in \mathcal{I}_p} \int_{\mathbb{R}^3} E_{\mathrm{A}_i} f_{\mathrm{A}_i} \, \mathrm{d}\mathbf{c}_{\mathrm{A}} \tag{2.49}$$

These constraints correspond to a grouping scheme in which only internal energy is grouped.

Because we assume all groups have the same velocity distribution, we find that the parameters corresponding to the momentum and total energy of the group are the same for all groups: $\mathbf{w}_{\mathrm{A}_p} = \mathbf{w}$ and $E^{\mathrm{tra}}_{\mathrm{A}_p} = E^{\mathrm{tra}}$. Before applying these constraints, it is useful to define the quantity $\mathbf{C}'_{\mathrm{A}} = \mathbf{c}_{\mathrm{A}} + \frac{1}{\delta_{\mathrm{A}_p}} \boldsymbol{\gamma}_{\mathrm{A}_p}$. Using this, the linear combination of collisional invariants can be written as:

$$\ln\left(\beta_{\mathrm{A}_i} f_{\mathrm{A}_i}\right) = \alpha_{\mathrm{A}_p} m_{\mathrm{A}} - \frac{m_{\mathrm{A}}}{2\delta_{\mathrm{A}_p}} \boldsymbol{\gamma}_{\mathrm{A}_p} \cdot \boldsymbol{\gamma}_{\mathrm{A}_p} + \delta_{\mathrm{A}_p}\left(\frac{1}{2} m_{\mathrm{A}} \mathbf{C}'_{\mathrm{A}} \cdot \mathbf{C}'_{\mathrm{A}} + E_{\mathrm{A}_i}\right) + \beta_{\mathrm{A}_p} E_{\mathrm{A}_i} \tag{2.50}$$

First, we apply the constraint on the group number density to find an expression for α_{A_p}:

$$m_{\mathrm{A}} \alpha_{\mathrm{A}_p} = \ln\left(n_{\mathrm{A}_p}\right) + \frac{m_{\mathrm{A}}}{2\delta_{\mathrm{A}_p}} \boldsymbol{\gamma}_{\mathrm{A}_p} \cdot \boldsymbol{\gamma}_{\mathrm{A}_p} + \ln\left(-\frac{\mathrm{h}_{\mathrm{P}}^2 \delta_{\mathrm{A}_p}}{2\pi m_{\mathrm{A}}}\right)^{3/2} - \ln\left\{\sum_{i \in \mathcal{I}_p} a_{\mathrm{A}_i} \exp\left[\left(\beta_{\mathrm{A}_p} + \delta_{\mathrm{A}_p}\right) E_{\mathrm{A}_i}\right]\right\} \tag{2.51}$$

Applying the conservation of momentum constraint, we find the following relationship:

$$\boldsymbol{\gamma}_{\mathrm{A}_p} = -\delta_{\mathrm{A}_p}\mathbf{w} \tag{2.52}$$

The total translational energy of a group is found to be:

$$n_{\mathrm{A}_p}E^{\mathrm{tra}} = -\frac{3n_{\mathrm{A}_p}}{2\delta_{\mathrm{A}_p}} \tag{2.53}$$

From classical thermodynamics, we know that the average translational energy of a given particle will be equivalent to $\frac{3}{2}\mathrm{k_B}T$ where T is the translational or kinetic temperature. The symbol E^{tra} gives the average translational energy of a single particle in the mixture. Therefore:

$$\delta_{\mathrm{A}_p} = -\frac{1}{\mathrm{k_B}T} \tag{2.54}$$

Let us re-visit the definition of $\mathbf{C}'_{\mathrm{A}} = \mathbf{c}_{\mathrm{A}} + \boldsymbol{\gamma}_{\mathrm{A}_p}/\delta_{\mathrm{A}_p}$: this can be re-written as $\mathbf{C}'_{\mathrm{A}} = \mathbf{c}_{\mathrm{A}} - \mathbf{w}$. Now, if we recall the definition of $\mathbf{w}$:

$$\rho\mathbf{w} = \sum_{\mathrm{A}\in\mathcal{S}}\sum_{p\in\mathrm{A}}\rho_{\mathrm{A}_p}\mathbf{w} = \sum_{\mathrm{A}\in\mathcal{S}}\sum_{p\in\mathrm{A}}\sum_{i\in\mathcal{I}_p}\int_{\mathbb{R}^3} m_{\mathrm{A}}\mathbf{c}_{\mathrm{A}}f_{\mathrm{A}_i}\,\mathrm{d}\mathbf{c}_{\mathrm{A}} = \rho\mathbf{v} \tag{2.55}$$

Therefore, the quantity $\mathbf{C}'_{\mathrm{A}} = \mathbf{C}_{\mathrm{A}}$ is identically the peculiar velocity defined earlier, and $\mathbf{w}$, the average velocity for the groups, is identically the hydrodynamic velocity $\mathbf{v}$.

To obtain an expression for β_{A_p}, we use the definition of kinetic entropy. First, evaluating the internal energy of a group, we find that the average energy of a particle in group p is:

$$E^{\mathrm{int}}_{\mathrm{A}_p} = \frac{\sum\limits_{i\in\mathcal{I}_p} a_{\mathrm{A}_i}E_{\mathrm{A}_i}\exp\left[\left(\beta_{\mathrm{A}_p} - \frac{1}{\mathrm{k_B}T}\right)E_{\mathrm{A}_i}\right]}{\sum\limits_{i\in\mathcal{I}_p} a_{\mathrm{A}_i}\exp\left[\left(\beta_{\mathrm{A}_p} - \frac{1}{\mathrm{k_B}T}\right)E_{\mathrm{A}_i}\right]} \tag{2.56}$$

We can define a new variable, $\beta'_{\mathrm{A}_p} = \beta_{\mathrm{A}_p} - \frac{1}{\mathrm{k_B}T}$. Using the internal energy of the group, the new variable β'_{A_p}, and the definition of kinetic entropy for a group p, the kinetic entropy of the group

can be written:

$$S^{\text{kin}}_{\text{A}_p} = -\text{k}_\text{B} n_{\text{A}_p} \Bigg\{ \ln\left(n_{\text{A}_p}\right) + \ln\left(\frac{\text{h}_\text{P}^2}{2\pi m_\text{A} \text{k}_\text{B} T}\right)^{3/2} - \frac{5}{2} - \ln\left[\sum_{i \in \mathcal{I}_p} a_{\text{A}_i} \exp\left(\beta'_{\text{A}_p} E_{\text{A}_i}\right)\right] + \beta'_{\text{A}_p} E^{\text{int}}_{\text{A}_p} \Bigg\} \tag{2.57}$$

Now recall the relationship from classical thermodynamics which relates the entropy to the temperature. However, we define it as the group internal temperature, because we have evaluated the entropy only for a group:

$$\left[\frac{\partial\left(S^{\text{kin}}_{\text{A}_p}/n_{\text{A}_p}\right)}{\partial E^{\text{int}}_{\text{A}_p}}\right]_{n,V} = \frac{1}{T^{\text{int}}_{\text{A}_p}} \tag{2.58}$$

Realizing that $\beta'_{\text{A}_p} = \beta'_{\text{A}_p}(E^{\text{int}}_{\text{A}_p})$, and using the chain rule, we find that:

$$\left[\frac{\partial\left(S^{\text{kin}}_{\text{A}_p}/n_{\text{A}_p}\right)}{\partial E^{\text{int}}_{\text{A}_p}}\right]_{V,N} = -\text{k}_\text{B}\beta'_{\text{A}_p} = \frac{1}{T^{\text{int}}_{\text{A}_p}} \tag{2.59}$$

Therefore, we arrive at the final expression for the distribution of states within a group:

$$f_{\text{A}_i} = n_{\text{A}_p}\left(\frac{m_\text{A}}{2\pi \text{k}_\text{B} T}\right)^{3/2} \exp\left(-\frac{m_\text{A}}{2\text{k}_\text{B} T}\mathbf{C}_\text{A}\cdot\mathbf{C}_\text{A}\right) \frac{a_{\text{A}_i}\exp\left(-\frac{E_{\text{A}_i}}{\text{k}_\text{B} T^{\text{int}}_{\text{A}_p}}\right)}{\sum\limits_{i\in\mathcal{I}_p} a_{\text{A}_i}\exp\left(-\frac{E_{\text{A}_i}}{\text{k}_\text{B} T^{\text{int}}_{\text{A}_p}}\right)} \tag{2.60}$$

As expected, this expression is simply a two-temperature Boltzmann distribution within each group. We have imposed separation of translational and internal energy relaxation by imposing separate time-scales for these two processes. We can separate the translational and internal contributions

to the velocity distribution function and write it as the product of these two terms:

$$f_{\mathrm{A}_i} = f_{\mathrm{A}_i}^{\mathrm{tra}} f_{\mathrm{A}_i}^{\mathrm{int}} \tag{2.61}$$

$$f_{\mathrm{A}_i}^{\mathrm{tra}} = \left(\frac{m_{\mathrm{A}}}{2\pi \mathrm{k_B} T}\right)^{3/2} \exp\left(-\frac{m_{\mathrm{A}}}{2\mathrm{k_B} T}\mathbf{C}_{\mathrm{A}} \cdot \mathbf{C}_{\mathrm{A}}\right) \tag{2.62}$$

$$f_{\mathrm{A}_i}^{\mathrm{int}} = n_{\mathrm{A}_p} \frac{a_{\mathrm{A}_i} \exp\left(-\frac{E_{\mathrm{A}_i}}{\mathrm{k_B} T_{\mathrm{A}_p}^{\mathrm{int}}}\right)}{\sum\limits_{i \in \mathcal{I}_p} a_{\mathrm{A}_i} \exp\left(-\frac{E_{\mathrm{A}_i}}{\mathrm{k_B} T_{\mathrm{A}_p}^{\mathrm{int}}}\right)} \tag{2.63}$$

However, as stated earlier, in this work we are only concerned with internal energy non-equilibrium. Therefore, at this point we will complete the integration over velocity space to determine the distribution of internal energy states within each group.

$$\mathcal{F}_{\mathrm{A}_p}^{i}\left(T_{\mathrm{A}_p}^{\mathrm{int}}\right) = \frac{1}{n_{\mathrm{A}_p}} \int\limits_{\mathbb{R}^3} f_{\mathrm{A}_i} \, \mathrm{d}\mathbf{c}_{\mathrm{A}} \tag{2.64}$$

After this integration, we finally arrive at an expression for the distribution of states for the MGMEL model:

$$\mathcal{F}_{\mathrm{A}_p}^{i}\left(T_{\mathrm{A}_p}^{\mathrm{int}}\right) = \frac{n_{\mathrm{A}_i}}{n_{\mathrm{A}_p}} = \frac{1}{Q_{\mathrm{A}_p}^{(0)}\left(T_{\mathrm{A}_p}^{\mathrm{int}}\right)} a_{\mathrm{A}_i} \exp\left(-\frac{E_{\mathrm{A}_i}}{\mathrm{k_B} T_{\mathrm{A}_p}^{\mathrm{int}}}\right) \tag{2.65}$$

where $\mathcal{F}_{\mathrm{A}_p}^{i}(T_{\mathrm{A}_p}^{\mathrm{int}})$ denotes the distribution of energy states in group p for species A containing states i, and $Q_{\mathrm{A}_p}^{(0)}(T_{\mathrm{A}_p}^{\mathrm{int}})$ denotes the zeroth order moment of the partition function for group p. The m^{th} moment of the partition function for group p can be written:

$$Q_{\mathrm{A}_p}^{(m)}\left(T_{\mathrm{A}_p}^{\mathrm{int}}\right) = \sum_{i \in \mathcal{I}_p} a_{\mathrm{A}_i} \left(E_{\mathrm{A}_i}\right)^m \exp\left(-\frac{E_{\mathrm{A}_i}}{\mathrm{k_B} T_{\mathrm{A}_p}^{\mathrm{int}}}\right) \tag{2.66}$$

In the MGMET model, the temperature within each bin, $T_{\mathrm{A}_p}^{\mathrm{int}}$, is assumed to be equal to the local translational temperature, T. This also eliminates the assumption that the internal energy is a collisional invariant, requiring only the first three collisional invariants (mass, momentum, and total energy). In this approach only the group number densities, n_{A_p}, must be evaluated, while in the MGMEL model, the group unknowns include both the group number densities as well as the group internal temperatures (n_{A_p}, $T_{\mathrm{A}_p}^{\mathrm{int}}$). The next step to constructing the reduced order model is to use

the Maxwell transfer equations, Eqs. (2.29) and (2.30), to obtain macroscopic governing equations.

2.4.2 Macroscopic governing equations

In order to derive the continuum flow equations from the Maxwell transfer equations, Eqs. (2.29) and (2.30), the collisional invariants, denoted as $\boldsymbol{\psi}_{\mathrm{A}_i}$, are defined. These collisional invariants comprise the same quantities used to derive the velocity distribution function for the grouping model:

$$\begin{cases} \psi_{\mathrm{A}_i}^{k} = & (m_{\mathrm{A}})_{i\in\mathcal{I}_p,\, p\in\mathrm{A},\, \mathrm{A}\in\mathcal{S}}, \quad k \in \mathcal{S}, \\ \psi_{\mathrm{A}_i}^{\mathcal{N}_s+\nu} = & (m_{\mathrm{A}}\mathbf{c}_{\mathrm{A}})_{i\in\mathcal{I}_p,\, p\in\mathrm{A},\, \mathrm{A}\in\mathcal{S}}, \quad \nu = 1,2,3, \\ \psi_{\mathrm{A}_i}^{\mathcal{N}_s+4} = & \left(\frac{1}{2}m_{\mathrm{A}}\mathbf{c}_{\mathrm{A}}\cdot\mathbf{c}_{\mathrm{A}} + E_{\mathrm{A}_i}\right)_{i\in\mathcal{I}_p,\, p\in\mathrm{A},\, \mathrm{A}\in\mathcal{S}}, \\ \psi_{\mathrm{A}_i}^{\mathcal{N}_s+4+l} = & (E_{\mathrm{A}_i})_{i\in\mathcal{I}_p,\, p\in\mathrm{A},\, \mathrm{A}\in\mathcal{S}}, \quad l \in \mathcal{S} \end{cases} \tag{2.67}$$

where $\mathcal{N}_s$ denotes the total number of species and energy levels. The advantage of defining these properties is that they satisfy the relation that for the "fast" processes, the collision operator for these quantities is identically zero. Therefore, when you sum over the entire mixture, the collision integrals disappear for these quantities. Using the vector of collisional invariants the continuum flow equations can be derived. For the first $\mathcal{N}_s$ and last $\mathcal{N}_s$ collisional invariants (mass and internal energy), the equations are derived by summing over energy levels within the group p. For the middle two collisional invariants (momentum and total energy) these are summed over the entire mixture. Therefore, for the MGMEL model we will retrieve conservation of mass and internal energy equations for the groups, a conservation of momentum equation, and a conservation of total energy equation.

Conservation of group mass

First, we use the first $\mathcal{N}_s$ collision invariants, m_{A}, and sum over the energy levels contained in group p in the Maxwell transfer equations to retrieve:

$$\sum_{i\in\mathcal{I}_p}\int_{\mathbb{R}^3} m_{\mathrm{A}}\frac{\partial f_{\mathrm{A}_i}}{\partial t}\,\mathrm{d}\mathbf{c}_{\mathrm{A}} + \sum_{i\in\mathcal{I}_p}\nabla_{\mathbf{x}}\cdot\int_{\mathbb{R}^3} m_{\mathrm{A}} f_{\mathrm{A}_i}\mathbf{c}_{\mathrm{A}}\,\mathrm{d}\mathbf{c}_{\mathrm{A}} = \sum_{i\in\mathcal{I}_p}\int_{\mathbb{R}^3} m_{\mathrm{A}}\left(Q_{\mathrm{A}_i}^{\mathrm{el}} + Q_{\mathrm{A}_i}^{\mathrm{in}} + Q_{\mathrm{A}_i}^{\mathrm{re}}\right)\,\mathrm{d}\mathbf{c}_{\mathrm{A}} \tag{2.68}$$

Next, we combine this expression and the definition of the group partial density, given by:

$$\rho_{\mathrm{A}_p} = \sum_{i \in \mathcal{I}_p} m_{\mathrm{A}} \int_{\mathbb{R}^3} f_{\mathrm{A}_i} \, \mathrm{d}\mathbf{c}_{\mathrm{A}} = \sum_{i \in \mathcal{I}_p} m_{\mathrm{A}} n_{\mathrm{A}_i} = \sum_{i \in \mathcal{I}_p} \rho_{\mathrm{A}_i} \tag{2.69}$$

After some algebra, using the fact that elastic collisions do not affect the group population, and realizing that the diffusion velocity is zero when the velocity distribution is Maxwellian, the group conservation of mass equation reads:

$$\frac{\partial \rho_{\mathrm{A}_p}}{\partial t} + \nabla_{\mathbf{x}} \cdot \left(\rho_{\mathrm{A}_p} \mathbf{v} \right) = \sum_{i \in \mathcal{I}_p} \int_{\mathbb{R}^3} m_{\mathrm{A}} \left(Q^{\mathrm{in}}_{\mathrm{A}_i} + Q^{\mathrm{re}}_{\mathrm{A}_i} \right) \, \mathrm{d}\mathbf{c}_{\mathrm{A}} \tag{2.70}$$

The collision terms were described previously in Sec. 2.2.1.

Conservation of momentum

The conservation of momentum equations are retrieved by using the collision invariants $m_{\mathrm{A}}\mathbf{c}_{\mathrm{A}}$, and applying this to the mixture Maxwell Transfer equation, Eq. (2.30):

$$\begin{aligned} \frac{\partial \rho \mathbf{v}}{\partial t} + \nabla_{\mathbf{x}} \cdot (\rho \mathbf{v} \otimes \mathbf{v}) + \nabla_{\mathbf{x}} \cdot \sum_{\substack{\mathrm{A} \in \mathcal{S} \\ i \in \mathcal{I}_{\mathrm{A}}}} \int_{\mathbb{R}^3} m_{\mathrm{A}} f_{\mathrm{A}_i} \mathbf{C}_{\mathrm{A}} \otimes \mathbf{c}_{\mathrm{A}} \, \mathrm{d}\mathbf{c}_{\mathrm{A}} \\ = \sum_{\substack{\mathrm{A} \in \mathcal{S} \\ i \in \mathcal{I}_{\mathrm{A}}}} \int_{\mathbb{R}^3} m_{\mathrm{A}} \mathbf{c}_{\mathrm{A}} \left(Q^{\mathrm{el}}_{\mathrm{A}_i} + Q^{\mathrm{in}}_{\mathrm{A}_i} + Q^{\mathrm{re}}_{\mathrm{A}_i} \right) \, \mathrm{d}\mathbf{c}_{\mathrm{A}} \end{aligned} \tag{2.71}$$

Evaluating the flux integral with the velocity distribution function derived earlier yields:

$$\nabla_{\mathbf{x}} \cdot \sum_{\mathrm{A} \in \mathcal{S}} \sum_{i \in \mathcal{I}_{\mathrm{A}}} \int_{\mathbb{R}^3} m_{\mathrm{A}} f_{\mathrm{A}_i} \mathbf{C}_{\mathrm{A}} \otimes \mathbf{c}_{\mathrm{A}} \, \mathrm{d}\mathbf{c}_{\mathrm{A}} = \nabla_{\mathbf{x}} \cdot (p \underline{I}) \tag{2.72}$$

where p denotes the gas pressure given by $p = \sum_{\mathrm{A} \in \mathcal{S}} \sum_{p \in \mathrm{A}} \left(n_{\mathrm{A}_p} \mathrm{k_B} T \right)$, and $\underline{\mathbf{I}}$ denotes the second order identity tensor. Using this definition, the general conservation of momentum equation can be written:

$$\frac{\partial \rho \mathbf{v}}{\partial t} + \nabla_{\mathbf{x}} \cdot (\rho \mathbf{v} \otimes \mathbf{v} + p \underline{\mathbf{I}}) = \mathbf{0} \tag{2.73}$$

Conservation of total energy

The total energy is used to retrieve the conservation of energy equation from the mixture Maxwell Transfer equation, Eq. (2.30). First, the gas molecular average property, ρe is defined as:

$$\begin{aligned}\rho e &= \sum_{\substack{\mathrm{A}\in\mathcal{S}\\ i\in\mathcal{I}_\mathrm{A}}} \int_{\mathbb{R}^3} f_{\mathrm{A}_i} \left(\frac{1}{2} m_\mathrm{A} \mathbf{c}_\mathrm{A}\cdot\mathbf{c}_\mathrm{A} + E_{\mathrm{A}_i}\right) \mathrm{d}\mathbf{c}_\mathrm{A} \\ &= \sum_{\substack{\mathrm{A}\in\mathcal{S}\\ i\in\mathcal{I}_\mathrm{A}}} \int_{\mathbb{R}^3} f_{\mathrm{A}_i} \left(\frac{1}{2} m_\mathrm{A} \mathbf{C}_\mathrm{A}\cdot\mathbf{C}_\mathrm{A} + \frac{1}{2} m_\mathrm{A} \mathbf{v}\cdot\mathbf{v} + E_{\mathrm{A}_i}\right) \mathrm{d}\mathbf{c}_\mathrm{A} \qquad (2.74)\\ &= \rho e^{\mathrm{tra}} + \rho e^{\mathrm{kin}} + \rho e^{\mathrm{int}} \qquad (2.75)\end{aligned}$$

where the translational, kinetic, and internal energy densities are defined as:

$$\rho e^{\mathrm{tra}} = \sum_{\substack{\mathrm{A}\in\mathcal{S}\\ i\in\mathcal{I}_\mathrm{A}}} \int_{\mathbb{R}^3} \frac{1}{2} m_\mathrm{A} f_{\mathrm{A}_i} \mathbf{C}_\mathrm{A}\cdot\mathbf{C}_\mathrm{A}\,\mathrm{d}\mathbf{c}_\mathrm{A}, \quad \rho e^{\mathrm{kin}} = \frac{1}{2}\rho \mathbf{v}\cdot\mathbf{v}, \quad \rho e^{\mathrm{int}} = \sum_{\substack{\mathrm{A}\in\mathcal{S}\\ i\in\mathcal{I}_\mathrm{A}}} n_{\mathrm{A}_i} E_{\mathrm{A}_i} \qquad (2.76)$$

Using this definition, the conservation of total energy equation can be written:

$$\begin{aligned}\frac{\partial \rho e}{\partial t} + \nabla_\mathbf{x}\cdot(\rho e \mathbf{v}) + \nabla_\mathbf{x}\cdot \sum_{\substack{\mathrm{A}\in\mathcal{S}\\ i\in\mathcal{I}_\mathrm{A}}} \int_{\mathbb{R}^3} \mathbf{C}_\mathrm{A} f_{\mathrm{A}_i} \left(\frac{1}{2} m_\mathrm{A} \mathbf{c}_\mathrm{A}\cdot\mathbf{c}_\mathrm{A} + E_{\mathrm{A}_i}\right) \mathrm{d}\mathbf{c}_\mathrm{A} \\ = \sum_{\substack{\mathrm{A}\in\mathcal{S}\\ i\in\mathcal{I}_\mathrm{A}}} \int_{\mathbb{R}^3} \left(\frac{1}{2} m_\mathrm{A} \mathbf{c}_\mathrm{A}\cdot\mathbf{c}_\mathrm{A} + E_{\mathrm{A}_i}\right) \left(Q^{\mathrm{el}}_{\mathrm{A}_i} + Q^{\mathrm{in}}_{\mathrm{A}_i} + Q^{\mathrm{re}}_{\mathrm{A}_i}\right) \mathrm{d}\mathbf{c}_\mathrm{A} \qquad (2.77)\end{aligned}$$

We can re-write the flux term as:

$$\nabla_\mathbf{x}\cdot \sum_{\substack{\mathrm{A}\in\mathcal{S}\\ i\in\mathcal{I}_\mathrm{A}}} \int_{\mathbb{R}^3} \mathbf{C}_\mathrm{A} f_{\mathrm{A}_i} \left(\frac{1}{2} m_\mathrm{A} \mathbf{C}_\mathrm{A}\cdot\mathbf{C}_\mathrm{A} + E_{\mathrm{A}_i}\right) \mathrm{d}\mathbf{c}_\mathrm{A} = \nabla_\mathbf{x}\cdot(p\mathbf{v}) \qquad (2.78)$$

Using the definition of the total enthalpy per unit volume, $\rho h = \rho e + p$, the final conservation of energy equation reads:

$$\frac{\partial \rho e}{\partial t} + \nabla_\mathbf{x}\cdot(\rho h \mathbf{v}) = 0 \qquad (2.79)$$

Conservation of group internal energy

Finally, to close the system of equations for the MGMEL model, the internal energy is applied to the Maxwell transfer equation. First using the definition of group energy density specified earlier and using Eq. (2.29) and summing over all states i in group p, we obtain:

$$\frac{\partial\left(n_{\mathrm{A}_p}E^{\mathrm{int}}_{\mathrm{A}_p}\right)}{\partial t}+\nabla_{\mathbf{x}}\cdot\left(n_{\mathrm{A}_p}E^{\mathrm{int}}_{\mathrm{A}_p}\mathbf{v}\right)+\nabla_{\mathbf{x}}\cdot\sum_{i\in\mathcal{I}_p}\int_{\mathbb{R}^3}\mathbf{C}_{\mathrm{A}}f_{\mathrm{A}_i}E_{\mathrm{A}_i}\,\mathrm{d}\mathbf{c}_{\mathrm{A}}$$
$$=\sum_{i\in\mathcal{I}_p}\int_{\mathbb{R}^3}E_{\mathrm{A}_i}\left(Q^{\mathrm{el}}_{\mathrm{A}_i}+Q^{\mathrm{in}}_{\mathrm{A}_i}+Q^{\mathrm{re}}_{\mathrm{A}_i}\right)\mathrm{d}\mathbf{c}_{\mathrm{A}} \tag{2.80}$$

Using the velocity distribution function defined earlier and the property of the elastic collision integral, the group conservation of energy equation reduces to:

$$\frac{\partial\left(n_{\mathrm{A}_p}E^{\mathrm{int}}_{\mathrm{A}_p}\right)}{\partial t}+\nabla_{\mathbf{x}}\cdot\left(n_{\mathrm{A}_p}E^{\mathrm{int}}_{\mathrm{A}_p}\mathbf{v}\right)=\sum_{i\in\mathcal{I}_p}\int_{\mathbb{R}^3}E_{\mathrm{A}_i}\left(Q^{\mathrm{in}}_{\mathrm{A}_i}+Q^{\mathrm{re}}_{\mathrm{A}_i}\right)\mathrm{d}\mathbf{c}_{\mathrm{A}} \tag{2.81}$$

2.5 Hydrodynamic governing equations

The final set of governing equations for the MGMEL model comprises the group conservation of mass equations, conservation of momentum, conservation of total energy, and conservation of group energy equations. This amounts to $(2N_{\mathrm{group}}+4)$ equations, where N_{group} is the number of groups considered. The set of conservation equations reads:

$$\frac{\partial\rho_{\mathrm{A}_p}}{\partial t}+\nabla_{\mathbf{x}}\cdot\left(\rho_{\mathrm{A}_p}\mathbf{v}\right)=\dot{\omega}_{\mathrm{A}_p} \tag{2.82}$$

$$\frac{\partial\rho\mathbf{v}}{\partial t}+\nabla_{\mathbf{x}}\cdot\left(\rho\mathbf{v}\otimes\mathbf{v}+p\underline{\mathbf{I}}\right)=\mathbf{0} \tag{2.83}$$

$$\frac{\partial\rho e}{\partial t}+\nabla_{\mathbf{x}}\cdot\left(\rho h\mathbf{v}\right)=0 \tag{2.84}$$

$$\frac{\partial\left(n_{\mathrm{A}_p}E^{\mathrm{int}}_{\mathrm{A}_p}\right)}{\partial t}+\nabla_{\mathbf{x}}\cdot\left(n_{\mathrm{A}_p}E^{\mathrm{int}}_{\mathrm{A}_p}\mathbf{v}\right)=\dot{\Omega}_{\mathrm{A}_p} \tag{2.85}$$

where the collisional terms are written simply as $\dot{\omega}_{\mathrm{A}_p}$ and $\dot{\Omega}_{\mathrm{A}_p}$ for the mass and internal energy source terms respectively.

2.6 Collision source terms

In this section the collision terms in the group conservation of mass and energy equations will be analyzed.

2.6.1 Mass source terms

The collision terms (right hand side) of the conservation of group mass equations account for the effect of inelastic and reactive collisions. Let us denote the production terms due to collisions in the conservation of mass equation as $\dot{\omega}_{\mathrm{A}_p}$:

$$\dot{\omega}_{\mathrm{A}_p} = \dot{\omega}^{\mathrm{in}}_{\mathrm{A}_p} + \dot{\omega}^{\mathrm{re}}_{\mathrm{A}_p} = \sum_{i\in\mathcal{I}_p}\int_{\mathbb{R}^3} m_{\mathrm{A}} Q^{\mathrm{in}}_{\mathrm{A}_i}\,\mathrm{d}\mathbf{c}_{\mathrm{A}} + \sum_{i\in\mathcal{I}_p}\int_{\mathbb{R}^3} m_{\mathrm{A}} Q^{\mathrm{re}}_{\mathrm{A}_i}\,\mathrm{d}\mathbf{c}_{\mathrm{A}} \tag{2.86}$$

The first term, which accounts for the effect of inelastic collisions can be expanded in terms of the partial collision operators:

$$\dot{\omega}^{\mathrm{in}}_{\mathrm{A}_p} = \sum_{i\in\mathcal{I}_p}\sum_{\substack{(\mathrm{B}_j,\mathrm{A}_k,\mathrm{B}_l)\\ \in\mathcal{C}^{\mathrm{in}}_{\mathrm{A}_i}}}\iiint_{\mathscr{L}^2\times\mathbb{R}^3\times\mathbb{R}^3} m_{\mathrm{A}}\left(\frac{\beta_{\mathrm{A}_k}\beta_{\mathrm{B}_l}}{\beta_{\mathrm{A}_i}\beta_{\mathrm{B}_j}} f'_{\mathrm{A}_k} f'_{\mathrm{B}_l} - f_{\mathrm{A}_i} f_{\mathrm{B}_j}\right) g\sigma^{\mathrm{A}_k\mathrm{B}_l}_{\mathrm{A}_i\mathrm{B}_j}\,\mathrm{d}\boldsymbol{\omega'}\,\mathrm{d}\mathbf{c}_{\mathrm{B}}\,\mathrm{d}\mathbf{c}_{\mathrm{A}} \tag{2.87}$$

In anticipation of the form which this integral will take, we will re-write this term as a depleting and replenishing term in terms of the group number densities. Further details on this procedure will be presented in the next chapter.

$$\dot{\omega}^{\mathrm{in}}_{\mathrm{A}_p} = \sum_{\mathrm{B}\in\mathcal{S}}\sum_{q\in\mathrm{B}}\sum_{r\in\mathrm{A}}\sum_{s\in\mathrm{B}}\left(-\,{}^0K_{pq,rs} n_{\mathrm{A}_p} n_{\mathrm{B}_q} + {}^0\bar{K}_{pq,rs} n_{\mathrm{A}_r} n_{\mathrm{B}_s}\right) \tag{2.88}$$

From this form, we can define the reaction rate coefficients, ${}^0K_{pq,rs}$ and ${}^0\bar{K}_{pq,rs}$ in terms of the collision integrals:

$${}^0K_{pq,rs} = \frac{1}{n_{\mathrm{A}_p} n_{\mathrm{B}_q}}\sum_{i\in\mathcal{I}_p}\sum_{j\in\mathcal{I}_q}\sum_{k\in\mathcal{I}_r}\sum_{l\in\mathcal{I}_s} m_{\mathrm{A}}\iiint_{\mathscr{L}^2\times\mathbb{R}^3\times\mathbb{R}^3} f_{\mathrm{A}_i} f_{\mathrm{B}_j} g\sigma^{\mathrm{A}_k\mathrm{B}_l}_{\mathrm{A}_i\mathrm{B}_j}\,\mathrm{d}\boldsymbol{\omega'}\,\mathrm{d}\mathbf{c}_{\mathrm{B}}\,\mathrm{d}\mathbf{c}_{\mathrm{A}} \tag{2.89}$$

$${}^0\bar{K}_{pq,rs} = \frac{1}{n_{\mathrm{A}_r} n_{\mathrm{B}_s}}\sum_{i\in\mathcal{I}_p}\sum_{j\in\mathcal{I}_q}\sum_{k\in\mathcal{I}_r}\sum_{l\in\mathcal{I}_s} m_{\mathrm{A}}\iiint_{\mathscr{L}^2\times\mathbb{R}^3\times\mathbb{R}^3} \frac{\beta_{\mathrm{A}_k}\beta_{\mathrm{B}_l}}{\beta_{\mathrm{A}_i}\beta_{\mathrm{B}_j}} f'_{\mathrm{A}_k} f'_{\mathrm{B}_l} g\sigma^{\mathrm{A}_k\mathrm{B}_l}_{\mathrm{A}_i\mathrm{B}_j}\,\mathrm{d}\boldsymbol{\omega'}\,\mathrm{d}\mathbf{c}_{\mathrm{B}}\,\mathrm{d}\mathbf{c}_{\mathrm{A}} \tag{2.90}$$

We will revisit these integrals in the next chapter and discuss how they are evaluated using the QCT method.

The reactive scattering term comprises two components corresponding to the exchange reactions and the combined dissociation-excitation reactions:

$$\dot{\omega}_{\mathrm{A}_p}^{\mathrm{re}} = \dot{\omega}_{\mathrm{A}_p}^{\mathrm{exc}} + \dot{\omega}_{\mathrm{A}_p}^{\mathrm{dis}} \tag{2.91}$$

First we will discuss the exchange term. This term reads:

$$\dot{\omega}_{\mathrm{A}_p}^{\mathrm{exc}} = \sum_{i \in \mathcal{I}_p} \int_{\mathbb{R}^3} m_{\mathrm{A}} Q_{\mathrm{A}_i}^{\mathrm{exc}} \, \mathrm{d}\mathbf{c}_{\mathrm{A}} \tag{2.92}$$

$$= \sum_{i \in \mathcal{I}_p} \sum_{\substack{(\mathrm{B}_j, \mathrm{C}_k, \mathrm{D}_l) \\ \in \mathcal{C}_{\mathrm{A}_i}^{\mathrm{exc}}}} m_{\mathrm{A}} \iiint_{\mathscr{L}^2 \times \mathbb{R}^3 \times \mathbb{R}^3} \left(\frac{\beta_{\mathrm{C}_k} \beta_{\mathrm{D}_l}}{\beta_{\mathrm{A}_i} \beta_{\mathrm{B}_j}} f'_{\mathrm{C}_k} f'_{\mathrm{D}_l} - f_{\mathrm{A}_i} f_{\mathrm{B}_j} \right) g \sigma_{\mathrm{A}_i \mathrm{B}_j}^{\mathrm{C}_k \mathrm{D}_l} \, \mathrm{d}\boldsymbol{\omega}' \, \mathrm{d}\mathbf{c}_{\mathrm{B}} \, \mathrm{d}\mathbf{c}_{\mathrm{A}} \tag{2.93}$$

Similarly, we can re-write this term in terms of the reaction rate coefficients, ${}^0K_{\mathrm{A}_p\mathrm{B}_q,\mathrm{C}_r\mathrm{D}_s}$ and ${}^0\bar{K}_{\mathrm{A}_p\mathrm{B}_q,\mathrm{C}_r\mathrm{D}_s}$:

$$\dot{\omega}_{\mathrm{A}_p}^{\mathrm{exc}} = \sum_{\substack{(\mathrm{B},\mathrm{C},\mathrm{D}) \\ \in \mathcal{S}}} \sum_{q \in \mathrm{B}} \sum_{r \in \mathrm{C}} \sum_{s \in \mathrm{D}} \left(- {}^0K_{\mathrm{A}_p\mathrm{B}_q,\mathrm{C}_r\mathrm{D}_s} n_{\mathrm{A}_p} n_{\mathrm{B}_q} + {}^0\bar{K}_{\mathrm{A}_p\mathrm{B}_q,\mathrm{C}_r\mathrm{D}_s} n_{\mathrm{C}_r} n_{\mathrm{D}_s} \right) \tag{2.94}$$

where

$${}^0K_{\mathrm{A}_p\mathrm{B}_q,\mathrm{C}_r\mathrm{D}_s} = \frac{1}{n_{\mathrm{A}_p} n_{\mathrm{B}_q}} \sum_{i \in \mathcal{I}_p} \sum_{j \in \mathcal{I}_q} \sum_{k \in \mathcal{I}_r} \sum_{l \in \mathcal{I}_s} m_{\mathrm{A}} \iiint_{\mathscr{L}^2 \times \mathbb{R}^3 \times \mathbb{R}^3} f_{\mathrm{A}_i} f_{\mathrm{B}_j} g \sigma_{\mathrm{A}_i \mathrm{B}_j}^{\mathrm{C}_k \mathrm{D}_l} \, \mathrm{d}\boldsymbol{\omega}' \, \mathrm{d}\mathbf{c}_{\mathrm{B}} \, \mathrm{d}\mathbf{c}_{\mathrm{A}} \tag{2.95}$$

$${}^0\bar{K}_{\mathrm{A}_p\mathrm{B}_q,\mathrm{C}_r\mathrm{D}_s} = \frac{1}{n_{\mathrm{C}_r} n_{\mathrm{D}_s}} \sum_{i \in \mathcal{I}_p} \sum_{j \in \mathcal{I}_q} \sum_{k \in \mathcal{I}_r} \sum_{l \in \mathcal{I}_s} m_{\mathrm{A}} \iiint_{\mathscr{L}^2 \times \mathbb{R}^3 \times \mathbb{R}^3} \frac{\beta_{\mathrm{C}_k} \beta_{\mathrm{D}_l}}{\beta_{\mathrm{A}_i} \beta_{\mathrm{B}_j}} f'_{\mathrm{C}_k} f'_{\mathrm{D}_l} g \sigma_{\mathrm{A}_i \mathrm{B}_j}^{\mathrm{C}_k \mathrm{D}_l} \, \mathrm{d}\boldsymbol{\omega}' \, \mathrm{d}\mathbf{c}_{\mathrm{B}} \, \mathrm{d}\mathbf{c}_{\mathrm{A}} \tag{2.96}$$

Finally, for the excitation-dissociation reaction, the mass source term reads:

$$\dot{\omega}^{\mathrm{dis}}_{\mathrm{A}_p} = \sum_{i\in\mathcal{I}_p} \int_{\mathbb{R}^3} m_{\mathrm{A}} Q^{\mathrm{dis}}_{\mathrm{A}_i} \,\mathrm{d}\mathbf{c}_{\mathrm{A}} \tag{2.97}$$

$$= \sum_{i\in\mathcal{I}_p} \sum_{\substack{(\mathrm{B}_j,\mathrm{C}_k,\mathrm{D}_l,\mathrm{B}_m)\\ \in\mathcal{C}^{\mathrm{dis}}_{\mathrm{A}_i}}} m_{\mathrm{A}} \iiint_{\mathscr{L}^2\times\mathbb{R}^3\times\mathbb{R}^3} \left(\frac{\beta_{\mathrm{C}_k}\beta_{\mathrm{D}_l}\beta_{\mathrm{B}_m}}{\beta_{\mathrm{A}_i}\beta_{\mathrm{B}_j}} f'_{\mathrm{C}_k} f'_{\mathrm{D}_l} f'_{\mathrm{B}_m} - f_{\mathrm{A}_i} f_{\mathrm{B}_j} \right) g\sigma^{\mathrm{C}_k\mathrm{D}_l\mathrm{B}_m}_{\mathrm{A}_i\mathrm{B}_j} \,\mathrm{d}\boldsymbol{\omega'} \,\mathrm{d}\mathbf{c}_{\mathrm{B}} \,\mathrm{d}\mathbf{c}_{\mathrm{A}} \tag{2.98}$$

Again, this can be re-written in terms of reaction rate coefficients ${}^0K_{\mathrm{A}_p\mathrm{B}_q,\mathrm{C}_r\mathrm{D}_s\mathrm{B}_t}$ and ${}^0\bar{K}_{\mathrm{A}_p\mathrm{B}_q,\mathrm{C}_r\mathrm{D}_s\mathrm{B}_t}$:

$$\dot{\omega}^{\mathrm{dis}}_{\mathrm{A}_p} = \sum_{\substack{(\mathrm{B},\mathrm{C},\mathrm{D})\\ \in\mathcal{S}}} \sum_{q\in\mathrm{B}} \sum_{r\in\mathrm{C}} \sum_{s\in\mathrm{D}} \sum_{t\in\mathrm{B}} \left(-{}^0C_{\mathrm{A}_p\mathrm{B}_q,\mathrm{C}_r\mathrm{D}_s\mathrm{B}_t} n_{\mathrm{A}_p} n_{\mathrm{B}_q} + {}^0\bar{C}_{\mathrm{A}_p\mathrm{B}_q,\mathrm{C}_r\mathrm{D}_s\mathrm{B}_t} n_{\mathrm{C}_r} n_{\mathrm{D}_s} n_{\mathrm{B}_t} \right) \tag{2.99}$$

such that the group excitation-dissociation and excitation-recombination rates can be expressed:

$${}^0C_{\mathrm{A}_p\mathrm{B}_q,\mathrm{C}_r\mathrm{D}_s\mathrm{B}_t} = \frac{1}{n_{\mathrm{A}_p} n_{\mathrm{B}_q}} \sum_{i\in\mathcal{I}_p} \sum_{j\in\mathcal{I}_q} \sum_{k\in\mathcal{I}_r} \sum_{l\in\mathcal{I}_s} \sum_{m\in\mathcal{I}_t} m_{\mathrm{A}} \iiint_{\mathscr{L}^2\times\mathbb{R}^3\times\mathbb{R}^3} f_{\mathrm{A}_i} f_{\mathrm{B}_j} g\sigma^{\mathrm{C}_k\mathrm{D}_l\mathrm{B}_m}_{\mathrm{A}_i\mathrm{B}_j} \,\mathrm{d}\boldsymbol{\omega'} \,\mathrm{d}\mathbf{c}_{\mathrm{B}} \,\mathrm{d}\mathbf{c}_{\mathrm{A}} \tag{2.100}$$

$${}^0\bar{C}_{\mathrm{A}_p\mathrm{B}_q,\mathrm{C}_r\mathrm{D}_s\mathrm{B}_t} = \frac{1}{n_{\mathrm{C}_r} n_{\mathrm{D}_s} n_{\mathrm{B}_t}} \sum_{i\in\mathcal{I}_p} \sum_{j\in\mathcal{I}_q} \sum_{k\in\mathcal{I}_r} \sum_{l\in\mathcal{I}_s} \sum_{m\in\mathcal{I}_t} m_{\mathrm{A}} \iiint_{\mathscr{L}^2\times\mathbb{R}^3\times\mathbb{R}^3} \frac{\beta_{\mathrm{C}_k}\beta_{\mathrm{D}_l}\beta_{\mathrm{B}_m}}{\beta_{\mathrm{A}_i}\beta_{\mathrm{B}_j}} f'_{\mathrm{C}_k} f'_{\mathrm{D}_l} f'_{\mathrm{B}_m} g\sigma^{\mathrm{C}_k\mathrm{D}_l\mathrm{B}_m}_{\mathrm{A}_i\mathrm{B}_j} \,\mathrm{d}\boldsymbol{\omega'} \,\mathrm{d}\mathbf{c}_{\mathrm{B}} \,\mathrm{d}\mathbf{c}_{\mathrm{A}} \tag{2.101}$$

2.6.2 Energy source terms

In a similar fashion, we can express the energy source terms as the product of a coefficient and group number densities or energies. For brevity the details will be skipped as the procedure is the same as that for the mass source terms. Only the final expressions will be presented.

The inelastic scattering source term for the energy equation reads:

$$\dot{\Omega}^{\mathrm{in}}_{\mathrm{A}_p} = \sum_{\mathrm{B}\in\mathcal{S}} \sum_{q\in\mathrm{B}} \sum_{r\in\mathrm{A}} \sum_{s\in\mathrm{B}} \left(-{}^1K_{pq,rs} n_{\mathrm{A}_p} n_{\mathrm{B}_q} + {}^1\bar{K}_{pq,rs} n_{\mathrm{A}_r} n_{\mathrm{B}_s} \right) \tag{2.102}$$

where the energy transfer coefficients, ${}^1K_{pq,rs}$ and ${}^1\bar{K}_{pq,rs}$ can be written:

$$ {}^1K_{pq,rs} = \frac{1}{n_{\mathrm{A}_p} n_{\mathrm{B}_q}} \sum_{i\in\mathcal{I}_p}\sum_{j\in\mathcal{I}_q}\sum_{k\in\mathcal{I}_r}\sum_{l\in\mathcal{I}_s} E_{\mathrm{A}_i} \iiint_{\mathscr{L}^2\times\mathbb{R}^3\times\mathbb{R}^3} f_{\mathrm{A}_i} f_{\mathrm{B}_j} g \sigma^{\mathrm{A}_k\mathrm{B}_l}_{\mathrm{A}_i\mathrm{B}_j} \,\mathrm{d}\boldsymbol{\omega'}\,\mathrm{d}\mathbf{c}_\mathrm{B}\,\mathrm{d}\mathbf{c}_\mathrm{A} \tag{2.103} $$

$$ {}^1\bar{K}_{pq,rs} = \frac{1}{n_{\mathrm{A}_r} n_{\mathrm{B}_s}} \sum_{i\in\mathcal{I}_p}\sum_{j\in\mathcal{I}_q}\sum_{k\in\mathcal{I}_r}\sum_{l\in\mathcal{I}_s} E_{\mathrm{A}_i} \iiint_{\mathscr{L}^2\times\mathbb{R}^3\times\mathbb{R}^3} \frac{\beta_{\mathrm{A}_k}\beta_{\mathrm{B}_l}}{\beta_{\mathrm{A}_i}\beta_{\mathrm{B}_j}} f'_{\mathrm{A}_k} f'_{\mathrm{B}_l} g \sigma^{\mathrm{A}_k\mathrm{B}_l}_{\mathrm{A}_i\mathrm{B}_j} \,\mathrm{d}\boldsymbol{\omega'}\,\mathrm{d}\mathbf{c}_\mathrm{B}\,\mathrm{d}\mathbf{c}_\mathrm{A} \tag{2.104} $$

The exchange energy source term reads:

$$ \dot{\Omega}^{\mathrm{exc}}_{\mathrm{A}_p} = \sum_{\substack{(\mathrm{B},\mathrm{C},\mathrm{D})\\ \in\mathcal{S}}} \sum_{q\in\mathrm{B}}\sum_{r\in\mathrm{C}}\sum_{s\in\mathrm{D}} \left(- {}^1K_{\mathrm{A}_p\mathrm{B}_q,\mathrm{C}_r\mathrm{D}_s} n_{\mathrm{A}_p} n_{\mathrm{B}_q} + {}^1\bar{K}_{\mathrm{A}_p\mathrm{B}_q,\mathrm{C}_r\mathrm{D}_s} n_{\mathrm{C}_r} n_{\mathrm{D}_s} \right) \tag{2.105} $$

where ${}^1K_{\mathrm{A}_p\mathrm{B}_q,\mathrm{C}_r\mathrm{D}_s}$ and ${}^1\bar{K}_{\mathrm{A}_p\mathrm{B}_q,\mathrm{C}_r\mathrm{D}_s}$ denote the energy transfer coefficients, defined:

$$ {}^1K_{\mathrm{A}_p\mathrm{B}_q,\mathrm{C}_r\mathrm{D}_s} = \frac{1}{n_{\mathrm{A}_p} n_{\mathrm{B}_q}} \sum_{i\in\mathcal{I}_p}\sum_{j\in\mathcal{I}_q}\sum_{k\in\mathcal{I}_r}\sum_{l\in\mathcal{I}_s} E_{\mathrm{A}_i} \iiint_{\mathscr{L}^2\times\mathbb{R}^3\times\mathbb{R}^3} f_{\mathrm{A}_i} f_{\mathrm{B}_j} g \sigma^{\mathrm{C}_k\mathrm{D}_l}_{\mathrm{A}_i\mathrm{B}_j} \,\mathrm{d}\boldsymbol{\omega'}\,\mathrm{d}\mathbf{c}_\mathrm{B}\,\mathrm{d}\mathbf{c}_\mathrm{A} \tag{2.106} $$

$$ {}^1\bar{K}_{\mathrm{A}_p\mathrm{B}_q,\mathrm{C}_r\mathrm{D}_s} = \frac{1}{n_{\mathrm{C}_r} n_{\mathrm{D}_s}} \sum_{i\in\mathcal{I}_p}\sum_{j\in\mathcal{I}_q}\sum_{k\in\mathcal{I}_r}\sum_{l\in\mathcal{I}_s} E_{\mathrm{A}_i} \iiint_{\mathscr{L}^2\times\mathbb{R}^3\times\mathbb{R}^3} \frac{\beta_{\mathrm{C}_k}\beta_{\mathrm{D}_l}}{\beta_{\mathrm{A}_i}\beta_{\mathrm{B}_j}} f'_{\mathrm{C}_k} f'_{\mathrm{D}_l} g \sigma^{\mathrm{C}_k\mathrm{D}_l}_{\mathrm{A}_i\mathrm{B}_j} \,\mathrm{d}\boldsymbol{\omega'}\,\mathrm{d}\mathbf{c}_\mathrm{B}\,\mathrm{d}\mathbf{c}_\mathrm{A} \tag{2.107} $$

Finally, the energy source term for the excitation-dissociation reaction reads:

$$ \dot{\Omega}^{\mathrm{dis}}_{\mathrm{A}_p} = \sum_{\substack{(\mathrm{B},\mathrm{C},\mathrm{D})\\ \in\mathcal{S}}} \sum_{q\in\mathrm{B}}\sum_{r\in\mathrm{C}}\sum_{s\in\mathrm{D}}\sum_{t\in\mathrm{B}} \left(- {}^1C_{\mathrm{A}_p\mathrm{B}_q,\mathrm{C}_r\mathrm{D}_s\mathrm{B}_t} n_{\mathrm{A}_p} n_{\mathrm{B}_q} + {}^1\bar{C}_{\mathrm{A}_p\mathrm{B}_q,\mathrm{C}_r\mathrm{D}_s\mathrm{B}_t} n_{\mathrm{C}_r} n_{\mathrm{D}_s} n_{\mathrm{B}_t} \right) \tag{2.108} $$

where ${}^1C_{\mathrm{A}_p\mathrm{B}_q,\mathrm{C}_r\mathrm{D}_s\mathrm{B}_t}$ and ${}^1\bar{C}_{\mathrm{A}_p\mathrm{B}_q,\mathrm{C}_r\mathrm{D}_s\mathrm{B}_t}$ denote the energy transfer coefficients defined as:

$$ {}^1C_{\mathrm{A}_p\mathrm{B}_q,\mathrm{C}_r\mathrm{D}_s\mathrm{B}_t} = \frac{1}{n_{\mathrm{A}_p} n_{\mathrm{B}_q}} \sum_{i\in\mathcal{I}_p}\sum_{j\in\mathcal{I}_q}\sum_{k\in\mathcal{I}_r}\sum_{l\in\mathcal{I}_s}\sum_{m\in\mathcal{I}_t} E_{\mathrm{A}_i} \iiint_{\mathscr{L}^2\times\mathbb{R}^3\times\mathbb{R}^3} f_{\mathrm{A}_i} f_{\mathrm{B}_j} g \sigma^{\mathrm{C}_k\mathrm{D}_l\mathrm{B}_m}_{\mathrm{A}_i\mathrm{B}_j} \,\mathrm{d}\boldsymbol{\omega'}\,\mathrm{d}\mathbf{c}_\mathrm{B}\,\mathrm{d}\mathbf{c}_\mathrm{A} \tag{2.109} $$

$$ \begin{aligned} {}^1\bar{C}_{\mathrm{A}_p\mathrm{B}_q,\mathrm{C}_r\mathrm{D}_s\mathrm{B}_t} = & \frac{1}{n_{\mathrm{C}_r} n_{\mathrm{D}_s} n_{\mathrm{B}_t}} \sum_{i\in\mathcal{I}_p}\sum_{j\in\mathcal{I}_q}\sum_{k\in\mathcal{I}_r}\sum_{l\in\mathcal{I}_s}\sum_{m\in\mathcal{I}_t} E_{\mathrm{A}_i} \\ & \iiint_{\mathscr{L}^2\times\mathbb{R}^3\times\mathbb{R}^3} \frac{\beta_{\mathrm{C}_k}\beta_{\mathrm{D}_l}\beta_{\mathrm{B}_m}}{\beta_{\mathrm{A}_i}\beta_{\mathrm{B}_j}} f'_{\mathrm{C}_k} f'_{\mathrm{D}_l} f'_{\mathrm{B}_m} g \sigma^{\mathrm{C}_k\mathrm{D}_l\mathrm{B}_m}_{\mathrm{A}_i\mathrm{B}_j} \,\mathrm{d}\boldsymbol{\omega'}\,\mathrm{d}\mathbf{c}_\mathrm{B}\,\mathrm{d}\mathbf{c}_\mathrm{A} \end{aligned} \tag{2.110} $$

In the next chapter, the procedure for evaluating the reaction rate coefficients and energy transfer coefficients will be presented.

2.7 Summary

In this chapter we present the MGME framework and use this approach in conjunction with the Boltzmann equation to construct macroscopic governing equations. The MGME method subdivides the energy space into groups containing energy levels which are linked by "fast" processes. Then, we make use of the Boltzmann H-Theorem as well as the condition that the entropy production within a group is identically zero to derive the distribution of energy levels within a group. The distribution of energy states relies on the definition of collisional invariants. The collisional invariants used in this work are defined by analyzing the time-scale of the various processes. We assume that processes within a group are much faster than those among groups, and the energy jumps which thermalize the distribution within a group are so small that the internal energy can be taken as the final collisional invariant to close the system. Finally, we arrive at a two temperature distribution of levels within a group. The corresponding governing equations for this approach comprise conservation of group mass, conservation of momentum, conservation of total energy, and conservation of group energy. In the next chapter, we will provide the link between the chemical source terms (collision integrals) and the QCT method for calculating kinetic data for the MGME model.

Chapter 3

Collision Theory

In this chapter we provide a link between collision terms in the governing equations derived in the previous chapter and the QCT method for determining rate coefficients. The QCT method is used to estimate the reaction rate coefficient or cross-section by simulating many collisions between particles to determine the probability that a given reaction occurred. This probability is related to the rate coefficient by averaging over the collision energy according to a Maxwellian velocity distribution. The dynamics of the collision are assumed to occur classically; however the particles are initialized by mapping discrete quantum states (vibrational and rotational quantum states) to continuum variables (position and momenta). The outcome of each collision is analyzed to determine the final "state" of the products of the reaction (*e.g.*, excited state, dissociated constituent atoms, etc.). After many collisions are simulated, the probability is calculated along with an estimated statistical error. This chapter is organized as follows: Section 3.1 presents the quantum description of the interaction between particles. Section 3.2 describes the QCT method used to compute rate coefficients or cross-sections. Section 3.3 provides the link between the QCT method with the MGME method described in Chapter 2. Finally, we summarize in Section 3.4.

3.1 Quantum description of molecule interactions

The interaction between particles can be described by means of the Schrödinger wave equation:

$$\hat{H}\psi(\mathbf{R},\mathbf{r}) = E\psi(\mathbf{R},\mathbf{r}) \tag{3.1}$$

where $\psi(\mathbf{R},\mathbf{r})$ denotes the wave-function as a function of nuclear, $\mathbf{R}$, and electron, $\mathbf{r}$, coordinates, E denotes the total system energy, and $\hat{H}$ denotes the Hamiltonian operator which comprises the nuclear kinetic energy ($\hat{T}_{\mathrm{n}}(\mathbf{R})$), electronic kinetic energy ($\hat{T}_e(\mathbf{r})$), nuclear repulsive potential energy

($\hat{V}_{\mathrm{nn}}(\mathbf{R})$), electron repulsive potential energy ($\hat{V}_{ee}(\mathbf{r})$), and the nuclear-electron attractive potential energy ($\hat{V}_{\mathrm{en}}(\mathbf{R},\mathbf{r})$):

$$\hat{H} = \hat{T}_{\mathrm{n}} + \hat{T}_e + \hat{V}_{\mathrm{nn}} + \hat{V}_{ee} + \hat{V}_{\mathrm{en}} \tag{3.2}$$

Let $\mathcal{H}$ denote the set of nuclei, and $\mathcal{E}$ denote the set containing all electrons. The potential and kinetic operators read:

$$\hat{T}_{\mathrm{n}} = -\sum_{I\in\mathcal{H}} \frac{\hbar^2}{2m_I}\nabla^2_{\mathbf{R}_I} \tag{3.3}$$

$$\hat{T}_e = -\sum_{I\in\mathcal{E}} \frac{\hbar^2}{2m_I}\nabla^2_{\mathbf{r}_I} \tag{3.4}$$

$$\hat{V}_{\mathrm{nn}} = \frac{e^2}{4\pi\varepsilon_0}\sum_{I\in\mathcal{H}}\sum_{\substack{J\in\mathcal{H}\\J>I}} \frac{Z_I Z_J}{|\mathbf{R}_I - \mathbf{R}_J|} \tag{3.5}$$

$$\hat{V}_{ee} = \frac{e^2}{4\pi\varepsilon_0}\sum_{I\in\mathcal{E}}\sum_{\substack{J\in\mathcal{E}\\J>I}} \frac{1}{|\mathbf{r}_I - \mathbf{r}_J|} \tag{3.6}$$

$$\hat{V}_{\mathrm{en}} = -\frac{e^2}{4\pi\varepsilon_0}\sum_{I\in\mathcal{H}}\sum_{J\in\mathcal{E}} \frac{Z_I}{|\mathbf{R}_I - \mathbf{r}_J|} \tag{3.7}$$

where $\hbar = \mathrm{h_P}/(2\pi)$ denotes the reduced Planck constant, m_I denotes the mass of species I either nucleus or electron, e denotes the magnitude of the elementary charge of an electron or proton, ε_0 denotes the permittivity of free space, and Z_I denotes the atomic number of species I.

Because the wave-function is a function of all nuclear and electronic coordinates, the dimensionality rapidly makes this equation computationally intractable. As a result, solving the Schrödinger equation for the wave-function even for simple systems is impossible (*e.g.*, N_2-N interactions). Realizing this, we must make some assumptions to render the Schrödinger equation computationally tractable. First, we assume that relativistic effects are negligible. Second, we assume that both the nuclei and electrons can be treated as point masses. Finally, we invoke the Born-Oppenheimer approximation, which posits that the motion of the nuclei is much slower than that of the electrons. This enables us to separate the Schrödinger equation into two parts: one describing the motion of the nuclei ($\chi(\mathbf{R})$) and one describing the motion of the electrons with fixed nuclei ($\phi(\mathbf{r};\mathbf{R})$), such that the total wave-function is the product of these two, $\psi(\mathbf{R},\mathbf{r}) = \chi(\mathbf{R})\phi(\mathbf{r};\mathbf{R})$. Therefore, we

can write the electronic and nuclear parts of the Schrödinger equation separately:

$$\left[\hat{T}_e(\mathbf{r}) + \hat{V}_{ee}(\mathbf{r}) + \hat{V}_{en}(\mathbf{r};\mathbf{R})\right]\phi(\mathbf{r};\mathbf{R}) = E_e(\mathbf{R})\phi(\mathbf{r};\mathbf{R}) \tag{3.8}$$

$$\left[\hat{T}_n(\mathbf{R}) + \hat{V}_{nn}(\mathbf{R}) + E_e(\mathbf{R})\right]\chi(\mathbf{R}) = E\chi(\mathbf{R}) \tag{3.9}$$

When written in this form, we can see that the $E_e(\mathbf{R})$ term describes the electronic potential energy as a function of nuclear distances. The summation of $E_e(\mathbf{R}) + \hat{V}_{nn}(\mathbf{R})$ describes the PES for the system. The PES describes the potential energy of the collection of nuclei in a cloud of electrons as a function of the nuclei positions. The spatial gradient of the PES provides the forces among nuclei and is used in dynamics calculations for the nuclei such as the QCT method. Therefore, it is necessary to calculate the PES at many geometric arrangements of the constituent atoms, and fit the PES to a differential function. In general (for non-linear geometries), the PES (technically a hypersurface) can be described by $3N - 6$ coordinates, where N is the number of nuclei (*e.g.*, 3 coordinates for N_2-N, and 6 coordinates for N_2-N_2). There has been significant work recently to calculate the PES for several systems relevant to air chemistry (in particular for application to chemistry in hypersonic flows) [74–84].

In this work, we apply the MGME-QCT method to the nitrogen systems, (N_2-N, and N_2-N_2). We consider nitrogen atoms and molecules in the ground electronic states, $N(^4S_u)$ and $N_2(X^1\Sigma_g^+)$ respectively. For both systems the PES used in this work is that developed at the NASA Ames Research Center by the computational chemistry group [75, 76, 125]. For the nitrogen molecules, there are 9390 rovibrational states, with vibrational quantum numbers v, and rotational quantum numbers J. The maximum vibrational state is $v = 60$ and the maximum rotational state is $J = 273$. The rovibrational states were determined using quantum mechanics calculations using the Wentzel-Kramers-Brillouin (WKB) approximation [126] with a modified $N_2(X^1\Sigma_g^+)$ potential based on the work of Le Roy *et al.* [88,127]. The absolute index for the rovibrational state, i, used in the previous chapter is determined by sorting the energy levels according to increasing energy such that $i = i(v, J)$. Of the 9390 levels, most have energy below the dissociation energy of 9.75 eV, referred to as the bound states. The remaining levels have energy above the dissociation energy, but below the J-dependent centrifugal barrier, referred to as quasi-bound states, because they have

a finite lifetime for spontaneous dissociation by tunneling.

$N_2(X^1\Sigma_g^+)$-$N(^4S_u)$ PES. Early work on the development of a PES for the N_2-N system was based on the empirical London-Eyring-Polanyi-Sato (LEPS) potential [128]. Following this, the first *ab initio* PES for the N_2-N system was developed by Wang *et al.* [74], and improved by Chaban *et al.* [76]. There has also been work on the low lying excited electronic states and allotropes of the N_2-N system [129–131]. However, in this work we will focus on the ground electronic state.

The PES used in this work for the $N_2(X^1\Sigma_g^+) - N(^4S_u)$ system is described in Refs. [74, 76]. It was constructed using 1344 geometry points calculated using the fifth order accurate triple energies functional. Further details on the calculation and fitting of the PES can be found in Refs. [38, 74, 76, 126]. The resulting PES for the $N_2(X^1\Sigma_g^+) - N(^4S_u)$ system is a function of three parameters, corresponding to the three degrees of freedom understanding the PES does not depend on the absolute location or angular momentum of the system of particles. This PES has previously been used to construct a database of rovibrational StS rate coefficients and study the non-equilibrium dissociation and energy transfer processes in a mixture of nitrogen atoms and molecules [38, 75].

$N_2(X^1\Sigma_g^+)$-$N_2(X^1\Sigma_g^+)$ PES. A review of previous work on the development of a PES for high energy collisions between nitrogen molecules reveals that there are two *ab initio* PESs available for this system: one developed by Jaffe *et al.* [76, 125], and one developed by Paukku *et al.* [77, 78]. A comparison of these two PESs is presented in Ref. [132], demonstrating that the thermal dissociation reaction rate coefficients obtained from both are similar.

In this work we use the PES developed by Jaffe *et al.* [76, 125]. For these calculations, the nuclear positions were divided into regions where both $N_2(X^1\Sigma_g^+)$ molecules had bond lengths near equilibrium, and where one or both $N_2(X^1\Sigma_g^+)$ molecules had a bond length far from equilibrium. In the first group, where both molecules have bond lengths near equilibrium, electronic structure calculations were performed using the closed-shell coupled-cluster-single-double method (CCSD(T)) to parametrize the wave-function [133, 134]. For this region, calculations were performed for 3821 nuclear geometries. In the second region, where one or both bond lengths are far from equilibrium, calculations were performed for 325 nuclear geometries using the multi-reference

averaged-coupled-pair-function method [135]. Following the electronic structure calculations, we must find an accurate analytical representation of the energy and forces on the grid of geometries where the electronic structure calculations were performed. This representation results in a six-dimensional hypersurface, depending on the six-degrees of freedom for this system of four particles. This fitting represents the PES, and was performed based on the form developed by Schwenke [126]. Further details on the calculation of the PES can be found in Refs. [75, 76, 125].

3.2 Quasi-classical trajectory method

The QCT method can be used to simulate the dynamics of the nuclei under interatomic forces determined by the PES. In this approach, instead of solving for the quantum description of the nuclei, as specified in Eq. (3.9), we assume that the nuclear motion can be approximated using classical mechanics. The QCT method relies on several assumptions. First, we assume that the masses of the nuclei are significantly large that any wave-effects of the nuclei can be neglected. Second, the results are more accurate when they are highly averaged such that the spread covered by a representative wave packet will be sufficiently small. Third, the total energy of the reactants should be sufficiently low relative to the energy barrier so that tunneling effects can be neglected. Fourth, when calculating StS reaction probabilities, the QCT method will not yield correct probabilities for processes that are classically forbidden unless a correction is applied in post-processing. Finally, the QCT method cannot predict resonance features or other interference phenomena.

The QCT method first initializes the particles to quantum states (*e.g.*, discrete rovibrational states), mapping the quantum states to initial positions and momenta. Then, the trajectory is obtained by solving Hamilton's equations of motion for the nuclei. Finally, after the trajectory has exceeded a certain number of time steps or distances between nuclei, the position and momenta of the nuclei are mapped back to quantum states. At the end of the trajectory, because the motion of the nuclei was estimated to occur classically, the quantum numbers (*i.e.*, v and J) are now real numbers, and must be truncated to integer values. At this point, if desired, selection rules on the allowed transitions can be applied.

In the following subsections the steps in the QCT procedure will be presented. In this work, we are using a modified version of the Vectorized Variable timestep Trajectory Code (VVTC) for

the QCT calculations written by D. W. Schwenke [126].

First, let us consider the integral which the QCT method is used to compute. The integral definition of the StS rate coefficient can be written as a function of the probability of that reaction occurring for a given impact parameter b, $P^{\mathrm{A}_k\mathrm{B}_l}_{\mathrm{A}_i\mathrm{B}_j}$ (different from the probability density, $W^{\mathrm{A}_k\mathrm{B}_l}_{\mathrm{A}_i\mathrm{B}_j}$, defined in Chapter 2). The impact parameter describes an offset between the projectile and target as shown in Fig. 3.1. The resulting integral which is determined in the QCT method is:

$$\kappa_{ij,kl} = \frac{1}{\chi}\left(\frac{\mu_{\mathrm{AB}}}{2\pi \mathrm{k_B} T}\right)^{3/2} \int_{\mathscr{L}^2} \int_{b=0}^{\infty} \int_{g=0}^{\infty} \exp\left[-\frac{\mu_{\mathrm{AB}}}{2\mathrm{k_B}T} g^2\right] 2\pi b g^3 P^{\mathrm{A}_k\mathrm{B}_l}_{\mathrm{A}_i\mathrm{B}_j} \, \mathrm{d}\boldsymbol{\omega} \, \mathrm{d}b \, \mathrm{d}g \tag{3.10}$$

where χ is introduced here as a symmetry factor. When the colliding particles, A and B, are the same, the symmetry factor is 2, otherwise it is 1. This ensures that collisions are not double counted; there is further discussion of this in Vincenti and Kruger [16]. Equation (3.10) forms the basis for the QCT method, and represents the ensemble averaged probability of a given reaction. The idea behind the QCT method is to compute this integral using a Monte Carlo sampling approach, by simulating many collisions between particles to calculate the probability that a given outcome was achieved. To accomplish this, we need a model for the dynamics of the collisions. The QCT method is so called because it assumes that the collision (*i.e.*, the motion of the nuclei) occurs *classically* but initializes the trajectory variables in a specific *quantum* state. An overview of the steps for the QCT method will be presented in the following sections. Further details on this approach can be found in in Refs. [86–88].

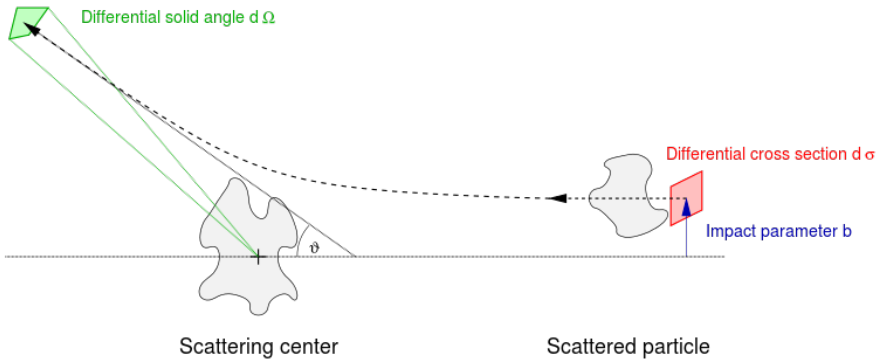

Figure 3.1: Diagram of impact parameter (Credit: Wikipedia).

3.2.1 Governing equations

The QCT method makes use of Hamilton's equations of motion for the dynamics of the nuclei. In this work, we are primarily concerned with solving for the kinetic data of two diatomic molecules colliding. Therefore, the equations in this section and the subsequent sections will focus on the QCT method applied to four-atom systems. However, the generalization to an arbitrary number of atoms is straightforward. First, the Hamiltonian for the system in a space-fixed Cartesian coordinate system can be written in terms of the twelve position coordinates $\mathbf{x} \equiv \{x_i;\, i = 1, \ldots, 12\}$ and twelve momenta $\mathbf{p} \equiv \{p_i;\, i = 1, \ldots, 12\}$ for nuclei denoted A, B, C, and D respectively:

$$H(\mathbf{x}, \mathbf{p_x}) = T(\mathbf{p_x}) + V(\mathbf{x}) \tag{3.11}$$

Where

$$T(\mathbf{p_x}) = \sum_{i=1}^{3} \left(\frac{1}{2m_{\mathrm{A}}} p_{x_i}^2 + \frac{1}{2m_{\mathrm{B}}} p_{x_{i+3}}^2 + \frac{1}{2m_{\mathrm{C}}} p_{x_{i+6}}^2 + \frac{1}{2m_{\mathrm{D}}} p_{x_{i+9}}^2 \right) \tag{3.12}$$

In this coordinate system, Hamilton's equations of motion read:

$$\dot{x}_i \equiv \frac{\partial x_i}{\partial t} = \frac{\partial H}{\partial p_{x_i}} = \frac{\partial T}{\partial p_{x_i}}, \qquad (i = 1, \ldots, 12) \tag{3.13}$$

$$\dot{p}_{x_i} \equiv \frac{\partial p_{x_i}}{\partial t} = -\frac{\partial H}{\partial x_i} = -\frac{\partial V}{\partial x_i}, \qquad (i = 1, \ldots, 12) \tag{3.14}$$

However, it is advantageous to do a transformation of coordinates to the center of mass reference frame. This allows for the elimination of three of the position and momenta, meaning we reduce the number of partial differential equations to solve from 24 to 18. While it is possible to also invoke conservation of total energy and angular momentum to further reduce the number of variables, it is not advantageous because the resulting equations are significantly more complicated. We denote the new vector of the positions as $\mathbf{Q} \equiv \{Q_i;\, i = 1, \ldots, 9\}$ and the vector of momenta as $\mathbf{P} \equiv \{P_i;\, i = 1, \ldots, 9\}$. Further details on this procedure can be found in Refs. [88, 126].

3.2.2 Initialization of trajectories

As discussed earlier, the quantization of energy states in the QCT method occurs in the initialization of the position and momentum variables. In order to fully specify the system, there are a total

of 18 parameters to initialize, corresponding to the 9 position and 9 momenta components. The position these correspond to the vector between the two diatoms (*i.e.*, a vector pointing from the center of mass of one molecule to the center of mass of the other), and the vector connecting the nuclei of each diatom (*i.e.*, a vector pointing from one nuclei to the other corresponding to the molecule). The parameters which determine the initial system comprise:

b	the impact parameter
ε	the polar angle between the centers-of-mass of A and B
R	the distance between the centers-of-mass of A and B
$\mathbf{V}_{rel}$	the relative velocity vector between the centers-of-mass of A and B
θ_1, θ_2	the azimuthal orientation angle of the A and B internuclear axes respectively
ϕ_1, ϕ_2	the polar orientation angle of the A and B internuclear axes respectively
η_1, η_2	the orientation of the rotational momentum perpendicular to the internuclear axes of molecules A and B respectively
$\lvert\mathbf{J}_1\rvert$, $\lvert\mathbf{J}_2\rvert$	the magnitude of the rotational momentum of molecules A and B respectively
r_1, r_2	the internuclear distance between the nuclei of molecules A and B respectively
$\dot{r}_1$, $\dot{r}_2$	the relative velocities between the nuclei of molecules A and B respectively

The position and velocity between the center-of-mass of the two molecules, described by (b, ε, R, $\mathbf{V}_{rel}$), can be simplified without loss of generality by placing the centers-of-mass of the colliding partners in the same plane, and aligning the relative velocity vector along an axis. Therefore, the relative speed, given by g, can be sampled from a Maxwellian distribution. The particles are initialized sufficiently far away from each other such that they feel no forces due to the other body. Finally, shifting to this polar coordinate system in the center-of-mass frame is advantageous because above a certain impact parameter, denoted by $b_{\max}$, interactions are extremely unlikely to occur. The impact parameter is sampled using a stratified sampling method below the maximum impact parameter. The 12 coordinates that specify the internal positions of each molecule must be related to the initial rovibrational states. Therefore, the variables $(\eta_1, |\mathbf{J}_1|, r_1, \dot{r}_1)$ can be related to the vibrational and rotational quantum numbers, (v_1, J_1), and the vibrational phase, ξ_1, for

molecule 1, and likewise for molecule 2. All these parameter are sampled from the appropriate distribution (*e.g.*, the group distribution for the states within a group) using a random number generator. Further details on the stratified sampling approach can be found in many references such as Truhlar and Muckerman. [86] Further details on the sampling of all other parameters can be found in Refs. [87, 88, 126].

3.2.3 Calculation of final states

After the collision is completed, determined either by exceeding a time condition or distance between nuclei, the outcome of the collision is analyzed. This is first accomplished by sorting the bond lengths among the four nuclei. If two of the nuclei are within a certain threshold of bond length, the momenta and position of these nuclei are mapped back to quantum states. However, because the collision was calculated under the assumption of classical motion, the states are not quantized and the quantum numbers are real values. If the molecule after collision is found to have internal angular momentum $\tilde{\mathbf{J}}'_r$, we can calculate the rotational quantum number from this using the definition of angular momentum:

$$\tilde{J}' = -\frac{1}{2} + \left(\frac{\tilde{\mathbf{J}}'_r \cdot \tilde{\mathbf{J}}'_r}{\hbar^2} \right)^{1/2} \tag{3.15}$$

The final vibrational quantum number, $\tilde{v}$ is assigned from the action integral:

$$J_v = \left(\tilde{v}' + \frac{1}{2} \right) \mathrm{h_P} = 2 \int_{r-}^{r+} \left\{ 2\mu \left[E_{v,J} - V_{\mathrm{NN}} - \frac{\hbar^2 (\tilde{J}' + 1/2)^2}{2\mu r^2} \right] \right\}^{1/2} \mathrm{d}r \tag{3.16}$$

where μ is the reduced mass of the molecule being analyzed, J_v is the vibrational action, $E_{v,J}$ is the total energy of the molecule, V^{NN} is the diatomic potential energy for the molecule, and r is the internuclear distance, which is integrated for one period. With both a vibrational and rotational quantum number calculated, $(\tilde{v}', \tilde{J}')$, we now need to round these to the nearest integer value. At this point we also take the opportunity to ensure that quantum selection rules are obeyed. Therefore, if the final molecule is made up the same nuclei as before the collision (*i.e.*, it was an excitation reaction, not exchange), the rotational quantum number is rounded to the nearest integer of the same parity as the initial quantum number.

If the internuclear distance for one pair of atoms exceeds some threshold value, the molecule

is considered dissociated. If all the atoms exceed this distance among each other, both molecules have dissociated.

3.2.4 Calculation of cross-section

When considering the expression for the rate coefficient, Eq. (3.10), the QCT calculates the probability $P^{\mathrm{A}_k\mathrm{B}_l}_{\mathrm{A}_i\mathrm{B}_j}$. The outcome of a single collision is a Boolean function, as each trajectory has either resulted in this specific transition or has not. Therefore this probability is simply the number of times the desired outcome was achieved, $N^{\mathrm{A}_k\mathrm{B}_l}_{\mathrm{A}_i\mathrm{B}_j}$ divided by the total number of trajectories originating from the given initial state, $N_{\mathrm{A}_i\mathrm{B}_j}$. The final integral we are evaluating can then be written:

$$\begin{aligned}\kappa_{ij,kl} = \left(\frac{\mu_{\mathrm{AB}}}{2\pi \mathrm{k_B} T}\right)^{3/2} & \int_{b=0}^{\infty}\int_{g=0}^{\infty}\int_{\theta_1=0}^{\pi}\int_{\phi_1=0}^{2\pi}\int_{r_1=\rho_{1-}}^{\rho_{1+}}\int_{\eta_1=0}^{2\pi}\int_{\theta_2=0}^{\pi}\int_{\phi_2=0}^{2\pi}\int_{r_2=\rho_{2-}}^{\rho_{2+}}\int_{\eta_2=0}^{2\pi} \\ & \times \exp\left[-\frac{\mu_{\mathrm{AB}}}{2\mathrm{k_B}T} g^2\right] 2\pi b g^3 \tilde{P}^{\mathrm{A}_k\mathrm{B}_l}_{\mathrm{A}_i\mathrm{B}_j}(g, b, \theta_1, \theta_2, \phi_1, \phi_2, r_1, r_2, \eta_1, \eta_2) \\ & \times \mathrm{d}b\,\mathrm{d}g \left[\frac{1}{2}\sin\theta_1\right] \mathrm{d}\theta_1 \left[\frac{1}{2\pi}\right] \mathrm{d}\phi_1 \left[G_1(r_1; v_1, J_1)\right] \mathrm{d}r_1 \left[\frac{1}{2\pi}\right] \mathrm{d}\eta_1 \\ & \times \left[\frac{1}{2}\sin\theta_2\right] \mathrm{d}\theta_2 \left[\frac{1}{2\pi}\right] \mathrm{d}\phi_2 \left[G_2(r_2; v_2, J_2)\right] \mathrm{d}r_2 \left[\frac{1}{2\pi}\right] \mathrm{d}\eta_2 \end{aligned} \tag{3.17}$$

where the functions $G_1(r_1; v_1, J_1)$ and $G_2(r_2; v_2, J_2)$ depend on the diatomic potential. All the parameters in this integral are sampled from the appropriate distribution as described earlier.

The statistical error on the probability is easy to estimate because it is simply a function of the number of times our desired outcome was achieved and the number of samples. One standard deviation is therefore:

$$\Delta P^{\mathrm{A}_k\mathrm{B}_l}_{\mathrm{A}_i\mathrm{B}_j} = \left[\frac{N^{\mathrm{A}_k\mathrm{B}_l}_{\mathrm{A}_i\mathrm{B}_j} - \left(N^{\mathrm{A}_k\mathrm{B}_l}_{\mathrm{A}_i\mathrm{B}_j}\right)^2}{N_{\mathrm{A}_i\mathrm{B}_j}}\right]^{1/2} \tag{3.18}$$

We will use this quantity to calculate the statistical error in our calculated rates.

3.2.5 Connection between QCT and kinetic theory

Recall the definition of the mass source term for inelastic scattering collisions derived in Chapter 2 as a function of the differential cross-section:

$$\frac{1}{m_{\mathrm{A}}}\dot{\omega}_{\mathrm{A}_i} = \sum_{\substack{(\mathrm{B}_j,\mathrm{A}_k,\mathrm{B}_l)\\ \in \mathcal{C}_{\mathrm{A}_i}}} \iiint_{\mathscr{L}^2\times\mathbb{R}^3\times\mathbb{R}^3} \left(\frac{\beta_{\mathrm{A}_k}\beta_{\mathrm{B}_l}}{\beta_{\mathrm{A}_i}\beta_{\mathrm{B}_j}} f'_{\mathrm{A}_k} f'_{\mathrm{B}_l} - f_{\mathrm{A}_i} f_{\mathrm{B}_j}\right) g\sigma^{\mathrm{A}_k\mathrm{B}_l}_{\mathrm{A}_i\mathrm{B}_j}\, \mathrm{d}\boldsymbol{\omega'}\, \mathrm{d}\mathbf{c}_{\mathrm{B}}\, \mathrm{d}\mathbf{c}_{\mathrm{A}} \tag{3.19}$$

In this case we are assuming nothing about the internal state distribution of the states i and j, only considering the translational distribution function for the species. If we wish to re-write this expression in terms of elementary rate coefficients, $\kappa_{ij,kl}$ and $\kappa_{kl,ij}$ such that:

$$\frac{1}{m_{\mathrm{A}}}\dot{\omega}_{\mathrm{A}_i} = \sum_{\substack{(\mathrm{B}_j,\mathrm{A}_k,\mathrm{B}_l)\\ \in \mathcal{C}_{\mathrm{A}_i}}} \left(-\kappa_{ij,kl} n_{\mathrm{A}_i} n_{\mathrm{B}_j} + \kappa_{kl,ij} n_{\mathrm{A}_k} n_{\mathrm{B}_l}\right) \tag{3.20}$$

we can define this rate coefficient, $\kappa_{ij,kl}$ as the rate of removal of state i due to this specific chemical process. Later we will re-visit this integral to understand how to do this for our groups described earlier and how to obtain the reverse rate ($\kappa_{kl,ij}$) in a consistent manner. However, we can write this elementary rate coefficient in the integral form by plugging in the Maxwellian velocity distribution for f_{A_i} and f_{B_j}, transforming to center of mass coordinates, and integrating out the center of mass velocity contribution:

$$\kappa_{ij,kl} = \frac{1}{\chi}\left(\frac{\mu_{\mathrm{AB}}}{2\pi \mathrm{k_B} T}\right)^{3/2} \int_{\mathscr{L}^2}\int_{\mathscr{L}^2}\int_{g=0}^{\infty} \exp\left[-\frac{\mu_{\mathrm{AB}}}{2\mathrm{k_B}T} g^2\right] g^3 \sigma^{\mathrm{A}_k\mathrm{B}_l}_{\mathrm{A}_i\mathrm{B}_j}\, \mathrm{d}\boldsymbol{\omega'}\, \mathrm{d}\boldsymbol{\omega}\, \mathrm{d}g \tag{3.21}$$

We can relate this differential cross-section to the probability that a given reaction occurred, $P^{\mathrm{A}_k\mathrm{B}_l}_{\mathrm{A}_i\mathrm{B}_j}$, (not probability density, $W^{\mathrm{A}_k\mathrm{B}_l}_{\mathrm{A}_i\mathrm{B}_j}$ as used in the previous chapter) through the impact parameter, b. The relationship between the scattered solid angle and the impact parameter exists because for a given final solid angle, $\mathrm{d}\boldsymbol{\omega'}$, the trajectory must have originated in some impact parameter ring corresponding to $2\pi b \mathrm{d}b$. Therefore, we can relate the differential cross section to this probability:

$$\sigma^{\mathrm{A}_k\mathrm{B}_l}_{\mathrm{A}_i\mathrm{B}_j}\, \mathrm{d}\boldsymbol{\omega'} = 2\pi b P^{\mathrm{A}_k\mathrm{B}_l}_{\mathrm{A}_i\mathrm{B}_j}\, \mathrm{d}b \tag{3.22}$$

Finally, using this relationship in the definition of the microscopic rate coefficient, we arrive at the same integral the QCT method is used to solve:

$$\kappa_{ij,kl} = \frac{1}{\chi}\left(\frac{\mu_{\mathrm{AB}}}{2\pi \mathrm{k_B} T}\right)^{3/2} \int\limits_{\mathscr{L}^2} \int\limits_{b=0}^{\infty} \int\limits_{g=0}^{\infty} \exp\left[-\frac{\mu_{\mathrm{AB}}}{2\mathrm{k_B}T} g^2\right] 2\pi b g^3 P^{\mathrm{A}_k\mathrm{B}_l}_{\mathrm{A}_i\mathrm{B}_j} \,\mathrm{d}\boldsymbol{\omega}\,\mathrm{d}b\,\mathrm{d}g \tag{3.23}$$

In the next section we will demonstrate how to link the MGME model with the QCT method by sampling initial states from the appropriate group distribution.

3.3 Multi-group maximum entropy quasi-classical trajectory method

In this section, we present the link between the MGME and QCT methods by using the distribution function derived in Chapter 2. This comprises expressing the collision integrals (the right hand side) of the conservation of group mass and group energy equations in terms of the parameters sampled in QCT. First we analyze the mass source terms. The production terms in the conservation of mass equations can be split into an inelastic part and a reactive part. If we recall in the previous chapter, we split the mass source terms into a rate coefficient and the product of the reactants or products for the replenishing and depleting terms respectively. The rate coefficients for inelastic processes read:

$${}^0K_{pq,rs} = \frac{1}{n_{\mathrm{A}_p} n_{\mathrm{B}_q}} \sum_{i\in\mathcal{I}_p}\sum_{j\in\mathcal{I}_q}\sum_{k\in\mathcal{I}_r}\sum_{l\in\mathcal{I}_s} m_{\mathrm{A}} \iiint\limits_{\mathscr{L}^2\times\mathbb{R}^3\times\mathbb{R}^3} f_{\mathrm{A}_i} f_{\mathrm{B}_j} g \sigma^{\mathrm{A}_k\mathrm{B}_l}_{\mathrm{A}_i\mathrm{B}_j} \,\mathrm{d}\boldsymbol{\omega'}\,\mathrm{d}\mathbf{c}_{\mathrm{B}}\,\mathrm{d}\mathbf{c}_{\mathrm{A}} \tag{3.24}$$

$${}^0\bar{K}_{pq,rs} = \frac{1}{n_{\mathrm{A}_r} n_{\mathrm{B}_s}} \sum_{i\in\mathcal{I}_p}\sum_{j\in\mathcal{I}_q}\sum_{k\in\mathcal{I}_r}\sum_{l\in\mathcal{I}_s} m_{\mathrm{A}} \iiint\limits_{\mathscr{L}^2\times\mathbb{R}^3\times\mathbb{R}^3} \frac{\beta_{\mathrm{A}_k}\beta_{\mathrm{B}_l}}{\beta_{\mathrm{A}_i}\beta_{\mathrm{B}_j}} f'_{\mathrm{A}_k} f'_{\mathrm{B}_l} g \sigma^{\mathrm{A}_k\mathrm{B}_l}_{\mathrm{A}_i\mathrm{B}_j} \,\mathrm{d}\boldsymbol{\omega'}\,\mathrm{d}\mathbf{c}_{\mathrm{B}}\,\mathrm{d}\mathbf{c}_{\mathrm{A}} \tag{3.25}$$

Making use of the distribution function derived earlier, we can transform to center of mass coordinates, include the symmetry factor ($\chi = 1 + \delta_{\mathrm{A}_p\mathrm{B}_q}$, where $\delta_{\mathrm{A}_p\mathrm{B}_q}$ is the Kronecker-Delta function), and integrate out the center of mass velocity to yield the following expression for the forward rate

coefficient:

$$
\begin{aligned}
{}^{0}K_{pq,rs} =& \frac{1}{n_{\mathrm{A}_p} n_{\mathrm{B}_q}} \frac{1}{\chi} \sum_{i \in \mathcal{I}_p} \sum_{j \in \mathcal{I}_q} \sum_{k \in \mathcal{I}_r} \sum_{l \in \mathcal{I}_s} m_{\mathrm{A}} f_{\mathrm{A}_i}^{\mathrm{int}} f_{\mathrm{B}_j}^{\mathrm{int}} \left(\frac{\mu_{\mathrm{AB}}}{2\pi \mathrm{k_B} T} \right)^{3/2} \\
& \times \iiint\limits_{\mathscr{L}^2 \times \mathbb{R}^3 \times \mathbb{R}^3} \exp\left(-\frac{\mu_{\mathrm{AB}}}{2\mathrm{k_B} T} g^2 \right) g \sigma_{\mathrm{A}_i \mathrm{B}_j}^{\mathrm{A}_k \mathrm{B}_l} g^2 \, \mathrm{d}g \, \mathrm{d}\boldsymbol{\omega'} \, \mathrm{d}\boldsymbol{\omega}
\end{aligned} \tag{3.26}
$$

Making use of the relationship between the cross-section and the transition probability computed through QCT calculations, we arrive at an expression which resembles the integral which the QCT method calculates:

$$
\begin{aligned}
{}^{0}K_{pq,rs} =& \sum_{i \in \mathcal{I}_p} \sum_{j \in \mathcal{I}_q} \sum_{k \in \mathcal{I}_r} \sum_{l \in \mathcal{I}_s} \left[\frac{a_{\mathrm{A}_i} \exp\left(-\frac{E_{\mathrm{A}_i}}{\mathrm{k_B} T_{\mathrm{A}_p}^{\mathrm{int}}} \right)}{Q_{\mathrm{A}_p}^{(0)}(T_{\mathrm{A}_p}^{\mathrm{int}})} \right] \left[\frac{a_{\mathrm{B}_j} \exp\left(-\frac{E_{\mathrm{B}_j}}{\mathrm{k_B} T_{\mathrm{B}_q}^{\mathrm{int}}} \right)}{Q_{\mathrm{B}_q}^{(0)}(T_{\mathrm{B}_q}^{\mathrm{int}})} \right] \\
& \times m_{\mathrm{A}} \frac{1}{\chi} \left(\frac{\mu_{\mathrm{AB}}}{2\pi \mathrm{k_B} T} \right)^{3/2} \int_{g=0}^{\infty} \int_{b=0}^{\infty} \int_{\mathscr{L}^2} \exp\left(-\frac{\mu_{\mathrm{AB}}}{2\mathrm{k_B} T} g^2 \right) g^3 2\pi b P_{\mathrm{A}_i \mathrm{B}_j}^{\mathrm{A}_k \mathrm{B}_l} \, \mathrm{d}b \, \mathrm{d}g \, \mathrm{d}\boldsymbol{\omega}
\end{aligned} \tag{3.27}
$$

The advantage of expressing the rate coefficient like this is that the form is nearly identical to the quantity which the QCT method computes. The primary difference is now we are sampling initial rovibrational states from group distributions at independent temperatures. We can carry out the same procedure for the reverse rate. However, we would like to express the reverse rate coefficient in terms of a grouped forward rate to aid in constructing a self-consistent model as well as to help down the line when we want to write recombination rates without simulating recombination trajectories. To do this, we use the conservation of momentum and energy expressions for the collisions along with the principle of micro-reversibility. After some algebra, we can write the

reverse rate coefficient as:

$$
\begin{aligned}
{}^{0}\bar{K}_{pq,rs} =& Q^{(0)}_{\mathrm{A}_p}(T) Q^{(0)}_{\mathrm{B}_q}(T) \sum_{i\in\mathcal{I}_p}\sum_{j\in\mathcal{I}_q}\sum_{k\in\mathcal{I}_r}\sum_{l\in\mathcal{I}_s} m_{\mathrm{A}} \frac{1}{\chi}\left(\frac{\mu_{\mathrm{AB}}}{2\pi \mathrm{k_B} T}\right)^{3/2} \\
&\times \left[\frac{\exp\left(-\frac{E_{\mathrm{A}_k}}{\mathrm{k_B} T^{\mathrm{int}}_{\mathrm{A}_r}} + \frac{E_{\mathrm{A}_k}}{\mathrm{k_B} T}\right)}{Q^{(0)}_{\mathrm{A}_r}(T^{\mathrm{int}}_{\mathrm{A}_r})}\right]\left[\frac{\exp\left(-\frac{E_{\mathrm{B}_l}}{\mathrm{k_B} T^{\mathrm{int}}_{\mathrm{B}_s}} + \frac{E_{\mathrm{B}_l}}{\mathrm{k_B} T}\right)}{Q^{(0)}_{\mathrm{B}_s}(T^{\mathrm{int}}_{\mathrm{B}_s})}\right] \\
&\times \left[\frac{a_{\mathrm{A}_i}\exp\left(-\frac{E_{\mathrm{A}_i}}{\mathrm{k_B} T}\right)}{Q^{(0)}_{\mathrm{A}_p}(T)}\right]\left[\frac{a_{\mathrm{B}_j}\exp\left(-\frac{E_{\mathrm{B}_j}}{\mathrm{k_B} T}\right)}{Q^{(0)}_{\mathrm{B}_q}(T)}\right] \\
&\times \int_{g=0}^{\infty}\int_{b=0}^{\infty}\iint_{\mathscr{L}^2} \exp\left(-\frac{\mu_{\mathrm{AB}} g^2}{2\mathrm{k_B} T}\right) g^3 2\pi b P^{\mathrm{A}_k\mathrm{B}_l}_{\mathrm{A}_i\mathrm{B}_j}\,\mathrm{d}b\,\mathrm{d}g\,\mathrm{d}\boldsymbol{\omega'} \qquad (3.28)
\end{aligned}
$$

The advantage of writing the reverse rate coefficient this way is not immediately obvious until we realize that the initial states are now sampled from a thermal distribution at the translational temperature and from this we can obtain the reverse rate coefficient by weighting the contribution to the rate by a factor related to the final state and three temperatures, T, $T^{\mathrm{int}}_{\mathrm{A}_r}$, and $T^{\mathrm{int}}_{\mathrm{B}_s}$. Therefore, we can obtain both forward and reverse rate coefficients through trajectories in only one direction. The expressions for the exchange reactions are very similar and are included in Appendix C.

Taking the same approach for the combined excitation-dissociation and combined excitation-recombination reactions, we can re-cast them in a form which we will solve using the QCT method. The dissociation and recombination rate coefficients read:

$$
{}^{0}C_{\mathrm{A}_p\mathrm{B}_q,\mathrm{C}_r\mathrm{D}_s\mathrm{B}_t} = \frac{1}{n_{\mathrm{A}_p} n_{\mathrm{B}_q}} \sum_{i\in\mathcal{I}_p} \sum_{\substack{(\mathrm{B}_j,\mathrm{C}_k,\mathrm{D}_l,\mathrm{B}_m)\\ \in\mathcal{C}^{\mathrm{dis}}_{\mathrm{A}_i}}} m_{\mathrm{A}} \frac{1}{\chi} \iiint_{\mathscr{L}^2\times\mathbb{R}^3\times\mathbb{R}^3} f_{\mathrm{A}_i} f_{\mathrm{B}_j} g \sigma^{\mathrm{C}_k\mathrm{D}_l\mathrm{B}_m}_{\mathrm{A}_i\mathrm{B}_j}\,\mathrm{d}\boldsymbol{\omega'}\,\mathrm{d}\mathbf{c}_{\mathrm{B}}\,\mathrm{d}\mathbf{c}_{\mathrm{A}} \qquad (3.29)
$$

$$
\begin{aligned}
{}^{0}\bar{C}_{\mathrm{A}_p\mathrm{B}_q,\mathrm{C}_r\mathrm{D}_s\mathrm{B}_t} =& \frac{1}{n_{\mathrm{C}_r} n_{\mathrm{D}_s} n_{\mathrm{B}_t}} \sum_{i\in\mathcal{I}_p} \sum_{\substack{(\mathrm{B}_j,\mathrm{C}_k,\mathrm{D}_l,\mathrm{B}_m)\\ \in\mathcal{C}^{\mathrm{dis}}_{\mathrm{A}_i}}} m_{\mathrm{A}} \frac{1}{\chi} \\
&\times \iiint_{\mathscr{L}^2\times\mathbb{R}^3\times\mathbb{R}^3} \frac{\beta_{\mathrm{C}_k}\beta_{\mathrm{D}_l}\beta_{\mathrm{B}_m}}{\beta_{\mathrm{A}_i}\beta_{\mathrm{B}_j}} f'_{\mathrm{C}_k} f'_{\mathrm{D}_l} f'_{\mathrm{B}_m} g \sigma^{\mathrm{C}_k\mathrm{D}_l\mathrm{B}_m}_{\mathrm{A}_i\mathrm{B}_j}\,\mathrm{d}\boldsymbol{\omega'}\,\mathrm{d}\mathbf{c}_{\mathrm{B}}\,\mathrm{d}\mathbf{c}_{\mathrm{A}} \qquad (3.30)
\end{aligned}
$$

First, if we plug in the distribution for the groups derived in the previous chapter for the dissociation rate coefficient, complete the change of variables, and integrate out the center-of-mass velocity, we

arrive at the following expression for the dissociation rate coefficient:

$$
\begin{aligned}
{}^{0}C_{\mathrm{A}_p\mathrm{B}_q,\mathrm{C}_r\mathrm{D}_s\mathrm{B}_t} = & \sum_{i\in\mathcal{I}_p}\sum_{j\in\mathcal{I}_q}\sum_{k\in\mathcal{I}_r}\sum_{l\in\mathcal{I}_s}\sum_{m\in\mathcal{I}_t}\left[\frac{a_{\mathrm{A}_i}\exp\left(-\frac{E_{\mathrm{A}_i}}{\mathrm{k_B}T^{\mathrm{int}}_{\mathrm{A}_p}}\right)}{Q^{(0)}_{\mathrm{A}_p}(T^{\mathrm{int}}_{\mathrm{A}_p})}\right]\left[\frac{a_{\mathrm{B}_j}\exp\left(-\frac{E_{\mathrm{B}_j}}{\mathrm{k_B}T^{\mathrm{int}}_{\mathrm{B}_q}}\right)}{Q^{(0)}_{\mathrm{B}_q}(T^{\mathrm{int}}_{\mathrm{B}_q})}\right] \\
& \times m_{\mathrm{A}}\frac{1}{\chi}\left(\frac{\mu_{\mathrm{AB}}}{2\pi\mathrm{k_B}T}\right)^{3/2}\int\limits_{\mathscr{L}^2}\int\limits_{b=0}^{\infty}\int\limits_{g=0}^{\infty}\exp\left(-\frac{\mu_{\mathrm{AB}}}{2\mathrm{k_B}T}g^2\right)g^3 2\pi P^{\mathrm{C}_k\mathrm{D}_l\mathrm{B}_m}_{\mathrm{A}_i\mathrm{B}_j}\,\mathrm{d}b\,\mathrm{d}g\,\mathrm{d}\boldsymbol{\omega} \quad (3.31)
\end{aligned}
$$

Using the same procedure as for the excitation reaction, we can write the recombination rate coefficient in terms of the probability of dissociation:

$$
\begin{aligned}
{}^{0}\bar{C}_{\mathrm{A}_p\mathrm{B}_q,\mathrm{C}_r\mathrm{D}_s\mathrm{B}_t} = & \frac{Q^{(0)}_{\mathrm{A}_p}(T)Q^{(0)}_{\mathrm{B}_q}(T)}{Q^{(0)}_{\mathrm{C}_r}(T^{\mathrm{int}}_{\mathrm{C}_r})Q^{(0)}_{\mathrm{D}_s}(T^{\mathrm{int}}_{\mathrm{D}_s})Q^{(0)}_{\mathrm{B}_l}(T^{\mathrm{int}}_{\mathrm{B}_l})}\left(\frac{\mu_{\mathrm{AB}}}{2\pi\mathrm{k_B}T}\right)^{3/2}\left(\frac{\mathrm{h_P}^2}{2\pi\mu_{\mathrm{CD}}\mathrm{k_B}T}\right)^{3/2} \\
& \times\sum_{i\in\mathcal{I}_p}\sum_{j\in\mathcal{I}_q}\sum_{k\in\mathcal{I}_r}\sum_{l\in\mathcal{I}_s}\sum_{m\in\mathcal{I}_t}\exp\left(-\frac{E_{\mathrm{C}_k}}{\mathrm{k_B}T^{\mathrm{int}}_{\mathrm{C}_r}}+\frac{E_{\mathrm{C}_k}}{\mathrm{k_B}T}\right)\exp\left(-\frac{E_{\mathrm{D}_l}}{\mathrm{k_B}T^{\mathrm{int}}_{\mathrm{D}_s}}+\frac{E_{\mathrm{D}_l}}{\mathrm{k_B}T}\right) \\
& \times\exp\left(-\frac{E_{\mathrm{B}_m}}{\mathrm{k_B}T^{\mathrm{int}}_{\mathrm{B}_t}}+\frac{E_{\mathrm{B}_m}}{\mathrm{k_B}T}\right)\left[\frac{a_{\mathrm{A}_i}\exp\left(-\frac{E_{\mathrm{A}_i}}{\mathrm{k_B}T}\right)}{Q^{(0)}_{\mathrm{A}_p}(T)}\right]\left[\frac{a_{\mathrm{B}_j}\exp\left(-\frac{E_{\mathrm{B}_j}}{\mathrm{k_B}T}\right)}{Q^{(0)}_{\mathrm{B}_q}(T)}\right] \\
& \times\frac{1}{\chi}\int\limits_{g=0}^{\infty}\int\limits_{b=0}^{\infty}\int\limits_{\mathscr{L}^2}\exp\left(-\frac{\mu_{\mathrm{AB}}}{2\mathrm{k_B}T}g^2\right)g^3 2\pi b P^{\mathrm{C}_k\mathrm{D}_l\mathrm{B}_m}_{\mathrm{A}_i\mathrm{B}_j}\,\mathrm{d}b\,\mathrm{d}g\,\mathrm{d}\boldsymbol{\omega} \quad (3.32)
\end{aligned}
$$

Moreover, if we assume that we are not interested in the internal structure of the constituent particles C and D (as would be the case if they are both atoms and we do not consider electronic excitation), and consider them to be in thermal equilibrium with the translational mode, this

expression simplifies to:

$$
\begin{aligned}
{}^{0}\bar{C}_{\mathrm{A}_p\mathrm{B}_q,\mathrm{C}_r\mathrm{D}_s\mathrm{B}_t} =& \frac{Q^{(0)}_{\mathrm{A}_p}(T)Q^{(0)}_{\mathrm{B}_q}(T)}{Q^{(0)}_{\mathrm{B}_l}(T^{\mathrm{int}}_{\mathrm{B}_l})}\left(\frac{\mu_{\mathrm{AB}}}{2\pi \mathrm{k_B}T}\right)^{3/2}\left(\frac{\mathrm{h_P}^2}{2\pi\mu_{\mathrm{CD}}\mathrm{k_B}T}\right)^{3/2} \\
&\times \sum_{i\in\mathcal{I}_p}\sum_{j\in\mathcal{I}_q}\sum_{k\in\mathcal{I}_r}\sum_{l\in\mathcal{I}_s}\sum_{m\in\mathcal{I}_t}\left[\frac{a_{\mathrm{A}_i}\exp\left(-\frac{E_{\mathrm{A}_i}}{\mathrm{k_B}T}\right)}{Q^{(0)}_{\mathrm{A}_p}(T)}\right]\left[\frac{a_{\mathrm{B}_j}\exp\left(-\frac{E_{\mathrm{B}_j}}{\mathrm{k_B}T}\right)}{Q^{(0)}_{\mathrm{B}_q}(T)}\right] \\
&\times \exp\left(-\frac{E_{\mathrm{B}_m}}{\mathrm{k_B}T^{\mathrm{int}}_{\mathrm{B}_t}}+\frac{E_{\mathrm{B}_m}}{\mathrm{k_B}T}\right) \\
&\times \frac{1}{\chi}\int_{g=0}^{\infty}\int_{b=0}^{\infty}\int_{\mathscr{L}^2}\exp\left(-\frac{\mu_{\mathrm{AB}}}{2\mathrm{k_B}T}g^2\right)g^3 2\pi b P^{\mathrm{C}_k\mathrm{D}_l\mathrm{B}_m}_{\mathrm{A}_i\mathrm{B}_j}\,\mathrm{d}b\,\mathrm{d}g\,\mathrm{d}\boldsymbol{\omega}
\end{aligned}
\tag{3.33}
$$

The advantage to this form of the rate coefficient is that the initial states for QCT calculations can be sampled from a thermal distribution where the group internal temperatures are identically the translational temperature. The exponential factors for the final states can be applied in the post-processing of the trajectories by tracking these factors. This framework can be used for the energy transfer coefficients as well. Further details on the expressions for all these processes can be found in Appendix C. In addition, Appendix D includes the expressions used to calculate the statistical error on the rate coefficients and energy transfer coefficients.

Finally, if the group internal temperatures are taken to be equal to the translational temperature, the detailed balance relationships for the MGMET model can be derived:

$$
\begin{aligned}
{}^{0}\bar{K}_{pq,rs} =& \frac{Q^{(0)}_{\mathrm{A}_p}(T)Q^{(0)}_{\mathrm{B}_q}(T)}{Q^{(0)}_{\mathrm{B}_s}(T)Q^{(0)}_{\mathrm{A}_r}(T)}\sum_{i\in\mathcal{I}_p}\sum_{j\in\mathcal{I}_q}\sum_{k\in\mathcal{I}_r}\sum_{l\in\mathcal{I}_s} m_{\mathrm{A}}\frac{1}{\chi}\left(\frac{\mu_{\mathrm{AB}}}{2\pi\mathrm{k_B}T}\right)^{3/2} \\
&\times \left[\frac{a_{\mathrm{A}_i}\exp\left(-\frac{E_{\mathrm{A}_i}}{\mathrm{k_B}T}\right)}{Q^{(0)}_{\mathrm{A}_p}(T)}\right]\left[\frac{a_{\mathrm{B}_j}\exp\left(-\frac{E_{\mathrm{B}_j}}{\mathrm{k_B}T}\right)}{Q^{(0)}_{\mathrm{B}_q}(T)}\right] \\
&\times \int_{g=0}^{\infty}\int_{b=0}^{\infty}\int_{\mathscr{L}^2}\exp\left(-\frac{\mu_{\mathrm{AB}}g^2}{2\mathrm{k_B}T}\right)g^3 2\pi b P^{\mathrm{A}_k\mathrm{B}_l}_{\mathrm{A}_i\mathrm{B}_j}\,\mathrm{d}b\,\mathrm{d}g\,\mathrm{d}\boldsymbol{\omega'}
\end{aligned}
\tag{3.34}
$$

$$
\begin{aligned}
{}^{0}\bar{C}_{\mathrm{A}_p\mathrm{B}_q,\mathrm{C}_r\mathrm{D}_s\mathrm{B}_t} =& \frac{Q^{(0)}_{\mathrm{A}_p}(T)Q^{(0)}_{\mathrm{B}_q}(T)}{Q^{(0)}_{\mathrm{B}_l}(T)} \left(\frac{\mu_{\mathrm{AB}}}{2\pi \mathrm{k_B} T}\right)^{3/2} \left(\frac{\mathrm{h_P}^2}{2\pi\mu_{\mathrm{CD}}\mathrm{k_B}T}\right)^{3/2} \\
&\times \sum_{i\in\mathcal{I}_p}\sum_{j\in\mathcal{I}_q}\sum_{k\in\mathcal{I}_r}\sum_{l\in\mathcal{I}_s}\sum_{m\in\mathcal{I}_t} \left[\frac{a_{\mathrm{A}_i}\exp\left(-\frac{E_{\mathrm{A}_i}}{\mathrm{k_B}T}\right)}{Q^{(0)}_{\mathrm{A}_p}(T)}\right]\left[\frac{a_{\mathrm{B}_j}\exp\left(-\frac{E_{\mathrm{B}_j}}{\mathrm{k_B}T}\right)}{Q^{(0)}_{\mathrm{B}_q}(T)}\right] \\
&\times \frac{1}{\chi}\int_{g=0}^{\infty}\int_{b=0}^{\infty}\int_{\mathscr{L}^2} \exp\left(-\frac{\mu_{\mathrm{AB}}}{2\mathrm{k_B}T}g^2\right) g^3 2\pi b P^{\mathrm{C}_k\mathrm{D}_l\mathrm{B}_m}_{\mathrm{A}_i\mathrm{B}_j}\,\mathrm{d}b\,\mathrm{d}g\,\mathrm{d}\boldsymbol{\omega}
\end{aligned} \tag{3.35}
$$

These expressions demonstrate that when the translational and group temperatures are the same, the detailed balance condition holds at a group level, and reverse rate coefficients can easily be obtained from forward rate coefficients. This can be used in the MGMET model, bypassing the need to compute the reverse rate coefficients through sampling. However, this procedure is essential to close the MGMEL model.

3.4 Summary

In this chapter we present the general procedure for computing kinetic data for the MGME model described in Chapter 2. First, the quantum description of the dynamics of a collision is shown, and the definition of the PES is presented. The PES used in this work for both the $\mathrm{N_2}(\mathrm{X}^1\Sigma^+_\mathrm{g}) - \mathrm{N}(^4\mathrm{S_u})$ and $\mathrm{N_2}(\mathrm{X}^1\Sigma^+_\mathrm{g}) - \mathrm{N_2}(\mathrm{X}^1\Sigma^+_\mathrm{g})$ systems are those of Jaffe *et al.* [75, 76]. Next, the QCT procedure is presented, which is used to compute rate coefficients or cross-sections by computing transition probabilities through sampling. Finally, this procedure is coupled with the MGME model by first linking the calculation of forward rate coefficients with the QCT method. Finally, by invoking the principle of micro-reversibility, we can derive expressions for reverse rate coefficients in terms of forward rate coefficients along with weighting terms. This allows for the construction of the full MGMEL model without the need to compute recombination trajectories.

Chapter 4

Heat Bath Study of Energy Transfer and Dissociation in Nitrogen (MGMET-QCT)

In this chapter, the results of the MGMET model will be presented. This corresponds to a model which assumes that each group is in thermal equilibrium with the translational mode. Using this approach, we compare two grouping schemes for nitrogen molecules for studying the physics of excitation and dissociation in a zero-dimensional heat bath. The heat bath simulation is a simplification of the full set of conservation equation described in Chapter 2 in which we shift to the Lagrangian frame, assuming that there is no bulk velocity, and that the temperature and density of the box remain constant. Therefore, the necessary conservation equations comprise only the conservation of group mass equations, and we only consider the temporal variation in composition due to chemical reactions. The first grouping scheme is a conventional approach in which groups contain all rotational states of a given vibrational state. This is identical to a vibrational StS approach in which the rotational mode is assumed to instantly thermalize with the translational mode. This yields 61 groups, corresponding to the 61 vibrational levels of the N_2 molecule. The second approach is a simple energy based binning approach in which energy states near in energy are lumped together. We use 60 bins for this approach, to yield a similar computational cost to the vibrational binning model. Comparing these two grouping strategies, it will be shown that the grouping scheme has a large impact on the results, and an adequate grouping strategy requires a fundamental understanding of the underlying physics. In this chapter, we compare the energy transfer and dissociation behavior of an isothermal and isochoric reactor. The molecules are initially cold, and the temperature of the box is instantaneously raised to force the system into strong non-equilibrium. In Section 4.1 the simulation set up is presented, including the simplified governing equations. Section 4.2 presents an analysis of the non-equilibrium distributions during the energy transfer and dissociation processes. Section 4.3 presents an analysis of the dissociation process. Section 4.4 presents an analysis of the energy transfer process. Section 4.5 presents a

comparison of macroscopic observables (*e.g.*, global dissociation rate, vibrational relaxation time) with existing experimental and computational data. Section 4.6 presents a discussion of the results, and Section 4.7 presents a summary. This chapter is reproduced from Ref. [116], with the permission of AIP Publishing.

4.1 Simulation set-up

In this section, we present the details of the zero-dimensional study. This includes the methods for energy level grouping, the simplified governing equations, and the initial conditions for the study.

4.1.1 Energy level grouping

Uniform width energy based grouping

In the uniform width energy based grouping strategy, the energy levels of the N_2 molecule are first split into bound and quasi-bound (or pre-dissociated) states. Then, given a number of bound and quasi-bound groups, denoted by N_B and N_{QB} respectively, the energy width of the bins can be determined by:

$$\Delta E_B = \frac{2E_{\mathrm{N}}}{N_B}, \quad \Delta E_{QB} = \frac{E^{\star}_{\mathrm{N}_2} - 2E_{\mathrm{N}}}{N_{QB}} \tag{4.1}$$

Where ΔE_B and ΔE_{QB} denote the energy width of the bound and quasi-bound bins respectively, E_{N} represents the formation energy of atomic nitrogen, and $E^{\star}_{\mathrm{N}_2}$ represents the energy of the rovibrational state of N_2 with the largest energy. A schematic of the energy based grouping strategy is shown in Fig. 4.1a, considering only three energy bins. In this schematic, the different colors denote different vibrational states, which in the energy based grouping strategy are lumped together. In this chapter, the energy based grouping method will be applied to the $\mathrm{N}_2(\mathrm{X}^1\Sigma_{\mathrm{g}}^+) - \mathrm{N}_2(\mathrm{X}^1\Sigma_{\mathrm{g}}^+)$ system using 60 bins (40 of bound states, and 20 of quasi-bound or pre-dissociated states). The resulting bin widths are $\Delta E_B = 0.24\,\mathrm{eV}$ and $\Delta E_{QB} = 0.26\,\mathrm{eV}$.

Vibrational based grouping

Vibrational based grouping instead considers the vibrational quantum numbers when constructing the groups. In this approach, all the rotational states which share a vibrational quantum number

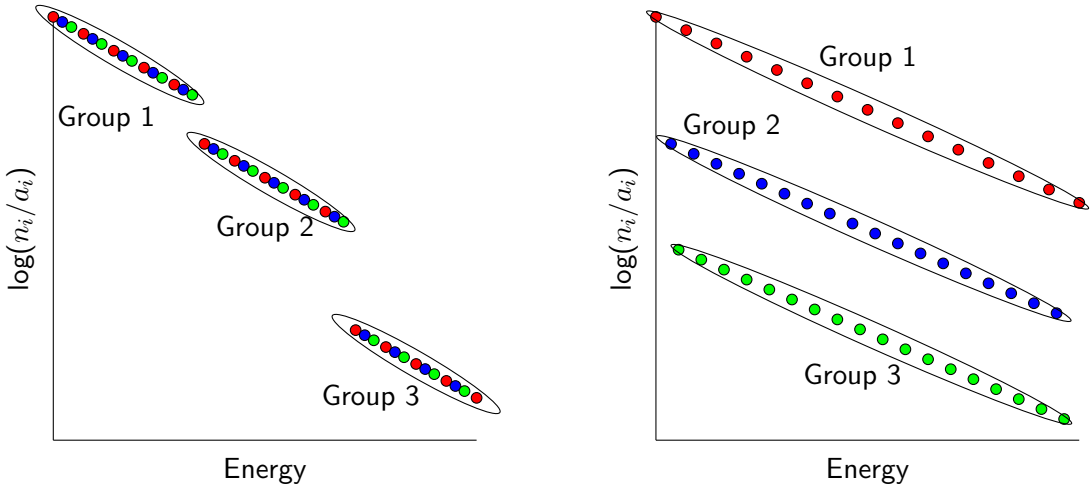

(a) Microscopic distribution of states and corresponding bins for energy based binning.

(b) Microscopic distribution of states and corresponding bins for vibrational based binning.

Figure 4.1: Schematic of binning strategies.

are grouped together. A schematic of this grouping strategy is shown in Fig. 4.1b for three example vibrational states, where the red states belong to $v = 0$, the blue states belong to $v = 1$, and the green states belong to $v = 2$. The resulting bins contain states which span the entire energy spectrum (*e.g.*, the $v = 0$ bin will contain states with all possible rotational quantum numbers and thus a wide range of energies).

4.1.2 Governing equations

The governing equations for the zero-dimensional study comprise the conservation of mass equations for the groups, as well as a conservation of mass equation for the atoms. In this chapter, only $N_2(X^1\Sigma_g^+) - N_2(X^1\Sigma_g^+)$ reactions are considered; these comprise excitation or de-excitation, combined excitation-dissociation or combined excitation-recombination, and double dissociation or four body recombination. In this chapter, we also include the four-body dissociation-recombination reactions and use the detailed balance relation at a group level. The reaction rate coefficients are only evaluated at thermal equilibrium with the translational mode. From here on, we will denote the number density of the group p of N_2 as n_p because it is the only species we consider groups for. Likewise, the formation energy of group p and state i and the degeneracy of state i for $N_2(X^1\Sigma_g^+)$ will be written as E_p, E_i, and a_i respectively. The internal partition functions will be written

as $Q_p^{(0)}(T)$ for group p. Furthermore, in the reaction rate coefficients we will drop the species identifiers, writing only indices for the groups. Moreover, because exchange type reactions and excitation reactions for the $N_2(X^1\Sigma_g^+) - N_2(X^1\Sigma_g^+)$ system are indistinguishable, we will sum these two processes and write a single excitation reaction rate coefficient for these two. That is to say that the following expressions will be used for the rates:

$$ {}^0C_{\mathrm{A}_p\mathrm{B}_q,\mathrm{C}_r\mathrm{D}_s\mathrm{B}_t} = {}^0C_{pq,r}, \qquad\qquad {}^0\bar{C}_{\mathrm{A}_p\mathrm{B}_q,\mathrm{C}_r\mathrm{D}_s\mathrm{B}_t} = {}^0\bar{C}_{pq,r} $$

Finally, we denote the set of groups for the N_2 molecule as $\mathcal{I}$. Therefore, the conservation equations for this system read:

$$\begin{aligned}
\frac{\mathrm{d}n_p}{\mathrm{d}t} =& \sum_{q\in\mathcal{I}}\sum_{r\in\mathcal{I}}\sum_{s\in\mathcal{I}}\left(-{}^0K_{pq,rs}n_pn_q + {}^0\bar{K}_{pq,rs}n_rn_s\right) \\
&+ \sum_{q\in\mathcal{I}}\sum_{r\in\mathcal{I}}\left(-{}^0C_{pq,r}n_pn_q + {}^0\bar{C}_{pq,r}n_rn_N^2\right) \\
&+ \sum_{q\in\mathcal{I}}\left(-{}^0C_{pq}n_pn_q + {}^0\bar{C}_{pq}n_N^4\right), \quad p\in\mathcal{I}, \qquad (4.2)\\
\frac{\mathrm{d}n_N}{\mathrm{d}t} =& 2\sum_{q\in\mathcal{I}}\sum_{r\in\mathcal{I}}\left({}^0C_{pq,r}n_pn_q - {}^0\bar{C}_{pq,r}n_rn_N^2\right) + 4\sum_{q\in\mathcal{I}}\left({}^0C_{pq}n_pn_q - {}^0\bar{C}_{pq}n_N^4\right) \qquad (4.3)
\end{aligned}$$

We make use of the Konig solver along with the Max-Entropy library for thermodynamics written by Alessandro Munafò to solve the conservation equations for this system.

For the MGMET-QCT model, trajectory calculations were carried out by starting in every possible pair of groups, and sampling the translational energy at four temperatures: 10 000 K, 13 000 K, 20 000 K, and 25 000 K. The maximum impact parameter was taken to be 7.41 Å based on previous work by Valentini *et al* [100], and 160 000 trajectories were simulated per pair of initial groups. Details on the convergence of the rates can be found in Appendix E. The reaction rate coefficients for the excitation processes are taken from exothermic trajectories which were found to have significantly smaller statistical error.

4.1.3 Reactor conditions

An isochoric reactor model is used to study the non-equilibrium dissociation process of nitrogen modeled using the MGMET-QCT method. In all the simulations the gas is initially composed of cold nitrogen molecules, populated according to a Boltzmann distribution at $T_I = 300\,\mathrm{K}$ with a density of 1.2 $\mathrm{kg/m^3}$ corresponding to a pressure of 1 atm. Under these assumptions, the initial population of the groups is given by:

$$\frac{n_p}{n_{\mathrm{N_2}}} = \frac{\tilde{Q}_p^{(0)}(T)\exp\left(-\frac{E_p}{\mathrm{k_B}T_I}\right)}{\sum\limits_{p\in\mathcal{I}}\tilde{Q}_p^{(0)}(T)\exp\left(-\frac{E_p}{\mathrm{k_B}T_I}\right)} \tag{4.4}$$

where $n_{\mathrm{N_2}}$ denotes the total number density of nitrogen molecules given by $n_{N_2} = \sum_{p\in\mathcal{I}} n_p$, ΔE_i^p is the energy of state i relative to the formation energy of group p such that $E_i = E_p + \Delta E_i^p$, T_I is the initial internal temperature, and $\tilde{Q}_p(T)$ is the partition function of a group relative to the group formation energy: $\tilde{Q}_p^{(0)}(T) = \sum_{i\in\mathcal{I}_p} a_i \exp\left(-\Delta E_i^p/(\mathrm{k_B}T)\right)$. At the beginning of the simulation, the translational temperature of the reactor is instantaneously raised and held constant, driving the gas out of equilibrium. Four different translational temperatures are considered: 10 000 K, 13 000 K, 20 000 K, and 25 000 K.

4.2 Analysis of non-equilibrium population distribution

4.2.1 Uniform width energy based grouping

At the beginning of the simulation, only the low-lying energy groups are significantly populated, given the initial values of T_I. With time, the random motion of molecules brings about collisions, thus enabling the transfer of kinetic energy into internal energy. Figure 4.2a shows the distribution of energy groups at various times in the 10 000 K reactor simulation. Early in the relaxation process, $t = 10^{-10}$ s, the distribution is still significantly colder than the final equilibrium distribution, indicating that the gas is still in the midst of the relaxation process. This phase is completed at about $t = 10^{-9}$ s. Between $t = 10^{-8}$ s and $t = 10^{-7}$ s, the distribution is frozen, indicating that the gas has reached the quasi-steady-state (QSS) distribution, during which time the distribution of states is unchanged due to a balance between excitation and dissociation processes. After $t = 10^{-7}$

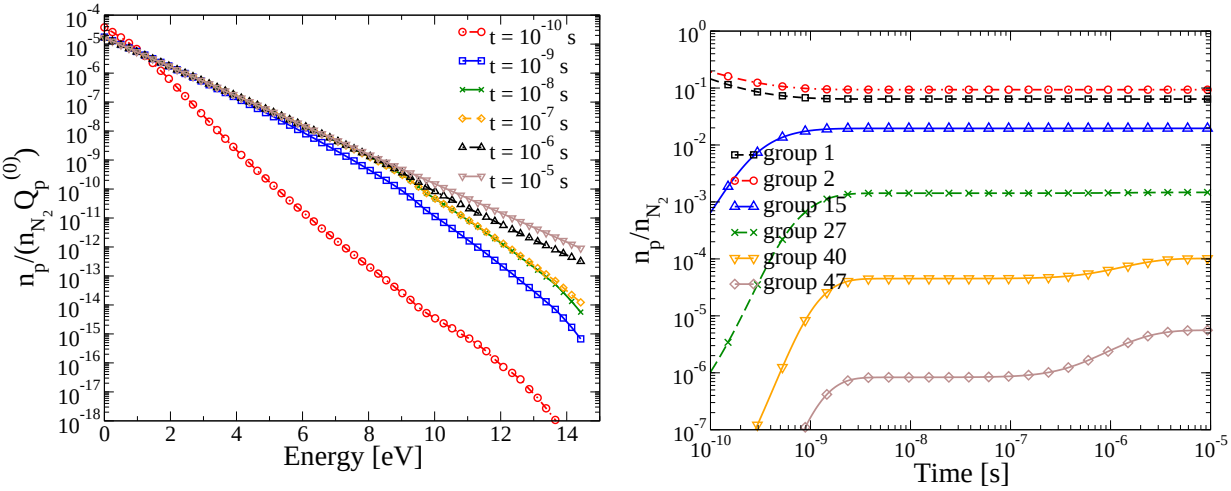

(a) Bin population from MGMET-QCT at various times.

(b) Time evolution of bin distributions

Figure 4.2: Bin distribution for isochoric reactor simulation at $T = 10\,000\,\mathrm{K}$ with 60 energy groups.

s, the high energy groups are replenished through recombination, and the gas approaches the final equilibrium distribution after $t \approx 10^{-5}$ s. Figure 4.2b shows the time evolution of the population for a subset of the groups. In this figure, the different phases of the thermochemical relaxation can be clearly observed along with the plateau in the population densities which represent the QSS state of the gas.

4.2.2 Vibrational based grouping

Figure 4.3a shows the distribution of vibrational groups at various times in the 10 000 K reactor simulation. Because of the difference in grouping strategies, the distribution looks very different from the energy binned results. Early in the relaxation process, $t < 10^{-9}$ s, the low energy vibrational states ($E_v < 1.5$ eV) appear nearly frozen at a colder temperature than the higher energy states. This bi-modal distribution persists until the QSS state is reached at $t = 10^{-7}$ s. The QSS state is clearly observable in Fig. 4.3b, which shows a narrow plateau in the population of the high vibrational energy level populations around this time. As observed for the other grouping strategy, the distribution shows significant deviation from equilibrium. It is important to note that the initial energy transfer process predicted by the vibrational based grouping model is significantly slower than the one predicted by the energy based grouping method.

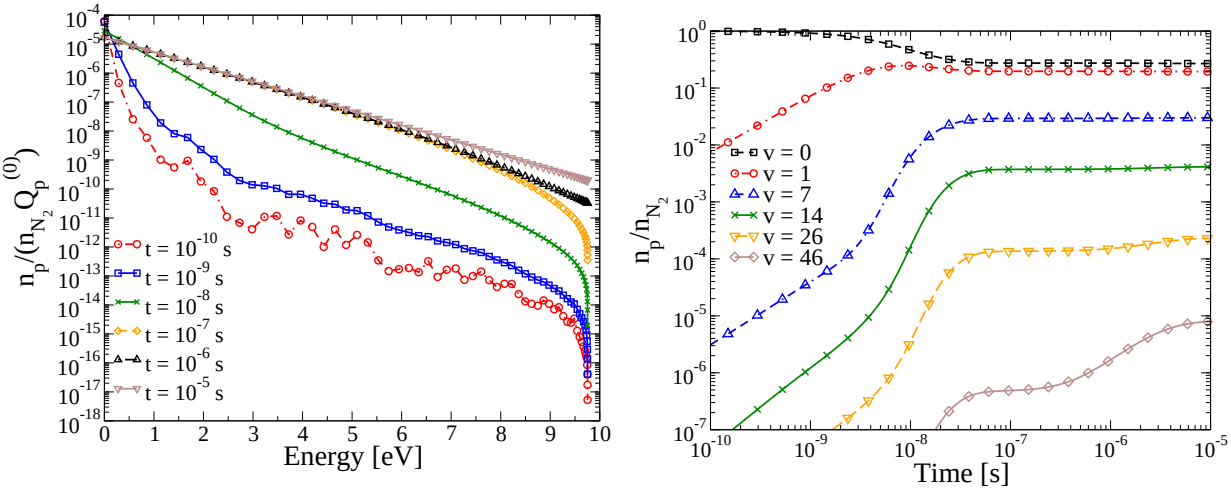

(a) Bin population from MGMET-QCT at various times.

(b) Time evolution of bin distributions.

Figure 4.3: Bin distribution for isochoric reactor simulation at $T = 10\,000\,\mathrm{K}$ with 61 vibrational specific groups.

To better illustrate the differences between the two grouping strategies on the microscopic level, the reconstructed distributions are shown in Fig. 4.4 at two different times in the 10 000 K reactor. Figure 4.4a shows the distribution during the relaxation process, at $t = 1.173 \times 10^{-10}$ s. At this instant, the total internal energy contained in the molecules is the same; however, due to different assumptions in the grouping strategy, the rovibrational distributions are very different. Since the energy based grouping assumes equilibrium over a small range of energies (*i.e.*, each energy bin is only 0.25 eV in width), the distribution is mostly continuous across the energy spectrum, with each bin approximating only a reduced number of levels in a narrow energy range. In contrast, the vibrational binning strategy assumes equilibrium at 10 000 K among all rotational states within a given vibrational state. This results in the strand like structure observed in Fig. 4.4a.

Figure 4.4b shows the reconstructed distribution of states during the dissociation process for both grouping strategies. In both groupings, the distribution of low energy states is very similar, and approaches equilibrium. However, nearing the dissociation energy (9.75 eV), the distribution predicted by the energy binning strategy deviates from the Boltzmann distribution. The population predicted by the vibrational grouping model is more complicated. The high-lying vibrational levels contain a reduced number of rotational levels, and therefore will capture the depopulation of the high-lying rovibrational states. On the contrary the low-lying vibrational levels contain a large

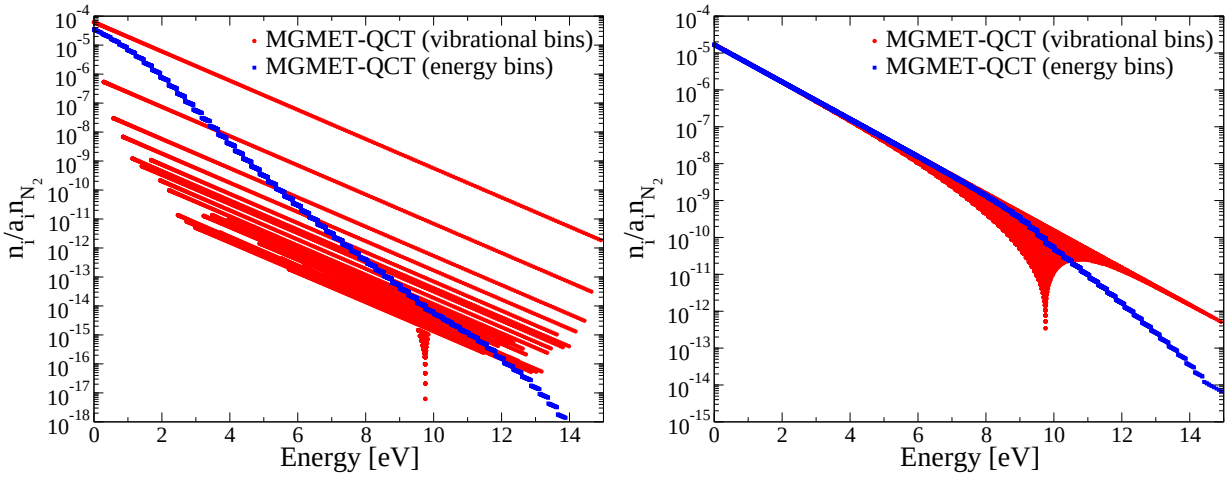

(a) Reconstructed distribution of states at $t = 1.173 \times 10^{-10}$ s.

(b) Reconstructed distribution of states at $t = 9.869 \times 10^{-8}$ s.

Figure 4.4: Reconstructed distribution of states from energy and vibrational binning models at 10 000 K.

number of rotational levels characterized by large rotational quantum number. These levels are forced to be in equilibrium with the low-lying rovibrational states by the averaging procedure, thus creating an artificial overpopulation in the tail of the distribution.

The two models provide a very different representation of rovibrational relaxation. The vibrational grouping appears adequate for the description of the low-lying vibrational level, characterized by a small rotational quantum number, where the mode separation is clearly significant. On the contrary, the energy binning strategy seems more adequate for the description of the relaxation of the high-lying states characterized by low vibrational quantum numbers and high rotational energy content.

4.3 Dissociation

The mole fraction of atomic nitrogen predicted by both grouping strategies at various temperatures is shown in Fig. 4.5. At 25 000 K, the two grouping strategies predict similar dissociation rates, even if the onset of dissociation occurs significantly earlier with the vibrational specific model. As the temperature decreases, the two grouping strategies diverge. At 10 000 K, the energy based groups predict faster dissociation, with a shorter incubation period. The discrepancy between the two grouping models is due to the treatment of the rotational energy mode. In the vibrational grouping

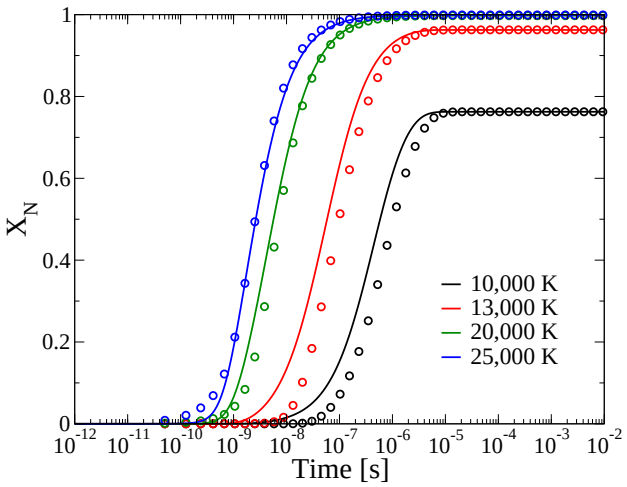

Figure 4.5: N mole fraction as a function of time using energy-based grouping (solid lines) and vibrational-based grouping (symbols) at various temperatures.

model, the rotational levels are assumed to be populated according to a Boltzmann distribution at the translational temperature. This assumption hinders dissociation at low temperature, because it artificially imposes equilibrium between low and high energy states (*e.g.*, $(v, J) = (0, 0)$ and $(v, J) = (0, 270)$), which is clearly incorrect. On the contrary, the energy based grouping is able to capture the non-equilibrium between high and low-lying rotational levels, since they belong to different groups.

The importance of the high energy states for predicting dissociation is highlighted in Fig. 4.6. This shows the fraction of molecules which dissociate from a given group when the molecules are in the QSS condition, given by:

$$P_{diss}(E_p) = \frac{\sum_{q\in\mathcal{I}}\sum_{r\in\mathcal{I}} {}^0K_{pq,r}n_p}{\sum_{p\in\mathcal{I}}\sum_{q\in\mathcal{I}}\sum_{r\in\mathcal{I}} {}^0K_{pq,r}n_p} \tag{4.5}$$

where p and q are the groups of the dissociating and exciting molecules respectively, and $P_{diss}(E_p)$ is the probability that a molecule in group p dissociates. Figure 4.6a presents the results obtained with the energy based grouping model. The distribution clearly shows that molecules climb nearly to the dissociation energy before dissociating. This effect is more pronounced at low temperatures, where there is less energy available in the translational mode to facilitate dissociation from the lower energy groups. Thus, the importance of the quasi-bound states increases with decreasing

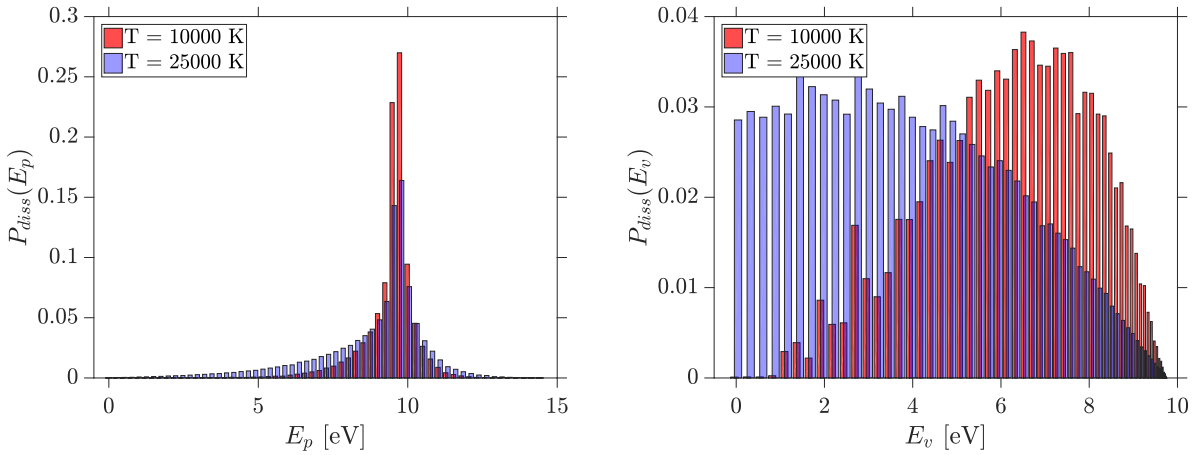

(a) 60 energy groups. **(b)** 61 vibrational groups.

Figure 4.6: Fraction of molecules dissociating during the QSS region from each group.

temperature. Table 4.1 gives the percent of dissociation occurring from quasi-bound states as predicted by the model. At low temperatures, nearly 50% of the dissociation occurs from quasi-bound states, highlighting their importance for the prediction of the dissociation process. This conclusion is similar to that reached by Bender *et al.* [79] for the $N_2(X^1\Sigma_g^+) - N_2(X^1\Sigma_g^+)$ system who observed up to 58% of dissociation events come from trajectories with at least one quasi-bound molecule, as well as Panesi *et al.* for the $N_2(X^1\Sigma_g^+) - N(^4S_u)$ system [38].

Table 4.1: Percent of dissociation from quasi-bound states in energy based grouping model.

Temperature	Dissociation from QB	$\Delta e_{vib}^{diss}/\Delta e_{tot}^{diss}$	$\Delta e_{rot}^{diss}/\Delta e_{tot}^{diss}$
10 000 K	46.9 %	60.1 %	39.9 %
13 000 K	45.0 %	59.0 %	41.0 %
20 000 K	40.8 %	57.2 %	42.8 %
25 000 K	38.6 %	56.4 %	43.6 %

The vibrational grouping method, shown in Fig. 4.6b, predicts very different behavior. At 10 000 K, the molecules generally climb to higher vibrational states (between $7 - 8$ eV) before dissociating, as predicted by the ladder climbing model. However, at 25 000 K, the molecules are much more likely to dissociate from low energy vibrational states (between $1 - 4$ eV). This behavior can be explained as follows: at high temperatures, the low vibrational states are rotationally excited (given the assumption of rotational equilibrium), and the high lying rotational states are

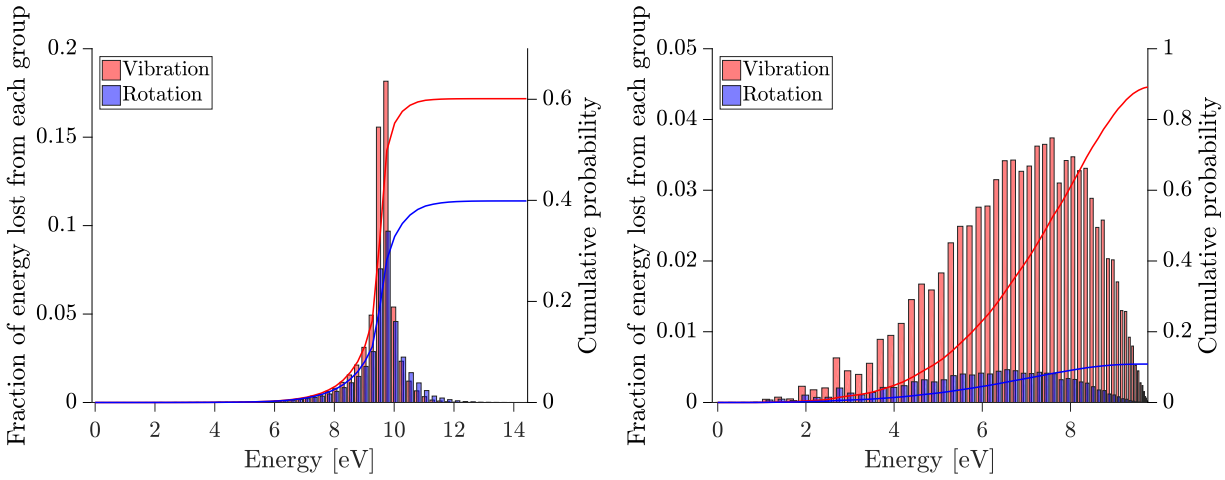

(a) 60 energy groups.

(b) 61 vibrational groups.

Figure 4.7: Fraction of rotational and vibrational energy lost in dissociation events by the molecules during QSS region from each group at 10 000 K.

therefore significantly populated, thus significantly contributing to dissociation. In other words, the dissociation energy of a molecule decreases as J increases. However at low temperatures, the Boltzmann weighting favors the lower lying rotational energy levels, characterized by significantly lower dissociation probability, thus hindering dissociation from the high-lying rotational states of a given group.

To gain more insight on the relative contribution of rotational and vibrational energy to dissociation, Fig. 4.7 shows the fraction of energy lost by the two modes during dissociation at 10 000 K, normalized by the total internal energy lost, given by:

$$\frac{\Delta e^{\text{diss}}_{rot,p}}{\Delta e^{\text{diss}}_{tot}} = \frac{\left[\sum_{i\in\mathcal{I}_p} n_i E^{rot}_i\right] P_{diss}(E_p)}{\sum_{p\in\mathcal{I}}\left[\sum_{i\in\mathcal{I}_p} n_i \left(E^{rot}_i + E^{vib}_i\right) P_{diss}(E_p)\right]}, \quad \frac{\Delta e^{\text{diss}}_{vib,p}}{\Delta e^{\text{diss}}_{tot}} = 1 - \frac{\Delta e^{\text{diss}}_{rot,p}}{\Delta e^{\text{diss}}_{tot}} \tag{4.6}$$

where $\Delta e^{\text{diss}}_{rot,p}$ and $\Delta e^{\text{diss}}_{vib,p}$ denote respectively the energy lost in dissociation from the rotational and vibrational modes of group p, $\Delta e^{\text{diss}}_{tot}$ denotes the total energy lost during dissociation, and E^{rot}_i and E^{vib}_i denote respectively the rotational and vibrational energy of state i. It is interesting to observe that the energy based bins predict a similar contribution between rotation and vibration, with the latter contributing slightly more. The percentage of energy lost from each mode in the energy

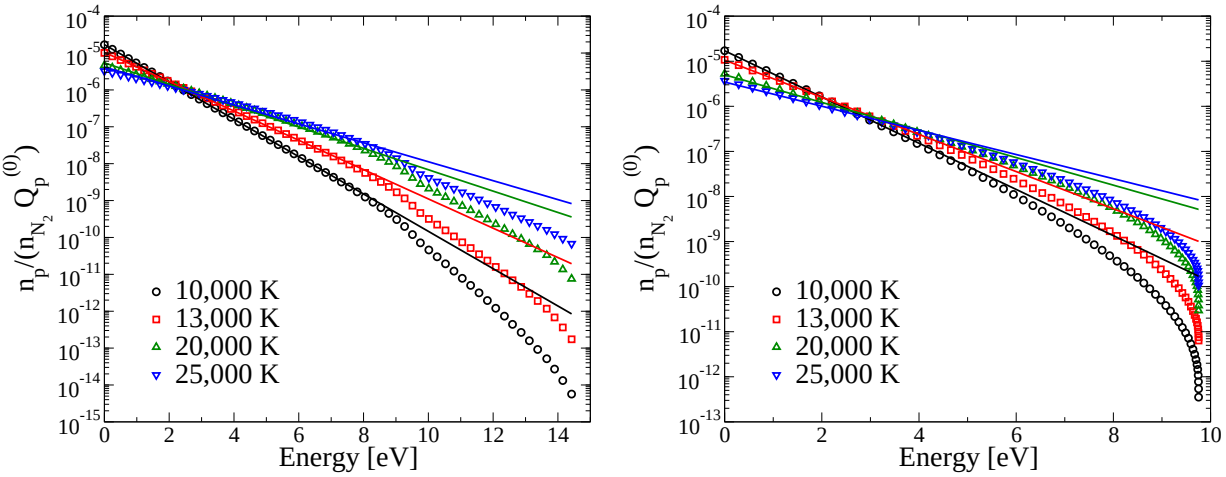

(a) 60 energy groups. **(b)** 61 vibrational groups.

Figure 4.8: Quasi-steady-state group distribution for various temperatures; symbols indicate the QSS distribution and lines indicate the equilibrium distribution at the QSS temperature.

based grouping model is also summarized in Table 4.1, highlighting that at high temperature the energy loss from each mode becomes comparable. In contrast, the vibrational grouping provides a completely different picture: the contribution of rotation does not exceed 10% of the total internal energy lost. In other words, as a result of the assumptions made, the importance of rotation on the kinetics is downplayed at low temperatures in the vibrational-based averaging. The work of Bender *et al.* [79] obtained similar results to what is observed in the vibrational grouping method, which finds that the rotational energy contribution to dissociation is significantly smaller than the vibrational contribution. However, this may be an artifact of the assumptions made in the model (*e.g.* rotation and vibrational modes are decoupled, thermal equilibrium of translational and rotational modes).

The group distribution during QSS for the energy and vibrational based bins is shown in Fig. 4.8 for various temperatures. In both cases, significant departures from the QSS temperature Boltzmann distributions are observed. The low energy groups appear to be close to equilibrium, whereas the distribution of the high energy tail appears significantly depopulated. The behavior of the distribution is consistent with the dissociation probability functions discussed above. The high energy molecules, more likely to dissociate, are responsible for the departures of the distribution from equilibrium.

Figure 4.9 shows the local dissociation rate profiles during the relaxation. These have been

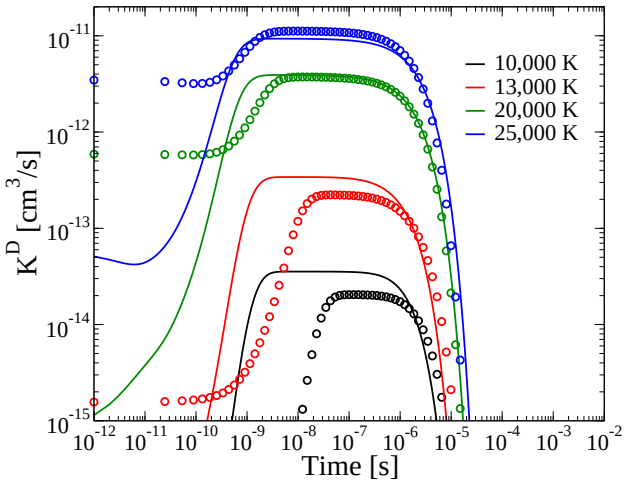

Figure 4.9: N_2-N_2 local dissociation rate computed from energy-based groups (solid lines) and vibrational-based groups (symbols).

calculated from the production rate of atomic nitrogen as follows:

$$K^{\mathrm{D}} = \left(\frac{1}{2}\right)\left(\frac{1}{n_{N_2} n_{N_2}}\right)\frac{\mathrm{d}n_N}{\mathrm{d}t} \tag{4.7}$$

The rate profiles are monotonically increasing in the early stage of the relaxation for both models, until the onset of the QSS distribution, responsible for the formation of a plateau in the profiles. A comparison of the nitrogen concentration profiles and the dissociation rates shows that, across a range of conditions analyzed, the entire dissociation process proceeds under QSS conditions for the N_2-N_2 processes. This was not the case for the N_2-N system, where a significant part of the dissociation occurred in non-QSS conditions [38]. The comparison of the rate profiles obtained with the two different grouping strategies shows that the QSS dissociation rate predicted at low temperatures by the vibrational grouping is approximately half that predicted by the energy based grouping. Moreover, the onset of the QSS region is significantly delayed for the vibrational grouping model. This indicates that not only is the dissociation process different between the two groupings, but also the energy transfer process has significant differences. As the temperature increases, the vibrational grouping QSS dissociation rate overshoots the rate predicted by the energy groups. This is due to the over-population of high energy rovibrational states in the vibrational grouping model discussed earlier.

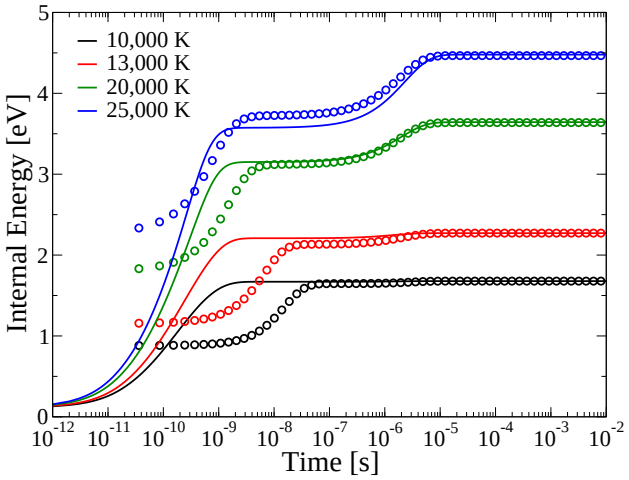

Figure 4.10: Internal energy of N_2 molecules as a function of time from energy (solid lines) and vibrational (symbols) grouping.

4.4 Energy transfer

The internal energy of the molecules, shown in Fig. 4.10, can be computed as:

$$E_{int} = \frac{\sum_{i \in \mathcal{I}} n_i E_i}{\sum_{i \in \mathcal{I}} n_i} \tag{4.8}$$

The energy based grouping starts with very low internal energy, and excites quickly to the QSS state, by 10^{-8} s at all temperatures. At the low temperatures, the total internal energy of the molecules is the same as the thermal internal energy, indicating that the QSS distribution is not much different from the thermal Boltzmann distribution. This is not surprising since most of the energy is contained in the low energy states, whose population is close to equilibrium at low temperatures, and the high energy states do not significantly contribute to the internal energy content. At higher temperatures, the QSS state has significantly lower internal energy from the final equilibrium value, indicating the presence of stronger non-equilibrium effects.

The vibrational specific bins exhibit very different behavior throughout the relaxation process. Despite the initial excess of internal energy, due to the assumption of equilibrium among rotation and translation, the vibrational grouping model predicts significantly slower relaxation across the range of temperatures, if compared with the energy based model.

Further insights on the energy transfer processes can be obtained by computing the second order

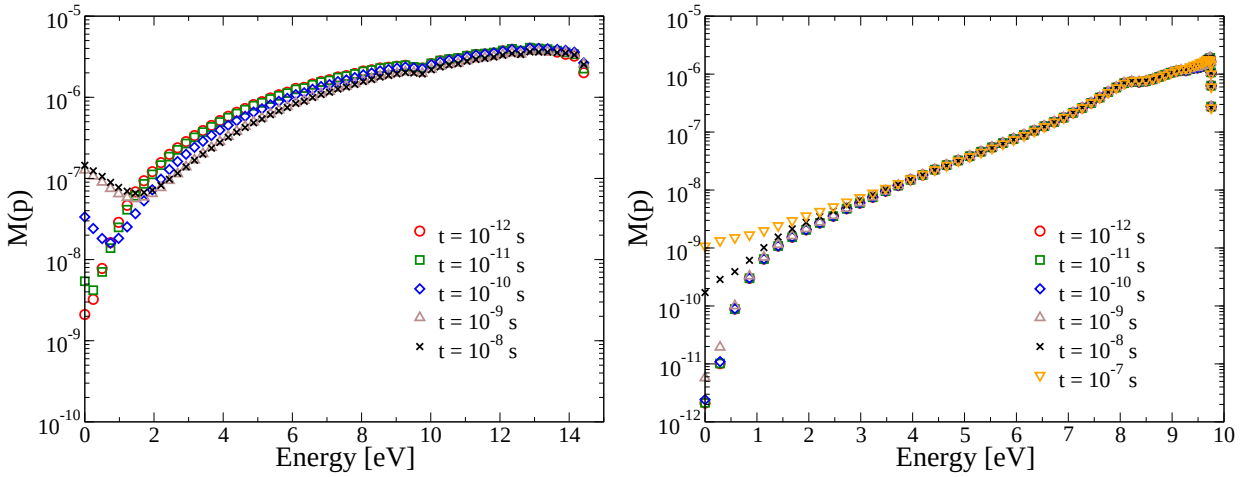

(a) 60 energy groups. **(b)** 61 vibrational groups.

Figure 4.11: Second order moment at various times at 10 000 K.

moment of the transition rates for both models. To this aim, the master equation is expressed as a diffusion or Fokker-Planck type equation [2, 11], for which the dynamics of relaxation is controlled by the diffusion coefficients, expressed as a function of the second order moment of the transition rates. The expression of the second order moment for the group p is:

$$M(p) = \frac{1}{2} \sum_{r \in \mathcal{I}} (p - r)^2 \cdot K(p, r) \tag{4.9}$$

where $K(p, r)$ is the effective rate of energy relaxation from group p to group r:

$$K(p, r) = \sum_{s \in \mathcal{I}} \sum_{q \in \mathcal{I}} \mathcal{F}_q{}^0 K_{pq,rs} \tag{4.10}$$

where $\mathcal{F}_q = \frac{n_q}{n_{N_2}}$ denotes the fraction of particles in group q.

Figure 4.11a shows the second order moment for the energy based bins formulation at 10 000 K. Initially, the moment exhibits a monotonically increasing behavior with the bin energy. At later times, however, the efficiency of the first few groups increases creating a shallow bottleneck between 1 and 2 eV. At high energies the dependence of the moment on the group energy is nearly exponential and appears to be unchanged during the relaxation.

Figure 4.11b shows the second order moment for the vibrational bins at 10 000 K. In general, the moments are several orders of magnitude smaller across the entire energy spectrum. In partic-

ular below 4 eV the coefficients are extremely small. This explains the formation of the bimodal distribution shown in Fig. 4.3a and in general the slow vibrational relaxation observed in Fig. 4.10. It is important to stress that, contrary to what is observed by other researchers, the vibrational relaxation does not exhibit a bottleneck [136]. This is due to the effect of rotation, that provides additional channels to vibrational processes, hence enhancing the relaxation.

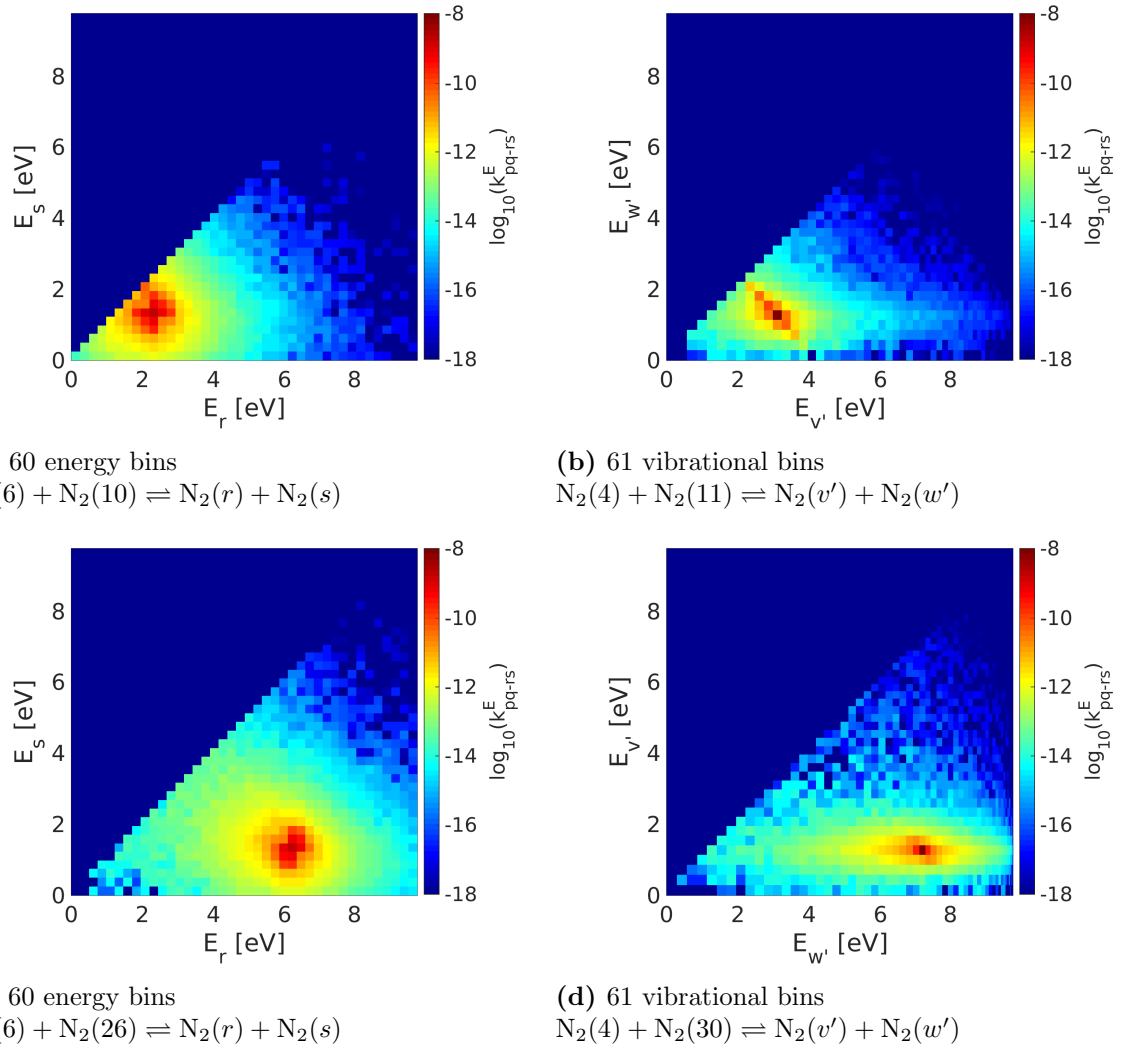

(a) 60 energy bins
$N_2(6) + N_2(10) \rightleftharpoons N_2(r) + N_2(s)$

(b) 61 vibrational bins
$N_2(4) + N_2(11) \rightleftharpoons N_2(v') + N_2(w')$

(c) 60 energy bins
$N_2(6) + N_2(26) \rightleftharpoons N_2(r) + N_2(s)$

(d) 61 vibrational bins
$N_2(4) + N_2(30) \rightleftharpoons N_2(v') + N_2(w')$

Figure 4.12: Excitation contours from a pair of fixed groups with energy and vibrational bins at 10 000 K.

Figure 4.12 shows the excitation rates contour plots, as a function of the energies of the products, for given pairs of initial groups. The analysis was repeated for the energy and vibrational grouping models. To facilitate the comparison between the models, we selected reactant groups with similar

energy. In both cases, the energy of the second reactant was increased to analyze the behavior of the rates for the lower and the upper part of the distribution.

The contours for the energy based grouping, shown in Figs. 4.12a and 4.12c, exhibit a maximum corresponding to the "elastic" processes in which neither of the groups change. The magnitude of the rates decays exponentially for increasing energies of the products. The behavior is nearly isotropic, indicating that both reactants have equal probability of being excited. It is interesting to note that all the possible energy transfer reactions follow this behavior, and it is possible to fit the rates with a unique exponential function with three parameters (A, σ, γ), based on the work of Barker *et al.* [137]:

$$ {}^{0}K_{pq,rs} = A \exp\left[- \left| \frac{\sqrt{(E_p - E_r)^2 + (E_q - E_s)^2}}{\sigma} \right|^{\gamma} \right] \tag{4.11} $$

In Figs. 4.12b and 4.12d, the reaction rate coefficients for the vibrational energy groups exhibit a different behavior. At low energies, the VT energy transfer processes are very inefficient compared with the high energy states. This is consistent with the results shown in Fig. 4.11b. In contrast, due to the anharmonicity of the vibrational states, multi-quantum jumps are very probable for the high lying vibrational energy levels (Fig. 4.12d). This justifies the establishment of a multimodal distribution in the early part of the relaxation. Moreover, at low energies, VV transfer appears very efficient, thus favoring the thermalization of the distribution.

4.5 Comparison against experimental data

Previous sections focused on the analysis of the dynamics of dissociation and energy transfer obtained with the two different grouping strategies. In order to assess the validity of each model, the results obtained are now compared against the available experimental data. Two different observables are used: phenomenological dissociation rate coefficient, and an energy transfer relaxation time.

The thermal and QSS dissociation rate coefficients predicted by both the grouping models are compared against experimental data in Fig. 4.13. The numerical values of the rate coefficients as a function of temperature can be found in Table 4.2. The thermal dissociation rate coefficient, shown

in Fig. 4.13a, is computed by assuming an equilibrium distribution between all the groups:

$$K^{\mathrm{D}} = \sum_{p\geq q}\sum_{q\in\mathcal{I}}\sum_{r\in\mathcal{I}} {}^{0}K_{pq,r}\left(\frac{Q_p^{(0)}(T)}{Q_{N_2}^{(0)}(T)}\right)\left(\frac{Q_q^{(0)}(T)}{Q_{N_2}^{(0)}(T)}\right) + 2\sum_{p\geq q}\sum_{q\in\mathcal{I}} {}^{0}K_{pq}\left(\frac{Q_p^{(0)}(T)}{Q_{N_2}^{(0)}(T)}\right)\left(\frac{Q_q^{(0)}(T)}{Q_{N_2}^{(0)}(T)}\right) \quad (4.12)$$

Although in excellent agreement with the work of Jaffe *et al.* [138], and Bender *et al.* [79], both predictions grossly overestimate the experimental rates from Appleton *et al.* [139] and Kewley and Hornung [140]. This is not surprising, since the population of the high-lying energy levels for both models was found to strongly deviate from equilibrium.

The QSS dissociation rates obtained from the plateau in Fig. 4.9 are shown in Fig. 4.13b for both models and are more consistent with the experimental data. In particular, the energy based groups show excellent agreement with the Appleton [139] data across the range of experimental conditions. The vibrational specific grouping predicts a lower rate coefficient at low temperatures (*e.g.* 10 000 K), and the slope of the rate does not agree with the experimental fit. At higher temperatures, both grouping strategies predict similar rate coefficients. The Kewley and Hornung data [140] predict a significantly different temperature dependence, inconsistent with what was predicted by the MGMET-QCT method, demonstrated by the different slope in the data in Fig. 4.13. It is the author's opinion, based on preliminary analysis, that the discrepancy in the Kewley and Hornung data compared with the MGMET-QCT method is due to the non-equilibrium model adopted by the experimentalists to interpret the experimental data (not shown). Additional experimental data, not included in the figure, have been used in the comparison. Hanson and Baganoff [141] predict the same temperature dependence as Kewley and Hornung, but their rates are significantly higher than all other experimental results. Park [5] reinterpreted the experimental data of Appleton, by including non-equilibrium effects in the post-processing. As a result, the Park dissociation rate coefficient appears larger than the original value given by Appleton; however, the temperature dependence is similar.

The vibrational relaxation time, τ_{VT} was computed using the e-folding method (the time required for the mode to reach 63.2% of its steady state energy) from the vibrational bins. The vibrational relaxation time is shown in Fig. 4.14, compared with the Millikan-White correlation, [17] and high-temperature correlations developed by Park [7] and Boyd and Josyula [142]. At low

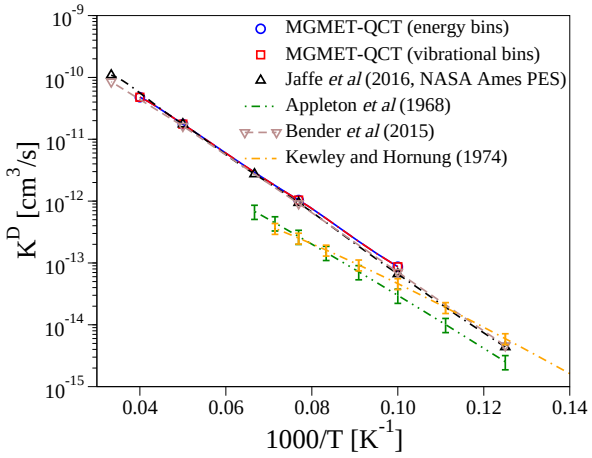

(a) Thermal equilibrium, compared with previous work of Jaffe *et al.* [138] and Bender *et al.* [79]

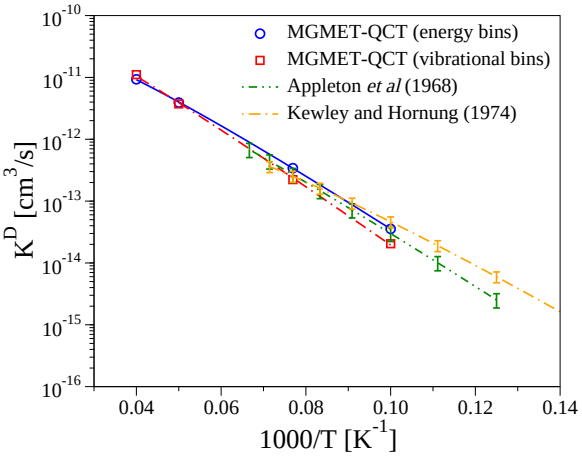

(b) Quasi-steady-state.

Figure 4.13: N_2-N_2 dissociation rate coefficients compared with previous experimental work from Appleton *et al.*, [139] and Kewley and Hornung. [140]

Table 4.2: Dissociation rate coefficients in cm^3/s.

	Thermal equilibrium		QSS	
Temperature	Energy bins	Vibrational bins	Energy bins	Vibrational bins
10 000 K	8.6844×10^{-14}	8.6693×10^{-14}	3.5509×10^{-14}	2.0462×10^{-14}
13 000 K	1.0397×10^{-12}	1.0376×10^{-12}	3.4085×10^{-13}	2.2250×10^{-13}
20 000 K	1.7563×10^{-11}	1.7552×10^{-11}	3.9152×10^{-12}	3.7318×10^{-12}
25 000 K	4.7894×10^{-11}	4.7800×10^{-11}	9.3343×10^{-12}	1.1089×10^{-11}

temperatures, the vibrational relaxation matches well with the Millikan-White correlation. The high-temperature corrections to Millikan-White match well at high temperatures with the vibrational binning data.

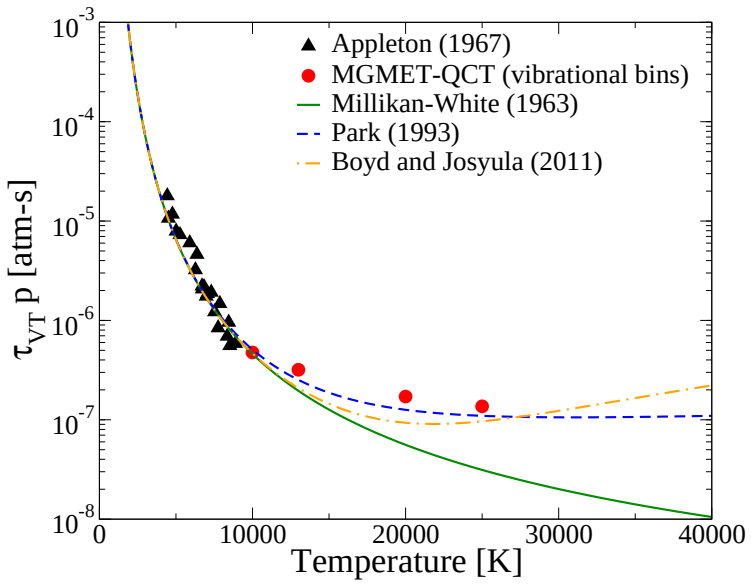

Figure 4.14: Vibrational relaxation time computed with Millikan-White [17], high temperature corrections [7, 142], and experimental data from Appleton and Steinberg. [143]

4.6 Discussion

The results have clearly shown how the choice of grouping strategy has a profound impact on the characteristics of the thermochemical relaxation. The two grouping strategies adopted in this chapter are based on two fundamentally different assumptions: the vibrational grouping is constructed on the assumption of rigid separation between the rotational and vibrational energy modes, while the energy based grouping, by lumping the levels independently of their vibrational and rotational characteristics, assumes exactly the opposite. Each of the governing assumptions has its merits: the separation of modes was clearly demonstrated experimentally and theoretically for the low lying energy levels. This justifies the use of a vibrational based grouping strategy. On the contrary the high energy states exhibit much stronger rovibrational coupling, which implies that energy based binning provides a more accurate description of their behavior.

Dissociation. The energy based grouping model predicts that molecules must climb to high energy rovibrational levels before dissociating, and that a significant amount of energy lost in dissociation comes from rotationally excited molecules. By dissecting the energy ladder into narrow rovibrational energy groups, the contribution of vibrational and rotational energy to dissociation can be separated without introducing significant artificial bias. The energy grouping model predicts

nearly equal contribution of rotational and vibrational energy to dissociation. This is not the case for the vibrational grouping method, which strongly underpredicts the role of rotation. Moreover, the narrow width of the energy bins (0.25 eV) limits the negative influence of the assumption of thermal equilibrium between translation and the group internal temperature.

In contrast, the vibrational binning strategy assumes equilibrium among rotational states across a wide range of energy, especially for the low vibrational energy groups (*e.g.*, $v = 0$ spans nearly 15 eV). As a result of the averaging process the importance of dissociation from the high energy states is overwhelmed by the improbability of the low energy states dissociating. The weakness of the vibrational grouping strategy originates from the fact that low and high energy states are governed by different kinetics. To accurately predict the non-equilibrium distribution of rovibrational states, those states with similar rates should be grouped together (or averaged together) [115].

Energy transfer. The energy transfer process predicted by the energy level grouping was very fast across the range of temperatures. Because states with very different quantum configurations are lumped together in this approach, the mode separation known to exist for low energy states during relaxation, is not captured. This problem is not present in the vibrational based grouping because the differences in the dynamics of slow and fast processes (*i.e.*, vibrational and rotational relaxation respectively) are correctly captured. Since internal energy relaxation and dissociation do not overlap in the thermochemical relaxation process at this condition, errors in the modeling of the relaxation are unlikely to affect the dynamics of dissociation.

4.7 Summary

In this chapter, we present the MGMET model for diatom-diatom interactions applied to the $N_2(X^1\Sigma_g^+) - N_2(X^1\Sigma_g^+)$ system. The energy states are lumped together into groups containing states with similar properties, and the distribution of states within each of these groups is prescribed by a Boltzmann distribution at the local translational temperature. The required grouped kinetic properties are obtained directly by the MGMET-QCT method. Two grouping strategies are considered: energy-based grouping, in which states of similar internal energy are lumped together, and vibrational grouping, in which states with the same vibrational quantum number are grouped

together. A zero-dimensional chemical reactor simulation, in which the molecules are instantaneously heated, forcing the system into strong non-equilibrium, is used to study the differences between the two grouping strategies. The comparison of the numerical results against available experimental data demonstrates that the energy-based grouping is more suitable to capture dissociation, while the energy transfer process is better described with a vibrational grouping scheme. The dissociation process is found to be strongly dependent on the behavior of the high energy states, which contribute up to 50% of the dissociating molecules. Furthermore, up to 40% of the energy required to dissociate the molecules comes from the rotational mode, underscoring the importance of accounting for this mode when constructing non-equilibrium kinetic models. In contrast, the relaxation process is governed primarily by low energy states, which exhibit significantly slower transitions in the vibrational binning model due to the prevalence of mode separation in these states.

Chapter 5

Validation of MGMEL-QCT Model using N_2-N System

In this chapter, results of the MGMEL-QCT model are presented. In this approach, the group internal temperatures are allowed to vary, and we must make use of detailed balance relationships derived for the group which depend on the energy of the states in the groups as well as the temperature in the group. In order to test whether this approach accurately reproduces the expected grouped kinetic properties (such as those computed by grouping microscopic StS kinetic data), a kinetic model was constructed using this approach for the $N_2(X^1\Sigma_g^+) - N(^4S_u)$ system. The results are compared with the grouped StS kinetic data for validation. This chapter is organized as follows: in Section 5.1 the set-up for the MGMEL-QCT model is presented for the $N_2(X^1\Sigma_g^+) - N(^4S_u)$ system. In Section 5.2 the kinetic data computed using the MGMEL-QCT method is presented and compared with that obtained using the StS approach. Section 5.3 makes use of the kinetic data obtained using the MGMEL-QCT method in a zero-dimensional heat bath study. Finally, Section 5.4 summarizes the chapter. This chapter is reproduced from Ref. [118], with the permission of AIP Publishing.

5.1 Simulation set-up

The StS data used to validate the MGMEL-QCT method is based on the NASA Ames PES for the $N_2(X^1\Sigma_g^+) - N(^4S_u)$ system, using only exothermic trajectories (these are characterized by lower statistical error). The kinetic data for the 9390 rovibrational levels of $N_2(X^1\Sigma_g^+)$ comprises approximately 13 million excitation reaction rate coefficients. Further details on the StS kinetic data can be found in Ref. [38]. Because we only consider N_2 in the MGMEL-QCT model, we can write reaction rate coefficients and energy transfer coefficients in terms of only group indices: ${}^mK_{p,r}$, ${}^m\bar{K}_{r,p}$, ${}^mC_p$, and ${}^m\bar{C}_p$ for excitation, de-excitation, dissociation, and recombination respectively.

Finally, because the MGMEL-QCT model only requires kinetic data in one direction by relating forward and reverse reactions through detailed balance, the MGMEL-QCT for excitation can be constructed using either only exothermic or only endothermic trajectory data.

The results will make use of a simple energy based grouping scheme using either 60 or 6 groups, which are denoted by MGMEL-QCT(60) and MGMEL-QCT(6) respectively. The trajectory data was calculated for the MGMEL-QCT(60) model using 192,000 trajectories from each initial group (p) at translational temperature $T = 10\,000\,\mathrm{K}$ and group internal temperatures of $T_p^{\mathrm{int}} = (2000\,\mathrm{K}, 5000\,\mathrm{K}, 10\,000\,\mathrm{K})$. The kinetic data for the MGMEL-QCT(6) model was retrieved by re-grouping the kinetic data for the MGMEL-QCT(60) model with the appropriate weighting. It is important to note that as a result of this re-grouping procedure the statistical error associated with the kinetic data for the MGMEL-QCT(6) model will be significantly lower: we are effectively using a stratified sampling method with ten times as many samples as the MGMEL-QCT(60) model. Details on this can be found in Appendix F.

As in the previous chapter, because we are only interested in studying a zero-dimensional isochoric and isothermal reactor, the conservation equations can be simplified down to comprise the group conservation of mass and energy equations:

$$\frac{\mathrm{d}n_p}{\mathrm{d}t} = \sum_{r\in\mathcal{I}} \left(-{}^0K_{p,r} n_p n_N + {}^0\bar{K}_{p,r} n_r n_N\right) + \left(-{}^0C_p n_p n_N + {}^0\bar{C}_p n_N^3\right), \qquad p \in \mathrm{N}_2, \tag{5.1}$$

$$\frac{\mathrm{d}n_N}{\mathrm{d}t} = 2\sum_{p\in\mathcal{I}} \left({}^0C_p n_p n_N - {}^0\bar{C}_p n_N^3\right), \tag{5.2}$$

$$\frac{\mathrm{d}e_p}{\mathrm{d}t} = \sum_{r\in\mathcal{I}} \left(-{}^1K_{p,r} n_p n_N + {}^1\bar{K}_{p,r} n_r n_N\right) + \left(-{}^1C_p n_p n_N + {}^1\bar{C}_p n_N^3\right), \qquad p \in \mathrm{N}_2 \tag{5.3}$$

Note that the atoms do not require a conservation of energy equation because they have no internal structure and do not have an internal temperature.

5.2 Grouped kinetic data

Figure 5.1 shows the forward energy transfer coefficients for the excitation reaction for the MGMEL-QCT(60) and MGMEL-QCT(6) models from a fixed initial group ($p = 15$ for MGMEL-QCT(60) and $p = 2$ for MGMEL-QCT(6)). For both the MGMEL-QCT(6) and MGMEL-QCT(60) models,

the rate has been shown for molecules with similar initial energy. For the MGMEL-QCT(60) model (Fig. 5.1a) the rates computed from exothermic trajectories are in excellent agreement with the rates computed from the StS data. Moreover, the statistical error associated with the exothermic rate data is generally very low (the mean error for all energy transfer coefficients computed using exothermic trajectory data is 8.8%). In contrast, the rate data computed using endothermic trajectories matches well for data in which the energy change is less than approximately 3 eV. However, the higher energy jumps exhibit large errors (the mean error for all energy transfer coefficients computed using endothermic trajectory data is 31.7%). The errors associated with the sampling are greatly reduced when the number of groups is reduced, though this may be a combination of both the reduced number of groups and the increased number of trajectories per group (now effectively 1,920,000 per group, using a stratified sampling scheme). In the MGMEL-QCT(6) model (Fig. 5.1b), although there is not endothermic MGMEL-QCT data available for the $2 \rightarrow 6$ transition, the statistical error with all other rates is significantly lower than the MGMEL-QCT(60) model. In this case the mean statistical error associated with the forward energy transfer coefficients is 1.5% and 14.1% for the exothermic and endothermic MGMEL-QCT models respectively.

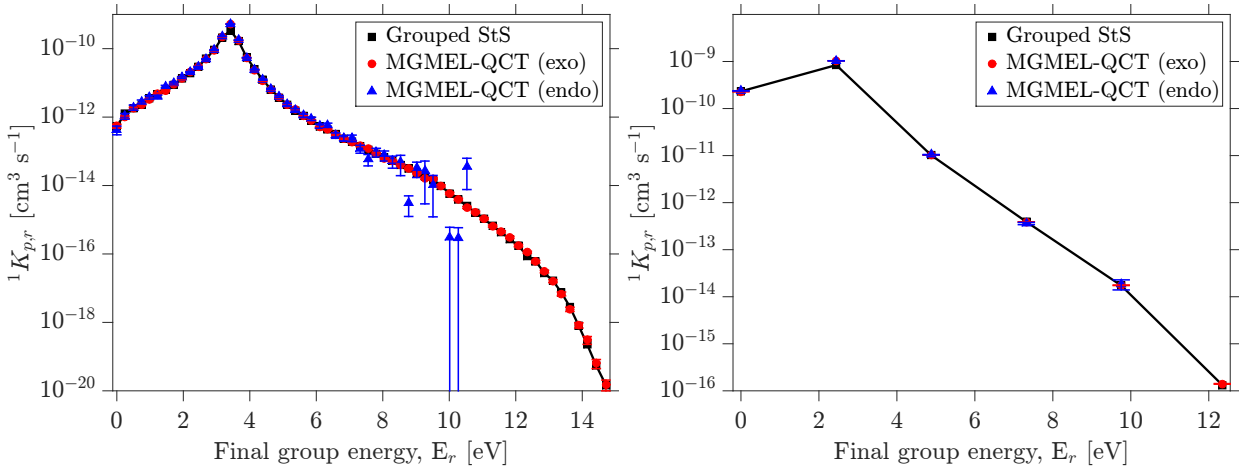

(a) MGMEL-QCT(60), $N_2(p = 15)+N \rightleftharpoons N_2(r)+N$. **(b)** MGMEL-QCT(6), $N_2(p = 2) + N \rightleftharpoons N_2(r) + N$.

Figure 5.1: Grouped energy transfer coefficients for excitation reaction ($^1K_{p,r}$) at T = 10 000 K and T_p^{int} = 5000 K; error bars denote one standard deviation.

Figure 5.2 shows the dissociation and recombination energy transfer rates for the MGMEL-QCT(60) model. Similar to what was observed for the excitation reaction, the energy transfer coefficients for high energy jumps (*e.g.*, dissociation from groups below around 4 eV) exhibit high

statistical error. Despite this fact, Fig. 5.2b highlights the key advantage to this framework: reaction rate coefficients and energy transfer coefficients for the recombination process can be computed. Because the recombination rates are obtained from dissociating trajectories through detailed balance, there are two key advantages: first, this ensures that detailed balance is obeyed, ensuring that the system will reach equilibrium given enough time; second, recombination rates and energy transfer coefficients can be obtained from dissociating trajectories, eliminating the need to run recombination trajectories (an impossible task due to the number of pathways for recombination). Because the recombination energy transfer coefficients are obtained from dissociation trajectories, the error of the recombination rates mirrors that observed for the dissociation rates.

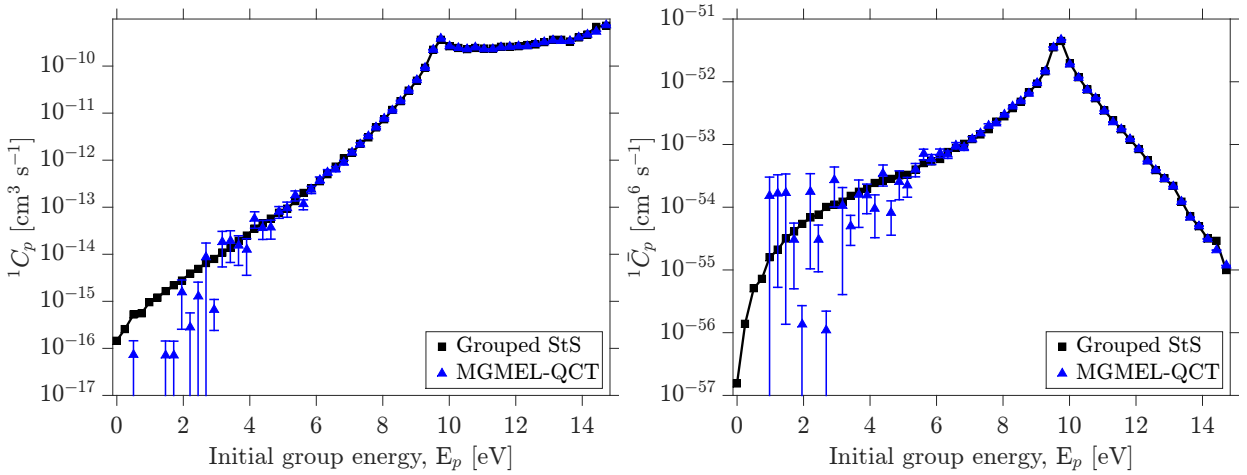

(a) C_q. **(b)** $\bar{C}_q$.

Figure 5.2: Grouped energy transfer coefficients for dissociation reaction for MGMEL-QCT(60) from group p, $N_2(p) + N \rightleftharpoons 3N$ at $T = 10\,000\,K$ and $T_p^{int} = 5000\,K$; error bars denote one standard deviation.

Figure 5.3 shows the variation of the excitation forward energy transfer coefficient for the MGMEL-QCT(6) model from group 2 to group 3 with the group internal and translational temperatures. This was computed by grouping the StS data to enable calculation at many internal temperatures. The variation of the rate with translational temperature is quite strong, as expected. However, the internal temperature also has a significant impact on the rates, particularly at high translational temperatures. The inset shows the variation of the coefficient due to internal temperature at $T = 10\,000\,K$ from the MGMEL-QCT models and the grouped StS as well as the variation at $T = 20\,000\,K$ from the grouped StS data. This demonstrates the importance of calculating

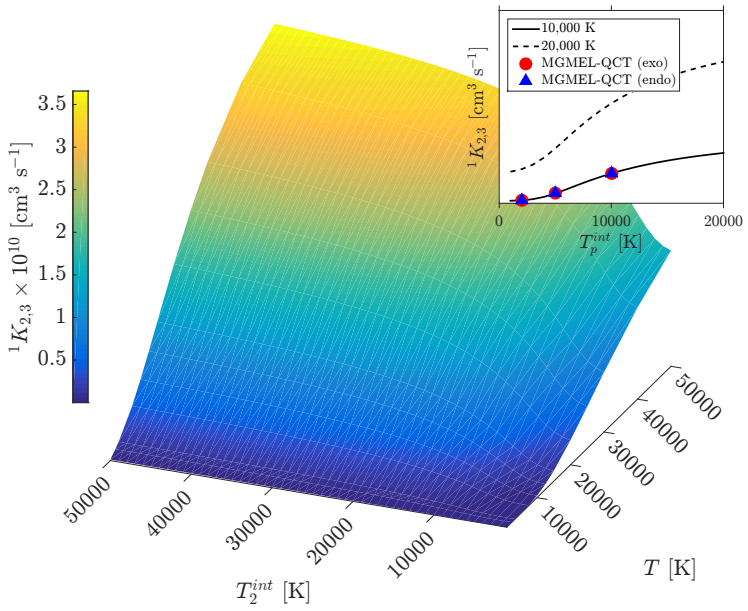

Figure 5.3: Excitation energy transfer coefficients for MGMEL-QCT(6) from group 2 to group 3 at varying translational and group internal temperature. Inset: variation of energy transfer coefficient on bin internal temperature at 10 000 K for grouped StS (solid line), exothermic MGMEL-QCT (circles), and endothermic MGMEL-QCT (triangles) and at 20 000 K for grouped StS (broken line).

kinetic data at various internal and translational temperatures, as the impact of both parameters on the kinetic data is significant.

5.3 Zero-dimensional heat bath

In order to assess the accuracy of the three approaches to computing the kinetic data on the resulting non-equilibrium distribution, a simple test case of a zero-dimensional isothermal and isochoric reactor was simulated. Initially, the gas is at 2000 K with a density of $\rho = 0.0164$ kg/m^3 and mole fractions of N_2 and N of $X_{N_2} = 0.95$ and $X_N = 0.05$ respectively. The gas is then instantaneously heated to 10 000 K, and equations (5.1), (5.2), and (5.3) are solved for the transient state of the gas using the MGMEL-QCT(6) model. This is done using the grouped StS rates, the exothermic MGMEL-QCT model, and the endothermic MGMEL-QCT model. Figure 5.4 shows the resulting composition (mole fraction of atomic nitrogen) and internal energy of molecules as a function of time during the excitation and dissociation processes. Initially the internal energy of the molecules is low, corresponding to an internal temperature of 2000 K. After some incubation time,

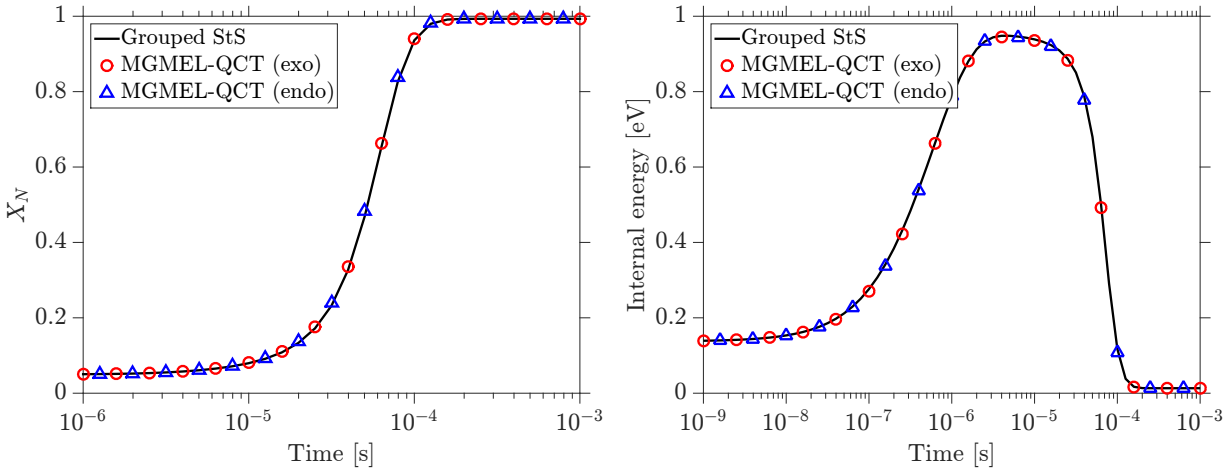

(a) Mole fraction atomic nitrogen as a function of time.

(b) Average internal energy of nitrogen molecules as a function of time.

Figure 5.4: Global properties for MGMEL-QCT(6) heat bath at T = 10 000 K.

the molecules begin to excite, with the internal energy reaching a maximum. Then, the dissociation process takes over, and the energy of contained in the molecules drops as they dissociate, and the mole fraction of atomic nitrogen increases. Finally, the system reaches a final equilibrium state in which most of the molecular nitrogen has dissociated. In the global properties, all three approaches agree well, with the composition and molecular internal energy matching perfectly among the three models. Moreover, this demonstrates the fact that the system will reach a final equilibrium state due to the application of detailed balance to derive reverse reaction rate and energy transfer coefficients.

However, the primary advantage of the MGMEL-QCT model is that it allows for the non-equilibrium state distribution to be retrieved from the global *bin* properties. Figure 5.5 shows one example of a non-equilibrium distribution early in the energy transfer process. The first two groups are frozen at the initial internal temperature, and both the endothermic and exothermic MGMEL-QCT models capture this behavior. For the higher groups, particularly groups 4-6, the endothermic MGMEL-QCT model fails to capture the distribution predicted by the grouped StS data. This is due to the high error associated with the kinetic data for the endothermic MGMEL-QCT model. However, the excellent agreement between the exothermic MGMEL-QCT model and the grouped StS data demonstrate the applicability of the MGMEL-QCT model constructed using exothermic trajectory data in a self consistent manner. Moreover, despite calculations at only three internal temperatures, by fitting the internal temperature dependence to a second order polynomial in log

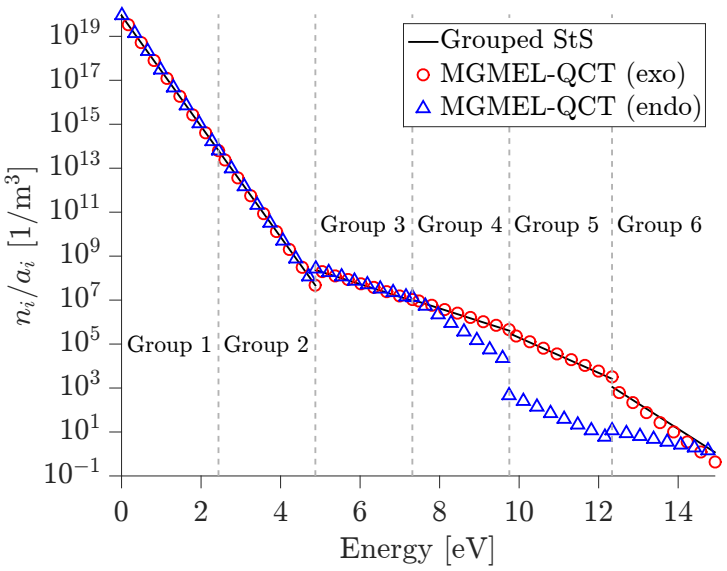

Figure 5.5: Distribution of states at $t = 7.94 \times 10^{-14}$ s for MGMEL-QCT(6) model.

space, detailed balance is satisfied, and the system is driven to equilibrium, as it should. Details on how the internal temperature dependence was fitted can be found in Appendix G.

5.4 Summary

In this chapter, we present the MGMEL-QCT framework and apply it to the $N_2(X^1\Sigma_g^+) - N(^4S_u)$ system for validation. Because the $N_2(X^1\Sigma_g^+) - N(^4S_u)$ system has known StS kinetics, it can be used as a benchmark on which to compare the model constructed directly from QCT. This comparison demonstrates the applicability of the MGMEL-QCT method and shows that the approach of applying detailed balance at a microscopic level reproduces the expected grouped kinetic data as predicted by applying the analytical grouping expressions to the rovibrational StS kinetic data. It is shown that the model constructed using endothermic trajectories for excitation processes is less accurate due to the poor statistical sampling. However, the model constructed using exothermic trajectories was in excellent agreement with the grouped StS rates.

Chapter 6

Validation of MGMET-QCT Method with DMS Method

In the following sections, a comparison between the MGMET-QCT model (the same as presented in Chapter 4) and the DMS method will be presented [117]. The DMS method was developed at the University of Minnesota and is a technique for directly determining the transient non-equilibrium behavior of a gas. It is similar to the DSMC method for modeling flows, but instead of relying on pre-computed data for kinetics, trajectory calculations are performed within the simulation [99–101, 144–147]. The only input to the DMS method is the PES; therefore, the DMS method can be used as a benchmark solution on which to evaluate other models. We will compare the results of the MGMET-QCT model from Chapter 4 with the DMS method in a similar zero-dimensional heat bath study. In Section 6.1 we present the simulation set-up and a brief description of the DMS method. In Section 6.2, a comparison between the microscopic and macroscopic properties during dissociation is made. In Section 6.3, a similar comparison is made for the energy transfer process. Finally, in Section 6.4, a discussion of the primary findings of this comparison is presented, and in Section 6.5 a summary of the chapter is presented. This chapter is reproduced from Ref. [117], with the permission of AIP Publishing.

6.1 Simulation set-up

To facilitate a meaningful comparison, both methods (DMS and MGMET-QCT) used the same NASA Ames PES and only considered collisions between two molecules, excluding atom-molecule ($N_2(X^1\Sigma_g^+) - N(^4S_u)$) interactions. Initially, the gas is composed of only molecules with a density of 1.28 kg/m^3, an internal temperature of 2000 K, and a corresponding pressure of 760.137 kPa. The temperature is then instantaneously heated to 10 000 K or 25 000 K, and the non-equilibrium energy transfer and dissociation processes are studied. The same two grouping strategies as those

presented in Chapter 4 are used (60 energy based groups and 61 vibrational groups), and the governing equations and kinetic data used are the same.

6.1.1 Direct molecular simulation method

Details on the DMS method can be found in Refs. [99–101]. Like the DSMC method, a fraction of the actual gas particles are simulated, with each particle representing a larger population of nearly identical physical particles. The ratio of the actual particles to the number of simulated particles is called the particle weight, W_p. The simulation uses a time step on the order of the mean collision time (τ_c) and cell volumes on the order of the mean collision path (λ_c). In this study, the particle weight is set to 1, and the time step is set to one one-hundredth of the mean collision time ($\Delta t_{\mathrm{DMS}} = \tau_c/100$). For the T = 10 000 K simulation, $6{\times}10^4$ molecules are used at $t = 0$, and for T = 25 000 K, 10^6 molecules are used at $t = 0$. Because the simulation is performed in zero-dimensions, the volume is set such that the density in the box is 1.28 kg/m^3.

6.2 Dissociation

Figure 6.1 shows the mole fraction of atomic nitrogen as a function of time at 10 000 K. The DMS prediction is well matched by the MGMET-QCT energy based grouping model. The vibrational specific MGMET-QCT model predicts significantly slower dissociation which stems from the inaccurate treatment of high energy states in this model: the vibrational grouping enforces mode separation across the entire energy spectrum. However, this effect is expected to breakdown for the high energy states, due to the rovibrational coupling of high energy states. Moreover, because all rotational states within a vibrational group are in equilibrium at a common rotational temperature ($T_{rot} = T$), the quasi-bound states are lumped with bound states, despite the distinct differences in the kinetics that characterize the dissociation process from these internal states (*e.g.*, the state $(v, J) = (0, 0)$ is very unlikely to dissociate, while $(v, J) = (0, 273)$ is extremely likely to dissociate). The discrepancy between the vibrational based grouping and the DMS data highlights the importance of considering the rotational state for predicting dissociation. This effect is amplified at 10 000 K because molecules are more likely to climb to quasi-bound states before dissociating at lower temperatures [116]. In addition, because the DMS method cannot simulate recombination

reactions, it can reach the QSS distribution, but not the equilibrium composition. The energy based MGMET-QCT method is included without recombination reactions. Until 10^{-6} seconds, the effect of recombination is negligible; however, after this the MGMET-QCT results demonstrate the effect of recombination in forcing the system to equilibrium.

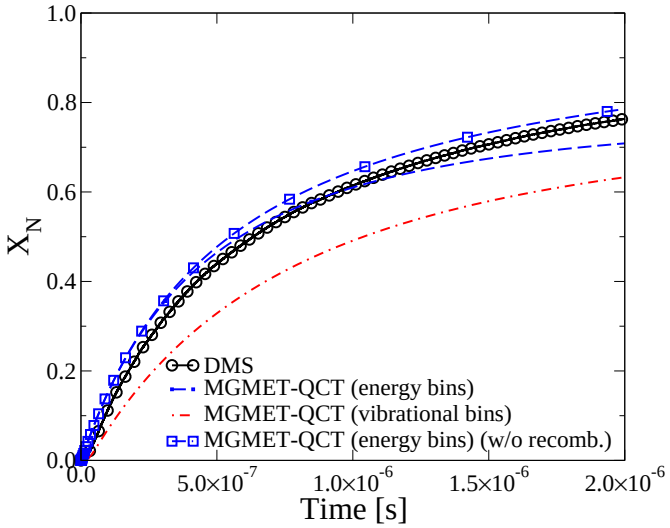

Figure 6.1: Mole fraction of atomic nitrogen as a function of time at 10 000 K.

The distribution function predicted by both methods can be compared both during the energy transfer and dissociation process. It was found that at the conditions studied, the dissociation process occurs when the distribution is in QSS, meaning that the relative distribution of states (or groups) is not changing in time. The resulting QSS distribution predicted by the energy based MGMET-QCT method is shown in Fig. 6.2a at 10 000 K. The DMS data is grouped using the same grouping strategy for comparison with the energy binning strategy, and averaged over several time-steps. The QSS distribution of groups predicted by the energy based MGMET-QCT method is in excellent agreement with that predicted by the DMS method. At the dissociation energy, 9.75 eV, the distribution of groups turns down, indicating that the quasi-bound states are significantly depleted in QSS. At 10 000 K using the energy based MGMET-QCT method, only 0.006% of the molecules are in the quasi-bound states (blue squares in Fig. 6.2a), while at 25 000 K the quasi-bound states are over 100 times more populated, with 0.7% of the molecules in quasi-bound states (blue squares in Fig. 6.3b). Figure 6.2b shows the vibrational distribution predicted by the MGMET-QCT method. Despite the differences in the dissociation rate observed by the mole

fraction of atomic nitrogen (Fig. 5.4a), the vibrational energy distribution deviates only slightly from the DMS data. This suggests that the overall dissociation rate is quite sensitive to the energy state populations, and that the rotational energy distribution (not shown explicitly in Fig. 6.2) may play a role.

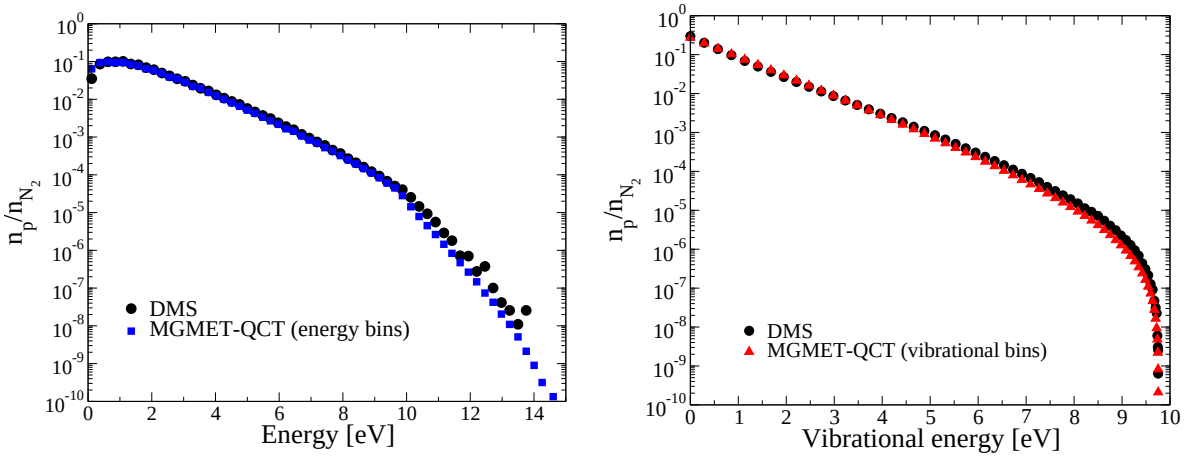

(a) Energy binned MGMET-QCT. **(b)** Vibrational binned MGMET-QCT.

Figure 6.2: QSS distributions from MGMET-QCT method at 10 000 K.

In order to compare the two grouping strategies directly, the state specific distribution was reconstructed with the vibrational based MGMET-QCT method, and regrouped according to the energy bins. This maps the vibrational based MGMET-QCT data to the energy based MGMET-QCT data for comparison, and is shown in Fig. 6.3 at both temperatures. In both cases, the quasi-bound groups are over-populated in the vibrational binned MGMET-QCT method compared to the DMS data. This stems from the assumption of equilibrium of all rotational states within a vibrational state made in this model. Despite the agreement between the vibrational distributions, capturing the rovibrational distribution is necessary for an accurate prediction of the dissociation process.

The QSS dissociation rate predicted from the MGMET-QCT and DMS methods is shown in Fig. 6.4 at various temperatures. At 10 000 K, the QSS dissociation rate predicted by the vibrational specific MGMET-QCT model is significantly slower than that predicted by both the energy based MGMET-QCT and DMS methods. This is due to the improper lumping of quasi-bound states with bound states in this approach, which hinders dissociation, particularly at lower temperatures. Across the entire range of temperatures, the energy binned MGMET-QCT method is in excellent

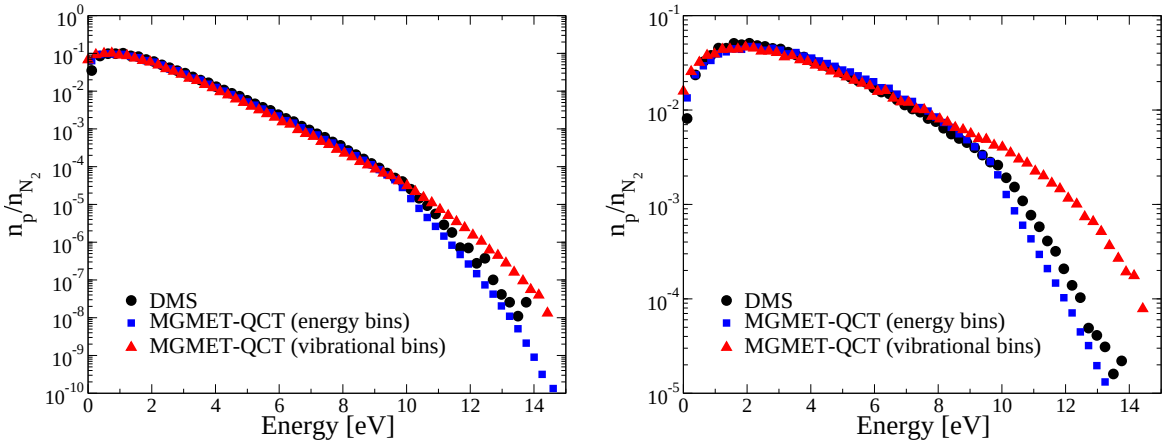

(a) T = 10 000 K. **(b)** T = 25 000 K.

Figure 6.3: QSS distributions from energy binned MGMET-QCT and vibrational bins regrouped as energy binned MGMET-QCT.

Table 6.1: Arrhenius fit coefficients for QSS dissociation rates from MGMET-QCT and DMS methods.

	A [cm^3/s]	η	E_A [K]
MGMET-QCT (vibrational bins)	2.41×10^{-7}	-0.54	1.132×10^5
MGMET-QCT (energy bins)	7.09×10^{-4}	-1.35	1.132×10^5
DMS	1.25×10^{-4}	-1.17	1.132×10^5

agreement with the DMS data. In contrast, at 25 000 K the vibrational specific model overshoots the dissociation rate predicted by the DMS data. Due to the excellent agreement across the entire range of temperatures, the energy bins can accurately capture the dissociation process in QSS regardless of temperature. Table 6.1 give the coefficients for the modified Arrhenius fits to the data computed by the MGMET-QCT and DMS methods. The modified Arrhenius form is given by:

$$K^{\mathrm{D}}_{QSS} = AT^{\eta} \exp\left(-\frac{E_A}{T}\right) \tag{6.1}$$

where A, η, and E_A are the coefficients given in Table 6.1, and the units of K^{D}_{QSS} are cm^3/s.

In order to understand the relative importance of energy states for dissociation, the distribution of dissociating molecules in QSS was computed. For the DMS method, this is computed by counting the molecules which dissociate at each time step and taking an average over several time-steps in the QSS region to obtain the distribution of molecules dissociating from various energies. For the

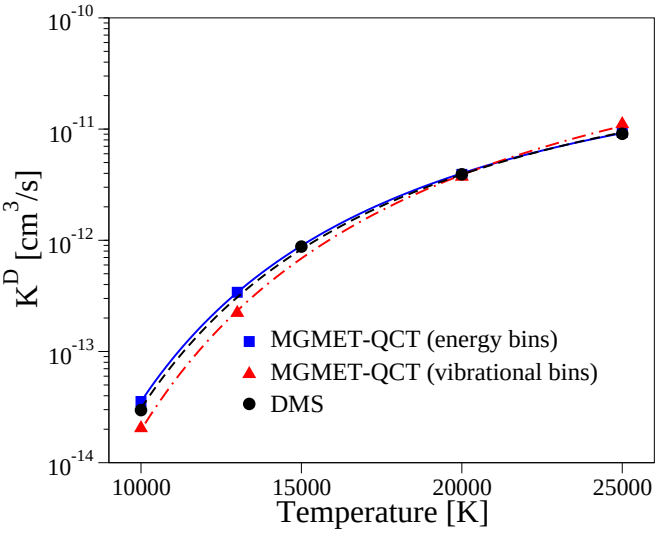

Figure 6.4: QSS dissociation rate [138].

MGMET-QCT model, this was done by weighting the dissociation rate from each group with the distribution of groups in QSS (Eq. (4.5)). This comparison is shown in Fig. 6.5 for the energy based MGMET-QCT and in Fig. 6.6 for the vibrational based MGMET-QCT. In the energy based MGMET-QCT method, the trend matches with the DMS results, showing that molecules climb to high energy states before dissociating, with the highest probability of dissociation occurring at the dissociation energy. However, the actual peak and width of the distribution is not well matched. In Fig. 6.6, the vibrational MGMET-QCT method distribution of dissociating molecules matches well at 10 000 K despite the overall dissociation rate being significantly slower than that predicted by the DMS method. At higher temperatures, the vibrational distribution of dissociating molecules deviates significantly from the DMS results, with significant dissociation occurring from the low vibrational states predicted by the MGMET-QCT method. The high proportion of dissociation from low vibrational states in the MGMET-QCT method is most likely caused by the increased weight of the high rotational states at the higher temperature. Therefore, the states which are highly probable to dissociate now hold higher weight from the Boltzmann factor, contributing to increased total dissociation rate from the low vibrational states.

To quantify the contribution to dissociation from each mode, the fraction of energy lost from each group in the energy binned approach from the rotational and vibrational modes (calculated using Eq. (4.6)) is shown in Fig. 6.7 at T = 10 000 K. The qualitative agreement between the

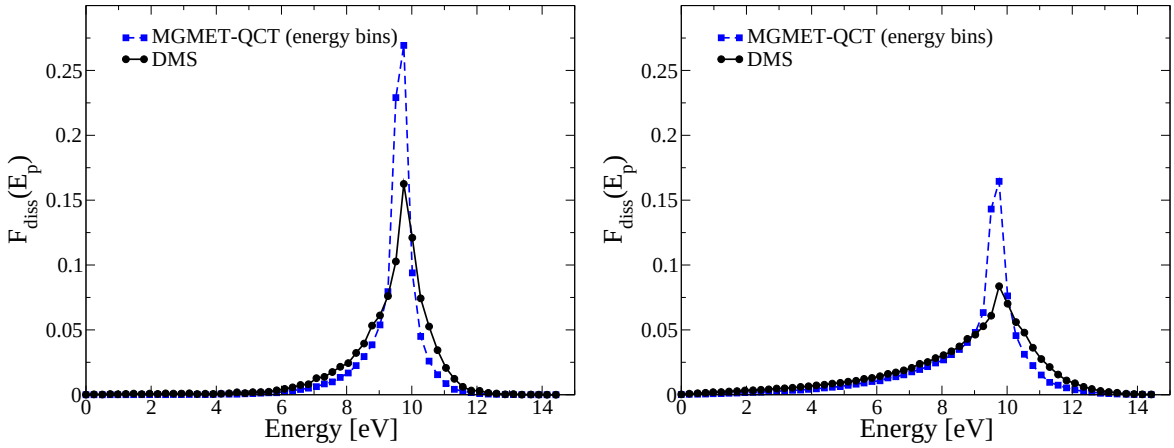

(a) T = 10 000 K. **(b)** T = 25 000 K.

Figure 6.5: Distribution of dissociating molecules in DMS versus energy based MGMET-QCT during QSS.

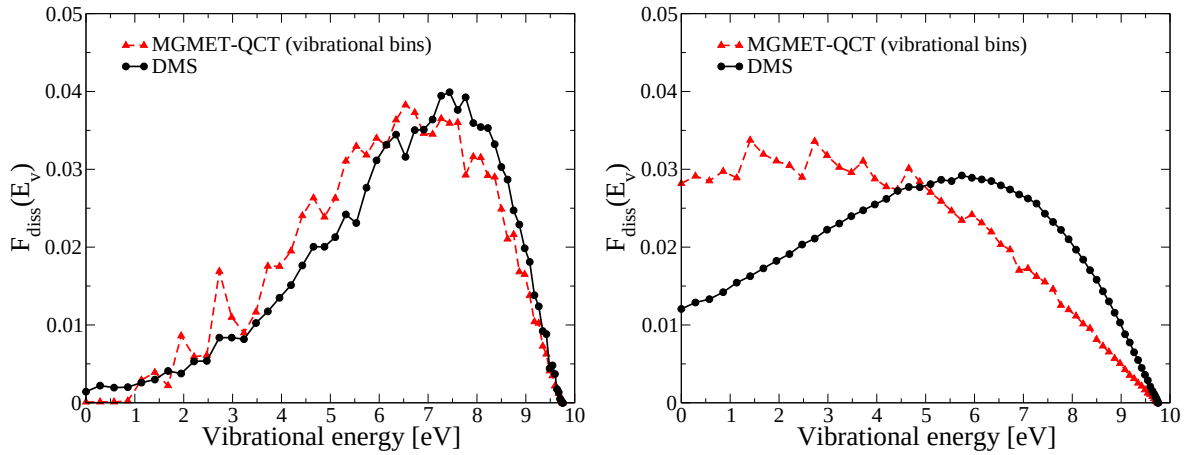

(a) T = 10 000 K. **(b)** T = 25 000 K.

Figure 6.6: Distribution of dissociating molecules in DMS versus vibrational based MGMET-QCT during QSS.

MGMET-QCT and DMS results is good, with both approaches losing a significant amount of energy from the rotational mode. The DMS results predict that 34% of the energy for dissociation comes from the rotational mode, while MGMET-QCT predicts 40%. The DMS results show a distinct bump in the rotational energy contribution at the dissociation energy. This occurs because quasi-bound states are primarily low-v/high-J states with a significant amount of rotational energy. Therefore, the contribution of the rotational energy to dissociation from the quasi-bound states overshoots the vibrational contribution for high energy states.

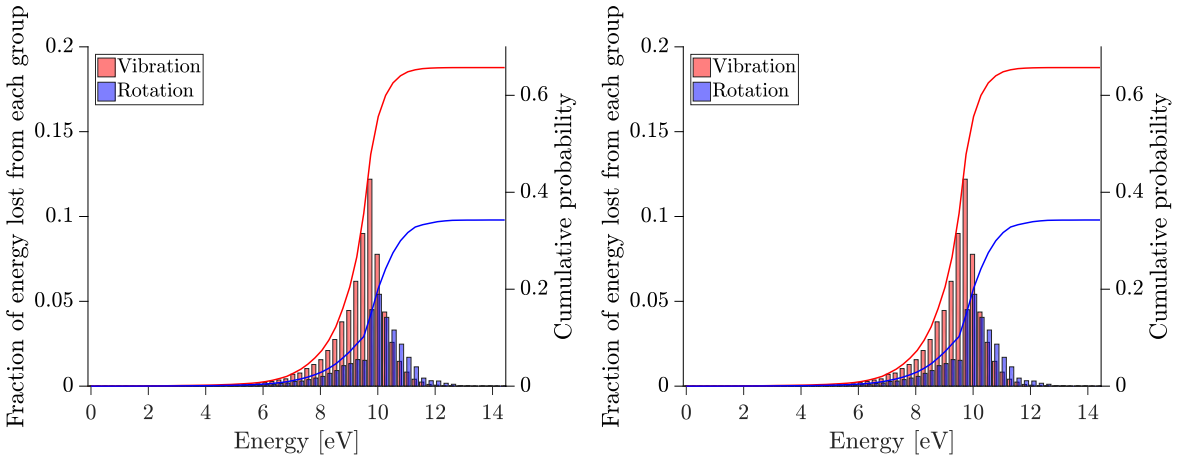

(a) Energy based MGMET-QCT. **(b)** DMS.

Figure 6.7: Fraction of rotational and vibrational energy lost by the molecules during the QSS region from each group at T = 10 000 K.

6.3 Energy transfer

The energy transfer process serves to excite the internal states of the molecule until they have enough energy for dissociation to take over. Therefore, understanding the time scale in which energy transfer occurs is necessary to accurately predict the onset of dissociation. Moreover, the $N_2(X^1\Sigma_g^+) - N_2(X^1\Sigma_g^+)$ energy transfer process is very important for air chemistry because in many situations of interest there are initially very few atoms present. The internal energy, as calculated by Eq. (4.8), at both temperatures predicted by the DMS method, energy based, and vibrational based MGMET-QCT models is shown in Fig. 6.8. At 10 000 K, the internal energy relaxation predicted by the energy based MGMET-QCT model is significantly faster than both the DMS method and vibrational specific MGMET-QCT model. The vibrational specific MGMET-QCT method starts with higher internal energy because the rotational mode is already excited; however, the energy of the molecules does not increase until 10^{-9} seconds, indicating that the molecules are not gaining significant energy from the translational mode until that point. When the vibrational excitation starts, corresponding to the second increase in internal energy in the DMS method, the vibrational MGMET-QCT method matches well with the DMS data. Similarly, at 25 000 K, the internal energy relaxation predicted by the energy based MGMET-QCT model is significantly faster than the DMS method. Again, the vibrational MGMET-QCT model starts with higher internal energy. At the higher temperature, the distinction between rotational and vibrational excitation is not present,

indicating that the two excitation processes are more closely coupled at this temperature. In both cases, the internal energy at the final time, corresponding to the QSS energy, differs by less than 5% due to differences in the rotational and vibrational energy in the QSS region.

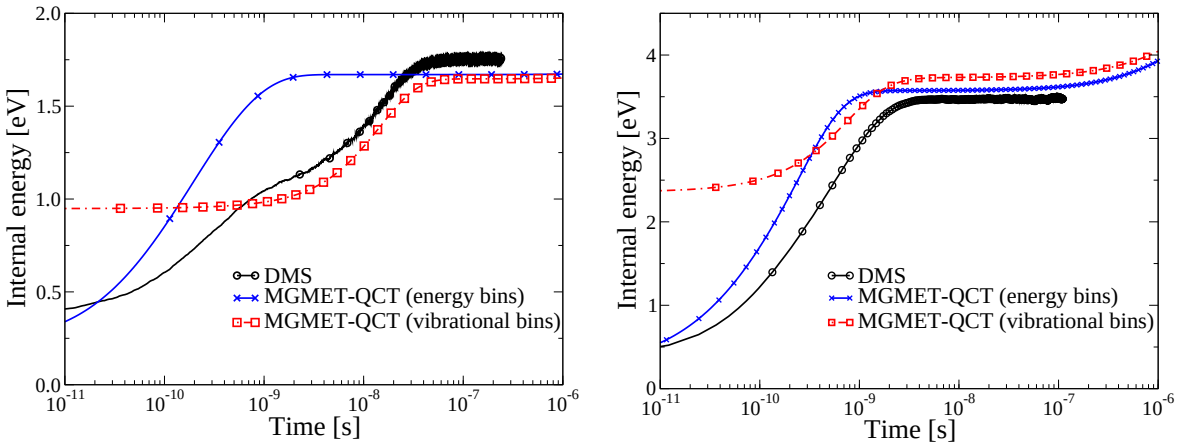

(a) T = 10 000 K. **(b)** T = 25 000 K.

Figure 6.8: Total internal energy predicted from DMS versus energy and vibrational based MGMET-QCT.

In addition to the total internal energy, the rotational and vibrational temperatures predicted from the DMS and vibrational based MGMET-QCT model were computed. For the vibrational MGMET-QCT model, the rotational temperature is assumed to be frozen at the translational temperature. The temperatures for both cases are shown in Fig. 6.9. The vibrational specific MGMET-QCT model matches very well with the vibrational temperature predicted by the DMS method. However, this is helped by the assumption of equilibrium between the rotational and translational temperatures. If this assumption were relaxed, the vibrational relaxation time predicted by the vibrational specific model would most likely become slower because the rotational mode would need to become excited first. Moreover, the assumption of equilibrium between rotation and translation is seen to breakdown particularly at higher temperatures, where the rotational temperature predicted by the DMS method only reaches 21 200 K.

Figure 6.10a shows the energy based MGMET-QCT group distribution during the relaxation process at 25 000 K. The group distribution is significantly different from the DMS data as it appears to be relaxing faster than the DMS data, as observed in the internal energy shown in Fig. 6.8b. In particular, the low energy groups which contain most of the internal energy show significantly

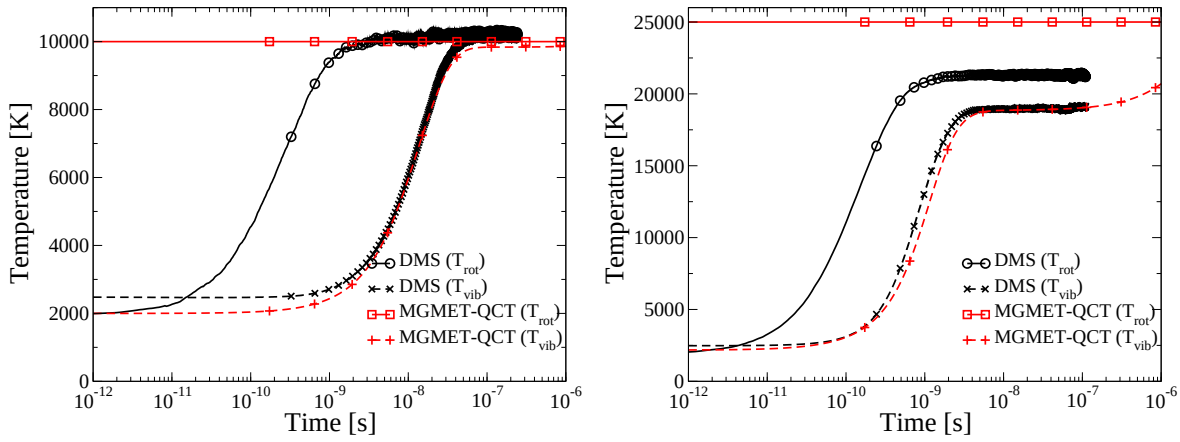

(a) T = 10 000 K. **(b)** T = 25 000 K.

Figure 6.9: Rotational and vibrational temperatures predicted from DMS versus vibrational based MGMET-QCT.

different behavior between the DMS and energy based binning data. A similar comparison for the vibrational binned data is shown in Fig. 6.10b, showing the vibrational distribution during the relaxation process at 25 000 K. In this case, the low energy vibrational states are in excellent agreement between the MGMET-QCT method and the DMS method. Although the agreement for the higher energy levels is not as good, the trend predicted by the two methods is similar, showing a bimodal distribution. Moreover, statistical noise is present in the high energy states from the DMS method. The agreement between the DMS method and the vibrational based MGMET-QCT method in predicting energy transfer is a result of the mode separation known to be present for low energy states. For low energy states ($v = 0, \ldots, 3$), which generally dictate the internal energy of the molecules, the separation of rotational and vibrational energy prevails, resulting in a strand structure in these states.

The vibrational relaxation time predicted by both the DMS method and vibrational specific MGMET-QCT model is shown in Fig. 6.11. At low temperatures, as seen in Fig. 6.9a, the vibrational relaxation time is well matched between the DMS method and the vibrational specific MGMET-QCT model. At higher temperature, the vibrational relaxation time predicted by the vibrational specific MGMET-QCT model is approximately 50% slower than the DMS method.

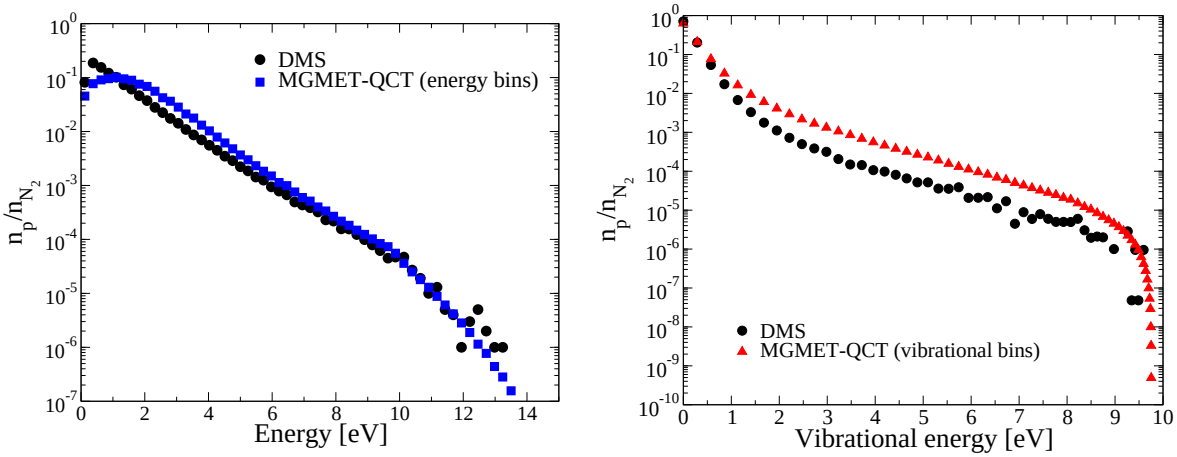

(a) Distribution of groups at 10^{-10} seconds from energy based groups.

(b) Distribution of groups at 10^{-10} seconds from vibrational based groups.

Figure 6.10: Transient distributions from MGMET-QCT and DMS methods at 25 000 K.

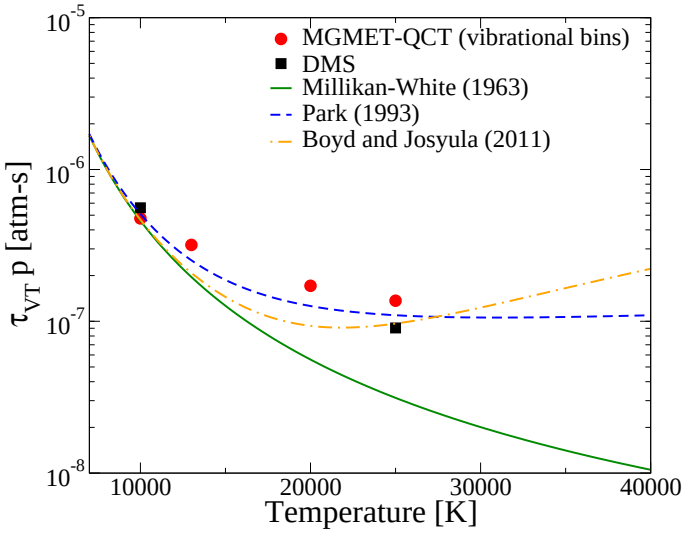

Figure 6.11: Vibrational relaxation parameter computed from DMS and MGMET-QCT methods compared with previous models. [7, 17, 142]

6.4 Discussion

This chapter presents an analysis of two grouping strategies used in the MGMET-QCT model compared to the DMS method for analyzing energy transfer and dissociation in an isothermal isochoric reactor. At the conditions studied, the energy transfer and dissociation processes are decoupled, with the gas relaxing to the QSS distribution and then dissociating from this state. Accurately describing these two different processes requires very different considerations. For the

energy transfer process, the low energy states are very important, as most of the internal energy is contained in approximately the first 2 eV. However, for dissociation the high energy states ($E_i \gtrsim 6$ eV) are crucial because they are most likely to dissociate and contribute significantly to the global dissociation rate.

6.4.1 Energy transfer

The vibrational specific MGMET-QCT model predicted the energy transfer process across the range of temperatures. This is because it captures well the vibrational strand structure caused by mode separation previously observed when studying the $N_2(X^1\Sigma_g^+) - N(^4S_u)$ system [115]. For low energy states, the states which share vibrational quantum numbers tend to equilibrium with each other; however, these strands are slower to equilibrate with each other. Initially, the energy transfer proceeds through a series of VT exchange reactions, which are significantly more efficient for vibrationally excited states. Therefore, the population of the high vibrational states is pumped up, creating a bi-modal distribution observed by Sharma *et al.* [136]. It was observed in Chapter 4 that initially the rate of excitation from the first few vibrational states is very slow, resulting in a significantly slower relaxation process than that predicted by the energy based MGMET-QCT method [116]. In contrast, the energy based MGMET-QCT model excitation reactions neglect all this information and excitation proceeds through a series of small energy jumps which occur very quickly. This is due to the lumping of different vibrational states together: the vibrational strand structure is lost, and all the states are assumed to equilibrate to some average temperature.

6.4.2 Dissociation

In contrast, the dissociation process in QSS is well captured across the range of temperatures by the energy based MGMET-QCT model. The dissociation process depends heavily on the accurate prediction of the high energy (including quasi-bound) states because molecules tend to climb to high energy states before dissociating. Therefore, grouping the high energy states considering only the energy (not the quantum configuration) results in accurate predictions of the dissociation process. In contrast, the vibrational specific MGMET-QCT model lumps states together across a large range of energies. As a result the high energy states are assumed to be in equilibrium

with low energy states. Because the dissociation behavior from the low and high energy states is very different, this averaging results in significant under-estimation of the dissociation from the low-v/high-J states. At high temperatures, because of the increased weight from these states, the exponential Boltzmann factor seems to take over, artificially enhancing the dissociation rate from the low-v states. Therefore, the vibrational grouped MGMET-QCT model cannot accurately account for dissociation as the energy grouped MGMET-QCT model can.

6.5 Summary

This chapter presents a detailed comparison between the two grouping strategies described in Chapter 4 and the DMS method. Using the MGMET-QCT method we simulate a zero-dimensional isothermal and isochoric heat bath. The comparison confirms the findings from Chapter 4 about the behavior of the distribution during the energy transfer and dissociation processes. It is seen that the vibrational MGMET-QCT method captures the vibrational relaxation process, but fails to accurately reproduce the dissociation process. In contrast, the energy based MGMET-QCT method accurately predicts the dissociation process, but predicts significantly faster excitation.

Chapter 7

Application to Computational Fluid Dynamics

In this chapter, the MGMET-QCT model is applied to several example CFD test cases. The objective is to demonstrate the applicability of the model in a variety of flow regimes, including both dissociating and recombining regimes. This is accomplished using a simple energy based binning approach. Future work will focus on using a spectral binning approach developed by Sahai *et al.* [115] to model more complex flows and study the flow physics. The focus of this chapter is to provide a proof-of-concept of the MGMET-QCT model in a variety of flow scenarios. Results for two different flowfields will be presented: the flow behind a standing normal shock wave, and the flow through a quasi-one-dimensional nozzle. This chapter is organized as follows: in Section 7.1 a standing normal shock wave test case is presented. In Section 7.2 the quasi-one-dimensional flow through a nozzle is presented. Finally, Section 7.3 summarizes the chapter.

7.1 Standing normal shock

The first test case presented is the flow behind a standing normal shock. The behavior of this flow is similar to the flow along the stagnation line in front a vehicle. This is a good test cast to evaluate the MGMET model because it has significant non-equilibrium and can be used to test the model in dissociating conditions.

7.1.1 Governing equations

The governing equations for a standing normal shock can be derived from the full set of governing equations from Chapter 2 by assuming the flow is one-dimensional and steady. For a mixture of nitrogen atoms and molecules, in which the molecules are modeled using the MGMET approach,

the governing equations read:

$$\frac{\partial}{\partial x}\left(\rho_{\mathrm{N}} u\right) = \dot{\omega}_{\mathrm{N}} \tag{7.1}$$

$$\frac{\partial}{\partial x}\left(\rho_{\mathrm{N}_{2_p}} u\right) = \dot{\omega}_{\mathrm{N}_{2_p}}, \quad p \in \mathrm{N}_2 \tag{7.2}$$

$$\frac{\partial}{\partial x}\left(\rho u^2 + p\right) = 0 \tag{7.3}$$

$$\frac{\partial}{\partial x}\left(\rho h u\right) = 0 \tag{7.4}$$

The mass source terms, $\dot{\omega}_{\mathrm{N}}$ and $\dot{\omega}_{\mathrm{N}_{2_p}}$ are the same as those specified in Chapter 2. Given freestream conditions, the post-shock values are computed using the Rankine-Hugoniot jump conditions, assuming the composition of the flow remains frozen across the shock. The MGMET model assumes that the bin internal temperature equilibrates instantaneously with the translational mode. As a result, when the translational temperature jumps across the shock, this in turn "excites" the groups. Therefore, the post-shock conditions need to be adjusted by accounting for conservation of energy. This results in a lower post-shock temperature than for example a rovibrational StS simulation. The freestream conditions are initialized to a pressure of 13.33 Pa, internal temperature of 300 K, and velocity of 10 km/s. The gas composition is initialized to 2.8% $\mathrm{N}(^4\mathrm{S_u})$ and 97.2% $\mathrm{N_2}(\mathrm{X}^1\Sigma_\mathrm{g}^+)$. A uniform width energy binning strategy is used here, comprised of 10 bound bins and 5 quasi-bound bins. Therefore, the kinetic data is re-grouped from Chapter 4 using the procedure detailed in Appendix F.

7.1.2 Macroscopic properties

The macroscopic properties (temperature, composition, and local dissociation rate) are compared in this section. Three cases are considered: one with only N3 reactions, one with only N4 reactions, and one with N3 and N4 reactions. Figure 7.1a shows the internal and translational temperatures, and Fig. 7.1b shows the mole fraction of atomic nitrogen for these three cases. The internal temperature is calculated by first unpacking the bin distributions and then solving for the internal temperature which contains the same internal energy as the non-equilibrium distribution. In all cases, the translational temperature starts at around 45 000 K, calculated from the jump conditions, while the internal temperature is frozen. It is important to note that the internal temperature

immediately behind the shock wave is no longer 300 K because the bin internal temperature is also heated to the translational temperature due to the assumption of thermal equilibrium between the translational mode and bin internal temperatures. Therefore, this energy is removed from the translational mode across the shock, lowering the post-shock temperature, and raising the $N_2(X^1\Sigma_g^+)$ internal temperature. Behind the shock wave, when only N3 reactions are considered, the relaxation occurs much slower, with the internal temperature reaching its peak 3 mm behind the shock wave, compared with reaching the peak 1 mm behind the shock when N4 reactions are considered. This is due to the small amount of atomic nitrogen available initially for reaction. However, when N3 reactions are considered, the rate of dissociation is significantly faster.

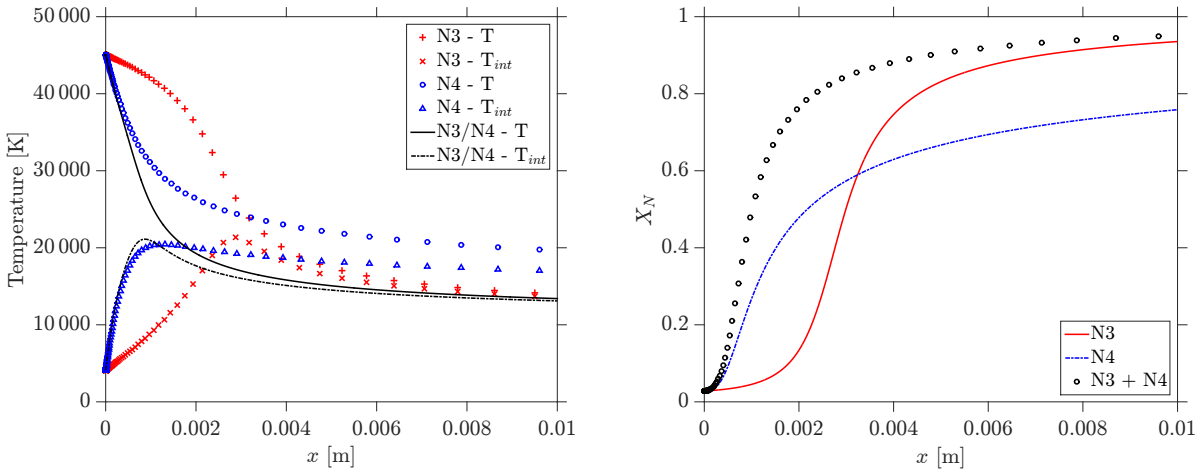

(a) Internal and translational temperatures. **(b)** Mole fraction of atomic nitrogen.

Figure 7.1: Macroscopic properties behind standing normal shock wave considered N3, N4, and N3 + N4 reactions.

To understand the non-equilibrium dissociation process, the local dissociation rates for the N3 and N4 systems are calculated as:

$$K_D^{\mathrm{N3}} = \sum_{p \in \mathrm{N_2}} {}^0K_p \frac{n_p}{n_{\mathrm{N_2}}} \tag{7.5}$$

$$K_D^{\mathrm{N4}} = \sum_{p \in \mathrm{N_2}} \sum_{q \in \mathrm{N_2}} \sum_{r \in \mathrm{N_2}} {}^0K_{pq,r} \frac{n_p}{n_{\mathrm{N_2}}} \frac{n_q}{n_{\mathrm{N_2}}} \tag{7.6}$$

These can be computed at each location behind the shock wave to determine the rate at which dissociation is occurring at each location behind the shock. It is also useful in the case in which

both processes are considered to calculate the relative contribution to dissociation from N3 and N4 processes, $\frac{\dot{\omega}^D_{\mathrm{N3}}}{\dot{\omega}^D}$ and $\frac{\dot{\omega}^D_{\mathrm{N4}}}{\dot{\omega}^D}$ respectively. These are computed from the source terms:

$$\dot{\omega}^D_{\mathrm{N3}} = \sum_{p \in \mathrm{N}_2} {}^0K_p n_p n_N \tag{7.7}$$

$$\dot{\omega}^D_{\mathrm{N4}} = \sum_{p \in \mathrm{N}_2} \sum_{q \in \mathrm{N}_2} \sum_{r \in \mathrm{N}_2} {}^0K_{pq,r} n_p n_q \tag{7.8}$$

$$\dot{\omega}^D = \dot{\omega}^D_{\mathrm{N3}} + \dot{\omega}^D_{\mathrm{N4}} \tag{7.9}$$

Figure 7.2a shows the composition and local dissociation rate for the N3 and N4 only test cases. From this, it is clear that throughout the non-equilibrium region (when the translational temperature and internal temperature are different), the dissociation rate due to N3 reactions is much higher. Further downstream it drops below the N4 dissociation rate, but this is most likely due to the decrease in temperature downstream. In Fig. 7.2b, the contribution to the source term for nitrogen atoms due to dissociation is plotted along with the composition as a function of distance behind the shock wave for the combined N3/N4 case. Initially, the N4 dissociation reactions contribute to about 80% of the mass source term. However, this rapidly drops off, and dissociation by atomic nitrogen prevails, contributing to most of the dissociation.

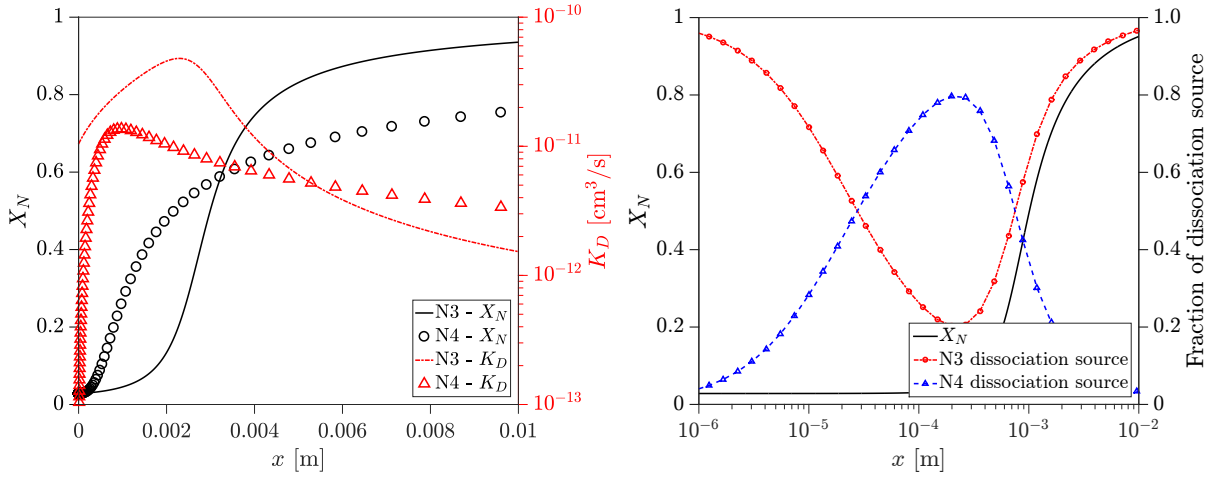

(a) Separate N3 and N4 local dissociation rates and compositions.

(b) Combined N3/N4 composition and contribution to dissociation source term from N3 and N4 reactions.

Figure 7.2: Macroscopic properties behind standing normal shock wave considered N3, N4, and N3 + N4 reactions.

7.1.3 Microscopic properties

The advantage of using the MGME method is that it allows for the modeling of non-Boltzmann effects in the distribution. This provides information about the microscopic distribution of states. Therefore, the distribution of groups is plotted in Fig. 7.3 at various locations behind the shock wave. In order to understand the degree of non-equilibrium, the two-temperature equilibrium distribution corresponding to the translational and internal temperatures is also shown in lines. For the N3 only reactions, initially the distribution shows overpopulation in the tail of the distribution, corresponding to the excitation process, which is enhanced when considering N3 reactions due to the rapid exchange pathways available. This overpopulation of the tail persists until around 3 mm behind the shock wave, when the dissociation process takes over and depletes the tail. In the N4 only simulation, the onset of dissociation occurs almost immediately, and all the distributions included show distinct depletion of the tail as the dissociation occurs mainly from those groups, as observed in Chapters 4 and 6. Finally, when both systems are considered for reaction, the evolution of states is similar to that observed in N4. However, because all processes are considered and the N3 dissociation process occurs faster, the distribution reaches equilibrium much faster.

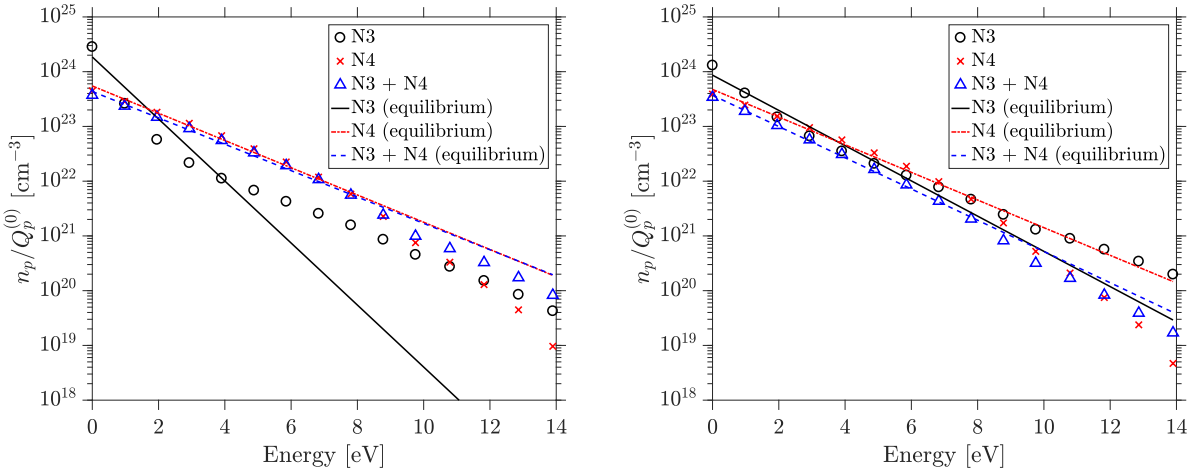

(a) $x = 0.001$ m. **(b)** $x = 0.002$ m.

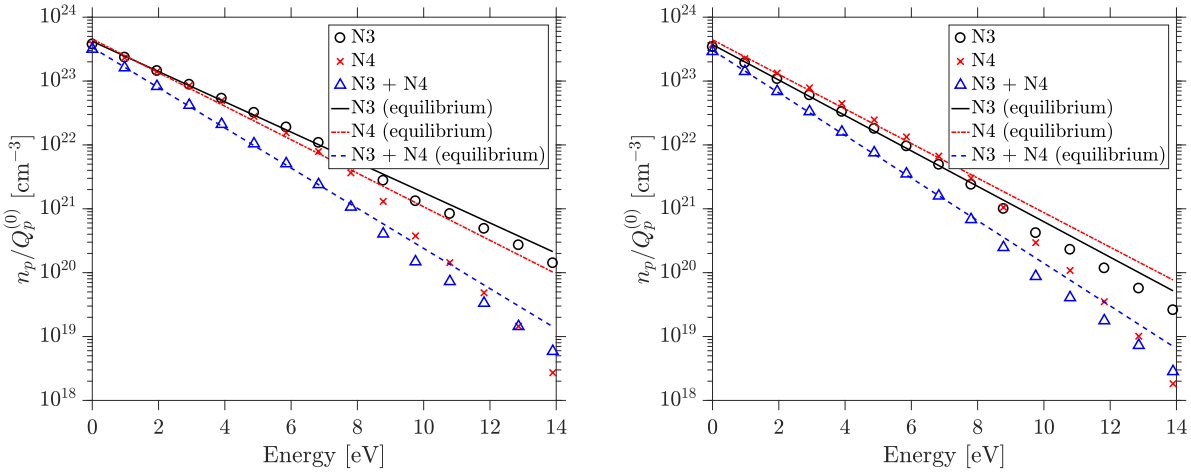

(c) $x = 0.003$ m. **(d)** $x = 0.004$ m.

Figure 7.3: Local distribution at various locations past the shock wave; symbols indicate the actual distribution, and lines indicate the distribution corresponding to the calculated translational and internal temperatures.

7.2 Quasi one-dimensional nozzle

7.2.1 Governing equations

The governing equations for a quasi-one-dimensional nozzle can be derived from the full set of governing equations from Chapter 2 by assuming the area change is given by the function $A = A(x)$. For a mixture of nitrogen atoms and molecules, in which the molecules are modeled using the

MGMET approach, the governing equations read:

$$\frac{\partial}{\partial t}\left(\rho_{\mathrm{N}} A\right)+\frac{\partial}{\partial x}\left(\rho_{\mathrm{N}} u A\right)=\dot{\omega}_{\mathrm{N}} A \tag{7.10}$$

$$\frac{\partial}{\partial t}\left(\rho_{\mathrm{N}_{2_p}} A\right)+\frac{\partial}{\partial x}\left(\rho_{\mathrm{N}_{2_p}} u A\right)=\dot{\omega}_{\mathrm{N}_{2_p}} A, \quad p \in \mathrm{N}_2 \tag{7.11}$$

$$\frac{\partial}{\partial t}\left(\rho u A\right)+\frac{\partial}{\partial x}\left[\left(\rho u^2+p\right) A\right]=\frac{p}{A}\frac{\partial A}{\partial x} \tag{7.12}$$

$$\frac{\partial}{\partial t}\left(\rho e A\right)+\frac{\partial}{\partial x}\left(\rho h u A\right)=0 \tag{7.13}$$

As in the previous section, the mass source terms are the same as those specified in Chapter 2. The inlet conditions for the nozzle are specified, and the flow time integrated to reach steady state. Results reported in this section are taken from the steady-state nozzle solution. Further details on the temporal and spatial integration of these equations can be found in Ref. [148]. The inlet conditions are taken to be at a pressure of 101 325 Pa and a temperature of 10 000 K. The inlet composition is set to 99.3% nitrogen atoms and 0.7% nitrogen molecules. The same 15 energy based grouping strategy as described in the previous section is used.

In this section, two nozzle geometries are analyzed: the Electric Arc Shock Tube (EAST) nozzle at NASA Ames Research Center, and the F4 nozzle from the Hot Shot wind tunnel at ONERA in France. These were selected based on the work of Munafò [148]. The area profile of each nozzle is shown in Fig. 7.4, along with the location of points at which the distribution will be extracted in later sections.

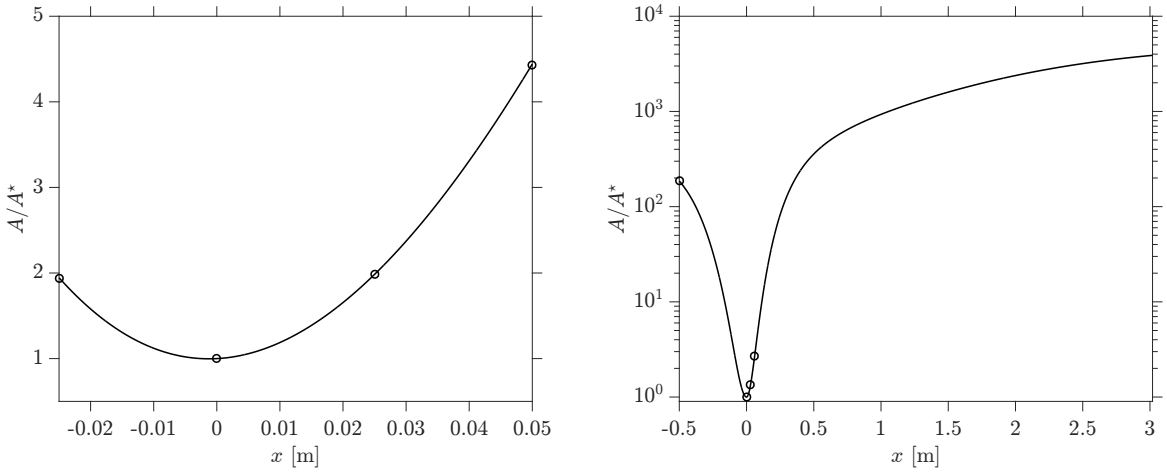

(a) EAST nozzle area profile.

(b) F4 nozzle area profile.

Figure 7.4: Nozzle geometries.

7.2.2 Electric arc shock tube nozzle

The mole fraction of molecular nitrogen and temperatures are throughout the EAST nozzle are shown in Fig. 7.5. Throughout the nozzle, the nitrogen atoms recombine to form molecules, and the temperature drops. In contrast to what was observed in the shock flows, there is nearly no difference between the N3 only and the combined N3 and N4 simulation. This is most likely due to the low concentration of nitrogen molecules present initially. Moreover, while there is some recombination, the overall concentration of nitrogen molecules never exceeds 1%. The temperatures also appear to remain in equilibrium with each other throughout the nozzle.

The group distribution throughout the nozzle is shown in Fig. 7.6. At the inlet the molecules are populated according to a Boltzmann distribution at 10 000 K. However, as the molecules recombine, the population of the mid-range energy states is pumped up. Just as dissociation occurs from the tail of the distribution, the molecules recombine into high energy states and then relax to low energy states. Moreover, while the internal temperature appeared to be in equilibrium with the translational temperature throughout the nozzle, the distribution of groups shows that there are non-equilibrium effects which result in overpopulation of the high-energy states.

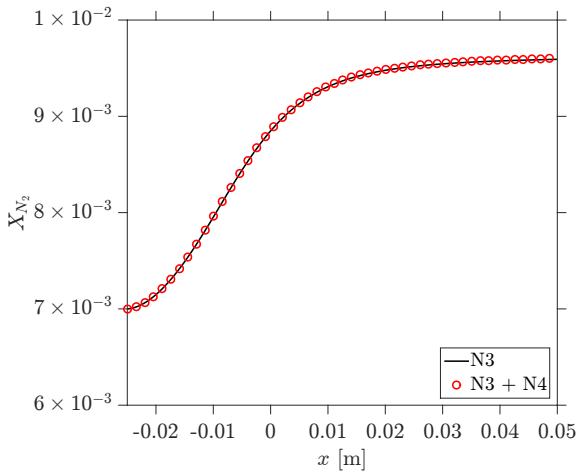

(a) Mole fraction of molecular nitrogen.

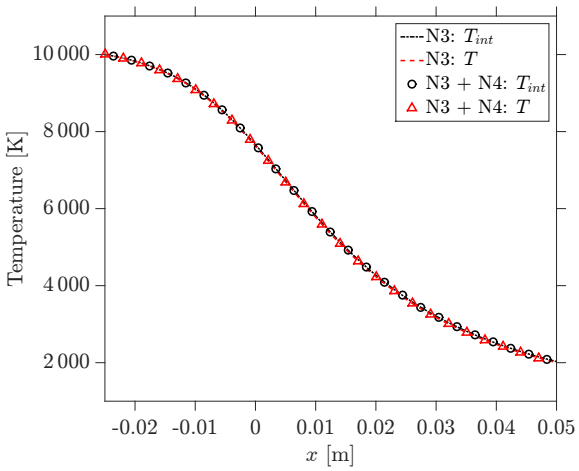

(b) Internal and translational temperatures.

Figure 7.5: Macroscopic properties throughout the EAST nozzle.

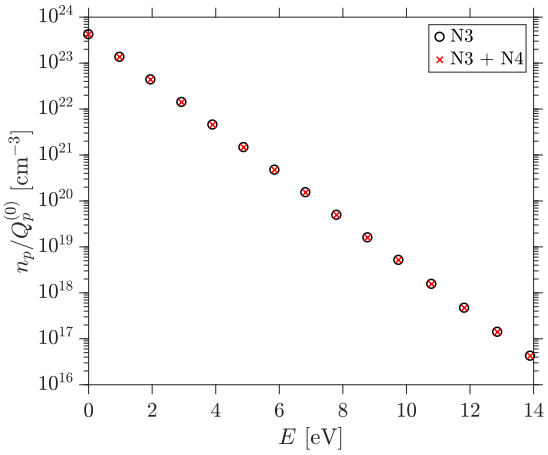

(a) $x = -2.5 \times 10^{-2}$ m (inlet).

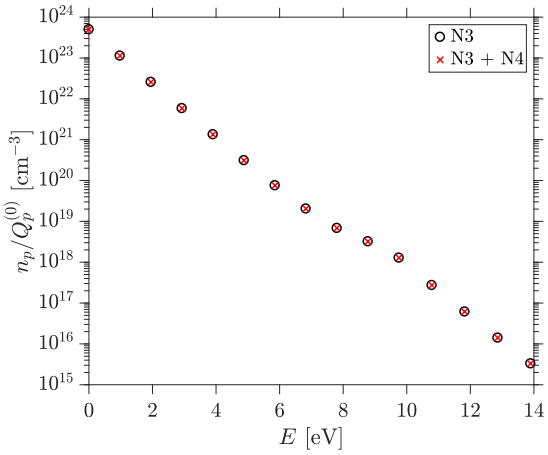

(b) $x = 0$ m (throat).

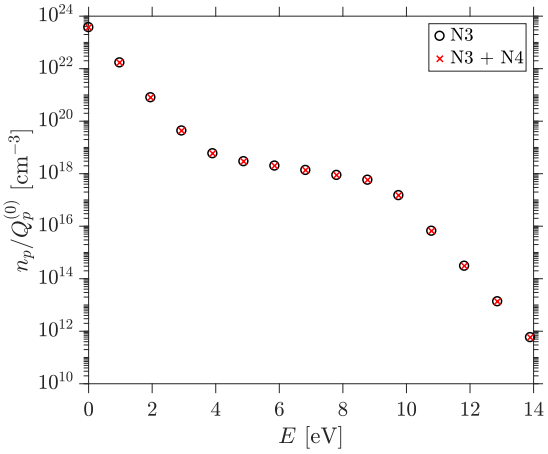

(c) $x = 2.5 \times 10^{-2}$ m.

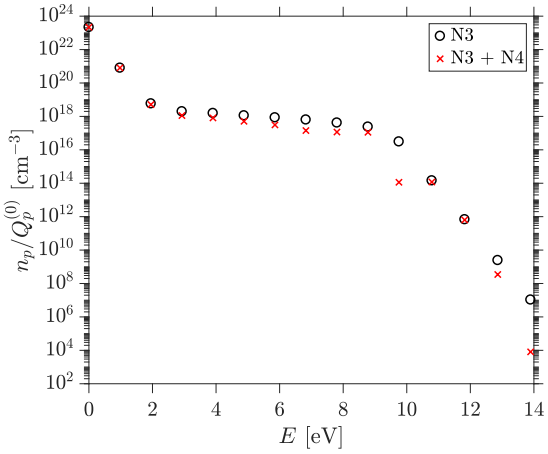

(d) $x = 5 \times 10^{-2}$ m (outlet).

Figure 7.6: Distribution of groups within the EAST nozzle.

7.2.3 F4 Nozzle

A similar analysis is shown for the F4 nozzle. While the EAST nozzle is fairly smooth, and the minimum temperature is approximately 2000 K, the F4 nozzle is much more aggressive. The temperature in the nozzle, shown in Fig. 7.7b, reaches approximately 20 K. At these low temperatures the rates are purely extrapolated and unlikely to be accurate. Therefore, this case is only included for demonstration of the properties throughout the nozzle. The composition and temperature behavior are similar to what was observed for the EAST nozzle, with the inclusion of N4 reactions having little influence on the results and the temperatures remaining approximately in equilibrium throughout the nozzle.

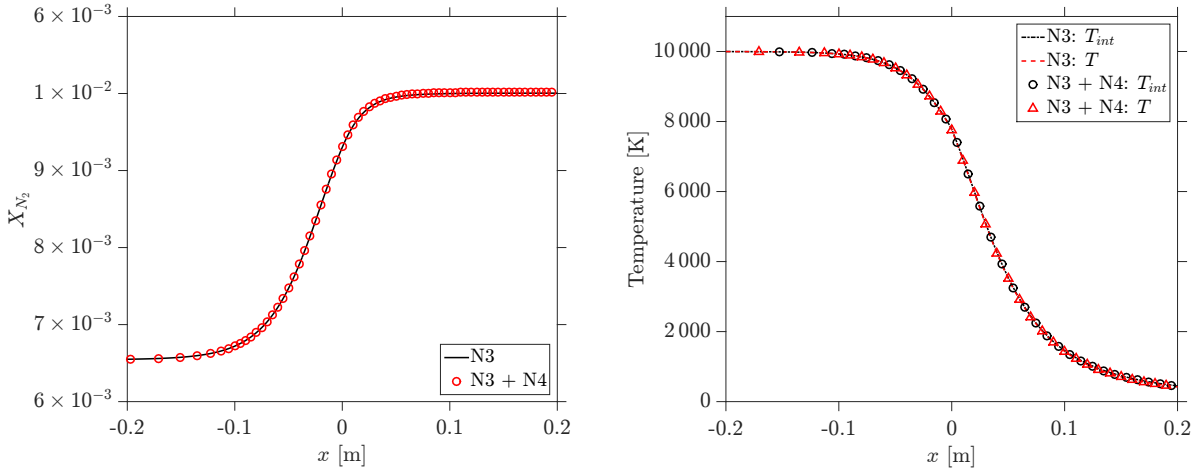

(a) Mole fraction of molecular nitrogen.

(b) Internal and translational temperatures.

Figure 7.7: Macroscopic properties throughout the F4 nozzle.

The distribution of groups for the F4 nozzle, shown in Fig. 7.8, have similar behavior to what was observed in the EAST nozzle. Again, the molecules tend to recombine into high-energy groups, and relax down to lower energy states. This pumps up the population of the high-energy states. The non-equilibrium is stronger in the F4 nozzle than the EAST nozzle due to the rapid expansion.

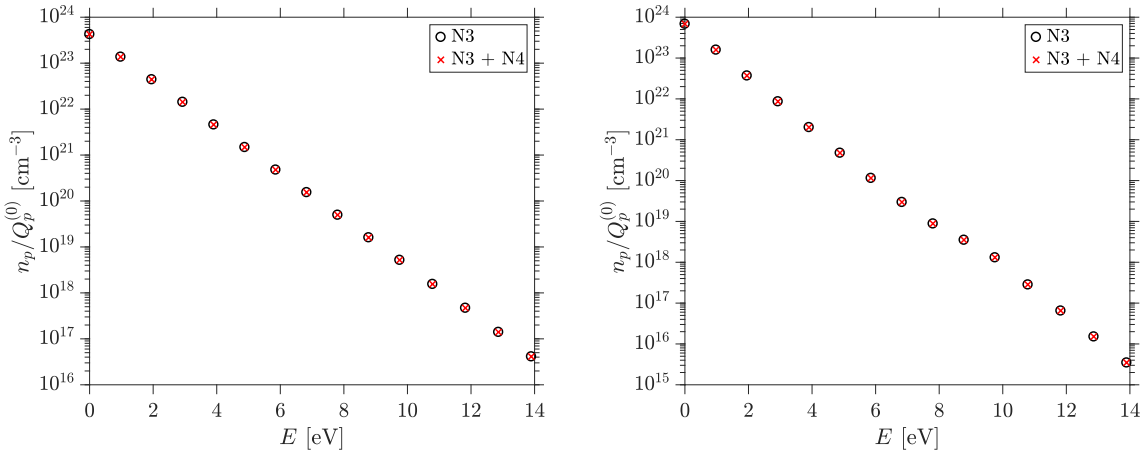

(a) $x = -0.5$ m (inlet). **(b)** $x = 0$ m (throat).

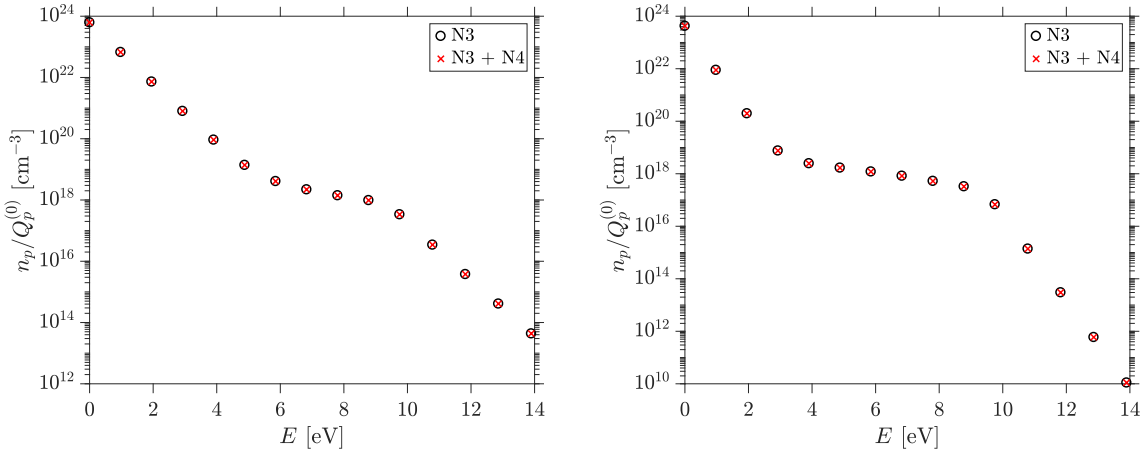

(c) $x = 0.03$ m. **(d)** $x = 0.06$ m.

Figure 7.8: Distribution of groups within the F4 nozzle.

7.3 Summary

This chapter presents the application of the MGMET-QCT method to two sample CFD calculations. The first, a standing normal shock wave, demonstrates the applicability of this approach to compressing or dissociating flowfields. Differences are observed in the simulations including and excluding the $N_2(X^1\Sigma_g^+) - N(^4S_u)$ and $N_2(X^1\Sigma_g^+) - N_2(X^1\Sigma_g^+)$ reactions. In particular, including the $N_2(X^1\Sigma_g^+) - N_2(X^1\Sigma_g^+)$ reactions pushes the onset of excitation and dissociation earlier, while including the $N_2(X^1\Sigma_g^+) - N(^4S_u)$ processes increases the rate of dissociation. Next, the MGMET-QCT model is applied to the flow through a quasi-one-dimensional nozzle. Although the degree of non-equilibrium is significantly less in this flowfield, the simulations demonstrate the ability of the MGMET-QCT method to capture the non-equilibrium distribution in a recombining flowfield.

Chapter 8

Summary and Future Work

8.1 Conclusions

The objective of this work is to provide a link between the *ab initio* PESs becoming available for species relevant to hypersonic air chemistry and the field of CFD. This is done by means of a reduced order model constructed using the maximum entropy principle. The MGME model is realized by lumping energy states assumed to equilibrate rapidly with each other into groups. Using a moment method, the grouped states are used to construct flow governing equations directly from the Boltzmann equation. Finally, using the distribution of states within the groups, QCT calculations are carried out to directly obtain kinetic data for the reduced-order model. The coupling of the MGME model with the QCT method is necessary to facilitate the application of the MGME model to systems with unknown StS kinetic data (*e.g.*, diatom-diatom systems such as N_2-N_2, O_2-O_2, and N_2-O_2). The advantage to the MGME model is that it can predict both macroscopic and microscopic properties with similar accuracy when compared with a full StS or DMS approach. However, the computational cost associated with the MGME model is drastically reduced when compared with a full StS or DMS approach. For the comparison presented in Chapter 6 the DMS simulation at 10 000 K took approximately 4 weeks 200 cores to run. The MGMET-QCT method required similar computational resources to construct the kinetic database. However, to run the zero-dimensional simulation took approximately 3 minutes to run on 1 core. Moreover, once the kinetic database is complete, it can be applied to a wide range of conditions. Finally, Sahai *et al.* [115] demonstrated that using as few as 15 bins predicted both microscopic and macroscopic properties of a full rovibrational StS model, which comprises nearly 10,000 states. The study was conducted using a zero-dimensional isothermal reactor simulation, an unrealistically harsh condition of non-equilibrium.

The MGMET model, in which the internal temperature of the bin is assumed to be in equilibrium with the translational mode, is used to study the non-equilibrium energy transfer and dissociation processes in a zero-dimensional isothermal heat bath. This is done using two grouping strategies: a conventional vibrational grouping strategy and an energy based grouping strategy. A comparison between macroscopic phenomenological properties revealed that the energy based grouping better captured the dissociation process, while the vibrational based grouping better predicted the energy transfer process. This finding was confirmed through comparison with the DMS method.

The MGMEL model accounts for variation in bin internal temperature in order to reduce the number of groups required. This is accomplished by invoking detailed balance at a microscopic level, and deriving group energy transfer rates from only trajectories in one direction (*i.e.*, exothermic or endothermic). This approach is demonstrated using the N_2-N system and compared with the grouped known StS kinetic data for the system. Using this framework, the number of groups required to capture both non-equilibrium dissociating and recombining processes can be reduced, while maintaining acceptable error.

Finally, the MGME thermal model is applied to several simple CFD simulations for demonstration. The test cases comprise the one-dimensional flow behind a normal shock wave, and the quasi-one-dimensional flow through a nozzle. This range of test cases is meant to demonstrate the flexibility of the MGME method as it can be applied in both dissociating and recombining regimes.

Through the detailed analysis of the MGMET model presented in Chapters 4 and 6, several important features of the non-equilibrium energy transfer and dissociation process were discovered. The comparison of the energy transfer relaxation rates, predicted by the vibrational grouping method, against available experimental data validates the classical picture of relaxation based on the rigid separation among the rotational and vibrational energy modes. It was found that the relaxation data provided by the Millikan and White correlation are in good agreement with the theoretical predictions provided by the vibrational grouping method for temperatures below 10 000 K. On the contrary, any attempt to ignore the mode separation by grouping rovibrational levels characterized by different vibrational quantum number leads to an overestimation of the relaxation rate. This finding was confirmed through comparison with DMS, where the internal energy excitation

predicted by the energy based grouping was significantly faster than that predicted by both DMS and vibrational bins. Moreover, while the MGMET vibrational binning approach can capture the vibrational excitation process, it cannot account for the rotational non-equilibrium which occurs at high temperatures.

In contrast, the dissociation process is controlled by the tail of the rovibrational distribution. For the high-lying states, the strong rovibrational coupling is well captured by the energy-based grouping. Molecules have to climb the rovibrational energy ladder before dissociating, thus acquiring significant vibrational and rotational energy. In all the cases analyzed, rotational energy accounts for more than 40% of the total energy required to dissociate the N_2 molecules. While vibrational bias is introduced in the conventional non-equilibrium models, no models include bias to account for the effect of rotational excitation of the molecules. When compared with the DMS method, it was found that while energy bins slightly over-predict the importance of rotational energy in dissociation (at 10 000 K, 40% predicted by MGMET energy bins compared with 35% predicted by the DMS method), vibrational bins vastly underpredict the importance of rotation in the dissociation process. At 10 000 K, vibrational bins predict a mere 10% of the energy lost in dissociation comes from the rotational mode. This is most likely due to the damping out of the highly excited rotational energy states when the group average rate is computed. Finally, it is important to note that during the dissociation process, the distribution of the N_2 molecules is in QSS. This is very different from what is observed in the N_2-N case, where a significant part of the dissociation takes place in non-QSS conditions.

8.2 Future work

This work represents a paradigm shift in the approach to the modeling of non-equilibrium flows: a multitude of previous work has built upon the same framework or governing equations. In this work, we start from the Boltzmann equation to construct governing equations, affording us a clear understanding of the assumptions and regime of validity. However, there is still work required to not only complete the MGME model, but also extend this approach to other species and systems of interest to chemistry in hypersonic flows.

One future avenue for research comprises using the Chapman-Enskog method to derive a full

set of Navier-Stokes equations for the MGME model. This will introduce the transport coefficients, such as thermal conductivity and viscosity, in terms of the microscopic properties (*i.e.*, velocity and internal energy states). This requires the definition of collisional invariants which are for the first time provided in Chapter 2. In addition, extending the MGME-QCT model to the other chemical systems relevant to air chemistry with *ab initio* PES data is necessary to construct a complete non-equilibrium chemistry model for air.

One limitation which currently exists in the MGME-QCT framework is the fact that the grouping needs to be prescribed *a priori*. However, it has been shown that the grouping strategy has a profound impact on the results. Therefore, it would be advantageous to couple the determination of the groups with the QCT calculations. This would allow the optimal grouping strategy to be determined on the fly while computing kinetic data. Moreover, it may elucidate the most important physical processes for the establishment of equilibrium for various systems.

Finally, while this work focused on addressing the problem of internal energy non-equilibrium, the grouping approach can also be applied to translational non-equilibrium. The foundation for the extension of MGME model to translational non-equilibrium was presented by Jayaraman *et al.* [149], making use of a simple Bhatnagar-Gross-Krook (BGK) collision operator. However, future work will focus on providing a unified theory for both translational and internal energy non-equilibrium. This would help extend the realm of applicability of continuum approaches into the transitional regime.

Appendix A

Transformation to Center of Mass Reference Frame

A.1 Elastic collision integral

The relationship between the relative and center-of-mass velocities is given by the following relationships:

$$\mathbf{g} = \mathbf{c}_\mathrm{A} - \mathbf{c}_\mathrm{B}, \qquad \mathbf{g}' = \mathbf{c}'_\mathrm{A} - \mathbf{c}'_\mathrm{B} \tag{A.1}$$

$$\mathbf{G} = \frac{m_\mathrm{A}\mathbf{c}_\mathrm{A} + m_\mathrm{B}\mathbf{c}_\mathrm{B}}{m_\mathrm{A} + m_\mathrm{B}}, \qquad \mathbf{G}' = \frac{m_\mathrm{A}\mathbf{c}'_\mathrm{A} + m_\mathrm{B}\mathbf{c}'_\mathrm{B}}{m_\mathrm{A} + m_\mathrm{B}} \tag{A.2}$$

The conservation of momentum and energy relations in the center of mass reference frame yield the following relations:

$$\mathbf{G} = \mathbf{G}', \quad g^2 = g'^2 \tag{A.3}$$

Therefore, we find that the following relationship for the differentials hold:

$$\mathrm{d}\mathbf{G} = \mathrm{d}\mathbf{G}', \quad g\,\mathrm{d}g = g'\,\mathrm{d}g' \tag{A.4}$$

These relations are used in the derivation of the relationship between the cross-sections for forward and reverse processes.

A.2 Inelastic collision integral

For the inelastic collision integral, again the center-of-mass coordinates can be specified as:

$$\mathbf{g} = \mathbf{c}_\mathrm{A} - \mathbf{c}_\mathrm{B}, \qquad \mathbf{g}' = \mathbf{c}'_\mathrm{A} - \mathbf{c}'_\mathrm{B} \tag{A.5}$$

$$\mathbf{G} = \frac{m_\mathrm{A}\mathbf{c}_\mathrm{A} + m_\mathrm{B}\mathbf{c}_\mathrm{B}}{m_\mathrm{A} + m_\mathrm{B}}, \qquad \mathbf{G}' = \frac{m_\mathrm{A}\mathbf{c}'_\mathrm{A} + m_\mathrm{B}\mathbf{c}'_\mathrm{B}}{m_\mathrm{A} + m_\mathrm{B}} \tag{A.6}$$

The conservation of momentum and energy relations in the center of mass reference frame yield the following relations:

$$\mathbf{G} = \mathbf{G}' \tag{A.7}$$

$$\frac{\mu_\mathrm{AB}}{2} g^2 + E_{\mathrm{A}_i} + E_{\mathrm{B}_j} = \frac{\mu_\mathrm{AB}}{2} g'^2 + E_{\mathrm{A}_k} + E_{\mathrm{B}_l} \tag{A.8}$$

Therefore, the following differential relations hold:

$$\mathrm{d}\,\mathbf{G} = \mathrm{d}\,\mathbf{G}' \tag{A.9}$$

$$\mu_\mathrm{AB} g \,\mathrm{d}g = \mu_\mathrm{AB} g' \,\mathrm{d}g' \tag{A.10}$$

Using this transformation along with the definition of the cross-section, the micro-reversibility condition reads:

$$\beta_{\mathrm{A}_k}\beta_{\mathrm{B}_l}\sigma^{\mathrm{A}_k\mathrm{B}_l}_{\mathrm{A}_i\mathrm{B}_j}(g, \boldsymbol{\omega'}) g^3 \,\mathrm{d}\boldsymbol{\omega'}\,\mathrm{d}g\,\mathrm{d}\boldsymbol{\omega}\,\mathrm{d}\mathbf{G} = \beta_{\mathrm{A}_i}\beta_{\mathrm{B}_j}\sigma^{\mathrm{A}_i\mathrm{B}_j}_{\mathrm{A}_k\mathrm{B}_l}(g', \boldsymbol{\omega}) g'^3 \,\mathrm{d}\boldsymbol{\omega}\,\mathrm{d}g'\,\mathrm{d}\boldsymbol{\omega'}\,\mathrm{d}\mathbf{G}' \tag{A.11}$$

This is re-arranged to yield expression 2.11.

A.3 Exchange collision integral

For the exchange collision integral, again the center-of-mass coordinates can be specified as:

$$\mathbf{g} = \mathbf{c}_\mathrm{A} - \mathbf{c}_\mathrm{B}, \qquad \mathbf{g}' = \mathbf{c}'_\mathrm{C} - \mathbf{c}'_\mathrm{D} \tag{A.12}$$

$$\mathbf{G} = \frac{m_\mathrm{A}\mathbf{c}_\mathrm{A} + m_\mathrm{B}\mathbf{c}_\mathrm{B}}{m_\mathrm{A} + m_\mathrm{B}}, \qquad \mathbf{G}' = \frac{m_\mathrm{C}\mathbf{c}'_\mathrm{C} + m_\mathrm{D}\mathbf{c}'_\mathrm{D}}{m_\mathrm{C} + m_\mathrm{D}} \tag{A.13}$$

The conservation of mass, momentum, and energy relations in the center of mass reference frame yield the following relations:

$$m_{\mathrm{A}} + m_{\mathrm{B}} = m_{\mathrm{C}} + m_{\mathrm{D}} \tag{A.14}$$

$$\mathbf{G} = \mathbf{G}' \tag{A.15}$$

$$\frac{\mu_{\mathrm{AB}}}{2} g^2 + E_{\mathrm{A}_i} + E_{\mathrm{B}_j} = \frac{\mu_{\mathrm{CD}}}{2} g'^2 + E_{\mathrm{C}_k} + E_{\mathrm{D}_l} \tag{A.16}$$

Therefore, the following differential relations hold:

$$\mathrm{d}\,\mathbf{G} = \mathrm{d}\,\mathbf{G}' \tag{A.17}$$

$$\mu_{\mathrm{AB}} g \,\mathrm{d}g = \mu_{\mathrm{CD}} g' \,\mathrm{d}g' \tag{A.18}$$

Using this transformation along with the definition of the cross-section, the micro-reversibility condition reads:

$$\beta_{\mathrm{C}_k} \beta_{\mathrm{D}_l} \sigma^{\mathrm{C}_k \mathrm{D}_l}_{\mathrm{A}_i \mathrm{B}_j}(g, \boldsymbol{\omega'}) g^3 \,\mathrm{d}\boldsymbol{\omega'} \,\mathrm{d}g \,\mathrm{d}\boldsymbol{\omega} \,\mathrm{d}\mathbf{G} = \beta_{\mathrm{A}_i} \beta_{\mathrm{B}_j} \sigma^{\mathrm{A}_i \mathrm{B}_j}_{\mathrm{C}_k \mathrm{D}_l}(g', \boldsymbol{\omega}) g'^3 \,\mathrm{d}\boldsymbol{\omega} \,\mathrm{d}g' \,\mathrm{d}\boldsymbol{\omega'} \,\mathrm{d}\mathbf{G}' \tag{A.19}$$

This is re-arranged to yield expression 2.15.

Appendix B

Boltzmann H-Theorem

B.1 Kinetic entropy conservation equation

To derive the kinetic entropy conservation equation, the Boltzmann equation is multiplied by $\ln(\beta_{\mathrm{A}_i} f_{\mathrm{A}_i})$ and integrated over all velocity space. The first term can be re-arranged to yield:

$$\begin{aligned}\sum_{\mathrm{A}\in\mathcal{S}}\sum_{i\in\mathcal{I}_{\mathrm{A}}}\int_{\mathbb{R}^3}\ln(\beta_{\mathrm{A}_i} f_{\mathrm{A}_i})\frac{\partial f_{\mathrm{A}_i}}{\partial t}\,\mathrm{d}\mathbf{c}_{\mathrm{A}} &= \sum_{\mathrm{A}\in\mathcal{S}}\sum_{i\in\mathcal{I}_{\mathrm{A}}}\int_{\mathbb{R}^3}\left[\frac{\partial}{\partial t}\left(f_{\mathrm{A}_i}\ln(\beta_{\mathrm{A}_i} f_{\mathrm{A}_i})\right) - f_{\mathrm{A}_i}\frac{\partial}{\partial t}\left(\ln(\beta_{\mathrm{A}_i} f_{\mathrm{A}_i})\right)\right]\mathrm{d}\mathbf{c}_{\mathrm{A}} \\ &= \sum_{\mathrm{A}\in\mathcal{S}}\sum_{i\in\mathcal{I}_{\mathrm{A}}}\int_{\mathbb{R}^3}\left[\frac{\partial}{\partial t}\left(f_{\mathrm{A}_i}\ln(\beta_{\mathrm{A}_i} f_{\mathrm{A}_i})\right) - \frac{\partial f_{\mathrm{A}_i}}{\partial t}\right]\mathrm{d}\mathbf{c}_{\mathrm{A}} \\ &= \frac{\partial}{\partial t}\left[\sum_{\mathrm{A}\in\mathcal{S}}\sum_{i\in\mathcal{I}_{\mathrm{A}}}\int_{\mathbb{R}^3} f_{\mathrm{A}_i}(\ln(\beta_{\mathrm{A}_i} f_{\mathrm{A}_i}) - 1)\,\mathrm{d}\mathbf{c}_{\mathrm{A}}\right] = \frac{\partial S^{\mathrm{kin}}}{\partial t}\end{aligned} \tag{B.1}$$

The second term can be re-written:

$$\begin{aligned}&\sum_{\mathrm{A}\in\mathcal{S}}\sum_{i\in\mathcal{I}_{\mathrm{A}}}\int_{\mathbb{R}^3}\ln(\beta_{\mathrm{A}_i} f_{\mathrm{A}_i})\mathbf{c}_{\mathrm{A}}\cdot\nabla_{\mathbf{x}} f_{\mathrm{A}_i}\,\mathrm{d}\mathbf{c}_{\mathrm{A}} \\ &\quad= \sum_{\mathrm{A}\in\mathcal{S}}\sum_{i\in\mathcal{I}_{\mathrm{A}}}\int_{\mathbb{R}^3}\left[\mathbf{c}_{\mathrm{A}}\cdot\nabla_{\mathbf{x}}\left(f_{\mathrm{A}_i}\ln(\beta_{\mathrm{A}_i} f_{\mathrm{A}_i})\right) - f_{\mathrm{A}_i}\mathbf{c}_{\mathrm{A}}\cdot\nabla_{\mathbf{x}}\left(\ln(\beta_{\mathrm{A}_i} f_{\mathrm{A}_i})\right)\right]\mathrm{d}\mathbf{c}_{\mathrm{A}} \\ &\quad= \sum_{\mathrm{A}\in\mathcal{S}}\sum_{i\in\mathcal{I}_{\mathrm{A}}}\int_{\mathbb{R}^3}\left[\mathbf{c}_{\mathrm{A}}\cdot\nabla_{\mathbf{x}}\left(f_{\mathrm{A}_i}\ln(\beta_{\mathrm{A}_i} f_{\mathrm{A}_i})\right) - \mathbf{c}_{\mathrm{A}}\cdot\nabla_{\mathbf{x}}\left(f_{\mathrm{A}_i}\right)\right]\mathrm{d}\mathbf{c}_{\mathrm{A}} \\ &\quad= \sum_{\mathrm{A}\in\mathcal{S}}\sum_{i\in\mathcal{I}_{\mathrm{A}}}\int_{\mathbb{R}^3}\left[\mathbf{c}_{\mathrm{A}}\cdot\nabla_{\mathbf{x}}\left(f_{\mathrm{A}_i}\left(\ln(\beta_{\mathrm{A}_i} f_{\mathrm{A}_i})\right) - 1\right)\right]\mathrm{d}\mathbf{c}_{\mathrm{A}}\end{aligned} \tag{B.2}$$

Using these two expressions along with the definition of the entropy source term given in Chapter 2, the kinetic entropy conservation equation is given in Eq. (2.36).

B.2 Proof of positivity of entropy production

The "fast" (intra-group inelastic scattering) entropy source term reads:

$$\mathfrak{v}^S_{\mathrm{A}_p} = -\mathrm{k_B} \sum_{\mathrm{B}\in\mathcal{S}} \sum_{q\in\mathrm{B}} \sum_{(i,k)\in\mathcal{I}_p} \sum_{(j,l)\in\mathcal{I}_q} \iiiint\limits_{\substack{\mathbb{R}^3\times\mathbb{R}^3\\ \times\mathbb{R}^3\times\mathbb{R}^3}} \left(\frac{\beta_{\mathrm{A}_k}\beta_{\mathrm{B}_l}}{\beta_{\mathrm{A}_i}\beta_{\mathrm{B}_j}} f'_{\mathrm{A}_k} f'_{\mathrm{B}_l} - f_{\mathrm{A}_i} f_{\mathrm{B}_j} \right) \times W^{\mathrm{A}'_k\mathrm{B}'_l}_{\mathrm{A}_i\mathrm{B}_j} \ln\left(\beta_{\mathrm{A}_i} f_{\mathrm{A}_i}\right) \mathrm{d}\mathbf{c}_\mathrm{A}\, \mathrm{d}\mathbf{c}_\mathrm{B}\, \mathrm{d}\mathbf{c}'_\mathrm{A}\, \mathrm{d}\mathbf{c}'_\mathrm{B} \tag{B.3}$$

Because the velocities $\mathbf{c}_{\mathrm{A}_i}$ and $\mathbf{c}_{\mathrm{B}_j}$ are both integrated over the entire velocity space, swapping these velocities will not change the resulting integral:

$$\begin{aligned} &\sum_{\mathrm{B}\in\mathcal{S}} \sum_{q\in\mathrm{B}} \sum_{(i,k)\in\mathcal{I}_p} \sum_{(j,l)\in\mathcal{I}_q} \iiiint\limits_{\substack{\mathbb{R}^3\times\mathbb{R}^3\\ \times\mathbb{R}^3\times\mathbb{R}^3}} \left(\frac{\beta_{\mathrm{A}_k}\beta_{\mathrm{B}_l}}{\beta_{\mathrm{A}_i}\beta_{\mathrm{B}_j}} f'_{\mathrm{A}_k} f'_{\mathrm{B}_l} - f_{\mathrm{A}_i} f_{\mathrm{B}_j} \right) W^{\mathrm{A}'_k\mathrm{B}'_l}_{\mathrm{A}_i\mathrm{B}_j} \ln\left(\beta_{\mathrm{A}_i} f_{\mathrm{A}_i}\right) \mathrm{d}\mathbf{c}_\mathrm{A}\, \mathrm{d}\mathbf{c}_\mathrm{B}\, \mathrm{d}\mathbf{c}'_\mathrm{A}\, \mathrm{d}\mathbf{c}'_\mathrm{B} \\ =&\sum_{\mathrm{B}\in\mathcal{S}} \sum_{q\in\mathrm{B}} \sum_{(i,k)\in\mathcal{I}_p} \sum_{(j,l)\in\mathcal{I}_q} \iiiint\limits_{\substack{\mathbb{R}^3\times\mathbb{R}^3\\ \times\mathbb{R}^3\times\mathbb{R}^3}} \left(\frac{\beta_{\mathrm{A}_k}\beta_{\mathrm{B}_l}}{\beta_{\mathrm{A}_i}\beta_{\mathrm{B}_j}} f'_{\mathrm{A}_k} f'_{\mathrm{B}_l} - f_{\mathrm{A}_i} f_{\mathrm{B}_j} \right) W^{\mathrm{A}'_k\mathrm{B}'_l}_{\mathrm{A}_i\mathrm{B}_j} \ln\left(\beta_{\mathrm{B}_j} f_{\mathrm{B}_j}\right) \mathrm{d}\mathbf{c}_\mathrm{A}\, \mathrm{d}\mathbf{c}_\mathrm{B}\, \mathrm{d}\mathbf{c}'_\mathrm{A}\, \mathrm{d}\mathbf{c}'_\mathrm{B} \end{aligned} \tag{B.4}$$

Therefore we can re-write the scattering entropy source term as the average of these two terms:

$$\mathfrak{v}^S_{\mathrm{A}_p} = -\frac{1}{2}\mathrm{k_B} \sum_{\mathrm{B}\in\mathcal{S}} \sum_{q\in\mathrm{B}} \sum_{(i,k)\in\mathcal{I}_p} \sum_{(j,l)\in\mathcal{I}_q} \iiiint\limits_{\substack{\mathbb{R}^3\times\mathbb{R}^3\\ \times\mathbb{R}^3\times\mathbb{R}^3}} \left(\ln\left(\beta_{\mathrm{A}_i} f_{\mathrm{A}_i}\right) + \ln\left(\beta_{\mathrm{B}_j} f_{\mathrm{B}_j}\right)\right) \left(\frac{\beta_{\mathrm{A}_k}\beta_{\mathrm{B}_l}}{\beta_{\mathrm{A}_i}\beta_{\mathrm{B}_j}} f'_{\mathrm{A}_k} f'_{\mathrm{B}_l} - f_{\mathrm{A}_i} f_{\mathrm{B}_j} \right) \times W^{\mathrm{A}'_k\mathrm{B}'_l}_{\mathrm{A}_i\mathrm{B}_j} \mathrm{d}\mathbf{c}_\mathrm{A}\, \mathrm{d}\mathbf{c}_\mathrm{B}\, \mathrm{d}\mathbf{c}'_\mathrm{A}\, \mathrm{d}\mathbf{c}'_\mathrm{B} \tag{B.5}$$

Now we must recall the characteristic of the inverse collision. The idea of the inverse collision is that if the collision is run in reverse, we must retrieve exactly the initial conditions we started with (*e.g.*, velocity magnitudes and directions). This gives the following relations between the "forward"

and "reverse" collisional processes:

$$\sum_{\mathrm{B}\in\mathcal{S}}\sum_{q\in\mathrm{B}}\sum_{(i,k)\in\mathcal{I}_p}\sum_{(j,l)\in\mathcal{I}_q}\iiiint\limits_{\substack{\mathbb{R}^3\times\mathbb{R}^3\\ \times\mathbb{R}^3\times\mathbb{R}^3}} f_{\mathrm{A}_i} f_{\mathrm{B}_j} W_{\mathrm{A}_i\mathrm{B}_j}^{\mathrm{A}'_k\mathrm{B}'_l} \ln\left(\beta_{\mathrm{A}_i} f_{\mathrm{A}_i}\right) \mathrm{d}\mathbf{c}_\mathrm{A}\,\mathrm{d}\mathbf{c}_\mathrm{B}\,\mathrm{d}\mathbf{c}'_\mathrm{A}\,\mathrm{d}\mathbf{c}'_\mathrm{B}$$

$$= \sum_{\mathrm{B}\in\mathcal{S}}\sum_{q\in\mathrm{B}}\sum_{(i,k)\in\mathcal{I}_p}\sum_{(j,l)\in\mathcal{I}_q}\iiiint\limits_{\substack{\mathbb{R}^3\times\mathbb{R}^3\\ \times\mathbb{R}^3\times\mathbb{R}^3}} \left(\frac{\beta_{\mathrm{A}_k}\beta_{\mathrm{B}_l}}{\beta_{\mathrm{A}_i}\beta_{\mathrm{B}_j}}\right) f'_{\mathrm{A}_k} f'_{\mathrm{B}_l} W_{\mathrm{A}_i\mathrm{B}_j}^{\mathrm{A}'_k\mathrm{B}'_l} \ln\left(\beta_{\mathrm{A}_k} f'_{\mathrm{A}_k}\right) \mathrm{d}\mathbf{c}_\mathrm{A}\,\mathrm{d}\mathbf{c}_\mathrm{B}\,\mathrm{d}\mathbf{c}'_\mathrm{A}\,\mathrm{d}\mathbf{c}'_\mathrm{B} \tag{B.6}$$

$$\sum_{\mathrm{B}\in\mathcal{S}}\sum_{q\in\mathrm{B}}\sum_{(i,k)\in\mathcal{I}_p}\sum_{(j,l)\in\mathcal{I}_q}\iiiint\limits_{\substack{\mathbb{R}^3\times\mathbb{R}^3\\ \times\mathbb{R}^3\times\mathbb{R}^3}} f_{\mathrm{A}_i} f_{\mathrm{B}_j} W_{\mathrm{A}_i\mathrm{B}_j}^{\mathrm{A}'_k\mathrm{B}'_l} \ln\left(\beta_{\mathrm{A}_k} f'_{\mathrm{A}_k}\right) \mathrm{d}\mathbf{c}_\mathrm{A}\,\mathrm{d}\mathbf{c}_\mathrm{B}\,\mathrm{d}\mathbf{c}'_\mathrm{A}\,\mathrm{d}\mathbf{c}'_\mathrm{B}$$

$$= \sum_{\mathrm{B}\in\mathcal{S}}\sum_{q\in\mathrm{B}}\sum_{(i,k)\in\mathcal{I}_p}\sum_{(j,l)\in\mathcal{I}_q}\iiiint\limits_{\substack{\mathbb{R}^3\times\mathbb{R}^3\\ \times\mathbb{R}^3\times\mathbb{R}^3}} \left(\frac{\beta_{\mathrm{A}_k}\beta_{\mathrm{B}_l}}{\beta_{\mathrm{A}_i}\beta_{\mathrm{B}_j}}\right) f'_{\mathrm{A}_k} f'_{\mathrm{B}_l} W_{\mathrm{A}_i\mathrm{B}_j}^{\mathrm{A}'_k\mathrm{B}'_l} \ln\left(\beta_{\mathrm{A}_i} f_{\mathrm{A}_i}\right) \mathrm{d}\mathbf{c}_\mathrm{A}\,\mathrm{d}\mathbf{c}_\mathrm{B}\,\mathrm{d}\mathbf{c}'_\mathrm{A}\,\mathrm{d}\mathbf{c}'_\mathrm{B} \tag{B.7}$$

Using this in Eq. (B.4), we can finally write the following expression for the in-elastic scattering entropy source term:

$$\mathfrak{v}^S_{\mathrm{A}_p} = -\frac{1}{4}\mathrm{k}_\mathrm{B}\sum_{\mathrm{B}\in\mathcal{S}}\sum_{q\in\mathrm{B}}\sum_{(i,k)\in\mathcal{I}_p}\sum_{(j,l)\in\mathcal{I}_q}\iiiint\limits_{\substack{\mathbb{R}^3\times\mathbb{R}^3\\ \times\mathbb{R}^3\times\mathbb{R}^3}} \left(\ln\left(\beta_{\mathrm{A}_i} f_{\mathrm{A}_i}\right) + \ln\left(\beta_{\mathrm{B}_j} f_{\mathrm{B}_j}\right) - \ln\left(\beta_{\mathrm{A}_k} f'_{\mathrm{A}_k}\right) - \ln\left(\beta_{\mathrm{B}_l} f'_{\mathrm{B}_l}\right)\right)$$
$$\times \left(\frac{\beta_{\mathrm{A}_k}\beta_{\mathrm{B}_l}}{\beta_{\mathrm{A}_i}\beta_{\mathrm{B}_j}} f'_{\mathrm{A}_k} f'_{\mathrm{B}_l} - f_{\mathrm{A}_i} f_{\mathrm{B}_j}\right) W_{\mathrm{A}_i\mathrm{B}_j}^{\mathrm{A}'_k\mathrm{B}'_l}\,\mathrm{d}\mathbf{c}_\mathrm{A}\,\mathrm{d}\mathbf{c}_\mathrm{B}\,\mathrm{d}\mathbf{c}'_\mathrm{A}\,\mathrm{d}\mathbf{c}'_\mathrm{B} \tag{B.8}$$

This can also be written as Eq. (2.42), which is shown in Chapter 2 to be either zero or positive.

Appendix C

MGME-QCT Expressions for QCT Sampling

This appendix provides all the expressions for the MGMEL-QCT and MGMET-QCT models for sampling in QCT.

C.1 MGMEL-QCT model

C.1.1 Inelastic processes

$$
\begin{aligned}
{}^{0}K_{pq,rs} =& \sum_{i\in\mathcal{I}_p}\sum_{j\in\mathcal{I}_q}\sum_{k\in\mathcal{I}_r}\sum_{l\in\mathcal{I}_s}\left[\frac{a_{\mathrm{A}_i}\exp\left(-\frac{E_{\mathrm{A}_i}}{\mathrm{k_B}T^{\mathrm{int}}_{\mathrm{A}_p}}\right)}{Q^{(0)}_{\mathrm{A}_p}(T^{\mathrm{int}}_{\mathrm{A}_p})}\right]\left[\frac{a_{\mathrm{B}_j}\exp\left(-\frac{E_{\mathrm{B}_j}}{\mathrm{k_B}T^{\mathrm{int}}_{\mathrm{B}_q}}\right)}{Q^{(0)}_{\mathrm{B}_q}(T^{\mathrm{int}}_{\mathrm{B}_q})}\right] \\
&\times m_{\mathrm{A}}\frac{1}{\chi}\left(\frac{\mu_{\mathrm{AB}}}{2\pi\mathrm{k_B}T}\right)^{3/2}\int_{g=0}^{\infty}\int_{b=0}^{\infty}\int_{\mathscr{L}^2}\exp\left(-\frac{\mu_{\mathrm{AB}}}{2\mathrm{k_B}T}g^2\right)g^3 2\pi b P^{\mathrm{A}_k\mathrm{B}_l}_{\mathrm{A}_i\mathrm{B}_j}\,\mathrm{d}b\,\mathrm{d}g\,\mathrm{d}\boldsymbol{\omega} \qquad \text{(C.1)}
\end{aligned}
$$

$$
\begin{aligned}
{}^{0}\bar{K}_{pq,rs} =& Q^{(0)}_{\mathrm{A}_p}(T)Q^{(0)}_{\mathrm{B}_q}(T)\sum_{i\in\mathcal{I}_p}\sum_{j\in\mathcal{I}_q}\sum_{k\in\mathcal{I}_r}\sum_{l\in\mathcal{I}_s} m_{\mathrm{A}}\frac{1}{\chi}\left(\frac{\mu_{\mathrm{AB}}}{2\pi\mathrm{k_B}T}\right)^{3/2} \\
&\times\left[\frac{\exp\left(-\frac{E_{\mathrm{A}_k}}{\mathrm{k_B}T^{\mathrm{int}}_{\mathrm{A}_r}}+\frac{E_{\mathrm{A}_k}}{\mathrm{k_B}T}\right)}{Q^{(0)}_{\mathrm{A}_r}(T^{\mathrm{int}}_{\mathrm{A}_r})}\right]\left[\frac{\exp\left(-\frac{E_{\mathrm{B}_l}}{\mathrm{k_B}T^{\mathrm{int}}_{\mathrm{B}_s}}+\frac{E_{\mathrm{B}_l}}{\mathrm{k_B}T}\right)}{Q^{(0)}_{\mathrm{B}_s}(T^{\mathrm{int}}_{\mathrm{B}_s})}\right] \\
&\times\left[\frac{a_{\mathrm{A}_i}\exp\left(-\frac{E_{\mathrm{A}_i}}{\mathrm{k_B}T}\right)}{Q^{(0)}_{\mathrm{A}_p}(T)}\right]\left[\frac{a_{\mathrm{B}_j}\exp\left(-\frac{E_{\mathrm{B}_j}}{\mathrm{k_B}T}\right)}{Q^{(0)}_{\mathrm{B}_q}(T)}\right] \\
&\times\int_{g=0}^{\infty}\int_{b=0}^{\infty}\int_{\mathscr{L}^2}\exp\left(-\frac{\mu_{\mathrm{AB}}g^2}{2\mathrm{k_B}T}\right)g^3 2\pi b P^{\mathrm{A}_k\mathrm{B}_l}_{\mathrm{A}_i\mathrm{B}_j}\,\mathrm{d}b\,\mathrm{d}g\,\mathrm{d}\boldsymbol{\omega'} \qquad \text{(C.2)}
\end{aligned}
$$

C.1.2 Exchange processes

$$
\begin{aligned}
{}^{0}K_{\mathrm{A}_p\mathrm{B}_q,\mathrm{C}_r\mathrm{D}_s} =& \sum_{i\in\mathcal{I}_p}\sum_{j\in\mathcal{I}_q}\sum_{k\in\mathcal{I}_r}\sum_{l\in\mathcal{I}_s}\left[\frac{a_{\mathrm{A}_i}\exp\left(-\frac{E_{\mathrm{A}_i}}{\mathrm{k_B}T^{\mathrm{int}}_{\mathrm{A}_p}}\right)}{Q^{(0)}_{\mathrm{A}_p}(T^{\mathrm{int}}_{\mathrm{A}_p})}\right]\left[\frac{a_{\mathrm{B}_j}\exp\left(-\frac{E_{\mathrm{B}_j}}{\mathrm{k_B}T^{\mathrm{int}}_{\mathrm{B}_q}}\right)}{Q^{(0)}_{\mathrm{B}_q}(T^{\mathrm{int}}_{\mathrm{B}_q})}\right] \\
&\times m_{\mathrm{A}}\frac{1}{\chi}\left(\frac{\mu_{\mathrm{AB}}}{2\pi\mathrm{k_B}T}\right)^{3/2}\int_{g=0}^{\infty}\int_{b=0}^{\infty}\int_{\mathscr{L}^2}\exp\left(-\frac{\mu_{\mathrm{AB}}}{2\mathrm{k_B}T}g^2\right)g^3 2\pi b P^{\mathrm{C}_k\mathrm{D}_l}_{\mathrm{A}_i\mathrm{B}_j}\,\mathrm{d}b\,\mathrm{d}g\,\mathrm{d}\boldsymbol{\omega} \qquad \text{(C.3)}
\end{aligned}
$$

$$
\begin{aligned}
{}^{0}\bar{K}_{\mathrm{A}_p\mathrm{B}_q,\mathrm{C}_r\mathrm{D}_s} =& Q^{(0)}_{\mathrm{A}_p}(T)Q^{(0)}_{\mathrm{B}_q}(T)\sum_{i\in\mathcal{I}_p}\sum_{j\in\mathcal{I}_q}\sum_{k\in\mathcal{I}_r}\sum_{l\in\mathcal{I}_s} m_{\mathrm{A}}\frac{1}{\chi}\left(\frac{\mu_{\mathrm{AB}}}{\mu_{\mathrm{CD}}}\right)^{3/2}\left(\frac{\mu_{\mathrm{AB}}}{2\pi\mathrm{k_B}T}\right)^{3/2} \\
&\times\left[\frac{\exp\left(-\frac{E_{\mathrm{C}_k}}{\mathrm{k_B}T^{\mathrm{int}}_{\mathrm{C}_r}}+\frac{E_{\mathrm{C}_k}}{\mathrm{k_B}T}\right)}{Q^{(0)}_{\mathrm{C}_r}(T^{\mathrm{int}}_{\mathrm{C}_r})}\right]\left[\frac{\exp\left(-\frac{E_{\mathrm{D}_l}}{\mathrm{k_B}T^{\mathrm{int}}_{\mathrm{D}_s}}+\frac{E_{\mathrm{D}_l}}{\mathrm{k_B}T}\right)}{Q^{(0)}_{\mathrm{D}_s}(T^{\mathrm{int}}_{\mathrm{D}_s})}\right] \\
&\times\left[\frac{a_{\mathrm{A}_i}\exp\left(-\frac{E_{\mathrm{A}_i}}{\mathrm{k_B}T}\right)}{Q^{(0)}_{\mathrm{A}_p}(T)}\right]\left[\frac{a_{\mathrm{B}_j}\exp\left(-\frac{E_{\mathrm{B}_j}}{\mathrm{k_B}T}\right)}{Q^{(0)}_{\mathrm{B}_q}(T)}\right] \\
&\times\int_{g=0}^{\infty}\int_{b=0}^{\infty}\int_{\mathscr{L}^2}\exp\left(-\frac{\mu_{\mathrm{AB}}g^2}{2\mathrm{k_B}T}\right)g^3 2\pi b P^{\mathrm{A}_k\mathrm{B}_l}_{\mathrm{A}_i\mathrm{B}_j}\,\mathrm{d}b\,\mathrm{d}g\,\mathrm{d}\boldsymbol{\omega'} \qquad \text{(C.4)}
\end{aligned}
$$

C.1.3 Dissociation-recombination processes

$$
\begin{aligned}
{}^{0}C_{\mathrm{A}_p\mathrm{B}_q,\mathrm{C}_r\mathrm{D}_s\mathrm{B}_t} =& \sum_{i\in\mathcal{I}_p}\sum_{j\in\mathcal{I}_q}\sum_{k\in\mathcal{I}_r}\sum_{l\in\mathcal{I}_s}\sum_{m\in\mathcal{I}_t}\left[\frac{a_{\mathrm{A}_i}\exp\left(-\frac{E_{\mathrm{A}_i}}{\mathrm{k_B}T^{\mathrm{int}}_{\mathrm{A}_p}}\right)}{Q^{(0)}_{\mathrm{A}_p}(T^{\mathrm{int}}_{\mathrm{A}_p})}\right]\left[\frac{a_{\mathrm{B}_j}\exp\left(-\frac{E_{\mathrm{B}_j}}{\mathrm{k_B}T^{\mathrm{int}}_{\mathrm{B}_q}}\right)}{Q^{(0)}_{\mathrm{B}_q}(T^{\mathrm{int}}_{\mathrm{B}_q})}\right] \\
&\times m_{\mathrm{A}}\frac{1}{\chi}\left(\frac{\mu_{\mathrm{AB}}}{2\pi\mathrm{k_B}T}\right)^{3/2}\int_{\mathscr{L}^2}\int_{b=0}^{\infty}\int_{g=0}^{\infty}\exp\left(-\frac{\mu_{\mathrm{AB}}}{2\mathrm{k_B}T}g^2\right)g^3 2\pi P^{\mathrm{C}_k\mathrm{D}_l\mathrm{B}_m}_{\mathrm{A}_i\mathrm{B}_j}\,\mathrm{d}b\,\mathrm{d}g\,\mathrm{d}\boldsymbol{\omega} \qquad \text{(C.5)}
\end{aligned}
$$

$$
\begin{aligned}
{}^{0}\bar{C}_{\mathrm{A}_p\mathrm{B}_q,\mathrm{C}_r\mathrm{D}_s\mathrm{B}_t} =& \frac{Q^{(0)}_{\mathrm{A}_p}(T)Q^{(0)}_{\mathrm{B}_q}(T)}{Q^{(0)}_{\mathrm{C}_r}(T^{\mathrm{int}}_{\mathrm{C}_r})Q^{(0)}_{\mathrm{D}_s}(T^{\mathrm{int}}_{\mathrm{D}_s})Q^{(0)}_{\mathrm{B}_l}(T^{\mathrm{int}}_{\mathrm{B}_l})}\left(\frac{\mu_{\mathrm{AB}}}{2\pi \mathrm{k_B}T}\right)^{3/2}\left(\frac{\mathrm{h_P^2}}{2\pi\mu_{\mathrm{CD}}\mathrm{k_B}T}\right)^{3/2} \\
&\times \sum_{i\in\mathcal{I}_p}\sum_{j\in\mathcal{I}_q}\sum_{k\in\mathcal{I}_r}\sum_{l\in\mathcal{I}_s}\sum_{m\in\mathcal{I}_t}\exp\left(-\frac{E_{\mathrm{C}_k}}{\mathrm{k_B}T^{\mathrm{int}}_{\mathrm{C}_r}}+\frac{E_{\mathrm{C}_k}}{\mathrm{k_B}T}\right)\exp\left(-\frac{E_{\mathrm{D}_l}}{\mathrm{k_B}T^{\mathrm{int}}_{\mathrm{D}_s}}+\frac{E_{\mathrm{D}_l}}{\mathrm{k_B}T}\right) \\
&\times \exp\left(-\frac{E_{\mathrm{B}_m}}{\mathrm{k_B}T^{\mathrm{int}}_{\mathrm{B}_t}}+\frac{E_{\mathrm{B}_m}}{\mathrm{k_B}T}\right)\left[\frac{a_{\mathrm{A}_i}\exp\left(-\frac{E_{\mathrm{A}_i}}{\mathrm{k_B}T}\right)}{Q^{(0)}_{\mathrm{A}_p}(T)}\right]\left[\frac{a_{\mathrm{B}_j}\exp\left(-\frac{E_{\mathrm{B}_j}}{\mathrm{k_B}T}\right)}{Q^{(0)}_{\mathrm{B}_q}(T)}\right] \\
&\times \frac{1}{\chi}\int_{g=0}^{\infty}\int_{b=0}^{\infty}\int_{\mathscr{L}^2}\exp\left(-\frac{\mu_{\mathrm{AB}}}{2\mathrm{k_B}T}g^2\right)g^3 2\pi b P^{\mathrm{C}_k\mathrm{D}_l\mathrm{B}_m}_{\mathrm{A}_i\mathrm{B}_j}\,\mathrm{d}b\,\mathrm{d}g\,\mathrm{d}\boldsymbol{\omega} \qquad \text{(C.6)}
\end{aligned}
$$

C.2 MGMET-QCT model

C.2.1 Inelastic processes

$$
\begin{aligned}
{}^{0}K_{pq,rs} =& \sum_{i\in\mathcal{I}_p}\sum_{j\in\mathcal{I}_q}\sum_{k\in\mathcal{I}_r}\sum_{l\in\mathcal{I}_s}\left[\frac{a_{\mathrm{A}_i}\exp\left(-\frac{E_{\mathrm{A}_i}}{\mathrm{k_B}T}\right)}{Q^{(0)}_{\mathrm{A}_p}(T)}\right]\left[\frac{a_{\mathrm{B}_j}\exp\left(-\frac{E_{\mathrm{B}_j}}{\mathrm{k_B}T}\right)}{Q^{(0)}_{\mathrm{B}_q}(T)}\right] \\
&\times m_{\mathrm{A}}\frac{1}{\chi}\left(\frac{\mu_{\mathrm{AB}}}{2\pi\mathrm{k_B}T}\right)^{3/2}\int_{g=0}^{\infty}\int_{b=0}^{\infty}\int_{\mathscr{L}^2}\exp\left(-\frac{\mu_{\mathrm{AB}}}{2\mathrm{k_B}T}g^2\right)g^3 2\pi b P^{\mathrm{A}_k\mathrm{B}_l}_{\mathrm{A}_i\mathrm{B}_j}\,\mathrm{d}b\,\mathrm{d}g\,\mathrm{d}\boldsymbol{\omega} \qquad \text{(C.7)}
\end{aligned}
$$

$$
\begin{aligned}
{}^{0}\bar{K}_{pq,rs} =& \frac{Q^{(0)}_{\mathrm{A}_p}(T)}{Q^{(0)}_{\mathrm{A}_r}(T)}\frac{Q^{(0)}_{\mathrm{B}_q}(T)}{Q^{(0)}_{\mathrm{B}_s}(T)}\sum_{i\in\mathcal{I}_p}\sum_{j\in\mathcal{I}_q}\sum_{k\in\mathcal{I}_r}\sum_{l\in\mathcal{I}_s}m_{\mathrm{A}}\frac{1}{\chi}\left(\frac{\mu_{\mathrm{AB}}}{2\pi\mathrm{k_B}T}\right)^{3/2} \\
&\times\left[\frac{a_{\mathrm{A}_i}\exp\left(-\frac{E_{\mathrm{A}_i}}{\mathrm{k_B}T}\right)}{Q^{(0)}_{\mathrm{A}_p}(T)}\right]\left[\frac{a_{\mathrm{B}_j}\exp\left(-\frac{E_{\mathrm{B}_j}}{\mathrm{k_B}T}\right)}{Q^{(0)}_{\mathrm{B}_q}(T)}\right] \\
&\times\int_{g=0}^{\infty}\int_{b=0}^{\infty}\int_{\mathscr{L}^2}\exp\left(-\frac{\mu_{\mathrm{AB}}g^2}{2\mathrm{k_B}T}\right)g^3 2\pi b P^{\mathrm{A}_k\mathrm{B}_l}_{\mathrm{A}_i\mathrm{B}_j}\,\mathrm{d}b\,\mathrm{d}g\,\mathrm{d}\boldsymbol{\omega'} \qquad \text{(C.8)}
\end{aligned}
$$

C.2.2 Exchange processes

$$
{}^{0}K_{\mathrm{A}_p\mathrm{B}_q,\mathrm{C}_r\mathrm{D}_s} = \sum_{i\in\mathcal{I}_p}\sum_{j\in\mathcal{I}_q}\sum_{k\in\mathcal{I}_r}\sum_{l\in\mathcal{I}_s}\left[\frac{a_{\mathrm{A}_i}\exp\left(-\frac{E_{\mathrm{A}_i}}{\mathrm{k_B}T}\right)}{Q^{(0)}_{\mathrm{A}_p}(T)}\right]\left[\frac{a_{\mathrm{B}_j}\exp\left(-\frac{E_{\mathrm{B}_j}}{\mathrm{k_B}T}\right)}{Q^{(0)}_{\mathrm{B}_q}(T)}\right]
$$
$$
\times m_{\mathrm{A}}\frac{1}{\chi}\left(\frac{\mu_{\mathrm{AB}}}{2\pi\mathrm{k_B}T}\right)^{3/2}\int_{g=0}^{\infty}\int_{b=0}^{\infty}\int_{\mathscr{L}^2}\exp\left(-\frac{\mu_{\mathrm{AB}}}{2\mathrm{k_B}T}g^2\right)g^3 2\pi b P^{\mathrm{C}_k\mathrm{D}_l}_{\mathrm{A}_i\mathrm{B}_j}\,\mathrm{d}b\,\mathrm{d}g\,\mathrm{d}\boldsymbol{\omega} \tag{C.9}
$$

$$
{}^{0}\bar{K}_{\mathrm{A}_p\mathrm{B}_q,\mathrm{C}_r\mathrm{D}_s} = \frac{Q^{(0)}_{\mathrm{A}_p}(T)Q^{(0)}_{\mathrm{B}_q}(T)}{Q^{(0)}_{\mathrm{C}_r}(T)Q^{(0)}_{\mathrm{D}_s}(T)}\sum_{i\in\mathcal{I}_p}\sum_{j\in\mathcal{I}_q}\sum_{k\in\mathcal{I}_r}\sum_{l\in\mathcal{I}_s} m_{\mathrm{A}}\frac{1}{\chi}\left(\frac{\mu_{\mathrm{AB}}}{\mu_{\mathrm{CD}}}\right)^{3/2}\left(\frac{\mu_{\mathrm{AB}}}{2\pi\mathrm{k_B}T}\right)^{3/2}
$$
$$
\times\left[\frac{a_{\mathrm{A}_i}\exp\left(-\frac{E_{\mathrm{A}_i}}{\mathrm{k_B}T}\right)}{Q^{(0)}_{\mathrm{A}_p}(T)}\right]\left[\frac{a_{\mathrm{B}_j}\exp\left(-\frac{E_{\mathrm{B}_j}}{\mathrm{k_B}T}\right)}{Q^{(0)}_{\mathrm{B}_q}(T)}\right]
$$
$$
\times\int_{g=0}^{\infty}\int_{b=0}^{\infty}\int_{\mathscr{L}^2}\exp\left(-\frac{\mu_{\mathrm{AB}}g^2}{2\mathrm{k_B}T}\right)g^3 2\pi b P^{\mathrm{A}_k\mathrm{B}_l}_{\mathrm{A}_i\mathrm{B}_j}\,\mathrm{d}b\,\mathrm{d}g\,\mathrm{d}\boldsymbol{\omega'} \tag{C.10}
$$

C.2.3 Dissociation-recombination processes

$$
{}^{0}C_{\mathrm{A}_p\mathrm{B}_q,\mathrm{C}_r\mathrm{D}_s\mathrm{B}_t} = \sum_{i\in\mathcal{I}_p}\sum_{j\in\mathcal{I}_q}\sum_{k\in\mathcal{I}_r}\sum_{l\in\mathcal{I}_s}\sum_{m\in\mathcal{I}_t}\left[\frac{a_{\mathrm{A}_i}\exp\left(-\frac{E_{\mathrm{A}_i}}{\mathrm{k_B}T}\right)}{Q^{(0)}_{\mathrm{A}_p}(T)}\right]\left[\frac{a_{\mathrm{B}_j}\exp\left(-\frac{E_{\mathrm{B}_j}}{\mathrm{k_B}T}\right)}{Q^{(0)}_{\mathrm{B}_q}(T)}\right]
$$
$$
\times m_{\mathrm{A}}\frac{1}{\chi}\left(\frac{\mu_{\mathrm{AB}}}{2\pi\mathrm{k_B}T}\right)^{3/2}\int_{\mathscr{L}^2}\int_{b=0}^{\infty}\int_{g=0}^{\infty}\exp\left(-\frac{\mu_{\mathrm{AB}}}{2\mathrm{k_B}T}g^2\right)g^3 2\pi P^{\mathrm{C}_k\mathrm{D}_l\mathrm{B}_m}_{\mathrm{A}_i\mathrm{B}_j}\,\mathrm{d}b\,\mathrm{d}g\,\mathrm{d}\boldsymbol{\omega} \tag{C.11}
$$

$$
{}^{0}\bar{C}_{\mathrm{A}_p\mathrm{B}_q,\mathrm{C}_r\mathrm{D}_s\mathrm{B}_t} = \frac{Q^{(0)}_{\mathrm{A}_p}(T)Q^{(0)}_{\mathrm{B}_q}(T)}{Q^{(0)}_{\mathrm{C}_r}(T)Q^{(0)}_{\mathrm{D}_s}(T)Q^{(0)}_{\mathrm{B}_l}(T)}\left(\frac{\mu_{\mathrm{AB}}}{2\pi\mathrm{k_B}T}\right)^{3/2}\left(\frac{\mathrm{h_P^2}}{2\pi\mu_{\mathrm{CD}}\mathrm{k_B}T}\right)^{3/2}
$$
$$
\times\sum_{i\in\mathcal{I}_p}\sum_{j\in\mathcal{I}_q}\sum_{k\in\mathcal{I}_r}\sum_{l\in\mathcal{I}_s}\sum_{m\in\mathcal{I}_t}\left[\frac{a_{\mathrm{A}_i}\exp\left(-\frac{E_{\mathrm{A}_i}}{\mathrm{k_B}T}\right)}{Q^{(0)}_{\mathrm{A}_p}(T)}\right]\left[\frac{a_{\mathrm{B}_j}\exp\left(-\frac{E_{\mathrm{B}_j}}{\mathrm{k_B}T}\right)}{Q^{(0)}_{\mathrm{B}_q}(T)}\right]
$$
$$
\times\frac{1}{\chi}\int_{g=0}^{\infty}\int_{b=0}^{\infty}\int_{\mathscr{L}^2}\exp\left(-\frac{\mu_{\mathrm{AB}}}{2\mathrm{k_B}T}g^2\right)g^3 2\pi b P^{\mathrm{C}_k\mathrm{D}_l\mathrm{B}_m}_{\mathrm{A}_i\mathrm{B}_j}\,\mathrm{d}b\,\mathrm{d}g\,\mathrm{d}\boldsymbol{\omega} \tag{C.12}
$$

Appendix D

Calculation of Statistical Error for Reaction Rate Coefficients and Energy Transfer Coefficients

The variance due to sampling can be retrieved through the relationship:

$$\mathrm{var}(x) = \langle x^2 \rangle - \langle x \rangle^2 \tag{D.1}$$

where x is the quantity of interest and $\langle x \rangle$ denotes the mean value of x. Extending this to the QCT samples for both reaction rate coefficients and energy transfer coefficients allows us to write the variance associated with the reaction rate coefficients and energy transfer coefficients for inelastic processes as:

$$\mathrm{var}\left({}^{m}K_{pq,rs}\right) = \langle v \rangle \pi b_{max}^2 \left\{ \frac{1}{N_{pq}} \sum_{j=1}^{N_{pq,rs}} \left(E_{\mathrm{A}}^i\right)^{2m} - \left[\frac{1}{N_{pq}} \sum_{j=1}^{N_{pq,rs}} \left(E_{\mathrm{A}}^i\right)^{m} \right]^2 \right\} \tag{D.2}$$

$$\begin{aligned} \mathrm{var}\left({}^{m}\bar{K}_{pq,rs}\right) = \langle v \rangle \pi b_{max}^2 \Bigg\{ & \frac{1}{N_{pq}} \sum_{j=1}^{N_{pq,rs}} \left(\left(E_{\mathrm{A}}^i\right)^{m} \frac{Q_{\mathrm{A}_k}^{(0)}(T_{\mathrm{A}_r}^{\mathrm{int}})}{Q_{\mathrm{A}_k}^{(0)}(T)} \frac{Q_{\mathrm{B}_l}^{(0)}(T_{\mathrm{B}_s}^{\mathrm{int}})}{Q_{\mathrm{B}_l}^{(0)}(T)} \right)^2 \\ & - \left[\frac{1}{N_{pq}} \sum_{j=1}^{N_{pq,rs}} \left(E_{\mathrm{A}}^i\right)^{m} \frac{Q_{\mathrm{A}_k}^{(0)}(T_{\mathrm{A}_r}^{\mathrm{int}})}{Q_{\mathrm{A}_k}^{(0)}(T)} \frac{Q_{\mathrm{B}_l}^{(0)}(T_{\mathrm{B}_s}^{\mathrm{int}})}{Q_{\mathrm{B}_l}^{(0)}(T)} \right]^2 \Bigg\} \end{aligned} \tag{D.3}$$

where $\langle v \rangle$ denotes the mean velocity factor which accounts for the integration over impact velocity and solid angle from a thermal distribution, b_{max} denotes the maximum impact parameter, and N_{pq} denotes the number of trajectories which start with molecule A in group p and molecule B in group q. The summations in these expressions are over the number of trajectories which result in a given outcome. That is, $N_{pq,rs}$ denotes the number of trajectories which start with molecule A in group p and molecule B in group q and end with molecule A in group r and molecule B in group s. These variances can be directly computed when the rate data is calculated from the individual trajectories. The variance associated with the reaction rate coefficients and energy

transfer coefficients for exchange processes can be written as:

$$\mathrm{var}\left({}^{m}K_{\mathrm{A}_p\mathrm{B}_q,\mathrm{C}_r\mathrm{D}_s}\right) = \langle v\rangle \pi b_{max}^2 \left\{ \frac{1}{N_{\mathrm{A}_p\mathrm{B}_q}} \sum_{j=1}^{N_{\mathrm{A}_p\mathrm{B}_q,\mathrm{C}_r\mathrm{D}_s}} \left(E_{\mathrm{A}}^i\right)^{2m} - \left[\frac{1}{N_{\mathrm{A}_p\mathrm{B}_q}} \sum_{j=1}^{N_{\mathrm{A}_p\mathrm{B}_q,\mathrm{C}_r\mathrm{D}_s}} \left(E_{\mathrm{A}}^i\right)^{m} \right]^2 \right\} \tag{D.4}$$

$$\begin{aligned}\mathrm{var}\left({}^{m}\bar{K}_{\mathrm{A}_p\mathrm{B}_q,\mathrm{C}_r\mathrm{D}_s}\right) =& \langle v\rangle \pi b_{max}^2 \left\{ \frac{1}{N_{\mathrm{A}_p\mathrm{B}_q}} \sum_{j=1}^{N_{\mathrm{A}_p\mathrm{B}_q,\mathrm{C}_r\mathrm{D}_s}} \left(\left(E_{\mathrm{A}}^i\right)^{m} \frac{Q_{\mathrm{C}_k}^{(0)}(T_{\mathrm{C}_r}^{\mathrm{int}})}{Q_{\mathrm{C}_k}^{(0)}(T)} \frac{Q_{\mathrm{D}_l}^{(0)}(T_{\mathrm{D}_s}^{\mathrm{int}})}{Q_{\mathrm{D}_l}^{(0)}(T)} \right)^2 \right. \\ & \left. - \left[\frac{1}{N_{\mathrm{A}_p\mathrm{B}_q}} \sum_{j=1}^{N_{\mathrm{A}_p\mathrm{B}_q,\mathrm{C}_r\mathrm{D}_s}} \left(E_{\mathrm{A}}^i\right)^{m} \frac{Q_{\mathrm{C}_k}^{(0)}(T_{\mathrm{C}_r}^{\mathrm{int}})}{Q_{\mathrm{C}_k}^{(0)}(T)} \frac{Q_{\mathrm{D}_l}^{(0)}(T_{\mathrm{D}_s}^{\mathrm{int}})}{Q_{\mathrm{D}_l}^{(0)}(T)} \right]^2 \right\}\end{aligned} \tag{D.5}$$

$$\tag{D.6}$$

where $N_{\mathrm{A}_p\mathrm{B}_q}$ denotes the number of trajectories which start with molecule A in group p and molecule B in group q. The summations in these expressions are over the number of trajectories which result in a given outcome. That is, $N_{\mathrm{A}_p\mathrm{B}_q,\mathrm{C}_r\mathrm{D}_s}$ denotes the number of trajectories which start with molecule A in group p and molecule B in group q and end with molecule C in group r and molecule D in group s. The variance associated with the reaction rate coefficients and energy transfer coefficients for combined dissociation-excitation processes can be written as:

$$\mathrm{var}\left({}^{m}C_{\mathrm{A}_p\mathrm{B}_q,\mathrm{C}_r\mathrm{D}_s\mathrm{B}_t}\right) = \langle v\rangle \pi b_{max}^2 \left\{ \frac{1}{N_{\mathrm{A}_p\mathrm{B}_q}} \sum_{j=1}^{N_{\mathrm{A}_p\mathrm{B}_q,\mathrm{C}_r\mathrm{D}_s\mathrm{C}_t}} \left(E_{\mathrm{A}}^i\right)^{2m} - \left[\frac{1}{N_{\mathrm{A}_p\mathrm{B}_q}} \sum_{j=1}^{N_{\mathrm{A}_p\mathrm{B}_q,\mathrm{C}_r\mathrm{D}_s\mathrm{B}_t}} \left(E_{\mathrm{A}}^i\right)^{m} \right]^2 \right\} \tag{D.7}$$

$$\begin{aligned}\mathrm{var}\left({}^{m}\bar{C}_{\mathrm{A}_p\mathrm{B}_q,\mathrm{C}_r\mathrm{D}_s\mathrm{B}_t}\right) =& \langle v\rangle \pi b_{max}^2 \\ & \times \left\{ \frac{1}{N_{\mathrm{A}_p\mathrm{B}_q}} \sum_{j=1}^{N_{\mathrm{A}_p\mathrm{B}_q,\mathrm{C}_r\mathrm{D}_s\mathrm{B}_t}} \left(\left(E_{\mathrm{A}}^i\right)^{m} \frac{Q_{\mathrm{C}_k}^{(0)}(T_{\mathrm{C}_r}^{\mathrm{int}})}{Q_{\mathrm{C}_k}^{(0)}(T)} \frac{Q_{\mathrm{D}_l}^{(0)}(T_{\mathrm{D}_s}^{\mathrm{int}})}{Q_{\mathrm{D}_l}^{(0)}(T)} \frac{Q_{\mathrm{B})m}^{(0)}(T_{\mathrm{B}_t}^{\mathrm{int}})}{Q_{\mathrm{B}_m}^{(0)}(T)} \right)^2 \right. \\ & \left. - \left[\frac{1}{N_{\mathrm{A}_p\mathrm{B}_q}} \sum_{j=1}^{N_{\mathrm{A}_p\mathrm{B}_q,\mathrm{C}_r\mathrm{D}_s\mathrm{B}_t}} \left(E_{\mathrm{A}}^i\right)^{m} \frac{Q_{\mathrm{C}_k}^{(0)}(T_{\mathrm{C}_r}^{\mathrm{int}})}{Q_{\mathrm{C}_k}^{(0)}(T)} \frac{Q_{\mathrm{D}_l}^{(0)}(T_{\mathrm{D}_s}^{\mathrm{int}})}{Q_{\mathrm{D}_l}^{(0)}(T)} \frac{Q_{\mathrm{B})m}^{(0)}(T_{\mathrm{B}_t}^{\mathrm{int}})}{Q_{\mathrm{B}_m}^{(0)}(T)} \right]^2 \right\}\end{aligned} \tag{D.8}$$

where $N_{\mathrm{A}_p\mathrm{B}_q}$ denotes the number of trajectories which start with molecule A in group p and molecule B in group q. The summations in these expressions are over the number of trajectories which result in a given outcome. That is, $N_{\mathrm{A}_p\mathrm{B}_q,\mathrm{C}_r\mathrm{D}_s\mathrm{B}_t}$ denotes the number of trajectories which

start with molecule A in group p and molecule B in group q and end with species C in group r, species D in group s, and species B in group t.

Appendix E

Convergence of Kinetic Data for MGMET-QCT Model

A comparison of results obtained using the MGMET-QCT model presented in Chapter 4 using uniform bins at 10 000 K and varying the number of trajectories used to compute kinetic data is shown in Figs. E.1 and E.2. Because the convergence of the QCT data generally improves with increasing temperature as we have more reacting trajectories, a similar analysis was done at higher temperatures but is not shown because the 10 000 K case was the worst case scenario. The macroscopic observables (composition and internal energy) are extremely close using varying numbers of total trajectories. However, looking at the percent difference between the highest number of trajectories (283.2 million) and a reduced set of trajectories demonstrates some small differences at early times in the simulation. These errors are very low, and occur in the very early stages of excitation and dissociation, before significant chemical reactions have occurred.

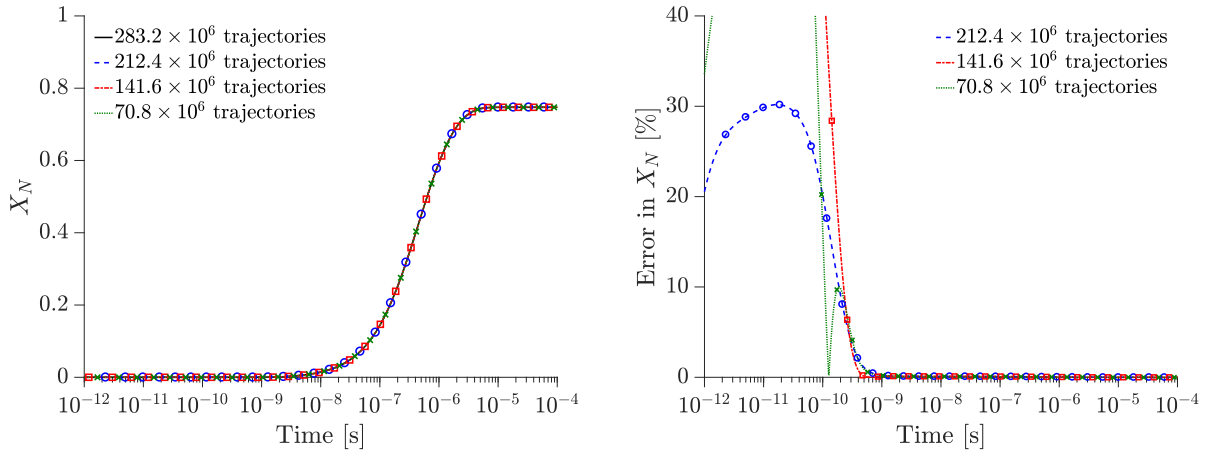

(a) Composition. **(b)** Error in composition.

Figure E.1: Convergence of kinetic data for energy binned MGMET-QCT model at 10 000 K (see Chapter 4).

A similar comparison for the vibrational bins at 10 000 K is shown in Figs. E.3 and E.4. Again,

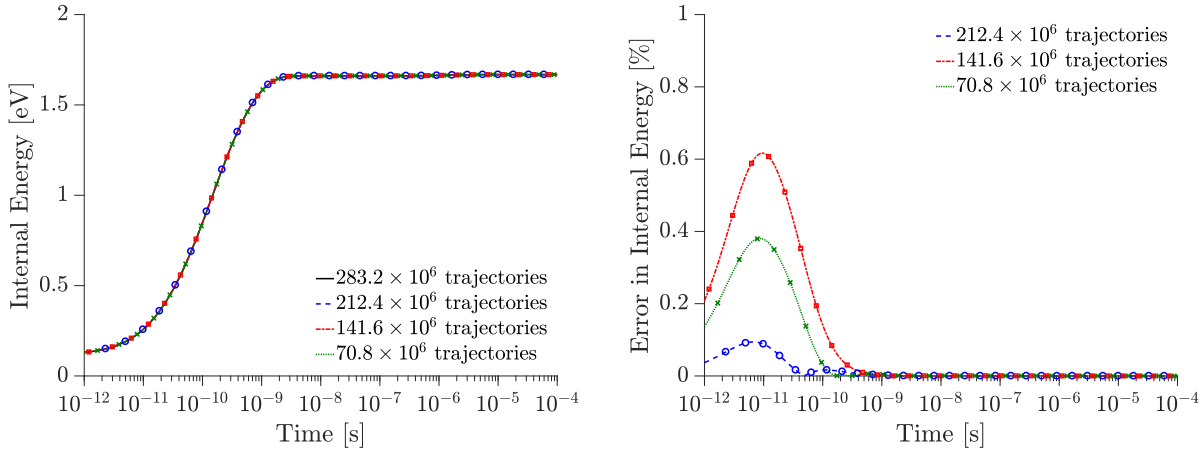

(a) Internal energy. **(b)** Error in internal energy.

Figure E.2: Convergence of kinetic data for energy binned MGMET-QCT model at 10 000 K (see Chapter 4).

the macroscopic observables (composition and internal energy) are extremely close using varying numbers of total trajectories, with errors arising in the very early stages of dissociation but decaying once significant dissociation has occurred.

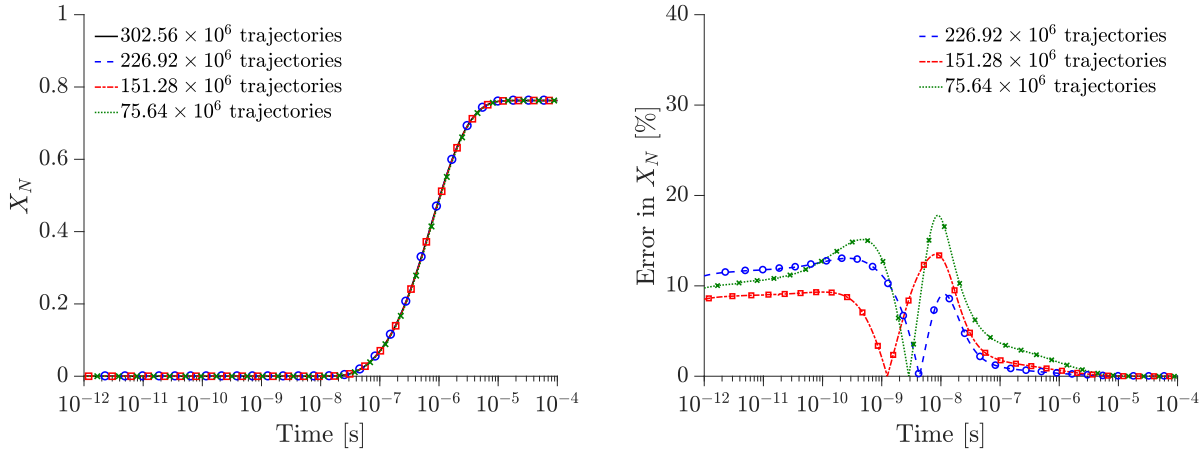

(a) Composition. **(b)** Error in composition.

Figure E.3: Convergence of kinetic data for vibrational binned MGMET-QCT model at 10 000 K (see Chapter 4).

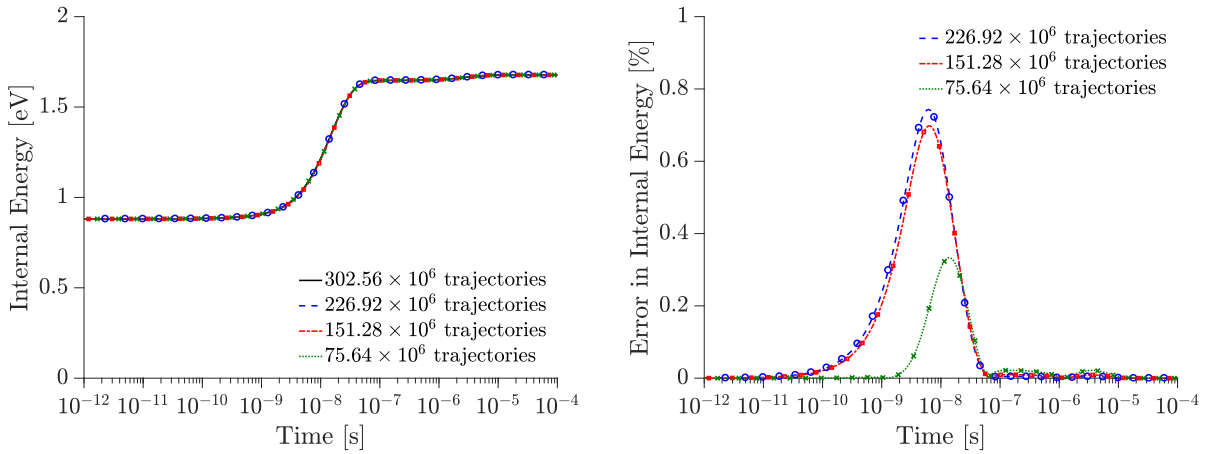

(a) Internal energy.

(b) Error in internal energy.

Figure E.4: Convergence of kinetic data for vibrational binned MGMET-QCT model at 10 000 K (see Chapter 4).

Appendix F

Calculating Kinetic Data for a Reduced Number of Groups

In order to bypass the cost of calculating kinetic data for each new grouping, using a mapping between the two groupings, we can construct the kinetic data for more coarse groupings.

F.1 Inelastic processes

Suppose now instead of calculating kinetic data for groups (p, q, r, s), we want it for groups (t, u, v, w), where groups (p, r) and (t, v) belong to molecule A and groups (q, s) and (u, w) belong to molecule B. Let the sets $(\mathcal{I}_t, \mathcal{I}_u, \mathcal{I}_v, \mathcal{I}_w)$ denote the groups (*i.e.*, p, q, r, s) which are contained in groups (t, u, v, w). Therefore, we can express the reaction rate coefficients ($m = 0$) and energy transfer coefficients ($m = 1$) for the coarse groups (t, u, v, w) in terms of those for the finer groups (p, q, r, s):

$$ {}^{m}K_{tu,vw} = \frac{1}{\sum\limits_{p\in\mathcal{I}_t} Q^{(0)}_{\mathrm{A}_p}(T^{\mathrm{int}}_{\mathrm{A}_t})} \frac{1}{\sum\limits_{q\in\mathcal{I}_u} Q^{(0)}_{\mathrm{B}_q}(T^{\mathrm{int}}_{\mathrm{B}_u})} \sum_{p\in\mathcal{I}_t}\sum_{q\in\mathcal{I}_u}\sum_{r\in\mathcal{I}_v}\sum_{s\in\mathcal{I}_w} {}^{m}K_{pq,rs} Q^{(0)}_{\mathrm{A}_p}(T^{\mathrm{int}}_{\mathrm{A}_t}) Q^{(0)}_{\mathrm{B}_q}(T^{\mathrm{int}}_{\mathrm{B}_u}) \qquad \text{(F.1)} $$

$$ {}^{m}\bar{K}_{vw,tu} = \frac{1}{\sum\limits_{r\in\mathcal{I}_v} Q^{(0)}_{\mathrm{A}_r}(T^{\mathrm{int}}_{\mathrm{A}_v})} \frac{1}{\sum\limits_{s\in\mathcal{I}_w} Q^{(0)}_{\mathrm{B}_s}(T^{\mathrm{int}}_{\mathrm{B}_w})} \sum_{p\in\mathcal{I}_t}\sum_{q\in\mathcal{I}_u}\sum_{r\in\mathcal{I}_v}\sum_{s\in\mathcal{I}_w} {}^{m}\bar{K}_{rs,pq} Q^{(0)}_{\mathrm{A}_r}(T^{\mathrm{int}}_{\mathrm{A}_v}) Q^{(0)}_{\mathrm{B}_s}(T^{\mathrm{int}}_{\mathrm{B}_w}) \qquad \text{(F.2)} $$

F.2 Exchange processes

For exchange processes, again we consider a "fine" grouping made up of groups (p, q, r, s) for molecules (A, B, C, D) respectively. The "coarse" grouping is made up of groups (t, u, v, w) again for molecules (A, B, C, D) respectively. Let the sets $(\mathcal{I}_t, \mathcal{I}_u, \mathcal{I}_v, \mathcal{I}_w)$ denote the groups (*i.e.*, p, q, r, s) which are contained in groups (t, u, v, w). Therefore, we can express the reaction rate coefficients ($m = 0$) and energy transfer coefficients ($m = 1$) for the coarse groups (t, u, v, w) in terms of those

for the finer groups (p, q, r, s):

$$
\begin{aligned}
{}^{m}K_{\mathrm{A}_t\mathrm{B}_u,\mathrm{C}_v\mathrm{D}_w} =& \frac{1}{\sum\limits_{p\in\mathcal{I}_t} Q^{(0)}_{\mathrm{A}_p}(T^{\mathrm{int}}_{\mathrm{A}_t})} \frac{1}{\sum\limits_{q\in\mathcal{I}_u} Q^{(0)}_{\mathrm{B}_q}(T^{\mathrm{int}}_{\mathrm{B}_u})} \\
& \times \sum_{p\in\mathcal{I}_t}\sum_{q\in\mathcal{I}_u}\sum_{r\in\mathcal{I}_v}\sum_{s\in\mathcal{I}_w} {}^{m}K_{\mathrm{A}_p\mathrm{B}_q,\mathrm{C}_r\mathrm{D}_s} Q^{(0)}_{\mathrm{A}_p}(T^{\mathrm{int}}_{\mathrm{A}_t}) Q^{(0)}_{\mathrm{B}_q}(T^{\mathrm{int}}_{\mathrm{B}_u}) \qquad \text{(F.3)} \\
{}^{m}\bar{K}_{\mathrm{A}_t\mathrm{B}_u,\mathrm{C}_v\mathrm{D}_w} =& \frac{1}{\sum\limits_{r\in\mathcal{I}_v} Q^{(0)}_{\mathrm{C}_r}(T^{\mathrm{int}}_{\mathrm{C}_v})} \frac{1}{\sum\limits_{s\in\mathcal{I}_w} Q^{(0)}_{\mathrm{D}_s}(T^{\mathrm{int}}_{\mathrm{D}_w})} \\
& \times \sum_{p\in\mathcal{I}_t}\sum_{q\in\mathcal{I}_u}\sum_{r\in\mathcal{I}_v}\sum_{s\in\mathcal{I}_w} {}^{m}\bar{K}_{\mathrm{A}_p\mathrm{B}_q,\mathrm{C}_r\mathrm{D}_s} Q^{(0)}_{\mathrm{C}_r}(T^{\mathrm{int}}_{\mathrm{C}_v}) Q^{(0)}_{\mathrm{D}_s}(T^{\mathrm{int}}_{\mathrm{D}_w}) \qquad \text{(F.4)}
\end{aligned}
$$

F.3 Dissociation-excitation processes

For combined dissociation-excitation processes, again we consider a "fine" grouping made up of groups (p, q, r, s, t) for species (A, B, C, D, B) respectively. The "coarse" grouping is made up group (u, v, w, x, y) again for species (A, B, C, D, B) respectively. Let the sets $(\mathcal{I}_u, \mathcal{I}_v, \mathcal{I}_w, \mathcal{I}_x, \mathcal{I}_y)$ denote the groups (*i.e.*, p, q, r, s, t) which are contained in groups (u, v, w, x, y). Therefore, we can express the reaction rate coefficients ($m = 0$) and energy transfer coefficients ($m = 1$) for the coarse groups (u, v, w, x, y) in terms of those for the finer groups (p, q, r, s, t):

$$
\begin{aligned}
{}^{m}C_{\mathrm{A}_u\mathrm{B}_v,\mathrm{C}_w\mathrm{D}_x\mathrm{E}_y} =& \frac{1}{\sum\limits_{p\in\mathcal{I}_t} Q^{(0)}_{\mathrm{A}_p}(T^{\mathrm{int}}_{\mathrm{A}_t})} \frac{1}{\sum\limits_{q\in\mathcal{I}_u} Q^{(0)}_{\mathrm{B}_q}(T^{\mathrm{int}}_{\mathrm{B}_u})} \\
& \times \sum_{p\in\mathcal{I}_u}\sum_{q\in\mathcal{I}_v}\sum_{r\in\mathcal{I}_w}\sum_{s\in\mathcal{I}_x}\sum_{t\in\mathcal{I}_y} {}^{m}C_{\mathrm{A}_p\mathrm{B}_q,\mathrm{C}_r\mathrm{D}_s\mathrm{B}_t} Q^{(0)}_{\mathrm{A}_p}(T^{\mathrm{int}}_{\mathrm{A}_t}) Q^{(0)}_{\mathrm{B}_q}(T^{\mathrm{int}}_{\mathrm{B}_u}) \qquad \text{(F.5)} \\
{}^{m}\bar{C}_{\mathrm{A}_u\mathrm{B}_v,\mathrm{C}_w\mathrm{D}_x\mathrm{B}_y} =& \frac{1}{\sum\limits_{r\in\mathcal{I}_w} Q^{(0)}_{\mathrm{C}_r}(T^{\mathrm{int}}_{\mathrm{C}_w})} \frac{1}{\sum\limits_{s\in\mathcal{I}_x} Q^{(0)}_{\mathrm{D}_s}(T^{\mathrm{int}}_{\mathrm{D}_x})} \frac{1}{\sum\limits_{t\in\mathcal{I}_y} Q^{(0)}_{\mathrm{B}_t}(T^{\mathrm{int}}_{\mathrm{B}_y})} \\
& \times \sum_{p\in\mathcal{I}_u}\sum_{q\in\mathcal{I}_v}\sum_{r\in\mathcal{I}_w}\sum_{s\in\mathcal{I}_x}\sum_{t\in\mathcal{I}_y} {}^{m}\bar{C}_{\mathrm{A}_p\mathrm{B}_q,\mathrm{C}_r\mathrm{D}_s\mathrm{B}_t} Q^{(0)}_{\mathrm{C}_r}(T^{\mathrm{int}}_{\mathrm{C}_w}) Q^{(0)}_{\mathrm{D}_s}(T^{\mathrm{int}}_{\mathrm{D}_x}) Q^{(0)}_{\mathrm{B}_t}(T^{\mathrm{int}}_{\mathrm{B}_y}) \qquad \text{(F.6)}
\end{aligned}
$$

This procedure eliminates the need to compute kinetic data for "coarser" groupings, as long as the "coarse" groups contain entire groups from a "finer" grouping. This can be done for either the MGME-QCT thermal or linear model (*i.e.*, for reaction rate coefficients only, or for both reaction rate coefficients and energy transfer coefficients).

Appendix G

Internal Temperature Fitting

For the reaction rate coefficients and energy transfer coefficients for the $N_2(X^1\Sigma_g^+) - N(^4S_u)$ system in the MGMEL model, the internal temperature dependence of the natural log of the reaction rate coefficients and energy transfer coefficients has been fitted using a second order polynomial in inverse temperature:

$$\ln({}^m K_{pq,rs}) = \left(\frac{a_1^m}{\left(T_S^p\right)^2} + \frac{a_2^m}{T_S^p} + a_3^m \right) \tag{G.1}$$

$$\ln({}^m \bar{K}_{pq,rs}) = \left(\frac{b_1^m}{\left(T_S^p\right)^2} + \frac{b_2^m}{T_S^p} + b_3^m \right) \tag{G.2}$$

$$\ln({}^m C_{pq,r}) = \left(\frac{c_1^m}{\left(T_S^p\right)^2} + \frac{c_2^m}{T_S^p} + c_3^m \right) \tag{G.3}$$

$$\ln({}^m \bar{C}_{pq,r}) = \left(\frac{d_1^m}{\left(T_S^p\right)^2} + \frac{d_2^m}{T_S^p} + d_3^m \right) \tag{G.4}$$

where (a_1^m, a_2^m, a_3^m), (b_1^m, b_2^m, b_3^m), (c_1^m, c_2^m, c_3^m), and (d_1^m, d_2^m, d_3^m) denote the fitting coefficients.

References

[1] Anderson, J. D., *Hypersonic and High Temperature Gasdynamics*, McGraw-Hill, New York, NY, 1989.

[2] Park, C., *Nonequilibrium Hypersonic Aerothermodynamics*, John Wiley & Sons, New York, NY, 1990.

[3] Appleton, J. P. and Bray, K. N. C., "The conservation equations for a non-equilibrium plasma," *Journal of Fluid Mechanics*, Vol. 20, No. 4, 1964, pp. 659–672.

[4] Lee, J.-H., "Basic Governing Equations for the Flight Regimes of Aeroassisted Orbital Transfer Vehicles," *19th AIAA Thermophysics Conference*, AIAA Paper 1984–1729, Snowmass, CO, 1984.

[5] Park, C., "Two-temperature interpretation of dissociation rate data for N_2 and O_2," *26th AIAA Aerospace Sciences Meeting*, AIAA Paper 1988–458, Reno, NV, 1988.

[6] Park, C., "Assessment of Two-Temperature Kinetic Model for Ionizing Air," *Journal of Thermophysics and Heat Transfer*, Vol. 3, No. 3, 1989, pp. 233–244.

[7] Park, C., "Review of Chemical-Kinetic Problems of Future NASA missions, I: Earth Entries," *Journal of Thermophysics and Heat Transfer*, Vol. 7, No. 3, 1993, pp. 385–398.

[8] Park, C., Howe, J. T., Jaffe, R. L., and Candler, G. V., "Review of Chemical-Kinetic Problems of Future NASA Missions, II: Mars Entries," *Journal of Thermophysics and Heat Transfer*, Vol. 8, No. 1, 1994, pp. 9–23.

[9] Gnoffo, P. A., Gupta, R. N., and Shinn, J. L., "Conservation equations and physical models for hypersonic air flows in thermal and chemical nonequilibrium," NASA Technical Paper 2867, NASA Langley Research Center, 1989.

[10] Rapp, D. and Sharp, T. E., "Vibrational Energy Transfer in Molecular Collisions Involving Large Transition Probabilities," *The Journal of Chemical Physics*, Vol. 38, No. 11, 1963, pp. 2641–2648.

[11] Capitelli, M., editor, *Nonequilibrium Vibrational Kinetics*, Vol. 39 of *Topics in Current Physics*, Springer, Berlin, 1986.

[12] Rapp, D. and Englander-Golden, P., "Resonant and Near-Resonant Vibrational-Vibrational Energy Transfer between Molecules in Collisions," *The Journal of Chemical Physics*, Vol. 40, No. 2, 1964, pp. 573–575.

[13] Treanor, C. E., Rich, J. W., and Rehm, R. G., "Vibrational Relaxation of Anharmonic Oscillators with Exchange-Dominated Collisions," *The Journal of Chemical Physics*, Vol. 48, No. 4, 1968, pp. 1798–1807.

[14] Marrone, P. V. and Treanor, C. E., "Chemical Relaxation with Preferential Dissociation from Excited Vibrational Levels," *The Physics of Fluids*, Vol. 6, No. 9, 1963, pp. 1215–1221.

[15] Schwartz, R. N., Slawsky, Z. I., and Herzfeld, K. F., "Calculation of Vibrational Relaxation Times in Gases," *The Journal of Chemical Physics*, Vol. 20, No. 10, 1952, pp. 1591–1599.

[16] Vincenti, W. J. and Kruger, C. H., *Introduction to Physical Gas Dynamics*, John Wiley & Sons, New York, NY, 1965.

[17] Millikan, R. C. and White, D. R., "Systematics of Vibrational Relaxation," *The Journal of Chemical Physics*, Vol. 39, No. 12, 1963, pp. 3209–3213.

[18] Park, C., "Problems of Rate Chemistry in the Flight Regimes of Aeroassisted Orbital Transfer Vehicles," *Thermal Design of Aeroassisted Orbital Transfer Vehicles*, edited by H. F. Nelson, Vol. 96 of *Progress in Astronautics and Aeronautics*, American Institute of Aeronautics and Astronautics, 1985, pp. 511–537.

[19] Capitelli, M., Ferreira, C. M., Gordiets, B. F., and Osipov, A. I., *Plasma Kinetics in Atmospheric Gases*, Vol. 31 of *Springer Series on Atomic, Optical, and Plasma Physics*, Springer, Berlin, 2000.

[20] Hammerling, P., Teare, J. D., and Kivel, B., "Theory of Radiation from Luminous Shock Waves in Nitrogen," *The Physics of Fluids*, Vol. 2, No. 4, 1959, pp. 422–426.

[21] Losev, S., "Two temperature chemical kinetics in gas dynamics," *AIAA Fluid Dynamics Conference*, AIAA Paper 1996–2026, New Orleans, LA, 1996.

[22] Park, C., "Assessment of Two-Temperature Kinetic Model for Dissociating and Weakly Ionizing Nitrogen," *Journal of Thermophysics and Heat Transfer*, Vol. 2, No. 1, 1988, pp. 8–16.

[23] Ford, D. I. and Johnson, R. E., "Dependence of Rate Constants on Vibrational Temperatures: An Arrhenius Description," *26th AIAA Aerospace Sciences Meeting*, AIAA Paper 1988–461, Reno, NV, 1988.

[24] Olynick, D. R. and Hassan, H. A., "A New Two-Temperature Dissociation Model for Reacting Flows," *Journal of Thermophysics and Heat Transfer*, Vol. 7, No. 4, 1993, pp. 687–696.

[25] Knab, O., Fruehauf, H. H., and Jonas, S., "Multiple temperature descriptions of reaction rate constants with regard to consistent chemical-vibrational coupling," *27th AIAA Thermophysics Conference*, AIAA Paper 1992–2947, Nashville, TN, 1992.

[26] Landrum, D. B. and Candler, G. V., "Development of a new model for vibration-dissociation coupling in nitrogen," *27th AIAA Thermophysics Conference*, AIAA Paper 1992–2853, Nashville, TN, 1992.

[27] Sergievskaya, A. L., Kovach, E. A., Losev, S. A., and Kuznetsov, N. M., "Thermal nonequilibrium models for dissociation and chemical exchange reactions at high temperatures," *31st AIAA Thermophysics Conference*, AIAA Paper 1996–1895, New Orleans, LA, 1996.

[28] Rusanov, V. D., Fridman, A. A., and Sholin, G. V., "The physics of a chemically active plasma with nonequilibirum vibrational excitation of molecules," *Soviet Physics Uspekhi*, Vol. 24, No. 6, 1981, pp. 447–474.

[29] Jaffe, R. L., "Rate Constants for Chemical Reactions in High-Temperature Nonequilibrium Air," *Thermophysical Aspects of Re-Entry Flows*, edited by J. N. Moss and C. D. Scott, Vol. 103 of *Progress in Astronautics and Aeronautics*, American Institute of Aeronautics and Astronautics, 1986, pp. 123–151.

[30] Gordiets, B. F., Osipov, A. I., and Shelepin, L. A., "Nonequilibrium Dissociation Processes and Molecular Lasers," *Soviet Physics JETP*, Vol. 34, No. 2, 1972, pp. 299–305.

[31] Macheret, S. O. and Rich, J. W., "Theory of nonequilibrium dissociation rates behind strong shock waves," *28th AIAA Thermophysics Conference*, AIAA Paper 1993–2860, Orlando, FL, 1993.

[32] Macheret, S. O., Fridman, A. A., Adamovich, I. V., Rich, J. W., and Treanor, C. E., "Mechanisms of nonequilibrium dissociation of diatomic molecules," *6th AIAA/ASME Joint Thermophysics and Heat Transfer Conference*, AIAA Paper 1994–1984, Colorado Springs, CO, 1994.

[33] Robben, F. and Talbot, L., "Measurement of Shock Wave Thickness by the Electron Beam Fluorescence Method," *The Physics of Fluids*, Vol. 9, No. 4, 1966, pp. 633–643.

[34] Marrone, P. V., "Temperature and Density Measurements in Free Jets and Shock Waves," *The Physics of Fluids*, Vol. 10, No. 3, 1967, pp. 521–538.

[35] Pattengill, M. D. and Bernstein, R. B., "Surprisal analysis of classical trajectory calculations of rotationally inelastic cross sections for the Ar-N_2 system; influence of the potential energy surface," *The Journal of Chemical Physics*, Vol. 65, No. 10, 1976, pp. 4007–4015.

[36] Procaccia, I. and Levine, R. D., "Cross sections for rotational energy transfer: An information-theoretic synthesis," *The Journal of Chemical Physics*, Vol. 64, No. 2, 1976, pp. 808–817.

[37] Pritchard, D. E., Smith, N., Driver, R. D., and Brunner, T. A., "Power law scaling for rotational energy transfer," *The Journal of Chemical Physics*, Vol. 70, No. 5, 1979, pp. 2115–2120.

[38] Panesi, M., Jaffe, R. L., Schwenke, D. W., and Magin, T. E., "Rovibrational internal energy transfer and dissociation of $N_2(^1\Sigma_g^+)$-$N(^4S_u)$ system in hypersonic flows," *The Journal of Chemical Physics*, Vol. 138, No. 4, 2013, pp. 044312.

[39] Bultel, A., Chéron, B. G., Bourdon, A., Motapon, O., and Schneider, I. F., "Collisional-radiative model in air for earth re-entry problems," *Physics of Plasmas*, Vol. 13, No. 4, 2006, pp. 043502.

[40] Panesi, M., Magin, T. E., Bourdon, A., Bultel, A., and Chazot, O., "Fire II Flight Experiment Analysis by Means of a Collisional-Radiative Model," *Journal of Thermophysics and Heat Transfer*, Vol. 23, No. 2, 2009, pp. 236–248.

[41] Panesi, M., Magin, T. E., Bourdon, A., Bultel, A., and Chazot, O., "Electronic Excitation of Atoms and Molecules for the FIRE II Flight Experiment," *Journal of Thermophysics and Heat Transfer*, Vol. 25, No. 3, 2011, pp. 361–374.

[42] Kapper, M. G. and Cambier, J.-L., "Ionizing shocks in argon. Part I: Collisional-radiative model and steady-state structure," *Journal of Applied Physics*, Vol. 109, No. 11, 2011, pp. 113308.

[43] Bultel, A. and Annaloro, J., "Elaboration of collisional-radiative models for flows related to planetary entries into the Earth and Mars atmospheres," *Plasma Sources Science and Technology*, Vol. 22, No. 2, Mar 2013, pp. 025008.

[44] Macdonald, R. L., Munafò, A., Johnston, C. O., and Panesi, M., "Nonequilibrium radiation and dissociation of CO molecules in shock-heated flows," *Physical Review Fluids*, Vol. 1, Aug 2016, pp. 043401.

[45] Gonzales, D. A. and Varghese, P. L., "Vibrational relaxation models for dilute shock heated gases," *Chemical Physics*, Vol. 195, No. 1, 1995, pp. 83 – 91.

[46] Colonna, G., Armenise, I., Bruno, D., and Capitelli, M., "Reduction of State-to-State Kinetic to Macroscopic Models in Hypersonic Flows," *Journal of Thermophysics and Heat Transfer*, Vol. 20, No. 3, 2006, pp. 477–486.

[47] Josyula, E., Bailey, W. F., and Ruffin, S. M., "Reactive and nonreactive vibrational energy exchanges in nonequilibrium hypersonic flows," *Physics of Fluids*, Vol. 15, No. 10, 2003, pp. 3223–3235.

[48] Aliat, A., Vedula, P., and Josyula, E., "State-to-state modeling of radiation coupled to vibration-translation relaxation and dissociation in nonequilibrium gas flows," *Physical Review E*, Vol. 83, Jun 2011, pp. 067302.

[49] Aliat, A., Vedula, P., and Josyula, E., "State-specific dissociation modeling with multiquantum vibration-translation transitions," *Physical Review E*, Vol. 83, Mar 2011, pp. 037301.

[50] Andrienko, D. A. and Boyd, I. D., "High fidelity modeling of thermal relaxation and dissociation of oxygen," *Physics of Fluids*, Vol. 27, No. 11, 2015, pp. 116101.

[51] Andrienko, D. and Boyd, I. D., "Investigation of oxygen vibrational relaxation by quasi-classical trajectory method," *Chemical Physics*, Vol. 459, No. Supplement C, 2015, pp. 1 – 13.

[52] Andrienko, D. A. and Boyd, I. D., "Master Equation Study of Vibrational and Rotational Relaxations in Oxygen," *Journal of Thermophysics and Heat Transfer*, Vol. 30, No. 3, 2016, pp. 533–552.

[53] Andrienko, D. A. and Boyd, I. D., "Rovibrational energy transfer and dissociation in O_2-O collisions," *The Journal of Chemical Physics*, Vol. 144, No. 10, 2016, pp. 104301.

[54] Andrienko, D. A. and Boyd, I. D., "Thermal relaxation of molecular oxygen in collisions with nitrogen atoms," *The Journal of Chemical Physics*, Vol. 145, No. 1, 2016, pp. 014309.

[55] Andrienko, D. A. and Boyd, I. D., "State-specific dissociation in O_2-O_2 collisions by quasi-classical trajectory method," *Chemical Physics*, Vol. 491, 2017, pp. 74 – 81.

[56] Neitzel, K., Andrienko, D., and Boyd, I. D., "Aerothermochemical Nonequilibrium Modeling for Oxygen Flows," *Journal of Thermophysics and Heat Transfer*, Vol. 31, No. 3, 2017, pp. 634–645.

[57] Andrienko, D. A. and Boyd, I. D., "Kinetic Models of Oxygen Thermochemistry Based on Quasi-Classical Trajectory Analysis," *Journal of Thermophysics and Heat Transfer*, Vol. 32, No. 4, 2018, pp. 904–916.

[58] Panesi, M., Magin, T. E., Munafò, A., Bourdon, A., Jaffe, R., and Schwenke, D. W., "Rovibrational internal energy excitation and dissociation of nitrogen in hypersonic flows," *Proceedings of the Summer Program*, Center for Turbulent Research, Stanford University, Stanford, CA, 2010.

[59] Kim, J. G. and Boyd, I. D., "State-resolved master equation analysis of thermochemical nonequilibrium of nitrogen," *Chemical Physics*, Vol. 415, 2013, pp. 237 – 246.

[60] Benson, S. W. and Fueno, T., "Mechanism of Atom Recombination by Consecutive Vibrational Deactivations," *The Journal of Chemical Physics*, Vol. 36, No. 6, 1962, pp. 1597–1607.

[61] Keck, J. and Carrier, G., "Diffusion Theory of Nonequilibrium Dissociation and Recombination," *The Journal of Chemical Physics*, Vol. 43, No. 7, 1965, pp. 2284–2298.

[62] Kerner, E. H., "NOTE ON THE FORCED AND DAMPED OSCILLATOR IN QUANTUM MECHANICS," *Canadian Journal of Physics*, Vol. 36, No. 3, 1958, pp. 371–377.

[63] Treanor, C. E., "Vibrational Energy Transfer in High-Energy Collisions," *The Journal of Chemical Physics*, Vol. 43, No. 2, 1965, pp. 532–538.

[64] Zelechow, A., Rapp, D., and Sharp, T. E., "Vibrational-Vibrational-Translational Energy Transfer between Two Diatomic Molecules," *The Journal of Chemical Physics*, Vol. 49, No. 1, 1968, pp. 286–299.

[65] Kelley, J. D., "Vibrational Energy Transfer Processes in Collisions between Diatomic Molecules," *The Journal of Chemical Physics*, Vol. 56, No. 12, 1972, pp. 6108–6117.

[66] Adamovich, I. V., Macheret, S. O., Rich, J. W., and Treanor, C. E., "Vibrational Energy Transfer Rates Using a Forced Harmonic Oscillator Model," *Journal of Thermophysics and Heat Transfer*, Vol. 12, No. 1, 1998, pp. 57–65.

[67] Kustova, E. and Nagnibeda, E., "Kinetic model for multi-temperature flows of reacting carbon dioxide mixture," *Chemical Physics*, Vol. 398, 2012, pp. 111 – 117, Chemical Physics of Low-Temperature Plasmas (in honour of Prof Mario Capitelli).

[68] Adamovich, I. V., Rich, J. W., and Macheret, S. O., "Existence of the Bottleneck in Vibrational Relaxation of Diatomic Molecules," *Journal of Thermophysics and Heat Transfer*, Vol. 11, No. 2, 1997, pp. 261–265.

[69] Macheret, S. O. and Adamovich, I. V., "Semiclassical modeling of state-specific dissociation rates in diatomic gases," *The Journal of Chemical Physics*, Vol. 113, No. 17, 2000, pp. 7351–7361.

[70] Rapp, D. and Kassal, T., "Theory of vibrational energy transfer between simple molecules in nonreactive collisions," *Chemical Reviews*, Vol. 69, No. 1, 1969, pp. 61–102.

[71] Procaccia, I. and Levine, R. D., "Vibrational energy transfer in molecular collisions: An information theoretic analysis and synthesis," *The Journal of Chemical Physics*, Vol. 63, No. 10, 1975, pp. 4261–4279.

[72] Haug, K., Truhlar, D. G., and Blais, N. C., "Monte Carlo trajectory and master equation simulation of the nonequilibrium dissociation rate coefficient for Ar+H_2 → Ar+2H at 4500 K," *The Journal of Chemical Physics*, Vol. 86, No. 5, 1987, pp. 2697–2716.

[73] Haug, K., Truhlar, D. G., and Blais, N. C., "Erratum: Monte Carlo trajectory and master equation simulation of the nonequilibrium dissociation rate coefficient for Ar+H_2 → Ar+2H at 4500 K [The Journal of Chemical Physics 86, 2697 (1987)]," *The Journal of Chemical Physics*, Vol. 96, No. 7, 1992, pp. 5556–5557.

[74] Wang, D., Stallcop, J. R., Huo, W. M., Dateo, C. E., Schwenke, D. W., and Partridge, H., "Quantal study of the exchange reaction for N+N_2 using an ab initio potential energy surface," *The Journal of Chemical Physics*, Vol. 118, No. 5, 2003, pp. 2186–2189.

[75] Jaffe, R. L., Schwenke, D. W., Chaban, G., and Huo, W., "Vibrational and rotational excitation and relaxation of nitrogen from accurate theoretical calculations," *46th AIAA Aerospace Sciences Meeting and Exhibit*, AIAA Paper 2008–1208, Reno, NV, 2008.

[76] Chaban, G., Jaffe, R. L., Schwenke, D. W., and Huo, W., "Dissociation cross-sections and rate coefficients for nitrogen from accurate theoretical calculations," *46th AIAA Aerospace Sciences Meeting and Exhibit*, AIAA Paper 2008–1209, Reno, NV, 2008.

[77] Paukku, Y., Yang, K. R., Varga, Z., and Truhlar, D. G., "Global *ab initio* ground-state potential energy surface of N_4," *The Journal of Chemical Physics*, Vol. 139, No. 4, 2013, pp. 044309.

[78] Paukku, Y., Yang, K. R., Varga, Z., and Truhlar, D. G., "Erratum: "Global *ab initio* ground-state potential energy surface of N_4" [The Journal of Chemical Physics 139, 044309 (2013)]," *The Journal of Chemical Physics*, Vol. 140, No. 1, 2014, pp. 019903.

[79] Bender, J. D., Valentini, P., Nompelis, I., Paukku, Y., Varga, Z., Truhlar, D. G., Schwartzentruber, T., and Candler, G. V., "An improved potential energy surface and multi-temperature quasiclassical trajectory calculations of N_2+N_2 dissociation reactions," *The Journal of Chemical Physics*, Vol. 143, No. 5, 2015.

[80] Varga, Z., Paukku, Y., and Truhlar, D. G., "Potential energy surfaces for O + O_2 collisions," *The Journal of Chemical Physics*, Vol. 147, No. 15, 2017, pp. 154312.

[81] Paukku, Y., Yang, K. R., Varga, Z., Song, G., Bender, J. D., and Truhlar, D. G., "Potential energy surfaces of quintet and singlet O_4," *The Journal of Chemical Physics*, Vol. 147, No. 3, 2017, pp. 034301.

[82] Paukku, Y., Varga, Z., and Truhlar, D. G., "Potential energy surface of triplet O_4," *The Journal of Chemical Physics*, Vol. 148, No. 12, 2018, pp. 124314.

[83] Lin, W., Varga, Z., Song, G., Paukku, Y., and Truhlar, D. G., "Global triplet potential energy surfaces for the $N_2(X^1\Sigma)$ + $O(^3P)$ → $NO(X^2\Pi)$ + $N(^4S)$ reaction," *The Journal of Chemical Physics*, Vol. 144, No. 2, 2016, pp. 024309.

[84] Varga, Z., Meana-Pañeda, R., Song, G., Paukku, Y., and Truhlar, D. G., "Potential energy surface of triplet N_2-O_2," *The Journal of Chemical Physics*, Vol. 144, No. 2, 2016, pp. 024310.

[85] Ulusoy, I. S., Andrienko, D. A., Boyd, I. D., and Hernandez, R., "Quantum and quasi-classical collisional dynamics of O_2-Ar at high temperatures," *The Journal of Chemical Physics*, Vol. 144, No. 23, 2016, pp. 234311.

[86] Truhlar, D. G. and Muckerman, J. T., "Reactive Scattering Cross Sections III: Quasiclassical and Semiclassical Methods," *Atom-Molecule Collision Theory. A Guide for the Experimentalist*, edited by R. B. Bernstein, chap. 16, Springer, Boston, MA, 1979, pp. 505–566.

[87] Karplus, M., Porter, R. N., and Sharma, R. D., "Exchange Reactions with Activation Energy. I. Simple Barrier Potential for (H, H_2)," *The Journal of Chemical Physics*, Vol. 43, No. 9, 1965, pp. 3259–3287.

[88] Jaffe, R. L., Schwenke, D. W., and Panesi, M., "First Principles Calculation of Heavy Particle Rate Coefficients," *Hypersonic Nonequilibrium Flows: Fundamentals and Recent Advances*, edited by E. Josyula, Vol. 247 of *Progress in Astronautics and Aeronautics*, chap. 3, American Institute of Aeronautics and Astronautics, 2015, pp. 103–158.

[89] Esposito, F., Garcia, E., and Laganà, A., "Comparisons and scaling rules between N+N_2 and N_2 + N_2 collision induced dissociation cross sections from atomistic studies," *Plasma Sources Science and Technology*, Vol. 26, No. 4, 2017, pp. 045005.

[90] Esposito, F. and Capitelli, M., "Quasiclassical molecular dynamic calculations of vibrationally and rotationally state selected dissociation cross-sections: N+$N_2(v, j)$ →3N," *Chemical Physics Letters*, Vol. 302, No. 1, 1999, pp. 49 – 54.

[91] Esposito, F., Capitelli, M., and Gorse, C., "Quasi-classical dynamics and vibrational kinetics of N+$N_2(v)$ system," *Chemical Physics*, Vol. 257, No. 2, 2000, pp. 193 – 202.

[92] Esposito, F. and Capitelli, M., "QCT calculations for the process $N_2(v)$+N→$N_2(v')$+N in the whole vibrational range," *Chemical Physics Letters*, Vol. 418, No. 4, 2006, pp. 581 – 585.

[93] Esposito, F., Armenise, I., and Capitelli, M., "N-N_2 state to state vibrational-relaxation and dissociation rates based on quasiclassical calculations," *Chemical Physics*, Vol. 331, No. 1, 2006, pp. 1 – 8.

[94] Esposito, F. and Capitelli, M., "The relaxation of vibrationally excited O_2 molecules by atomic oxygen," *Chemical Physics Letters*, Vol. 443, No. 4, 2007, pp. 222 – 226.

[95] Esposito, F., Armenise, I., Capitta, G., and Capitelli, M., "O-O_2 state-to-state vibrational relaxation and dissociation rates based on quasiclassical calculations," *Chemical Physics*, Vol. 351, No. 1, 2008, pp. 91 – 98.

[96] Chaudhry, R. S., Bender, J. D., Schwartzentruber, T. E., and Candler, G. V., "Quasiclassical Trajectory Analysis of Nitrogen for High-Temperature Chemical Kinetics," *Journal of Thermophysics and Heat Transfer*, Vol. 32, No. 4, 2018, pp. 833–845.

[97] Voelkel, S., Varghese, P. L., and Raman, V., "Multitemperature Dissociation Rate of N_2 + N_2 → N_2 + N + N Calculated Using Selective Sampling Quasi-Classical Trajectory Analysis," *Journal of Thermophysics and Heat Transfer*, Vol. 31, No. 4, 2017, pp. 965–975.

[98] Singh, N. and Schwartzentruber, T., "Nonequilibrium internal energy distributions during dissociation," *Proceedings of the National Academy of Sciences*, Vol. 115, No. 1, 2018, pp. 47–52.

[99] Schwartzentruber, T. E., Grover, M. S., and Valentini, P., "Direct Molecular Simulation of Nonequilibrium Dilute Gases," *Journal of Thermophysics and Heat Transfer*, Vol. 32, No. 4, 2018, pp. 892–903.

[100] Valentini, P., Schwartzentruber, T. E., Bender, J. D., Nompelis, I., and Candler, G. V., "Direct molecular simulation of nitrogen dissociation based on an *ab initio* potential energy surface," *Physics of Fluids*, Vol. 27, No. 8, 2015, pp. 086102.

[101] Valentini, P., Schwartzentruber, T. E., Bender, J. D., and Candler, G. V., "Dynamics of nitrogen dissociation from direct molecular simulation," *Physical Review Fluids*, Vol. 1, Aug 2016, pp. 043402.

[102] Kulakhmetov, M., Gallis, M., and Alexeenko, A., "Ab initio-informed maximum entropy modeling of rovibrational relaxation and state-specific dissociation with application to the O_2 + O system," *The Journal of Chemical Physics*, Vol. 144, No. 17, 2016, pp. 174302.

[103] Levine, R. D. and Bernstein, R. B., *Molecular Reaction Dynamics and Chemical Reactivity*, Oxford University Press, New York, NY, 1987.

[104] Panesi, M. and Lani, A., "Collisional radiative coarse-grain model for ionization in air," *Physics of Fluids*, Vol. 25, No. 5, 2013, pp. 057101.

[105] Le, H. P., Karagozian, A. R., and Cambier, J.-L., "Complexity reduction of collisional-radiative kinetics for atomic plasma," *Physics of Plasmas*, Vol. 20, No. 12, 2013, pp. 123304.

[106] Liu, Y., Panesi, M., Sahai, A., and Vinokur, M., "General multi-group macroscopic modeling for thermo-chemical non-equilibrium gas mixtures," *The Journal of Chemical Physics*, Vol. 142, No. 13, 2015, pp. 134109.

[107] Liu, Y., Vinokur, M., Panesi, M., and Magin, T. E., "A multi-group maximum entropy model for thermo-chemical nonequilibrium," *10th AIAA/ASME Joint Thermophysics and Heat Transfer Conference*, AIAA Paper 2010–4332, Chicago, IL, 2010.

[108] Liu, Y., Panesi, M., Sahai, A., and Vinokur, M., "General multi-group macroscopic modeling for thermo-chemical non-equilibrium gas mixtures," *7th AIAA Theoretical Fluid Mechanics Conference*, AIAA Paper 2014–3205, Atlanta, GA, 2014.

[109] Munafò, A., Panesi, M., Jaffe, R. L., Colonna, G., Bourdon, A., and Magin, T. E., "QCT-based vibrational collisional models applied to nonequilibrium nozzle flows," *European Physical Journal D*, Vol. 66, 2012, pp. 188.

[110] Munafò, A., Panesi, M., and Magin, T. E., "Boltzmann rovibrational collisional coarse-grained model for internal energy excitation and dissociation in hypersonic flows," *Physical Review E*, Vol. 89, Feb 2014, pp. 023001.

[111] Munafò, A. and Magin, T. E., "Modeling of stagnation-line nonequilibrium flows by means of quantum based collisional models," *Physics of Fluids*, Vol. 26, No. 9, 2014, pp. 097102.

[112] Munafò, A., Liu, Y., and Panesi, M., "Modeling of dissociation and energy transfer in shock-heated nitrogen flows," *Physics of Fluids*, Vol. 27, No. 12, 2015, pp. 127101.

[113] Munafò, A., Mansour, N. N., and Panesi, M., "A Reduced-order NLTE Kinetic Model for Radiating Plasmas of Outer Envelopes of Stellar Atmospheres," *Astrophysical Journal*, Vol. 838, No. 2, 2017, pp. 126.

[114] Guy, A., Bourdon, A., and Perrin, M.-Y., "Consistent multi-internal-temperatures models for nonequilibrium nozzle flows," *Chemical Physics*, Vol. 420, 2013, pp. 15 – 24.

[115] Sahai, A., Lopez, B., Johnston, C. O., and Panesi, M., "Adaptive coarse graining method for energy transfer and dissociation kinetics of polyatomic species," *The Journal of Chemical Physics*, Vol. 147, No. 5, 2017, pp. 054107.

[116] Macdonald, R. L., Jaffe, R. L., Schwenke, D. W., and Panesi, M., "Construction of a coarse-grain quasi-classical trajectory method. I. Theory and application to N_2-N_2 system," *The Journal of Chemical Physics*, Vol. 148, No. 5, 2018, pp. 054309.

[117] Macdonald, R. L., Grover, M. S., Schwartzentruber, T. E., and Panesi, M., "Construction of a coarse-grain quasi-classical trajectory method. II. Comparison against the direct molecular simulation method," *The Journal of Chemical Physics*, Vol. 148, No. 5, 2018, pp. 054310.

[118] Macdonald, R. L., Jaffe, R. L., and Panesi, M., "Hybrid Reduced Order Model For N_2-N Interactions For Application To Dissociation And Energy Transfer Processes," *Proceedings of the 31st International Symposium on Rarefied Gas Dynamics*, 2018, Accepted.

[119] Esposito, F., Macdonald, R., Boyd, I. D., Neitzel, K., and Andrienko, D. A., "Heavy-particle elementary processes in hypersonic flows," *Hypersonic Meteoroid Entry Physics*, edited by M. C. Gianpiero Colonna and A. Laricchiuta, IOP Series in Plasma Physics, chap. 16, IOP Publishing, 2019.

[120] Ferziger, J. H. and Kaper, H. G., *Mathematical Theory of Transport Processes in Gases*, North Holland Publishing Company, Amsterdam, 1972.

[121] Giovangigli, V., *Multicomponent Flow Modeling*, Modeling and Simulation in Science, Engineering and Technology, Birkhäuser, Basel, 1999.

[122] Oxenius, J., *Kinetic Theory of Particles and Photons: Theoretical Foundations of Non-LTE Plasma Spectroscopy*, Vol. 20 of *Springer Series in Electronics and Photonics*, Springer, Berlin, 1986.

[123] Nagnibeda, E. and Kustova, E., *Non-Equilibrium Reacting Gas Flows*, Heat and Mass Transfer, Springer, Berlin, 2009.

[124] Kennard, E. H., *The Kinetic Theory of Gases: With an Introduction to Statistical Mechanics*, McGraw-Hill, New York, NY, 1938.

[125] Jaffe, R. L., Schwenke, D. W., and Chaban, G., "Vibration-rotation excitation and dissociation in N_2-N_2 collisions from accurate theoretical calculations," *10th AIAA/ASME Joint Thermophysics and Heat Transfer Conference*, AIAA Paper 2010–4517, Chicago, IL, 2010.

[126] Schwenke, D. W., "Calculations of rate constants for the three-body recombination of H_2 in the presence of H_2," *The Journal of Chemical Physics*, Vol. 89, No. 4, 1988, pp. 2076–2091.

[127] Le Roy, R. J., Huang, Y., and Jary, C., "An accurate analytic potential function for ground-state N_2 from a direct-potential-fit analysis of spectroscopic data," *The Journal of Chemical Physics*, Vol. 125, No. 16, 2006, pp. 164310.

[128] Lagana, A., Garcia, E., and Ciccarelli, L., "Deactivation of vibrationally excited nitrogen molecules by collision with nitrogen atoms," *The Journal of Physical Chemistry*, Vol. 91, No. 2, 1987, pp. 312–314.

[129] Babikov, D., Zhang, P., and Morokuma, K., "Cyclic-N_3. I. An accurate potential energy surface for the ground doublet electronic state up to the energy of the $^2A_2/^2B_1$ conical intersection," *The Journal of Chemical Physics*, Vol. 121, No. 14, 2004, pp. 6743–6749.

[130] Wang, Z., Kerkines, I. S. K., Morokuma, K., and Zhang, P., "Analytical potential energy surfaces for N_3 low-lying doublet states," *The Journal of Chemical Physics*, Vol. 130, No. 4, 2009, 044313.

[131] Galvão, B. R. L. and Varandas, A. J. C., "Ab Initio Based Double-Sheeted DMBE Potential Energy Surface for $N_3(^2A'')$ and Exploratory Dynamics Calculations," *The Journal of Physical Chemistry A*, Vol. 115, No. 44, 2011, pp. 12390–12398, PMID: 21928767.

[132] Jaffe, R. L., Grover, M., Venturi, S., Schwenke, D. W., Valentini, P., Schwartzentruber, T. E., and Panesi, M., "Comparison of Potential Energy Surfaces and Computed Rate Coefficients for N_2 Dissociation," *Journal of Thermophysics and Heat Transfer*, Vol. 32, No. 4, 2018, pp. 869–881.

[133] Purvis, G. D. and Bartlett, R. J., "A full coupled-cluster singles and doubles model: The inclusion of disconnected triples," *The Journal of Chemical Physics*, Vol. 76, No. 4, 1982, pp. 1910–1918.

[134] Raghavachari, K., Trucks, G. W., Pople, J. A., and Head-Gordon, M., "A fifth-order perturbation comparison of electron correlation theories," *Chemical Physics Letters*, Vol. 157, No. 6, 1989, pp. 479 – 483.

[135] Gdanitz, R. J. and Ahlrichs, R., "The averaged coupled-pair functional (ACPF): A size-extensive modification of MR CI(SD)," *Chemical Physics Letters*, Vol. 143, No. 5, 1988, pp. 413 – 420.

[136] Sharma, S. P., Huo, W. M., and Park, C., "Rate Parameters for Coupled Vibration-Dissociation in a Generalized SSH Approximation," *Journal of Thermophysics and Heat Transfer*, Vol. 6, No. 1, 1992, pp. 9–21.

[137] Barker, J. R., Yoder, L. M., and King, K. D., "Vibrational Energy Transfer Modeling of Nonequilibrium Polyatomic Reaction Systems," *The Journal of Physical Chemistry A*, Vol. 105, No. 5, 2001, pp. 796–809.

[138] Jaffe, R. L., Schwenke, D. W., Grover, M., Valentini, P., Schwartzentruber, T. E., Venturi, S., and Panesi, M., "Comparison of quantum mechanical and empirical potential energy surfaces and computed rate coefficients for N_2 dissociation," *54th AIAA Aerospace Sciences*, AIAA Paper 2016–0503, San Diego CA, 2016.

[139] Appleton, J. P., Steinberg, M., and Liquornik, D. J., "Shock-Tube Study of Nitrogen Dissociation using Vacuum-Ultraviolet Light Absorption," *The Journal of Chemical Physics*, Vol. 48, No. 2, 1968, pp. 599–608.

[140] Kewley, D. and Hornung, H., "Free-piston shock-tube study of nitrogen dissociation," *Chemical Physics Letters*, Vol. 25, No. 4, 1974, pp. 531 – 536.

[141] Hanson, R. K. and Baganoff, D., "Shock-Tube Study of Nitrogen Dissociation Rates Using Pressure Measurements," *AIAA Journal*, Vol. 10, No. 2, 1972, pp. 211–215.

[142] Boyd, I. D. and Josyula, E., "State resolved vibrational relaxation modeling for strongly nonequilibrium flows," *Physics of Fluids*, Vol. 23, No. 5, 2011, pp. 057101.

[143] Appleton, J. P. and Steinberg, M., "Vacuum-Ultraviolet Absorption of Shock-Heated Vibrationally Excited Nitrogen," *The Journal of Chemical Physics*, Vol. 46, No. 4, 1967, pp. 1521–1529.

[144] Koura, K., "Monte Carlo direct simulation of rotational relaxation of diatomic molecules using classical trajectory calculations: Nitrogen shock wave," *Physics of Fluids*, Vol. 9, No. 11, 1997, pp. 3543–3549.

[145] Koura, K., "Monte Carlo direct simulation of rotational relaxation of nitrogen through high total temperature shock waves using classical trajectory calculations," *Physics of Fluids*, Vol. 10, No. 10, 1998, pp. 2689–2691.

[146] Matsumoto, H. and Koura, K., "Comparison of velocity distribution functions in an argon shock wave between experiments and Monte Carlo calculations for Lennard-Jones potential," *Physics of Fluids A: Fluid Dynamics*, Vol. 3, No. 12, 1991, pp. 3038–3045.

[147] Norman, P., Valentini, P., and Schwartzentruber, T., "GPU-accelerated Classical Trajectory Calculation Direct Simulation Monte Carlo applied to shock waves," *Journal of Computational Physics*, Vol. 247, 2013, pp. 153 – 167.

[148] Munafò, A., *Multi-Scale Models and Computational Methods for Aerothermodynamics*, Ph.D. thesis, Ecole Centrale Paris, Châtenay-Malabry, France, 2014.

[149] Jayaraman, V., Liu, Y., and Panesi, M., "Multi-Group Maximum Entropy Model for Translational Non-Equilibrium," *47th AIAA Thermophysics Conference*, AIAA Paper 2017–4024, Denver, CO, 2017.